UNIVERSIDAD COMPLUTENSE DE MADRID
FACULTAD DE CIENCIAS QUÍMICAS
DEPARTAMENTO DE QUÍMICA FÍSICA

TESIS DOCTORAL

Estudio por simulación de fluctuaciones capilares:

interfases fluidas, adsorbidas y sólida

MEMORIA PARA OPTAR AL GRADO DE DOCTOR
PRESENTADA POR

Jorge Benet Villanueva

Directores

Eduardo Sanz García
Luis González MacDowell

Madrid, 2015

Universidad Complutense de Madrid
Facultad de Ciencias Químicas
Departamento de Química Física I

Estudio por simulación de fluctuaciones capilares: interfases fluidas, adsorbidas y sólidas

Memoria para optar
al grado de Doctor en Ciencias Químicas
realizada por

Jorge Benet Villanueva

Directores:
Dr. Eduardo Sanz García
Dr. Luis González MacDowell

Dpto. Química-Física I

Madrid, 2015

Los resultados de esta Tesis están basados en las siguientes publicaciones:

Capítulo 1: "Disjoining Pressure, Healing Distance, and Film Height Dependent Surface Tension of Thin Wetting Films", Jorge Benet, Jose G. Palanco, Eduardo Sanz and Luis G. MacDowell, *J. Phys. Chem. C*, **118**, 22079-22089 (2014)

Capítulo 2: "Computer simulation study of surface wave dynamics at the crystal–melt interface", Jorge Benet, Luis G. MacDowell and Eduardo Sanz, *J. Chem. Phys.*, **141**, 024307 (2014)

Capítulo 3: "Study of the solid–fluid interface for the Lennard–Jones system", Jorge Benet, Luis G. MacDowell and Eduardo Sanz, *To be submitted*

Capítulo 4: "Interfacial free energy of NaCl solid–liquid interfaces from Capillary Wave Fluctuations", Jorge Benet, Luis G. MacDowell and Eduardo Sanz, *Submitted*

Capítulo 5: "A study of the ice-water interface using the TIP4P/2005 water model", Jorge Benet, Luis G. MacDowell and Eduardo Sanz, *Phys. Chem. Chem. Phys*, **16**, 22159-22166, (2014)

Capítulo 6: "Structure and fluctuations of the premelted liquid film of ice at the triple point", Jorge Benet, Eduardo Sanz and Luis G. MacDowell, *To be submitted*

Capítulo 7: "The area distribution of the intrinsic surface", Jorge Benet, Eduardo Sanz and Luis G. MacDowell, *To be submitted*

Otras publicaciones no incluidas en la tesis:

"Liquid–vapor phase equilibria and surface tension of ethane as predicted by the TraPPe and OPLS models", Jorge Benet, Luis G, MacDowell and Carlos Menduiña, *J. Chem. Eng. Data*, **55**, 5465-5470 (2010)

"Semi–infinite boundary conditions for the simulation of interfaces: The Ar/CO_2 model revisited", Rocío de Gregorio, Jorge Benet, Nebil A. Katcho, Felipe J. Blas and Luis G. MacDowell, *J. Chem. Phys* , **136**, 104703 (2012)

"Capillary fluctuactions and film–height–dependent surface tension of an adsorbed liquid film", Luis G. MacDowell, Jorge Benet and Nebil A. Katcho, *Phys. Rev. Lett*, **111**, 047802 (2013)

"Field–induced sublimation in perfect two–dimensional colloidal crystals" F. Martínez–Pedrero, J. Benet, J. E. F. Rubio, E. Sanz, R. G. Rubio and F. Ortega, , *Phys. Rev. E*, **89**, 012306 (2014)

"Disjoining pressure and the film–height–dependent surface tension of thin liquid films: New insight from capillary wave fluctuations", Luis G. MacDowell, Jorge Benet, Nebil A. Katcho and Jose M. G. Palanco *Advances in Colloid and Interface Science*, **206** , 150–171 (2014)

ÍNDICE

Summary

Introduction

In this thesis we study interfaces of different nature by means of molecular simulation. Specifically we analyse surface waves using the interfacial Hamiltonian model for four different kinds of interfaces: liquid–vapor, solid–liquid, solid–vapor and adsorbed interfaces.

From a theoretical perspective the interfacial Hamiltonian model is revisited with the aim of improving it. This improvement implies the incorporation of the surface tension dependence on the film width for adsorbed films.

The huge variety of systems employed enables us to study a wide range of properties, both static and dynamic. Among all of them, a great part of this work is devoted to the calculation of solid–liquid interfacial free energies, given that they are hardly accessible experimentally and their relevance in nucleation and growth of a crystalline solid.

Finally, we also address the structural caracterisation of interfaces by calculating their interfacial density profiles and by studying their crystalline structure.

With the aim of sustaining our work we perform studies in which we test several methodological aspects.

We carry out all of these studies by employing very relevant models, either because of their wide use or because of the complexity of the systems described. In particular in this thesis we employ the Hard Spheres model, the Lennard–Jones model, the Tosi–Fumi model for sodium chloride and the TIP4P/2005 model of Abascal and Vega for real water.

For the development of the thesis we make use of several methods and analysis tools. In this sense, we use the methods of Monte Carlo, Molecular Dynamics and Molecular Dynamics for hard spheres to perform the simulations, we employ order parameters to distinguish between phases at the interface, and we utilize the Capillary Fluctuation Method to calculate solid–liquid interfacial free energies.

Objectives

This thesis consist of six objectives ranging from theoretical aspects to methodological ones.

1. Study the behaviour of adsorbed interfaces to improve the description given by the interfacial Hamiltonian model. In particular we want to study the surface tension dependence with the film width.

2. Characterise the relaxation of the waves present in the solid–liquid interface. In particular we want to recognise the relaxation mechanisms of surface waves and the time scales in which they occur; as well as calculate the kinetic coefficients which determine the crystal growth velocity.

3. Determine the solid–liquid interfacial free energy of some systems of high relevance such as sodium chloride or water, where experimental measurements are difficult to be carried out and simulation studies provide contradictory results.

4. Characterise the structure of the interfaces studied. Particularly, we want to study structural features such as interfacial profiles and crystalline structure of the solid near the interface.

5. Study some methodological aspects of the capillary fluctuation method such as the interface geometry, system size effects or the way of obtaining the interfacial free energy from the stiffness.

6. Obtain thermodynamic information of an interface from the probability distribution of its intrinsic surface area.

Results

Here we present the results obtained in Part II of this thesis:

- Chapter 1: *Disjoining pressure, healing distance and film height dependet surface tension of thin wetting films.*

  For this study we use a model of Ar adsorbed on a solid substrate under complete wetting conditions. With this model we perform Monte Carlo simulations for films of different width.

  In first place we calculate the disjoining pressure by two different methods. One of them calculates the precise disjoining pressure from bulk properties, while the

other one only accounts for the external field. Both models provide a disjoining pressure whose behaviour can be explained with the Hamaker–Derjaguin model if the films'width is larger than three molecular diameters.

In second place we analyse the capillary fluctuation spectrum in fourier space obtaining the second derivative of the interfacial potential with respect to the film width (h), $g''(h)$, and the surface tension. We compare the results thus obtained for $g''(h)$ with results obtained by thermodynamic integration and results obtained by a new model proposed in this chapter, based on density profiles. Given that the three of them are in good agreement we confirm that $g''(h)$ is dominated by van der Waals interactions. In this case the validity of the Hamaker–Derjaguin model extends for films of more than five molecular diameters.

The analysis of the surface tension reveals a dependence of its value with the film width form thin films. In this chapter we show that such dependence can be explained by taking into account only the influence of the external field.

Finally we calculate the healing parallel correlation length showing the presence of a lower threshold value of about one molecular diameter.

- Chapter 2: *Computer simulation study of surface wave dynamics at the crystal–melt interface.*

  Here we study the relaxation of surface waves at the solid–liquid interface for three different systems, namely, hard spheres, Lennard–Jones and TIP4P/2005 water. By Fourier analysis of these waves we obtain autocorrelation functions of the Fourier modes, which allow us to notice the presence of two distinct time scales: a slow and a fast one.

  For the relaxation process of the slow scale we obtain a power law valid for all the systems. This law can be explained by a diffusive process of the interfacial front as a consequence of its continuous recrystallization and melting.

  We have not managed to characterise the fast relaxation process with such precision, but we think that it is associated with the vibration of interfacial atoms and phonons of the crystal.

  The relaxation process of water is an order of magnitude slower than in the two other models, due to the presence of orientational degrees of freedom.

  Finally we calculate the kinetic coefficients of all the crystalline structures studied.

- Chapter 3: *Study of the solid–fluid interface for the Lennard–Jones system.*

  In this chapter we study the solid–liquid interface for the Lennard–Jones model by means of Molecular Dynamics.

On the one hand we compare quasi-monodimensional and bidimensional geometries for the interface in order to see if the geometry affects the calculation of the stiffness. Both geometries give similar results for all the planes studied but for the (111). In this case the quasi-monodimensional geometry gives two different values for the stiffness of two orientations which should be equivalent according to the theory. Moreover, for one of these orientations we observe a phase transition from an fcc structure to an hcp.

On the other hand we evaluate the ability of the order parameter (employed in the thesis to distinguish if the particles are in a solid or liquid environment) to distinguish the crystalline structure of particles near the interface. We observe a tendency to mistakenly label as hcp particles which are in an fcc network.

- Chapter 4: *Interfacial free energy of NaCl solid–liquid interfaces from Capillary Wave Fluctuations.*

  In this chapter we calculate the γ_{sl} for sodium chloride by means of Molecular Dynamics simulations obtaining a value of 89 $\pm$ 6 mN·m^{-1}. In this study we compare both quasi-monodimensional and bidimensional interface geometries and we observe that all the orientations give similar results except for the (111) plane.

  On the other hand we observe that the stiffness of some orientations show an anomalous behaviour with a sharp drop when approaching the thermodynamic limit. This drop might be interpreted as an unstability of those orientations.

  After rejecting the anomalous results we obtain a value for γ_{sl} of 89 $\pm$ 6 mN·m^{-1}, in good agreement with those obtained from the measurement of nucleation barriers and at odds with those obtained by the measurement of contact angles.

- Chapter 5: *A study of the ice–water interface using the* TIP4P/2005 *water model.*

  In this chapter we study the solid–liquid interface of the TIP4P/2005 model by means of Molecular Dynamics simulations. The orientations here studied include the main crystallographic planes of hexagonal ice.

  The results show that the interfacial width is about 4–5 molecular diameters regardless the plane exposed, and that when we exhibit the basal plane recrystallization may occur as cubic ice in some regions of the interface.

  In this study we also calculate γ_{sl}, obtaining an average value of 27 $\pm$ 2 mN·m^{-1}, and values of 27 $\pm$ 2 mN·m^{-1}, 28 $\pm$ 2 mN·m^{-1} and 28 $\pm$ 2 mN·m^{-1} for the basal, primary prismatic and secondary prismatic planes, respectively.

- Chapter 6: *Structure and fluctuations of the premelted liquid film of ice at the triple point.*

Here we study the triple point of the TIP4P/2005 model by means of Molecular Dynamics simulations. In particular we study the roughness of the interfaces and the behaviour of the fluid film formed on the ice in the ice/vapor interfaces.

The presence of this film creates two surfaces (ice/film and film/vapor), that in a microscopic scale fluctuate as the corresponding independent interfaces ice/water and ice/vapor. However, in a mesoscopic scale such fluctuations are governed by the roughness of the underlying solid and are given by a stiffness which is the sum of the ice/water stiffness and the water/vapor surface tension.

The behaviour of the film can be explained by a model proposed in this chapter and the results show that all the interfaces are rough, at odds with experimental findings.

- Chapter 7: *The area distribution of the intrinsic surface.*

  Here it is studied for the first time the probability distribution of the intrinsic area of an interface. By a theoretical analysis, which incorporates an energetic term and an entropic one, we get an expression for such distribution. With this expression we calculate the surface tension of a liquid–vapor interface for the Lennard–Jones model, showing that its value depends on the resolution chosen to locate the interface.

Conclusions

The more relevant conclusions of this thesis are shown here, classified in three main groups:

General physic behaviour:

- The surface tension of a liquid film adsorbed on a solid substrate depends in the film width. This dependence can be explained taking into account only the field that the solid substrate exerts on the adsorbed film.

  As a consequence of this dependence the parallel correlation length is modified in a term given by the correlation length of the bulk phase.

- Surface waves of the solid–liquid interface relax in two different temporal regimes. The slow regime follows an exponential relaxation, whose characteristic time scales with q^{-2} and it is given by a diffusion process of the interface. This process is due to the continuous recrystallization and melt of the interface. The fast regime, which we have not been able to characterise in such detail, might be consequence of the phonons of the crystal and atomic vibration processes.

- The probability distribution of the intrinsic area of a rough interface depends on the balance between entropy, which tends to increase the area, and the interfacial energy which tends to decrease it. The values we obtained for the surface tension from such distributions depend on the resolution employed to measure the area. There exists a microscopic resolution for which a surface tension obtained by this method agrees with the macroscopic surface tension.

Behaviour of specific systems:

- The solid–liquid interfacial free energy of the Tosi–Fumi model for sodium chloride, obtained with the capillary fluctuation method, is 89 ± 6 mN·m^{-1}. This value is in good agreement with the one obtained by the measure of nucleation barriers and at odds with the one obtained by measurements of contact angles. Within our precision all the planes studied have the same interfacial free energy.

- The stiffness of some orientations of sodium chloride show an anomalous drop when approaching the thermodynamic limit. This drop may be understood as an unstability of the planes involved for some directions of wave propagation.

- Ice/vapor and ice/water interfaces for the TIP4P/2005 model are rough.

- The average solid–liquid interfacial free energy of the TIP4P/2005 model is 27 ± 2 mN·m^{-1}. Although the anisotropy of the interfacial free energy of each plane has not been resolved, our results suggest that the basal plane is the less energetic.

- The TIP4P/2005 model predicts that when the basal plane of hexagonal ice is exposed at the interface, the latter presents alternating regions of cubic and hexagonal ice which change dynamically.

- In the ice/vapor interface appears a film of liquid adsorbed on the ice that results in the existence of two surfaces: ice/film and film/vapor. We have found that in a microscopic scale both surfaces fluctuate as the corresponding independent surfaces ice/water and water/vapor. However, in a mesoscopic scale such fluctuations are governed by the roughness of the underlying solid and are given by an stiffness which is the sum of the ice/water stiffness and the water/vapor surface tension.

Methodological aspects:

- The capillary fluctuation method is capable of providing values for the interfacial energy of rough interfaces, both solid–vapor and solid–liquid, for systems of different nature and complexity such as hard spheres, Lennard–Jones, water or sodium chloride.

- The cubic and hexagonal expansions provide a reliable means for the estimation of the interfacial free energy from the stiffness.
- The accuracy of the capillary fluctuation method has not been capable of determining the anisotropic interfacial free energy for the majority of the systems studied.
- The quasi-monodimensional and bidimensional interface geometries provide the same value for the interfacial stiffness for all the crystallographic orientations studied except when the (111) is exposed at the interface.

Introducción

En nuestro día a día, muchas veces sin ser conscientes de ello, observamos una gran cantidad de situaciones que involucran la existencia de interfases. Por ejemplo, un cubito de hielo formándose en el congelador presenta una interfase entre una fase sólida (el hielo) y una fase líquida (el agua), mientras que cuando calentamos agua en una olla tenemos una interfase entre un líquido (el agua) y un gas (el vapor). El interés que suscitan las interfases se encuentra en que sus propiedades son diferentes a las propiedas volumétricas de las fases involucradas. Así, una interfase formada entre un gas y un líquido, ¿se comportará de forma parecida a como lo hace un gas? ¿lo hará de forma más similar a un líquido? ¿o quizá lo haga de una forma intermedia entre ambos sistemas? Estos cambios en las propiedades, junto con la aparición de otras nuevas por el mero hecho de poner dos fases distintas en contacto, hacen de las interfases unos de los sistemas más interesantes que nos podemos encontrar.

La historia moderna del estudio de interfases se remonta a 1709, cuando Hauksbee realiza los primeros estudios sobre capilaridad [1]. Poco después, en 1751, von Sergen introduce el concepto de tensión superficial para un líquido [2], tan conocido en la actualidad. Sin embargo, el gran avance se produce en 1805 cuando Young publica sus experimentos sobre el ángulo de contacto de un fluido en un capilar [3]. Simultáneamente, y de forma independiente, Laplace publica un estudio formal matemático [4] en el que se obtenían los mismos resultados descritos por Young. Así, de la combinación de ambos trabajos surge la famosa Ecuación de Young-Laplace, que sentó las bases para los estudios de interfases curvas. Cuando salimos del mundo de las interfases curvas y entramos en el de las interfases planas, la forma tradicional de abordar su estudio ha sido mediante la consideración de que estas son superficies o regiones perfectamente planas. Así, en estas regiones, las propiedades van cambiando gradualmente desde las propiedas volumétricas de una fase hasta las de la otra a medida que avanzamos en perpendicular a la interfase. Esta es la idea que esta detrás, por ejemplo, de la superficie divisoria de Gibbs [5], que es la base de la termodinámica de superficies.

Sin embargo, gracias al avance de la ciencia y al desarrollo de técnicas de análisis cada vez más sofisticadas, el estudio de interfases ha ido ganando en complejidad y precisión. Actualmente se sabe que las interfases no son superficies planas sino que,

debido a la agitación térmica, presentan oscilaciones relativamente grandes conocidas como ondas superficiales. Cuando las fuerzas restauradoras de estas ondas son fuerzas debidas a la energía interfacial reciben el nombre de ondas capilares y los primeros estudios sobre ellas, realizados a principios del siglo XX, se deben a Smoluchowski y Kelvin [6, 7]. Como se verá a lo largo de esta tesis, el estudio de las ondas capilares presenta, además del interés teórico en sí, la posibilidad de obtener propiedades tanto estáticas [8] como dinámicas [9] de las interfases.

Otro fenómeno de especial relevancia es el de las transiciones de mojado, descrito independientemente por Cahn[10] y Ebner y Saam [11] en 1977 y observado experimentalmente por primera vez en 1980 [12]. Éstas consisten en una transición de fase que puede ocurrir cuando se coloca un vapor en condiciones de coexistencia con su fase líquida en un recipiente con un sustrato sólido. El estudio de estas transiciones es un área de gran interés debido a la complejidad que presentan ya que pueden aparecer numerosos escenarios[13]. Así, dependiendo de la magnitud de las interacciones sólido–líquido, sólido–vapor y líquido–vapor el sistema podrá pasar de tener una fina película adsorbida sobre el sólido a formar sobre él una película macroscópica. Cuando estas películas son suficientemente gruesas basta con una descripición basada en la termodinámica clásica de superficies para afrontar su estudio. En cambio, en la escala del nanómetro esta descripción ya no es suficiente y se requiere hacer uso de una descripción mas detallada de las interacciones moleculares. Una forma de dar cuenta de estas interacciones es mediante el concepto de presión interfacial o, en inglés, *disjoining pressure*, introducido por Derjaguin [14] y que permite aglutinar todas las interacciones moleculares en una interacción efectiva entre el sustrato sólido y la interfase líquido–vapor. Alternativamente se puede emplear el correspondiente potencial interfacial $g(h)$, definido como la energía libre de una película plana de espesor h en condiciones de coexistencia. Haciendo uso de éste se desarrolla el modelo del Hamiltoniano interfacial, que proporciona una expresión sencilla para las fluctuaciones de las ondas capilares, la cual puede ser comparada tanto con resultados experimentales como de simulación. Este modelo se detallará más adelante.

Como podemos imaginar, en la naturaleza existen multitud de tipos de interfases, cada una de ellas con unas características y complejidades distintas: líquido–gas, líquido–líquido, sólido–gas, sólido–líquido, etc., además de existir interfases de películas adsorbidas, como las mencionadas anteriormente. Para poder entender el comportamiento y propiedades de cualquiera de ellas es importante tener una descripción precisa de su estructura. Para ello se dispone de técnicas como la difracción de luz [15], la difracción de rayos X [16] o la microscopía confocal, técnica galardonada con el premio Nobel en Química en 2014 mediante la cual se ha conseguido la observación directa de ondas capilares para un sistema polimérico coloidal [17].

No menos importante que la caracterización estructural es la caracterización energética, donde aparecen dos términos fundamentales: la tensión superficial, y la energía

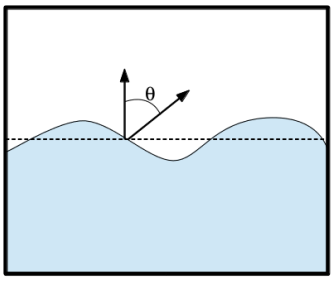

Figura 1. Representación del ángulo θ formado entre la posición promedio de la interfase plana, representada por la línea discontinua, y la posición local intantánea de la interfase.

libre interfacial de exceso, γ. La tensión superficial se define como el trabajo reversible por unidad de área requerido para elongar una superficie preexistente, mientras que la energía libre interfacial de exceso se define como la cantidad de trabajo reversible requerido por unidad de área para crear una nueva superficie entre dos fases en condiciones de coexistencia termodinámica. En el caso de fases fluidas, cuando la energía libre de exceso está expresada en términos del Gran potencial, Ω, la tensión superficial y la energía libre interfacial de exceso son equivalentes [18], por lo que de aquí en adelante utilizaremos el término tensión superficial, expresado como γ, cuando trabajemos con interfases fluidas. Por otra parte, cuando al menos una de las fases implicadas es un sólido aparece un nuevo concepto: la rigidez interfacial, $\widetilde{\gamma}$, ó *stiffness* en inglés. Ésta está definida como la resistencia que presenta la interfase a la deformación, y al igual que la tensión superficial tiene dimensiones de fuerza por unidad de longitud. Energía libre interfacial y rigidez están relacionadas entre sí según [19]

$$\widetilde{\gamma}(\theta) = \gamma(\theta) + \frac{d^2\gamma(\theta)}{d\theta^2} \tag{1}$$

donde θ es el ángulo formado entre el vector normal a la interfase plana y el vector normal a la posición local instantánea de la interfase tal y como se muestra en la Fig. 1.

Finalmente, también es posible caracterizar las propiedades dinámicas de las interfases. En este contexto es muy útil el cálculo de funciones de correlación temporales, puesto que permiten estudiar los tiempos de relajación característicos de los distintos procesos que ocurren en ellas. Por ejemplo, a partir del tiempo de relajación de las ondas capilares presentes en una interfase es posible obtener el coeficiente cinético, μ. Este coeficiente es un parámetro de especial interés dentro del campo del crecimiento cristalino, puesto que corresponde a la constante de proporcionalidad entre la velocidad a la cual avanza el frente cristalino y el grado de subenfriamiento al cual se encuentra

el líquido donde está creciendo el cristal.

De entre todos los tipos de interfases, las más estudiadas son las formadas entre dos fases fluidas, concretamente las formadas entre un líquido y un gas. En estos sistemas la estructura ha sido caracterizada en un gran número de trabajos tanto desde el punto de vista teórico como experimental [20, 18]. Existen, además, multitud de técnicas experimentales que permiten medir su tensión superficial. De entre todas ellas, se pueden destacar el método del anillo de Du Nouy, el método de la placa de Wilhelmy o el método de ascenso capilar. A pesar de todo esto, a nivel microscópico, un campo cada vez más interesante debido al auge de la nanotecnología, aparecen aún muchas incógnitas por resolver. Dentro de este nivel, donde la descripción atomística de los sistemas cobra una importancia vital, la simulación por ordenador se presenta como una herramienta muy útil para el avance del conocimiento en esta dirección [21, 22, 23, 24].

Una gran parte de esta tesis esta dirigida al estudio de interfases sólidas. En estas interfases la complejidad aumenta con respecto a la de las interfases fluidas debido a que la estructura cristalina tiene una gran influencia sobre muchas de sus propiedades [25]. En esta tesis nos enfrentamos a dos tipos de interfases con presencia de sólidos: interfases sólido–liquido e interfases sólido–vapor. Mientras que las interfases sólido–vapor son más fáciles de caracterizar experimentalmente (difracción de rayos X, microscopía de fuerza atómica, etc.), las interfases sólido–líquido presentan mayor dificultad. Uno de los principales retos, y que aún esta lejos de ser resuelto definitivamente, es la determinación de la energía libre interfacial γ_{sl}. Esto se debe a que experimentalmente es muy difícil de medir, llevándose a cabo principalmente bien mediante estudios de nucleación o bien mediante estudios de ángulo de contacto. A partir de estudios de nucleación se puede calcular la γ_{sl}, ya que la teoría clásica de nucleación la relaciona directamente con la temperatura de subenfriamiento crítico para la cristalización del sólido desde el líquido subenfriado [26]. Este método presenta el problema de que γ_{sl} no se mide directamente, sino que se estima en base a una interpretación teórica de la medida de la tasa de nucleación. Por otra parte, los experimentos de nucleación suelen llevar asociado un elevado grado de error debido a la presencia de impurezas y de inhomogeneidades. Además, el valor de γ_{sl} obtenido es el promedio sobre todas las orientaciones cristalográficas, por lo que no es posible resolver la anistropía energética del cristal. El método del ángulo de contacto consiste en medir el ángulo de intersección entre un sólido, un líquido y una frontera de grano (o entre un sólido, un líquido y un vapor) y calcular γ_{sl} mediante la ecuación de Young. En principio es posible determinar γ_{sl} con precisión mediante este método, pero en la práctica hay bastantes aproximaciones y fuentes de error.

Como complemento a los estudios experimentales se han desarrollado importantes estudios teóricos para el cálculo de γ_{sl} [27, 28], donde además se detallan fórmulas explícitas para el perfil de densidad y se establecen conexiones con la interfase líquido–vapor. Igualmente se ha empleado la simulación molecular para calcular γ_{sl} en una gran

cantidad de sistemas entre los que se encuentran: Lennard Jones [29, 30, 31], esferas duras [32, 33, 34, 35], agua [36, 37], metales [38, 39, 40, 41] y cloruro sódico [42, 43, 44, 45].

Como venimos viendo en los párrafos anteriores la simulación molecular es una potente herramienta para el estudio de sistemas a nivel microscópico. Esta técnica está basada en la mecánica estadística, que permite la predicción de propiedades macroscópicas de la materia a partir de su descripción microscópica. El origen de la simulación molecular se debe a Metropolis y colaboradores [46], que en 1953 publicaron el conocido algoritmo de Metropolis, base de la simulación por el método de Monte Carlo. Mediante este método se lleva un sistema a una situación de equilibrio termodinámico a partir de modificaciones aleatorias del mismo. Poco después, en 1959, Alder y Wainwright desarrollaron la técnica de la Dinámica Molecular [47], basada en la resolución numérica de las ecuaciones de Newton, y complementaria al método de Monte Carlo.

Desde la aparición de la simulación molecular su empleo ha ido creciendo exponencialmente y se ha aplicado en prácticamente todos los campos de la ciencia. A pesar del enorme potencial de esta técnica y los buenos resultados que lleva proporcionando durante más de medio siglo, hay que tener siempre presentes las limitaciones existentes. La principal limitación es que, al basarse en el cálculo de interacciones entre moléculas, es necesario conocer con precisión el potencial de interacción entre ellas. Esta tarea es imposible de hacer de forma exacta, y siempre se utilizan aproximaciones de las que hay que ser consciente a la hora de interpretar los resultados. Además hay que tener en cuenta que el cálculo de estos potenciales es una tarea muy costosa computacionalmente, por lo que el tamaño de los sistemas de estudio se ve limitado a sistemas pequeños. Una de las formas más habituales de reducir el tamaño del sistema cuando se realizan estudios de ondas capilares consiste en crear interfases quasi-monodimensionales, donde uno de los lados de la interfase es mucho más pequeño que el otro. De esta forma es posible estudiar la propagación de una onda en la dirección del lado largo de la interfase reduciendo considerablemente el número de moléculas presentes en el sistema. Igualmente, a la hora de llevar experimentos de simulación se recurre a "trucos" como el empleo de termostatos y barostatos, que nos permiten reproducir las condiciones termodinámicas de un laboratorio real, a costa de perturbar el sistema de forma artificial. Por tanto, aunque estas técnicas han demostrado ser eficaces y proporcionar resultados satisfactorios, es necesario saber en todo momento con qué aproximaciones se está trabajando.

Tal y como se ha comentado anteriormente la simulación molecular se ha empleado en numerosos estudios para el cálculo de propiedades en sistemas con interfases. Cuando éstas están compuestas por un único tipo de moléculas es necesario buscar algún criterio que nos permita discernir entre moléculas pertenecientes a cada una de las fases. Con este fin se utilizan parámetros de orden, que son capaces de clasificar a las moléculas en función de su entorno local. En la bibliografía existen multitud de ellos [48, 49, 50, 51], y la elección de uno u otro dependerá tanto del sistema que estemos estudiando como de las fases que queramos separar. En esta tesis se aborda tanto el estudio de propiedades

estáticas como dinámicas de las interfases. Uno de los aspectos fundamentales estudiados en esta tesis es el cálculo de la energía libre interfacial de distintos sistemas, especialmente de aquellos sistemas con interfases sólido–fluido. Actualmente existen distintos métodos que nos permiten obtener la energía libre interfacial de estas interfases, entre los que se encuentran el método de *cleaving* [29], el método de fluctuaciones capilares [38], el método de la metadinámica [52], el método de *seeding* [53], el método de *tethered Monte Carlo* [54] o el método de integración de molde [55]. Sin embargo, a pesar de toda esta variedad, existen muchos sistemas para los cuales no se ha llegado aún a un acuerdo sobre el valor de su γ_{sl}. En esta tesis se estudian algunos de ellos mediante el método de fluctuación de ondas capilares.

En definitiva, existen multitud de tipos de interfases, cada uno de ellos con unas propiedades características distintas a las de las fases volumétricas que las componen. Actualmente estamos viviendo el auge de la nanotecnología, debido a que en esta escala las propiedades de los materiales cambian drásticamente. Con esto se abre la puerta al desarrollo de nuevos dispositivos cada vez más eficaces, no sólo enfocados al desarrollo de la ciencia sino también a mejorar nuestra vida cotidiana. En este contexto, donde las propiedades interfaciales son al menos tan importantes como las propiedades volumétricas parece de especial importancia profundizar en el conocimiento de las primeras y así facilitar el desarrollo de la nanotecnología. Siguiendo este objetivo se han desarrollado diversas técnicas experimentales, algunas de ellas muy sofisticadas, aunque la complejidad de algunos estos sistemas hace que aún queden muchos aspectos por resolver. Por todos estos motivos, esta tesis se centra en el estudio de las ondas capilares presentes en algunos tipos de interfases, empleando para ello la simulación molecular.

Objetivos

El principal objetivo de esta tesis es profundizar en el conocimiento de las interfases mediante el estudio del fenómeno de ondas capilares. Este objetivo tan general se puede concretar en los siguientes puntos:

- Estudiar el comportamiento de interfases adsorbidas con el fin de mejorar la descripción proporcionada por el modelo del Hamiltoniano interfacial. Concretamente se quiere estudiar la dependencia de la tensión superficial y la presión de disjunción con el espesor de la película.

- Caracterizar la relajación de las ondas presentes en una interfase sólido–líquido. En particular se pretende conocer los mecanismos de relajación de las ondas capilares y las escalas de tiempo en las que suceden; además de calcular los coeficientes cinéticos que determinan la velocidad de crecimiento cristalino.

- Estudiar algunos aspectos metodológicos del métodos de fluctuaciones capilares, tales como la geometría de la interfase, el efecto del tamaño del sistema, o el modo de obtención de la energía interfacial a partir de la rigidez.

- Determinar mediante el método de fluctuaciones capilares la energía libre interfacial sólido–liquido de algunos sistemas de interés como el cloruro sódico o el agua. Con esto se pretende avanzar en la caracterización de este tipo de interfases donde las medidas experimentales son difíciles de realizar y los estudios de simulación proporcionan resultados contradictorios. En este contexto el cloruro sódico es un sistema muy controvertido, puesto que las discrepancias en los valores publicados para su energía libre interfacial mediante simulación molecular oscilan entre los 36 y 99 $\mathrm{mN{\cdot}m^{-1}}$.

- Caracterizar la estructura de las interfases investigadas. En concreto se quieren estudiar aspectos estructurales tales como el perfil de densidad a través de la interfase o la estructura cristalina del sólido en las cercanías de la interfase para distintos sistemas.

Se pretende hacer un estudio comparativo detallado de la estructura de las tres posibles interfases existentes en el punto triple del agua.

- Obtener información termodinámica de una interfase a partir de su superficie intrínseca. Desde un punto de vista energético las interfases deberían ser planas, dado que esta geometría minimiza el área de la interfase. Sin embargo, las ondas capilares introducen una entropía que aumenta la superficie de la interfase de tal manera que el área intrínseca de la interfase es mayor que el área nominal correspondiente a una interfase plana. Así, mediante el estudio de la distribución de probabilidades de áreas intrínsecas se pretende obtener información termodinámica de la interfase.

Discusión integradora

La Tesis Doctoral que aquí se presenta recoge el trabajo realizado por el candidato durante los últimos cuatro años. Con el objetivo de exponer este trabajo de una manera clara, la memoria se ha dividido en tres partes principales: la Parte I, dedicada al desarrollo del fundamento teórico de las técnicas y modelos empleados en esta tesis, la Parte II, donde se exponen y discuten los resultados más relevantes obtenidos durante este tiempo, y la Parte III, donde se recogen las principales conclusiones. La intención de este apartado es mostrar la relación entre los distintos capítulos que componen la parte de resultados de esta tesis, así como aclarar la contribución del candidato en cada uno de ellos.

El tema central de esta tesis es el estudio de las ondas capilares por medio del modelo del Hamiltoniano interfacial, empleando para ello la simulación molecular. Según este modelo la energía libre de una interfase viene dada por

$$H[h] = \int [g(h) + \frac{1}{2}\gamma\sqrt{1 + (\nabla h)^2} - h\Delta p]d\vec{r} \tag{2}$$

En él aparecen tres contribuciones bien diferenciadas. Por un lado, el término $g(h)$ da cuenta de las interacciones de la interfase con un campo externo. Por otra parte, el segundo término consta de dos componentes: γ y $\int \sqrt{1 + (\nabla h)^2}d\vec{r}$. Si la interfase es fluida γ es la tensión superficial, mientras que en el caso de fases sólidas el correspondiente coeficiente es la llamada rigidez interfacial. En ambos casos $\int \sqrt{1 + (\nabla h)^2}d\vec{r}$ es el área de la interfase. Por tanto, este término tiene en cuenta el coste energético debido al aumento del área interfacial como consecuencia de la presencia de ondas capilares. Y por último, el término $h\Delta p$, donde Δp es la diferencia de presión volumétrica entre las fases que componen la interfase, refleja la energía libre en función de la saturación del sistema.

A lo largo de la tesis se han estudiado distintos escenarios posibles para este Hamiltoniano, tal y como se muestra a continuación:

Caso 1: En ausencia de campo externo, $g(h) = 0$**.** Dentro de este escenario nuestras simulaciones se han llevado a cabo en condiciones de saturación; esto es, $\Delta p = 0$. Además hemos estudiado dos posibles situaciones:

- Interfases fluidas, donde se cumple que $\gamma = \gamma_{lv}$. Este escenario lo encontramos en el Capítulo 7.
- Interfases con presencia de una fase sólida donde la energía libre interfacial depende de la orientación cristalina $\gamma \equiv \gamma(\theta)$. Este escenario se estudia en los Capítulos 2, 3, 4, 5 y 6 de resultados, parte II.

A pesar de trabajar en condiciones de saturación, las ondas capilares provocan una curvatura en la interfase que genera fluctuaciones locales de presión, dando lugar a una diferencia de presión entre las dos fases En este caso, el sistema no se encuentra localmente en equilibrio, sino que existe una diferencia de presión que viene dada por $\Delta p = \gamma \nabla^2 h$ (ecuación de Young–Laplace). Esta diferencia de presión está relacionada con una diferencia de temperatura ΔT entre la temperatura del sistema y la temperatura de coexistencia. La aparición de estas fluctuaciones locales permite hacer uso de teorías dinámicas para relacionar la dinámica del equilibrio con la tasa de crecimiento cristalino haciendo uso de la teoría de respuesta lineal. En esta tesis se hace uso de este fenómeno, análogo a un escenario en en condiciones de no saturación, en el Capítulo 2, donde se estudian propiedades dinámicas de la interfase sólido–líquido.

Caso 2: En presencia de campo externo, $g(h) \neq 0$.

- Presencia explícita de $g(h)$. En este caso, la interfase siente un potencial externo debido a fuerzas de van der Waals y cuya forma es $g(h) \sim 1/h^2$. Aquí la tensión superficial presenta una dependencia con el espesor de la película. Esta dependencia aparece a través de un término adicional sobre la γ_{lv}, y ha sido identíficado en esta Tesis. Así, se obtiene que $\gamma(h) = \gamma_{lv} + \xi^2 g''(h)$, donde ξ es la longitud de correlación de las fluctuaciones.
  Este escenario se emplea en el Capítulo 1
- Aparición de un $g(h)$ efectivo. Este escenario se estudia en el Capítulo 6 y permite explicar las propiedades de la película que se forma al prefundir el hielo antes de alcanzar el punto triple.
- Las fluctuaciones de una interfase sólido–fluido se describen efectivamente mediante un campo externo que sujeta la interfase sólida. Si $g(h) \neq 0$ nos encontramos ante una interfase lisa, mientras que si $g(h) = 0$ la superficie es rugosa.
  En el Capítulo 6 se estudia este posible escenario.

A continuación se realiza una breve descripción de cada capítulo de resultados, mostrando la contribución del candidato en cada uno de ellos.

En el Capítulo 1 la contribución del candidato se centró en la realización de los estudios de simulación, así como en el tratamiento de los resultados obtenidos.

El sistema empleado para el estudio es un modelo de Ar adsorbido sobre un sustrato sólido en condiciones de *complete wetting*. Con este modelo se realizan simulaciones de Monte Carlo para películas de distinto espesor.

En un primer lugar se calcula la *disjoining pressure*, $\Pi(h)$, por dos métodos distintos, de los cuales uno de ellos la calcula de forma precisa a partir de propiedades volumétricas, mientras que el otro únicamente da cuenta de las contribuciones del potencial externo. En ambos casos el resultado muestra una *disjoning pressure* que se puede explicar mediante el modelo de Hamaker-Derjaguin para películas de tamaño superior a tres diámetros moleculares.

En segundo lugar se analiza el espectro de las fluctuaciones capilares en el espacio de Fourier, obteniéndose tanto la segunda derivada del potencial interfacial respecto de h, $g''(h)$, como la energía libre interfacial. En el caso de $g''(h)$, los resultados se comparan con los obtenidos por integración termodinámica y con el modelo propuesto obteniéndose muy buen acuerdo entre los tres. Este hecho confirma que $g''(h)$ está dominado por las interacciones de van der Waals. En este caso el modelo de Hamaker-Derjaguin funciona para películas que superen los cinco diámetros moleculares. En el caso de la tensión superficial se obtiene una dependencia clara con el espesor de película para películas pequeñas. Esta dependencia, ya mostrada anteriormente [56, 57], se puede explicar considerando únicamente la influencia del campo externo.

Finalmente se calcula la longitud de correlación paralela, obteniéndose un valor mínimo umbral en torno a un diámetro molecular.

En el Capítulo 2, que también está desarrollado en su totalidad por el candidato, se estudia la dinámica de las ondas superficiales de la interfase sólido–fluido para tres sistemas distintos, véase, esferas duras, Lennard-Jones y agua TIP4P/2005.

Mediante un análisis de dichas ondas se obtienen las funciones de autocorrelación de sus modos de Fourier. Un cuidadoso análisis de estas funciones de autocorrelación permite observar que el proceso de relajación de las ondas capilares se produce en dos escalas temporales bien diferenciadas: una lenta y una rápida. Para el proceso de relajación responsable de la escala lenta se obtiene una ley de escala válida para todos los sistemas, que se puede explicar mediante un proceso de difusión de la interfase como consecuencia de su continuo fundido y recristalización. El proceso rápido no ha podido ser caracterizado en tanto detalle pero creemos que está asociado con la vibración de átomos interfaciales y los fonones del cristal.

Comparando los tres modelos se observa que el proceso de relajación en el agua es un orden de magnitud más lento que en los otros dos sistemas, debido a los grados de libertad orientacionales.

Finalmente se obtienen los coeficientes cinéticos que determinan la tasa de crec-

imiento cristalino para todos las caras cristalinas estudiadas.

El Capítulo 3 está igualmente desarrollado en su totalidad por el candidato. Este capítulo se centra en el estudio de la geometría de la interfase mediante el empleo del modelo de Broughton y Gilmer para el Lennard–Jones. Concretamente se estudia si existen diferencias entre los resultados obtenidos para las stiffness y la energía libre interfacial de distintas orientaciones del cristal cuando se pasa de tener interfase elongada quasi–monodimensional a una interfase cuadrada.

Los resultados obtenidos muestran que ambas geometrías proporcionan resultados compatibles salvo cuando en la interfase se expone el plano (111). En este caso, la geometría cuadrada proporciona el mismo valor de la stiffness para dos direcciones de propagación de la onda de acuerdo con consideraciones teóricas. Por el contrario la geometría quasi–monodimensional no muestra el comportamiento esperado sino que proporciona valores claramente distintos para cada una de las direcciones de propagación. Un análisis detallado de este plano muestra que, para una da las orientaciones de la geometría quasi–monodimensional, se produce una transición de fase desde la estructura fcc a una estructura hcp.

Finalmente se estudia la influencia que tiene en el parámetro de orden el hecho de colocar una fase líquida junto a una fase fcc perfecta, obteniéndose como resultado una caracterización errónea de la estructura cristalina de la fase cristalina.

El Capítulo 4, también realizado íntegramente por el candidato, está dedicado el estudio del NaCl mediante el modelo de Tosi-Fumi. En este trabajo se emplea la Dinámica Molecular para calcular la γ_{sl} promedio del sistema mediante el análisis de distintas orientaciones cristalográficas.

Al igual que en el Capítulo 3 se estudian dos geometrías distintas de la interfase observándose igualmente discrepancias entre ambas cuando el plano (111) se expone en la interfase. El valor obtenido para γ_{sl} de 89 ± 6 mN·m^{-1} es compatible con otros publicados previamente, concretamente con aquellos obtenidos mediante el cálculo de barreras de energía libre de nucleación mediante simulación molecular [44]. Sin embargo, choca drásticamente con el obtenido, también por simulación molecular, mediante la medición del ángulo de contacto [43]. Este último método proporciona un valor de γ_{sl} de 36 mN·m^{-1}, y en este capítulo se discute su bondad debido al efecto de la tensión de linea [58].

Este trabajo muestra además que algunas orientaciones presentan un comportamiento anómalo, con una stiffness que parece no converger al límite termodinámico a medida que aumenta la escala de longitud de las ondas capilares. En este capítulo se argumenta que dicha anomalía se puede deber a inestabilidades en ciertas direcciones de propagación de la onda.

El Capítulo 5 está desarrollado íntegramente por el candidato. En él se lleva a cabo un estudio de la interfase sólido–líquido para el modelo de agua TIP4P/2005 mediante Dinámica Molecular, estudiándose distintas orientaciones que incluyen los principales planos cristalográficos del hielo hexagonal (Ih).

Los resultados de este estudio muestran que el ancho de la interfase es de unos 4-5 diámetros moleculares independientemente de la orientación, y que cuando el plano expuesto en la interfase es el plano basal puede ocurrir recristalización en forma de hielo Ic en algunas regiones de dicha interfase.

En cuanto a los valores de γ_{sl} se obtiene un valor promedio de 27 ± 2 mN·m^{-1}, y valores de 27 ± 2, 28 ± 2 y 28 ± 2 mN·m^{-1} para los planos basal, prismático primario y prismático secundario, respectivamente. A pesar de que el error en el cálculo no permite sacar conclusiones definitivas sobre la anisotropía energética de las caras, si que parece que el plano basal es menos energético que los planos primarios, de acuerdo con lo obtenido para otros modelos de agua de la familia TIP4P.

En el Capítulo 6 el candidato contribuyó mediante la realización de las simulaciones y el tratamiento y discusión de los resultados obtenidos. En este capítulo se estudia el punto triple del agua TIP4P/2005 mediante Dinámica Molecular. En concreto se estudia la rugosidad de las interfases para sistemas hielo–agua y el comportamiento de la película líquida formada sobre el hielo en las interfases hielo–vapor.

Los resultados de las simulaciones muestran la existencia de una interfase rugosa para todas las caras cristalográficas estudiadas, en desacuerdo con las observaciones experimentales. Además, hemos visto que para longitudes de onda largas la superficie hielo/película se comporta como la interfase hielo/agua, mientras que la superficie película–vapor lo hace como la agua/vapor. El comportamiento de las películas líquidas se intenta modelizar mediante el Hamiltoniano interfacial. Para ello se considera que el hielo actúa como un sustrato sólido sobre el cual aparece una película adsorbida. Así, se puede considerar que dicha película se encuentra bajo la influencia de un campo externo.

En el Capítulo 7 la contribución del candidato se centró en la obtención y discusión de los resultados, así como en el desarrollo de la teoría. En este capítulo, se estudia la distribución de probabilidad de obtener un valor determinado del área intrínseca de la interfase. Para ello se emplea un modelo Lennard–Jones y desarrolla un método de localización de dicha interfase, así como un método para el cálculo de su correspondiente área. Esta distribución de probabilidad se analiza mediante un modelo teórico que da cuenta de las contribuciones energéticas y entrópicas al área intrínseca.

Los resultados obtenidos mediante el análisis de las distribuciones muestran una tensión superficial dependiente del área intrínseca. Se observa, además, que existe una resolución para la cual la distribución del área intrínseca proporciona la tensión superficial macroscópica.

Bibliografía

[1] F. Hauksbee, *Physico–mechanical experiments on various subjects*, pp. 139–169. London, 1709.

[2] J. A. von Segner *Comment. Soc. Reg. Götting*, 1751.

[3] T. Young, "An essay on the cohesion of fluids," *Philosophical Transactions of the Royal Society of London*, vol. 95, pp. 65–87, 1805.

[4] P. S. Laplace, *Traité de Méchanique Céleste*, vol. 2, p. 479. Bachelier, Paris, 2nd ed., 1805.

[5] J. W. Gibbs, "On the equilibrium of heterogeneous substances," *Transactions of the Connecticut Academy of Arts and Science*, vol. III, pp. 108–248 and 343–524, 1876-1878.

[6] M. V. von Smoluchowski *Annals of Physics*, vol. 25, p. 205, 1908.

[7] L. D. Landau and E. M. Lifshitz, *Mecánica de Fluidos*. Barcelona: Reverté, 1991.

[8] L. G. MacDowell, J. Benet, N. A. Katcho, and J. M. Palanco, "Disjoining pressure and the film-height-dependent surface tension of thin liquid films: New insight from capillary wave fluctuations," *Advances in Colloid and Interface Science*, vol. 206, pp. 150 – 171, 2014.

[9] A. Karma, "Fluctuations in solidification," *Phys. Rev. E*, vol. 48, pp. 3441–3458, Nov 1993.

[10] J. W. Cahn, "Critical point wetting," *J. Chem. Phys.*, vol. 66, p. 3667, 1977.

[11] C. Ebner and W. F. Saam, "New phase transition in thin argon films," *Phys. Rev. Lett.*, vol. 38, pp. 1486–1489, 1977.

[12] M. R. Moldover and J. W. Cahn, "An interface phase transition: complete to partial wetting," *Science*, vol. 207, no. 4435, pp. 1073–1075, 1980.

[13] P. Tarazona and R. Evans, "Wetting transitions at models of a solid–gas interface," *Molec. Phys.*, vol. 48, pp. 799–831, 1983.

[14] B. Derjaguin, "Modern state of the investigation of long-range surface forces," *Langmuir*, vol. 3, no. 5, pp. 601–606, 1987.

[15] A. Vrij, "Light scattering from liquid interfaces," *Advances in Colloid and Interface Science*, vol. 2, no. 1, pp. 39 – 64, 1968.

[16] A. W. Adamson and A. P. Gast, *Physical Chemistry of Surfaces*. New York: Wiley-Interscience, 1997.

[17] D. G. A. L. Aarts, M. Schmidt, and H. N. W. Lekkerkerker, "Direct visual observation of thermal capillary waves," *Science*, vol. 304, no. 5672, pp. 847–850, 2004.

[18] J. Rowlinson and B. Widom, *Molecular Theory of Capillarity*. Dover books on chemistry, Dover Publications, 2002.

[19] D. S. Fisher and J. D. Weeks, "Shape of crystals at low temperatures: Absence of quantum roughening," *Phys. Rev. Lett.*, vol. 50, pp. 1077–1080, Apr 1983.

[20] V. Bergeron, "Forces and structure in thin liquid soap films," *Journal of Physics: Condensed Matter*, vol. 11, no. 19, p. R215, 1999.

[21] S. Toxvaerd and J. Stecki, "Density profiles at a planar liquid-liquid interface," *The Journal of Chemical Physics*, vol. 102, no. 18, 1995.

[22] M. Mecke, J. Winkelmann, and J. Fischer, "Molecular dynamics simulation of the liquid-vapor interface: The Lennard-Jones fluid," *J. Chem. Phys.*, vol. 107, p. 9264, 1997.

[23] A. Trokhymchuk and J. Alejandre, "Computer simulations of liquid/vapor interface in Lennard-Jones fluids: Some questions and answers," *The Journal of Chemical Physics*, vol. 111, no. 18, 1999.

[24] L. G. MacDowell and P. Bryk, "Direct calculation of interfacial tensions from computer simulation: Results for freely jointed tangent hard sphere chains," *Phys. Rev. E*, vol. 75, p. 061609, Jun 2007.

[25] E. G. Noya, J. P. Doye, D. J. Wales, and A. Aguado, "Geometric magic numbers of sodium clusters: Interpretation of the melting behaviour," *The European Physical Journal D*, vol. 43, no. 1-3, pp. 57–60, 2007.

[26] D. Turnbull, "Formation of crystal nuclei in liquid metals," *Journal of Applied Physics*, vol. 21, no. 10, pp. 1022–1028, 1950.

[27] A. D. J. Haymet and D. W. Oxtoby, "A molecular theory for the solid-liquid interface," *The Journal of Chemical Physics*, vol. 74, no. 4, pp. 2559–2565, 1981.

[28] D. W. Oxtoby and A. D. J. Haymet, "A molecular theory of the solid-liquid interface. II. Study of bcc crystal-melt interfaces," *The Journal of Chemical Physics*, vol. 76, no. 12, pp. 6262–6272, 1982.

[29] J. Q. Broughton and G. H. Gilmer, "Molecular dynamics investigation of the crystal–fluid interface. VI. Excess surface free energies of crystal–liquid systems," *J. Chem. Phys.*, vol. 84, no. 10, pp. 5759–5768, 1986.

[30] R. L. Davidchack and B. B. Laird, "Direct calculation of the crystal–melt interfacial free energies for continuous potentials: Application to the Lennard-Jones system," *J. Chem. Phys.*, vol. 118, no. 16, pp. 7651–7657, 2003.

[31] J. R. Morris and X. Song, "The anisotropic free energy of the Lennard Jones crystal melt interface," *J. Chem. Phys.*, vol. 119, p. 3920, 2003.

[32] R. L. Davidchack and B. B. Laird, "Direct calculation of the hard-sphere crystal /melt interfacial free energy," *Phys. Rev. Lett.*, vol. 85, pp. 4751–4754, Nov 2000.

[33] R. L. Davidchack, J. R. Morris, and B. B. Laird, "The anisotropic hard-sphere crystal-melt interfacial free energy from fluctuations," *The Journal of Chemical Physics*, vol. 125, no. 9, p. 094710, 2006.

[34] R. L. Davidchack, "Hard spheres revisited: Accurate calculation of the solid–liquid interfacial free energy," *J. Chem. Phys.*, vol. 133, no. 23, p. 234701, 2010.

[35] A. Härtel, M. Oettel, R. E. Rozas, S. U. Egelhaaf, J. Horbach, and H. Löwen, "Tension and stiffness of the hard sphere crystal-fluid interface," *Phys. Rev. Lett.*, vol. 108, p. 226101, May 2012.

[36] R. L. Davidchack, R. Handel, J. Anwar, and A. V. Brukhno, "Ice ih-water interfacial free energy of simple water models with full electrostatic interactions," *Journal of Chemical Theory and Computation*, vol. 8, no. 7, pp. 2383–2390, 2012.

[37] R. Handel, R. L. Davidchack, J. Anwar, and A. Brukhno, "Direct calculation of solid-liquid interfacial free energy for molecular systems: TIP4P ice-water interface," *Phys. Rev. Lett.*, vol. 100, p. 036104, Jan 2008.

[38] J. J. Hoyt, M. Asta, and A. Karma, "Method for computing the anisotropy of the solid-liquid interfacial free energy," *Phys. Rev. Lett.*, vol. 86, pp. 5530–5533, Jun 2001.

[39] J. R. Morris, "Complete mapping of the anisotropic free energy of the crystal-melt interface in Al," *Phys. Rev. B*, vol. 66, p. 144104, Oct 2002.

[40] D. Y. Sun, M. Asta, and J. J. Hoyt, "Crystal-melt interfacial free energies and mobilities in fcc and bcc Fe," *Phys. Rev. B*, vol. 69, p. 174103, May 2004.

[41] D. Y. Sun, M. I. Mendelev, C. A. Becker, K. Kudin, T. Haxhimali, M. Asta, J. J. Hoyt, A. Karma, and D. J. Srolovitz, "Crystal-melt interfacial free energies in hcp metals: A molecular dynamics study of Mg," *Phys. Rev. B*, vol. 73, p. 024116, Jan 2006.

[42] J. Huang, X. Zhu, and L. S. Bartell, "Molecular dynamics studies of the kinetics of freezing of $(NaCl)_{108}$ clusters," *J. Phys. Chem. A*, vol. 102, p. 2708, 1998.

[43] T. Zykova-Timan, D. Ceresoli, U. Tartaglino, and E. Tosatti, "Why are alkali halide surfaces not wetted by their own melt?," *Phys. Rev. Lett.*, vol. 94, p. 176105, May 2005.

[44] C. Valeriani, E. Sanz, and D. Frenkel, "Rate of homogeneous crystal nucleation in molten NaCl," *J. Chem. Phys.*, vol. 122, p. 194501, 2005.

[45] T. Zykova-Timan, C. Valeriani, E. Sanz, D. Frenkel, and E. Tosatti, "Irreducible finite-size effects in the surface free energy of NaCl crystals from crystal-nucleation data," *Phys. Rev. Lett.*, vol. 100, p. 036103, Jan 2008.

[46] N. Metropolis, A. W. Rosenbluth, M. N. Rosenbluth, A. H. Teller, and E. Teller, "Equation of state calculations by fast computing machines," *J. Chem. Phys.*, vol. 21, p. 1087, 1953.

[47] B. J. Alder and T. E. Wainwright, "Studies in molecular dynamics. I. General method," *J. Chem. Phys.*, vol. 31, p. 459, 1959.

[48] P. J. Steinhardt, D. R. Nelson, and M. Ronchetti, "Bond-orientational order in liquids and glasses," *Phys. Rev. B*, vol. 28, pp. 784–805, Jul 1983.

[49] P.-R. ten Wolde, M. J. Ruiz-Montero, and D. Frenkel, "Simulation of homogeneous crystal nucleation close to coexistence," *Faraday Discuss.*, vol. 104, pp. 93–110, 1996.

[50] W. Lechner and C. Dellago, "Accurate determination of crystal structures based on averaged local bond order parameters," *The Journal of Chemical Physics*, vol. 129, no. 11, p. 114707, 2008.

[51] A. Reinhardt, J. P. K. Doye, E. G. Noya, and C. Vega, "Local order parameters for use in driving homogeneous ice nucleation with all-atom models of water," *The Journal of Chemical Physics*, vol. 137, no. 19, p. 194504, 2012.

[52] S. Angioletti-Uberti, M. Ceriotti, P. D. Lee, and M. W. Finnis, "Solid-liquid interface free energy through metadynamics simulations," *Phys. Rev. B*, vol. 81, p. 125416, Mar 2010.

[53] X.-M. Bai and M. Li, "Calculation of solid-liquid interfacial free energy: A classical nuclea tion theory based approach," *J. Chem. Phys.*, vol. 124, no. 12, p. 124707, 2006.

[54] L. A. Fernández, V. Martín-Mayor, B. Seoane, and P. Verrocchio, "Equilibrium fluid-solid coexistence of hard spheres," *Phys. Rev. Lett.*, vol. 108, p. 165701, Apr 2012.

[55] J. R. Espinosa, C. Vega, and E. Sanz, "The mold integration method for the calculation of the crystal-fluid interfacial free energy from simulations," *The Journal of Chemical Physics*, vol. 141, no. 13, p. 134709, 2014.

[56] E. M. Fernández, E. Chacón, and P. Tarazona, "Capillary waves spectrum at adsorbed liquid films," vol. 86, p. 085401, 2012.

[57] L. G. MacDowell, J. Benet, and N. A. Katcho, "Capillary fluctuations and film-height-dependent surface tension of an adsorbed liquid film," *Phys. Rev. Lett.*, vol. 111, p. 047802, Jul 2013.

[58] P. Tarazona and G. Navascues, "A statistical mechanical theory for line tension," *J. Chem. Phys.*, vol. 75, no. 6, pp. 3114–3120, 1981.

Parte I

Fundamento teórico

Capítulo 1
Métodos de Simulación Molecular

La simulación molecular es una herramienta que permite obtener propiedades macróscópicas de un sistema a partir de su descripción atómica. Su fundamento está en el cálculo de interacciones entre moléculas a partir de sus potenciales de interacción, y la relación entre la descripción atomística y las propiedades macroscópicas se lleva a cabo mediante la termodinámica estadística. Debido a su carácter predictivo tiene un enorme rango de aplicación, permitiendo realizar experimentos en condiciones extremas que pueden llegar a ser imposibles de alcanzar en un laboratorio real. En este capítulo se describen los dos métodos de simulación existentes, el método de Monte Carlo y la Dinámica Molecular, centrándonos en las técnicas empleadas en esta tesis.

1.1 Monte Carlo

El método de Monte Carlo (MC) es un método de simulación que permite obtener propiedades macroscópicas de equilibrio de un sistema mediante el estudio de distintas configuraciones representativas del mismo generadas al azar.

Según la termodinámica estadística, cualquier observable O que se quiera estudiar va a depender de las coordenadas de todas las partículas del sistema $O(r^N)$ [1, 2] según

$$< O >= \frac{\int O(r^N) e^{-\beta U(r^N)} dr^N}{\int e^{-\beta U(r^N)} dr^N} \tag{1.1}$$

donde r^N son las coordenadas de las N partículas del sistema, $\beta = 1/k_B T$ y $U(r^N)$ es la energía potencial del sistema.

Según esto, a priori sería posible hallar el valor del observable resolviendo ambas integrales. Sin embargo, resolver integrales del tipo $\int e^{-\beta U(r^N)} dr^N$ es muy complicado y sólo puede realizarse analíticamente en algunos casos muy sencillos. Por esta razón es necesario utilizar un método numérico que permita evaluar dichas integrales.

El método de Monte Carlo propone una solución numérica más eficaz que, por ejemplo, una cuadratura de Simpson. En él, las integrales no se resuelven en puntos

determinados de antemano, sino que se evalúan en puntos generados al azar. Lógicamente, el promedio será más exacto cuantos mas puntos se empleen en su cálculo. Es aquí donde aparece el principal problema del método. Como se puede observar en la Ec. 1.4, las integrales contienen un factor de Boltzmann, que tiende a cero en la mayoría de los casos, y que hace que la mayor parte del tiempo de cálculo se invierta en puntos cuya información es irrelevante. Por este motivo se emplea la técnica de *Muestreo Significativo*, basada en la idea de evaluar las integrales preferentemente en puntos donde el factor de Boltzmann no sea despreciable.

Sin embargo, en una gran parte de los casos nuestro interés no es evaluar ambas integrales por separado, sino que nos basta con conocer su razón. Con este objetivo, el método de Metropolis [3] propone una estrategia que permite aplicar un Monte Carlo más eficiente para el cálculo de dicha razón. A continuación se detalla este método.

Si se define la parte configuracional de la función de partición como Z:

$$Z = \int e^{-\beta U(r^N)} dr^N \tag{1.2}$$

se puede expresar la densidad de probabilidad de encontrar al sistema en una configuración determinada en torno a r^Ncomo

$$P(r^N) \equiv \frac{e^{-\beta U(r^N)}}{Z} \tag{1.3}$$

Si ahora se pueden generar puntos al azar en una configuración espacial que siga esta distribución de probabilidad se puede establecer,

$$< O > \approx \frac{1}{L} \sum_i O(r_i^N) \tag{1.4}$$

donde L es el número total de puntos generados y el sumatorio corre únicamente sobre los estados visitados, es decir aquellos cuyo factor de Boltzmann es no nulo.

Así pues, el método de Monte Carlo permite evaluar la Ec. 1.4 determinando la probabilidad relativa $e^{-\beta \Delta U(r^N)}$ entre estados sucesivos, obviando así la evaluación exlpícita de Z.

Con el objetivo de evaluar el potencial únicamente en aquellos puntos donde el factor de Boltzmann es significativo, lo que hace el método de Metropolis es partir de una configuración inicial r^Ndenominada o (del inglés old) cuyo factor de Boltzmann es $e^{-\beta U(o)}$. Desde esta configuración se intenta pasar a una nueva configuración de prueba r'^N, en este caso llamada n (del inglés new) y con factor de Boltzmann $e^{-\beta U(n)}$, mediante la adición de un pequeño desplazamiento Δ a la cofiguración o. Ahora hay que ver si este movimiento se acepta o se rechaza. Para ello hay que determinar la probabilidad de realizar una transición $\pi(o \to n)$ desde o hasta n. Además se debe cumplir la condición

de que cualquier variación que se produzca en el sistema no afecte a su distribución de equilibrio, por lo que el número de movimientos aceptados desde o hasta n debe ser exactamente igual al número de movientos aceptados desde n hasta o. Esta condición, llamada de *balance detallado*, se puede expresar como

$$P(o)\pi(o \to n) = P(n)\pi(n \to o) \tag{1.5}$$

donde $P(o)$ y $P(n)$ son las probabilidades de encontrarnos en los estados antiguo y nuevo, respectivamente.

Para construir la matriz $\pi(o \to n)$ hay que tener en cuenta que un movimiento de Monte Carlo consta de dos etapas. La primera consiste en realizar un movimiento al azar desde o hasta n con una probabilidad determinada. A esta matriz de probabilidad se le conoce como $\alpha(o \to n)$. A continuación hay que determinar si el movimiento es aceptado o rechazado, definiendo la probabilidad de aceptación como $acc(o \to n)$. Por tanto,

$$\pi(o \to n) = \alpha(o \to n) \times acc(o \to n) \tag{1.6}$$

En el método original de Monte Carlo α se escoge de forma que sea una matriz simétrica; esto es, $\alpha(o \to n) = \alpha(n \to o)$, lo que permite escribir

$$P(o) \times acc(o \to n) = P(n) \times acc(n \to o) \tag{1.7}$$

aunque en métodos posteriores se puede definir de distintas formas.

De la ecuación anterior se puede establecer

$$\frac{acc(o \to n)}{acc(n \to o)} = \frac{P(n)}{P(o)} = e^{-\beta[U(n)-U(o)]} \tag{1.8}$$

De entre todas las opciones que existen para $acc(o \to n)$ y que satisfacen la ecuación anterior, el método de Metropolis escoge aquella en la que

$$\begin{array}{rcccl} acc(o \to n) & = & P(n)/P(o) & si & P(n) < P(o) \\ & = & 1 & si & P(n) \geq P(o) \end{array} \tag{1.9}$$

En resumen, en el método de Metropolis la probabilidad de que se realice una transición desde un estado o hasta un estado n viene dada por

$$\begin{array}{rcll} \pi(o \to n) & = & \alpha(o \to n) & P(n) \geq P(o) \\ & = & \alpha(o \to n)[P(n)/P(o)] & P(n) < P(o) \\ \pi(o \to o) & = & 1 - \sum_{n \neq o} \pi(o \to n) & \end{array} \tag{1.10}$$

Una gran ventaja de este método es la gran libertad que se consigue a la hora de elegir la matriz α, pues la única condición que se le ha impuesto es que debe ser

simétrica. Hasta ahora se ha hablado de la probabilidad de aceptar un movimiento, pero no se ha explicado cómo se decide si el movimiento se acepta o se rechaza. El procedimiento habitual es el siguiente. Supongamos que se produce un movimiento de prueba, con una probabilidad de ser aceptado

$$acc(o \rightarrow n) = e^{-\beta[U(n)-U(o)]} < 1 \tag{1.11}$$

Para ver si el movimiento se acepta o se rechaza lo que se hace es generar un número al azar denominado Ranf a partir de una distribución uniforme en el intervalo [0,1]. Si Ranf $<acc(o \rightarrow n)$ el movimiento se acepta, mientras que en el caso contrario se rechaza. Esto garantiza que la probabilidad de aceptar un movimiento sea exactamente igual a $acc(o \rightarrow n)$. Obviamente es imprescindible que los números generados al azar estén distribuidos de manera perfectamente uniforme en el intervalo [0,1].

A este proceso, en el cual cada nueva configuración que alcanza el sistema se obtiene mediante una pequeña modificación de la configuración anterior, se le conoce con el nombre de *Cadena de Markov*.

En resumen, el algoritmo de Metropolis Monte Carlo consta de las siguientes etapas:

1. Seleccionar una configuración o al azar y calcular su factor de Boltzmann $e^{-\beta U(o)}$.
2. Producir una perturbación Δ en el sistema para obtener la nueva configuración n.
3. Calcular el factor de Boltzmann de la nueva configuración $e^{-\beta U(n)}$.
4. Aceptar el movimiento de o a n con probabilidad

$$acc(o \rightarrow n) = min\left(1, e^{-\beta[U(n)-U(o)]}\right) \tag{1.12}$$

1.1.1 Monte Carlo Gran Canónico

Las ecuaciones presentadas en el apartado anterior corresponden al colectivo canónico, donde las variables termodinámicas número de moléculas, volumen y temperatura se mantienen constantes. Sin embargo, el método de Monte Carlo se puede aplicar en otros colectivos mediante la fijación de las variables termodinámicas adecuadas. La elección de las variables que han de mantenerse constates durante la simulación, o lo que es lo mismo el colectivo que vamos a simular, dependerá del tipo de experimento que queramos realizar y la información que queramos extraer de él.

En algunos casos, por ejemplo en estudios de adsorción, nuestro interés se centra en obtener información sobre el número medio de partículas presentes en un sistema en función de las condiciones externas. Por tanto para estos estudios es necesario un colectivo que permita tener fluctuaciones en el número de partículas presentes en el

sistema. Este colectivo, que se conoce como colectivo *Gran Canónico*, fue originalmente descrito por Norman y Filinov [4] y más tarde desarrollado por Adams [5, 6]. En él, las variables termodinámicas que se fijan son el potencial químico μ, el volumen V y la temperatura T.

Para su implantación en un programa de simulación, inicialmente se escoge al azar si se va intentar aumentar el número de moléculas del sistema, N, (movimiento de inserción) o si por el contrario se va a intentar disminuir (movimiento de borrado). Siguiendo el criterio de Metropolis, estos movimientos se aceptan con una probabilidad

$$acc(o \to n) = min(1, q) \tag{1.13}$$

donde q viene dada por

$$q = \frac{\alpha(n \to o)}{\alpha(o \to n)} \frac{P(n)}{P(o)} \tag{1.14}$$

Teniendo en cuenta que las partículas de un sistema son indistinguibles, la expresión para P es

$$P = \Lambda^{-3N} e^{\beta\mu N} e^{-\beta U_N} \tag{1.15}$$

donde Λ es la longitud de onda térmica de de Broglie.

Si ahora suponemos que estamos intentando un movimiento de inserción, la relación entre las probabilidades de los estados nuevo y antiguo viene dada por

$$\frac{P(N+1)}{P(N)} = \Lambda^{-3} e^{\beta\mu} e^{-\beta(U_{N+1} - U_N)}. \tag{1.16}$$

La peculiaridad de este colectivo reside en que, en él, la matriz de probabilidad α no es simétrica. En el caso de un movimiento de inserción depende del volumen del sistema según

$$\alpha(N \to N+1) = \frac{1}{2} V, \tag{1.17}$$

mientras que cuando se intenta un movimiento de borrado depende del número de partículas que haya en el sistema

$$\alpha(N+1 \to N) = \frac{1}{2}(N+1) \tag{1.18}$$

Así, la relación que queda entre ambas matrices es

$$\frac{\alpha(n \to o)}{\alpha(o \to n)} = \frac{\alpha(N+1 \to N)}{\alpha(N \to N+1)} = \frac{1}{2} \frac{1}{N+1} \tag{1.19}$$

Es necesario comentar que el factor de 1/2 presente en las Ec. 1.17 y 1.18 aparece como consecuencia de intentar un movimiento u otro con la misma probabilidad.

Si ahora introducimos las Ec. 1.16 y 1.19 en la Ec. 1.13 obtenemos para el movimiento de inserción

$$acc(N \rightarrow N+1) = \frac{V\Lambda^{-3}}{N+1} e^{\beta\mu} e^{-\beta(U_{N+1}-U_N)} \tag{1.20}$$

Análogamente, para el movimiento de borrado obtendríamos

$$acc(N \rightarrow N-1) = \frac{N}{V\Lambda^{-3}} e^{-\beta\mu} e^{-\beta(U_{N-1}-U_N)} \tag{1.21}$$

1.1.2 Movientos de muestreo especiales: *Sesgo Configuracional*

En algunas ocasiones la aceptación de los movimientos de muestreo del sistema es muy baja, por lo que es necesario diseñar movimientos "originales" que permitan un mejor muestreo. Uno de estos movimientos es el *Sesgo Configuracional*, conocido en inglés como *Configurational Bias*. Este método, diseñado en un origen para el cálculo del potencial químico de polímeros en red, fue desarrollado originariamente por Siepmann en 1990 [7]. Posteriormente, en 1992 el método se desarrolló como método de muestreo para polímeros en red dentro del colectivo canónico [8], y se aplicó al continuo [9]. Simultáneamente Frenkel y colaboradores también extendieron el método al continuo, empleándolo bien para el cálculo de potenciales químicos o bien como método de muestreo [10]. Desde entonces el método ha ido ampliando su campo de aplicación y se ha extendido a otros colectivos como el colectivo de Gibbs [11, 12, 13] o el colectivo Gran Canónico [14]. La idea de este método es favorecer el crecimiento secuencial de aquellas cadenas poliméricas con una alta probabilidad de ocurrir. Para ello se divide la cadena polimérica en l segmentos, cuya orientación está determinada por un vector b_l, y que se hacen crecer según la estrategia de Rosenbluth [15]. Para ello se calculan tanto el factor de peso correspondiente a la nueva configuración, $W(n)$, como el factor de la configuración de partida $W(o)$. Por último, el movimiento se acepta o se rechaza con una probabilidad

$$acc(o \rightarrow) = min\,(1, W(n)/W(o)) \tag{1.22}$$

donde

$$W(n) = \prod_l w_l(n) \tag{1.23}$$

siendo $w_l(n)$ los factores de Rosenbluth parciales, que dependen de la orientación de los segmentos. El empleo de los factores W, conocidos como factores de Rosenbluth globales, garantiza que todas las conformaciones están muestreadas con el peso de Boltzman correcto. En nuestro caso, este movimiento no se aplica a cadenas poliméricas sino a

átomos, por lo que el movimiento consiste en retirar una molécula al azar del sistema e intentar colocarla en otro punto donde la probabilidad de aceptar el movimiento es alta.

1.2 Dinámica Molecular

Alternativamente al método de Monte Carlo, la técnica de Dinámica Molecular (MD) permite obtener propiedades de equilibrio y de transporte de un sistema mediante la integración de las ecuaciones de movimiento de Newton [1, 16]. Al integrar dichas ecuaciones para cada una de las partículas que componen el sistema, es posible conocer la variación de sus posiciones y momentos con el tiempo. De esta forma, si somos capaces de expresar una propiedad en función de las posiciones y momentos de las partículas del sistema, podremos calcular su promedio temporal. Al igual que ocurre con los experimentos reales, cuanto mayor sea el tiempo de observación, mejor será el promedio obtenido.

Aunque hasta el momento hemos dicho que durante las simulaciones de Dinámica Molecular se obtienen las posiciones y los momentos de las partículas, lo que se calcula en realidad no son las velocidades de las partículas sino las fuerzas que actúan sobre ellas. Así, la fuerza que siente una partícula i debido a la interacción con el resto de partículas del sistema, en un tiempo t determinado, vendrá dada por

$$f_i(r,t) = -\nabla U(r^N, t). \tag{1.24}$$

Una vez que se tienen calculadas las fuerzas se pasa a la integración de las ecuaciones de Newton. Para ello, existen distintos algoritmos, siendo el más empleado el algoritmo de Verlet [17] debido a su simplicidad [1, 16]. A continuación se muestra el funcionamiento de este algoritmo.

En primer lugar se lleva a cabo un desarrollo en series de Taylor de la posición de una partícula i en torno al tiempo t

$$r_i(t+\Delta t) = r_i(t) + v_i(t)\Delta t + \frac{1}{2}a_i(t)\Delta t^2 + \frac{1}{3!}\frac{d^3 r_i}{dt^3}\Delta t^3 + O(\Delta t^4), \tag{1.25}$$

y de la misma forma se puede hacer la expansión para un tiempo anterior según

$$r_i(t-\Delta t) = r_i(t) - v_i(t)\Delta t + \frac{1}{2}a_i(t)\Delta t^2 - \frac{1}{3!}\frac{d^3 r_i}{dt^3}\Delta t^3 + O(\Delta t^4). \tag{1.26}$$

Y sumando ambas expresiones se obtiene

$$r_i(t+\Delta t) + r_i(t-\Delta t) = 2r_i(t) + a_i(t)\Delta t^2 + O(\Delta t^4). \tag{1.27}$$

Ahora podemos truncar esta expresión en el término correspondiente a la aceleración de la partícula, y estaremos cometiendo un error del orden de Δt^4, donde Δt es el paso de tiempo empleado en la simulación. De esta forma la Ec. 1.27 queda como

$$r_i(t + \Delta t) \approx 2r_i(t) - r_i(t - \Delta t) + a_i(t)\Delta t^2. \tag{1.28}$$

Como se puede observar el algoritmo de Verlet requiere conocer las posiciones en un tiempo $(t - \Delta t)$ para poder calcular las nuevas y no es necesario conocer las velocidades de las partículas. Sin embargo, el cálculo de las velocidades es muy útil, puesto que permite calcular la energía cinética del sistema. En este sentido, el algoritmo de Verlet permite calcular la velocidad de una partícula a partir de suma de las Ec. 1.25 y 1.26 obteniéndose:

$$r_i(t + \Delta t) - r_i(t - \Delta t) = 2v_i(t)\Delta t + O(\Delta t^2) \tag{1.29}$$

por lo que

$$v_i(t) = \frac{r_i(t + \Delta t) - r_i(t - \Delta t)}{2\Delta t} + O(\Delta t^2) \tag{1.30}$$

Un aspecto fundamental de las simulaciones de Dinámica Molecular es, como se ha comentado anteriormente, que el error cometido en el truncamiento de la serie de Taylor es del orden de Δt^4. Por este motivo la elección de este parámetro es crucial, y en la práctica es necesario buscar un compromiso entre un valor suficientemente pequeño que permita la estabilidad numérica de la simulación (y con ello la conservación de la energía) y uno lo suficientemente grande que haga que nuestras simulaciones no sean desorbitadamente largas.

1.2.1 Simulaciones a temperatura constante: termostato velocity–rescaling modificado

Hasta ahora, hemos hablado de simulaciones en el colectivo NVE, donde se mantienen fijas el número de moléculas, N, el volumen, V, y la energía, E. Sin embargo, en muchos casos es más práctico fijar algunas variables termodinámicas con el objetivo de realizar simulaciones en otros colectivos. En el caso del colectivo canónico (NVT) es necesario hacer uso de un termostato que permita mantener constante la temperatura del sistema.

En las simulaciones de Dinámica Molecular, la temperatura del sistema se define a partir de la energía cinética, de acuerdo con el principio de equipartición de la energía. En concreto tenemos que el promedio de la energía cinética por cada grado de libertad del sistema es

$$\left\langle \frac{1}{2} m v_\omega^2 \right\rangle = \frac{1}{2} k_B T \tag{1.31}$$

donde m es la masa de la partícula y ω representa una componente de la velocidad.

Puesto que en la práctica lo que nos interesa es mantener constante la temperatura del sistema en su conjunto, debemos calcular la temperatura mediante la medida de la energía cinética total del sistema dividida por el número de grados de libertad. Teniendo en cuenta que la energía total de un sistema puede fluctuar, también lo puede hacer la temperatura, por lo que la temperatura instantánea en un tiempo t determinado se define como

$$T(t) = \sum_{i=1}^{N} \frac{m_i v_i^2(t)}{k_B N_l} \tag{1.32}$$

donde $N_l = 3N - 3$ es el número de grados de libertad de un sistema con N partículas y v_i es la velocidad de cada una de las partículas del sistema en un instante de tiempo t.

Como se puede observar, para poder calcular la temperatura es necesario conocer la velocidad de las partículas, cuya expresión viene por la Ec. 1.30.

Por tanto, con el objetivo de mantener constante la temperatura, en las simulaciones de dinámica molecular se hace uso de termostatos, que actúan modificando las velocidades de las partículas cada cierto tiempo. Actualmente se dispone de una gran variedad de termostatos [18, 19, 20, 21, 22, 23], pero aquí sólo se va a describir una versión mejorada del termostato velocity–rescaling [24], que ha sido el que se ha empleado en las simulaciones de la tesis.

La idea de este termostato es que las velocidades de todas las partículas se pueden multiplicar simultáneamente por un mismo factor α de forma que la energía cinética total del sistema, K, sea igual a la energía cinética objetivo, K_o, correspondiente a la temperatura deseada. De esta forma el factor α se calcula como

$$\alpha = \sqrt{\frac{K_o}{K}} \tag{1.33}$$

A diferencia del termostato velocity–rescaling clásico, donde la energía cinética objetivo se extrae al azar de la distribución canónica de equilibrio, en este caso no es necesario extraerla de dicha distribución, sino que basta con que los cambios aleatorios que se producen en la energía cinética permitan que ésta mantenga su distribución canónica inalterada.

Para ello lo que se hace es lo siguiente:

1. Dejar evolucionar el sistema resolviendo las ecuaciones de Newton.

2. Calcular la energía cinética.

3. Dejar evolucionar la energía cinética del sistema durante un tiempo equivalente al que ha evolucionado el sistema utilizando una dinámica estocástica auxiliar dada por

$$dK = (K_o - K)\frac{dt}{\tau} + 2\sqrt{\frac{KK_o}{N_l}}\frac{dW}{\sqrt{\tau}} \tag{1.34}$$

donde dW es un ruido de Wiener y τ es un parámetro con unidades de tiempo que determina la escala de tiempo del termostato.

4. Reescalar la energía cinética del sistema al valor obtenido en el punto anterior.

Esta variación, donde la única restricción es que la energía cinética mantenga su distribución canónica, presenta dos ventajas claras frente a la versión original del termostato. Por un lado, se puede obtener K_o a partir del valor anterior K, de forma que las velocidades de las partículas sufren cambios mucho menos drásticos que cuando K_o se obtiene directamente de la distribución de probabilidad gaussiana. Y por el otro, existe una magnitud, análoga a la energía en el colectivo microcanónico, que se debe conservar durante la simulación. Este segundo hecho es de especial relevancia, ya que nos permite saber si las configuraciones que se están obteniendo pertenecen al colectivo canónico.

1.2.2 Simulaciones a presión constante: barostato de Parrinello–Rahman

En muchas ocasiones el colectivo canónico (NVT) puede no ser el más adecuado para llevar a cabo las simulaciones. Esto ocurre, por ejemplo, cuando queremos conocer las dimensiones de equilibrio de un sólido a una determinada presión o el efecto de la composición de un disolvente en una mezcla. En estos casos es mucho más útil usar el colectivo NpT. Para poder llevar a cabo simulaciones en este colectivo es necesario hacer uso de un barostato que nos permita mantener la presión del sistema en el valor deseado. Al igual que en el caso de los termostatos, existen diversos tipos de barostatos [18, 25] pero igualmente sólo se va a comentar el barostato empleado en las simulaciones: el barostato de Parrinello–Rahman [26]. Este barostato es una extensión del barostato de Andersen [18] en el que se permite modificar la forma de la caja de simulación. Su funcionamiento consiste en modificar una matriz b, cuyos componentes definen la forma de la forma de la caja de simulación, de acuerdo a un Hamiltoniano extendido que incorpora las dimensiones de la caja como variables mecánicas, de forma que:

$$\frac{d^2b}{dt^2} = VW^{-1}b'^{-1}(P - P_o) \tag{1.35}$$

donde V es el volumen de la caja, P es la presión del sistema, P_o es la presión objetivo y W es la matriz de parámetros que determina la fortaleza de acoplamiento del barostato. Por tanto es necesario conocer el valor de W, que viene dado por

$$W^{-1} = \frac{4\pi^2\beta}{3\tau_p^2 L} \tag{1.36}$$

donde β es la compresibilidad isotérmica, τ_p es la constante de tiempo y L es el elemento más grande de la matriz de la caja, b.

Una gran ventaja de este barostato es que, en principio, es capaz de conseguir el verdadero colectivo NpT, además de poder combinarse con cualquier termostato.

Capítulo 2
Modelo del Hamiltoniano Interfacial

El coste energético de una interfase juega un papel fundamental en fenómenos de nucleación y crecimiento de una fase estable en el seno de otra metaestable. Así, por ejemplo, la tasa de aparición de cristales en un líquido subenfriado y la forma con que dichos cristales crecen, están ampliamente determinadas por la energía interfacial líquido–cristal. Además, la nanotecnología es una ciencia en pleno auge que permite el desarrollo de dispositivos a escala nanométrica, los cuales ofrecen la posibilidad de trabajar con cantidades ínfimas de líquidos [27, 28]. En este contexto los fenómenos de superficie cobran especial importancia [29].

Al adentrarnos en la escala microscópica es posible observar que las interfases se desvían de la planaridad debido a las ondas capilares producidas por la agitación térmica, fenómeno que se observa tanto en interfases líquidas como sólidas. En este sentido es importante establecer un vínculo entre el comportamiento microscópico del sistema, a nivel de ondas capilares, con la energía macroscópica interfacial.

Una forma de establecer dicho vínculo es mediante el empleo de Hamiltonianos, que pueden ser de distinta naturaleza [30]. En esta tesis, se va trabajar bajo la aproximación del Modelo del Hamiltoniano Interfacial (IHM). Este Hamiltoniano se caracteriza por ser capaz de describir propiedades de un sistema de geometría arbitraria a partir de propiedades de películas planas. Así, en él aparece un término asociado a la tensión superficial correspondiente a una interfase plana, y un término asociado al potencial interfacial $g(h)$ ó energía libre de una película plana. A continuación se muestran los detalles de este modelo [31].

Para comenzar vamos a considerar una interfase fluida, por ejemplo entre un líquido y un gas. En reposo, esta interfase no es plana sino que, debido a la agitación térmica, presenta ondulaciones relativamente grandes conocidas como ondas superficiales. Para una escala de longitudes por debajo de la longitud capilar, estas ondas se conocen como ondas capilares [32, 33] y están gobernadas básicamente por la tensión superficial. Por tanto, la posición local de la interfase en un instante determinado se puede definir como una función $h(\vec{r}_{x,y})$, que determina la altura de la película de líquido medida desde un plano de referencia. Así, a cada elemento diferencial de área de la interfase $d\vec{r}_{x,y}$ le

corresponde, como consecuencia de la interacción con un campo externo, una energía libre $g(h(\vec{r}_{x,y}))$ determinada por la altura de la película en ese punto. Además de esta contribución, hay que tener en cuenta que la interfase es inhomogénea, por lo que hay que dar cuenta del efecto que el aumento del área interfacial tiene sobre la energía total de la interfase. Con esto podemos escribir el Hamiltoniano Interfacial como

$$H[h(\vec{r}_{x,y})] = \int \left[g(h(\vec{r}_{x,y})) + \gamma \left(\sqrt{1 + [\nabla h(\vec{r}_{x,y})]^2} \right) \right] d\vec{r}_{x,y} \tag{2.1}$$

donde γ es la tensión superficial líquido–vapor. Analizando en detalle esta ecuación podemos ver que el primer término da cuenta de la energía libre de la película en función de su altura, mientras que el segundo da cuenta del aumento que se produce en la energía al aumentar el área interfacial a través de la tensión superficial.

La importancia de este Hamiltoniano es muy grande, ya que sirve como base para la mayor parte de estudios de fenómenos de superficie incluyendo el estudio de ondas capilares [34], fenómenos de wetting [35], la predicción de la forma de gotas [36], la medida de tensiones de linea [37], la determinación de la estructura de películas adsorbidas sobre superficies estructuradas [38], y la dinámica de dewetting [39].

En este caso nos vamos a centrar únicamente en el estudio de ondas capilares, mostrando la información que es posible extraer de este Hamiltoniano.

En un primer lugar consideramos un límite de pequeños gradientes, $(\nabla h(\vec{r}_{x,y}))^2 << 1$. Esto nos permite deshacernos de la raíz cuadrada en 2.1 obteniendo :

$$H[h(\vec{r}_{x,y})] = \int \left[g(h(\vec{r}_{x,y})) + \gamma \left(1 + \frac{1}{2} \left(\nabla h(\vec{r}_{x,y}) \right)^2 \right) \right] d\vec{r}_{x,y} \tag{2.2}$$

Si ahora tomamos como plano de referencia para medir la altura el plano medio de la interfase, $\bar{h}$, y definimos las fluctuaciones locales de la interfase en torno a este plano $\delta h(\vec{r}_{x,y}) = h(\vec{r}_{x,y}) - \bar{h}$, podemos hacer un desarrollo de Taylor de $g(h(\vec{r}_{x,y}))$ en torno a $\bar{h}$ de forma que

$$H[h(\vec{r}_{x,y})] = \int \left[g(\bar{h}) + g'(\bar{h})\delta h(\vec{r}_{x,y}) + \frac{1}{2} g''(\bar{h})\delta h^2(\vec{r}_{x,y}) + \gamma \left(1 + \frac{1}{2} \left(\nabla h(\vec{r}_{x,y}) \right)^2 \right) \right] d\vec{r}_{x,y} \tag{2.3}$$

De esta forma podemos expresar el aumento de la energía de la interfase como consecuencia de las fluctuaciones como

$$\Delta H[h(\vec{r}_{x,y})] = \int \left[g'(\bar{h})\delta h(\vec{r}_{x,y}) + \frac{1}{2} g''(\bar{h})\delta h^2(\vec{r}_{x,y}) + \frac{1}{2}\gamma \left(\nabla h(\vec{r}_{x,y}) \right)^2 \right] d\vec{r}_{x,y} \tag{2.4}$$

siendo

$$\Delta H[h(\vec{r}_{x,y})] = H[h(\vec{r}_{x,y})] - A[g(\bar{h}) + \gamma] \tag{2.5}$$

es decir, la energía total de la interfase real menos la energía de la correspondiente interfase plana.

El siguiente paso consiste en describir las fluctuaciones de la interfase en términos de modos de Fourier según

$$\delta h(\vec{r}_{x,y}) = \sum_{\mathbf{q}} \delta h_{\mathbf{q}} e^{i\mathbf{q}\vec{r}} \tag{2.6}$$

siendo $\mathbf{q}$ el vector de onda dado por $\mathbf{q} = 2\pi/\lambda$.

Introduciendo este resultado en la Ec. 2.4 llegamos a

$$\Delta H[h(\vec{r}_{x,y})] = \int \left[g'(\bar{h}) \sum_{\mathbf{q}} \delta h_{\mathbf{q}} e^{i\mathbf{q}\vec{r}} - \frac{1}{2} \sum_{\mathbf{q}} \sum_{\mathbf{q}'} \left(g''(\bar{h}) + \gamma \mathbf{q} \cdot \mathbf{q}' \right) \delta h_{\mathbf{q}} \delta h_{\mathbf{q}'} e^{i(\mathbf{q}+\mathbf{q}')\vec{r}} \right] d\vec{r}_{x,y} \tag{2.7}$$

donde $\mathbf{q}'$ es el vector complejo conjugado de $\mathbf{q}$.

Teniendo en cuenta que la integral sobre $e^{i\mathbf{q}\vec{r}}$ es $A\delta(\mathbf{q})$, donde $\delta(\mathbf{q})$ es la función delta de Kronecker en $\mathbf{q}$, y que análogamente la integral sobre $e^{i(\mathbf{q}+\mathbf{q}')\vec{r}}$ es $A\delta(\mathbf{q}+\mathbf{q}')$, podemos integrar la Ec. 2.7 obteniendo

$$\Delta H[h(\vec{r}_{x,y})] = A \left[g'(\bar{h}) \sum_{\mathbf{q}} \delta h_{\mathbf{q}} \delta(\mathbf{q}) + \frac{1}{2} \sum_{\mathbf{q}} \sum_{\mathbf{q}'} \left(g''(\bar{h}) - \gamma \mathbf{q} \cdot \mathbf{q}' \right) \delta h_{\mathbf{q}} \delta h_{\mathbf{q}'} \delta(\mathbf{q}+\mathbf{q}') \right] \tag{2.8}$$

Si tenemos en cuenta que $\delta h(\vec{r}_{x,y})$ describe las fluctuaciones de la interfase respecto del plano medio, el vector de onda del modo correspondiente a $q = 0$ es nulo, por lo que la Ec. 2.8 se puede escribir de forma mucho más compacta como

$$\Delta H[h(\vec{r}_{x,y})] = \frac{1}{2} A \sum_{\mathbf{q}} \left[g''(\bar{h}) + \gamma \mathbf{q}^2 \right] |\delta h_{\mathbf{q}}|^2 \tag{2.9}$$

Así con este resultado podemos obtener la energía correspondiente a una configuración instantánea de la interfase. La probabilidad de obtener una configuración determinada viene dada según la termodinámica estadística por

$$P(h(\vec{r}_{x,y})) = \frac{e^{-\beta \Delta H[h(\vec{r}_{x,y})]}}{Z_{cw}} \tag{2.10}$$

donde Z_{cw}, la función de partición, es la suma sobre todas las posibles ondas capilares. Si lo escribimos en términos de modos de Fourier obtenemos

$$Z_{cw} = \int \prod e^{-\beta \Delta H[h(\vec{r}_{x,y})]} dh_{\mathbf{q}} \tag{2.11}$$

Puesto que H viene dado en términos de modos de Fourier aditivos, se puede factorizar en un producto de integrales simples, de tal forma que podemos escribir

$$Z_{cw} = \prod_{\mathbf{q}} \int e^{-\frac{1}{2}\beta A\left[g''(\bar{h})+\gamma \mathbf{q}^2\right]|\delta h_q|^2} dh_{\mathbf{q}} \tag{2.12}$$

Llegados a este punto vamos a ver qué información se puede extraer de la Ec. 2.12. Es posible demostrar que dicha ecuación cumple el teorema de equipartición [40], similar al que le es aplicable a la distribución de velocidad $e^{\frac{1}{2}mv^2}$ en un sistema atómico, donde

$$\left\langle \frac{1}{2} m v^2 \right\rangle = \frac{1}{2} k_B T \tag{2.13}$$

y, por tanto

$$\left\langle v^2 \right\rangle = \frac{k_B T}{m} \tag{2.14}$$

Así, si consideramos que $|\delta h_{\mathbf{q}}|^2$ desempeña el papel de la velocidad al cuadrado, y $A\left[g''(\bar{h}) + \gamma q^2\right]$ el de la masa, podemos escribir

$$A \left\langle |\delta h_{\mathbf{q}}|^2 \right\rangle = \frac{k_B T}{\left(g''(\bar{h}) + \gamma q^2\right)} \tag{2.15}$$

Este resultado se ha confirmado en muchos estudios de simulación [41, 42, 43, 44, 45], especialmente para el caso de interfases libres, donde $g''(\bar{h}) = 0$. En estos casos la Ec. 2.15 se simplifica, obteniéndose

$$A \left\langle |\delta h_{\mathbf{q}}|^2 \right\rangle = \frac{k_B T}{\gamma q^2} \tag{2.16}$$

Así, representando la parte izquierda de esta ecuación frente a q^2 se debe obtener una constante proporcional a la tensión superficial líquido–vapor. Sin embargo, debido a los pequeños tamaños accesibles en las simulaciones, este régimen constante no llega a aparecer. Aún así se pueden obtener valores fiables de la tensión superficial mediante una extrapolación a $q = 0$. Además, fenomenológicamente, se puede observar en las simulaciones una dependencia de la tensión superficial con q, que describe las desviaciones de $A \left\langle |\delta h_{\mathbf{q}}|^2 \right\rangle$ del régimen lineal esperado para bajos valores de q. De esta forma obtenemos que $\gamma \equiv \gamma(q)$.

Según consideraciones teóricas se conoce que el término lineal de $\gamma(q)$ es nulo, por lo que en la aproximación de más bajo orden podemos escribir [46, 47]

$$\gamma(q) = \gamma_0 + \kappa q^2 \tag{2.17}$$

donde γ_0 es la tensión superficial macroscópica y κ es conocida como la resistencia a la curvatura.

De esta forma, introduciendo este resultado en la Ec. 2.15 llegamos a

$$A\left\langle|\delta h_{\mathbf{q}}|^2\right\rangle = \frac{k_B T}{g''(\bar{h}) + \gamma_0 q^2 + \kappa q^4} \tag{2.18}$$

Por tanto, el Modelo del Hamiltoniano Interfacial, nos permite obtener información sobre $g''(\bar{h})$, es decir, sobre las fuerzas externas presentes sobre el fluido, la tensión superficial macroscópica γ_0 y la resistencia a la curvatura κ.

Otra aplicación interesante de este Hamiltoniano es que permite obtener la rugosidad interfacial Δ^2_{cw}. Este hecho es importante puesto que es esta magnitud, y no el espectro completo de ondas capilares, lo que se puede obtener experimentalmente en la inmensa mayoría de los casos. Se puede comprobar [31] que Δ^2_{cw} viene dado por

$$\Delta^2_{cw} = \frac{k_B T}{4\pi\gamma_0} \ln \frac{1 + \xi^2_{\parallel} q^2_{max}}{1 + \xi^2_{\parallel} q^2_{min}} \tag{2.19}$$

donde

$$\xi_{\parallel} = \sqrt{\gamma_0 / g''} \tag{2.20}$$

es la longitud de correlación paralela, y dicta el alcance de las fluctuaciones de las ondas capilares en la dirección transversal. En el caso de interfases líquido–vapor bajo el efecto del campo de la gravedad se corresponde con la longitud capilar; mientras que para películas adsorbidas sobre un sustrato, también se conoce bajo el nombre de *healing distance* [36] y determina la capacidad de un líquido para sentir la rugosidad del sustrato sólido.

Para terminar es importante comentar que el espectro de los modos de Fourier de la Ec. 2.18 puede proporcionar mejores resultados si se sustituye el termino de la tensión superficial macroscópica γ_0 por una tensión superficial dependiente de la altura de la película $\gamma(\bar{h})$. Esta observación se detalla en el Capítulo 1 de la parte de resultados, así como en las referencias allí mostradas.

Aplicación a interfases sólido–fluido

Hasta ahora únicamente hemos hablado de interfases fluidas, si bien es posible realizar un tratamiento similar del Modelo del Hamiltoniano Interfacial para interfases sólido–fluido. En la Fig. 2.1 se muestra como una interfase, descrita por la función $h(x)$, fluctúa en torno a su orientación promedio, que viene definida por el vector $\vec{u}$. Como consecuencia de estas fluctuaciones, la orientación local instantánea de la interfase no tiene que

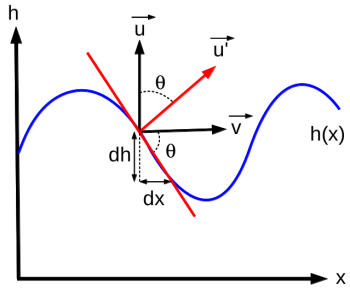

Figura 2.1. Representación de una onda interfacial descrita por la función h, propagándose en una interfase monodimensional. El vector $\vec{u'}$, perpendicular al plano local de la interfase, está definido por el ángulo θ.

coincidir necesariamente con la orientación promedio. Concrétamente la orientación local instantánea está definida por un vector $\vec{u'}$, que forma un ángulo θ con el vector $\vec{u}$. Mientras que para interfases fluidas la energía libre interfacial es isotrópica, es decir, independiente de θ, en interfases con presencia de sólidos deja de serlo y pasa a depender de la orientación de la interfase, es decir, $\gamma = \gamma(\theta)$. Por ello, para este tipo de interfases podemos desarrollar el modelo del Hamiltoniano Interfacial partiendo igualmente de la Ec. 2.1 pero tomando ahora en consideración que $\gamma = \gamma(\theta)$.

La dependencia de γ con la orientación se puede expresar como un desarrollo de Taylor en torno a θ, según el cual:

$$\gamma(\theta) = \gamma_0 + \frac{d\gamma}{d\theta}\theta + \frac{1}{2}\frac{d^2\gamma}{d\theta^2}\theta^2 \tag{2.21}$$

Por otro lado, puesto que las fluctuaciones de h son pequeñas, es decir, $dh/dx << 1$, podemos escribir:

$$\theta = \text{arc tg}(\frac{dh}{dx}) \approx \frac{dh}{dx} \tag{2.22}$$

Y si ahora utilizamos las Ec. 2.21 y 2.22 para reemplazar γ en la Ec. 2.2 obtenemos, para una sola dimensión y considerando ausencia de campo externo:

$$H[h] = \int \left[\gamma_0 + \frac{d\gamma}{d\theta}\frac{dh}{dx} + \frac{1}{2}\frac{d^2h}{d\theta^2}\left(\frac{dh}{dx}\right)^2\right]\left[1 + \frac{1}{2}(\nabla h)^2\right] dx \tag{2.23}$$

Fijándonos en el sistema de referencia mostrado en la Fig. 2.1 se puede comprobar que:

$$(\nabla h)^2 = \left(\frac{dh}{dx}\right)^2 \tag{2.24}$$

que introducido en la ecuación anterior resulta en

$$H[h] = \int \left[\gamma_0 + \frac{d\gamma}{d\theta}\frac{dh}{dx} + \frac{1}{2}\frac{d^2\gamma}{d\theta^2}\left(\frac{dh}{dx}\right)^2\right]\left[1 + \frac{1}{2}\left(\frac{dh}{dx}\right)^2\right]dx \tag{2.25}$$

Si ahora se tiene en cuenta que el término impar se anula por simetría se obtiene

$$H[h] = \int \gamma_0 dx + \frac{1}{2}\int \left(\gamma_0 + \frac{d^2\gamma}{d\theta^2}\right)\left(\frac{dh}{dx}\right)^2 d\vec{x} + \mathcal{O}\left(\left(\frac{dh}{dx}\right)^4\right) \tag{2.26}$$

o lo que es lo mismo:

$$H[h] = \gamma_0 l + \frac{1}{2}\int \widetilde{\gamma}\left(\frac{dh}{dx}\right)^2 dx \tag{2.27}$$

donde l es la longitud de la interfase monodimensional y el coeficiente $\widetilde{\gamma}$ es la rigidez interfacial. Comparando las Ec. 2.26 y 2.27 se obtiene que la rigidez y la energía libre interfacial están relacionadas según

$$\widetilde{\gamma}(\theta) = \gamma(\theta) + \frac{d^2\gamma(\theta)}{d\theta^2} \tag{2.28}$$

Este coeficiente es de gran relevancia cuando se trabaja con interfases sólidas puesto que reemplaza a la tensión superficial γ_{lv} de las interfases líquido–vapor.

Como se puede observar la Ec. 2.27 es equivalente a la Ec. 2.2 particularizada para una interfase sólida en ausencia de campo externo. Por tanto un desarrollo para la Ec. 2.27 idéntico al realizado para la Ec. 2.2 lleva a

$$A\left\langle|\delta h_{\mathbf{q}}|^2\right\rangle = \frac{k_B T}{\widetilde{\gamma} q^2} \tag{2.29}$$

Aunque esta ecuación ha sido deducida para una interfase monodimensional, es posible realizar un desarrollo análogo en dos dimensiones. Para ello se introduce un vector $\vec{n}$ perpendicular a $\vec{u}$ y $\vec{v}$, y se define el eje $y \parallel \vec{n}$. El resultado de este desarrollo es que la rigidez pasa a depender de la dirección de propagación de la onda y el vector $\mathbf{q}$ pasa a ser un vector bidimensional, $\mathbf{q} = (q_x, q_y)$. Así, el espectro de fluctuaciones a lo largo de los ejes principales se puede expresar como:

$$A\left\langle|\delta h_{\mathbf{q}}|^2\right\rangle = \frac{k_B T}{\widetilde{\gamma}_x q_x^2 + \widetilde{\gamma}_y q_y^2} \tag{2.30}$$

Finalmente, con el objetivo de mostrar la relevancia de las ecuaciones aquí descritas a continuación se detalla en qué contexto han sido utilizadas a lo largo de esta tesis.

Por un lado, la Ec. 2.18 se ha empleado en los Capítulos 1 y 7 para obtener el espectro de ondas capilares de interfases liquido–vapor.

Por otra parte la Ec. 2.20 se ha empleado en el Capítulo 1 para calcular la longitud de correlación paralela.

La Ec. 2.29 se emplea en los Capítulos 2, 3, 4, 5 y 6 para obtener la rigidez a partir de las fluctuaciones capilares. Con este mismo objetivo, la Ec. 2.30 se emplea en los Capítulos 3 y 4 ya que en ellos se analizan interfases bidimensionales.

Finalmente, la Ec. 2.28 se emplea en los Capítulos 3, 4 y 5 para obtener la energía libre interfacial a partir de la rigidez.

Capítulo 3
Determinación de la energía libre interfacial

Uno de los temas centrales de esta tesis es la determinación de energías libres interfaciales para interfases sólidas. El interés por esta magnitud se debe, en gran parte, a que su valor determina las tasas de nucleación de cristales a partir de sus fundidos subenfriados, así como la forma de estos cristales. Dentro del campo de la simulación molecular, existen en la actualidad varios métodos que permiten su cálculo basándose en distintos fundamentos. A continuación se realiza una breve descripción de algunos de los más importantes entre los que se encuentran el método de *cleaving* [48], el método de fluctuaciones capilares [49], el método de la metadinámica [50], el método de *seeding* [51], el método de *tethered Monte Carlo* [52] y el método de integración de molde [53].

El primer método propuesto fue el método de *cleaving*, diseñado por Broughton y Gilmer en 1986. En él, la γ_{sl} se obtiene directamente mediante el cálculo por integración termodinámica del trabajo reversible requerido para partir las fases sólida y líquida y después recombinarlas. Actualmente este método se sigue utilizando, y distintas versiones se han aplicado a sistemas como esferas duras [54], Lennard–Jones [55], fluidos dipolares [56] o agua [57, 58]. El método de fluctuaciones capilares, desarrollado en 2001, permite obtener γ_{sl} mediante el análisis de las fluctuaciones de la posición de la interfase en torno a su posición de equilibrio y ha sido aplicado en numerosos sistemas tales como esferas duras [43], Lennard-Jones [59], Yukawa [60] o diversos metales [45, 49, 61, 62]. Por otra parte, el método de la metadinámica, de 2006, se basa en la técnica de simulación de eventos raros conocida como metadinámica [63] y en él se calcula el trabajo de formación de una interfase a partir de un fluido en condiciones de coexistencia. En el trabajo original el método se aplica a un modelo de Lennard–Jones. También de 2006 es el método de *seeding*, propuesto por Bai y Li [51], y que permite determinar la energía libre interfacial promedio de un sólido mediante la inserción de un agregado en un fluido metaestable haciendo uso de la teoría de nucleación. Este método, propuesto originalmente para el estudio de clatratos también ha sido empleado para la determinación de γ_{sl} en el agua [64]. En el método de *tethered Monte Carlo*, de 2012, se hace uso de parámetros de

orden complejos para seguir una transición continua entre las las fases sólida y fluida, y ha sido aplicado en sistemas de esferas duras. Por último, el método de integración de molde, desarrollado en 2014, consiste en el empleo de un molde compuesto por pozos de potencial que inducen la formación de un bloque cristalino en el seno de un fluido en condiciones de coexistencia. Así, mediante la medición del trabajo reversible requerido para formar dicho bloque se puede calcular γ_{sl}. Este método se ha probado tanto para esferas duras como para Lennard-Jones proporcionando excelentes resultados.

Puesto que esta tesis está dirigida al estudio de ondas capilares, el resto del capítulo se centra en describir cómo aplicar el método de fluctuaciones capilares para el cáculo de energías libres interfaciales. Para ello es necesario localizar la posición de la interfase, obteniéndose una función en espacio real a la cual se le realiza una transformada de Fourier. A continuación se aplica la Ec. 2.29 obtenida mediante el Modelo del Hamiltoniano Interfacial, obteniéndose así la rigidez. Por último, una vez obtenida la rigidez se procede al cálculo de la energía libre interfacial. A continuación se detalla cada uno de estos pasos.

3.1 Obtención del perfil interfacial

El primer paso en el cálculo de la energía libre interfacial consiste en obtener una función discreta $h(x_j, y_k)$ correspondiente al perfil interfacial. Para obtenerla, lo primero que hay que hacer es etiquetar las partículas del sistema como sólidas o líquidas, de forma que sea posible separar ambas fases. Para ello se hace uso de parámetros de orden que permiten realizar dicho etiquetado de una forma eficaz (ver Apéndice A). Una vez hecha esta separación se desechan las partículas etiquetadas como líquidas y, de entre todas las partículas etiquetadas como sólidas, se seleccionan únicamente aquellas que pertenecen al agregado de mayor tamaño. De esta forma se consigue aislar la fase cristalina. A continuación se lleva a cabo una discretización de la interfase. Para ello se divide el eje x en n_x puntos equiespaciados. Igualmente se divide el eje y en n_y puntos también equiespaciados. De esta forma se obtiene un conjunto de n puntos con coordenadas (x_j, y_k) donde hay que evaluar la función $h(x_j, y_k)$, siendo $n = n_x \cdot n_y$. El valor de dicha función en cada punto n se calcula como el valor promedio de las n_0 partículas más externas situadas dentro de un cuadrado de lado Δ cuyo centro tiene coordenadas (x_j, y_k). En resumen, la posición de la interfase se puede localizar mediante una discretización en la que aparecen cuatro parámetros ajustables: n_x, n_y, Δ y n_0. En la Figura 3.1 se muestra un esquema de este proceso.

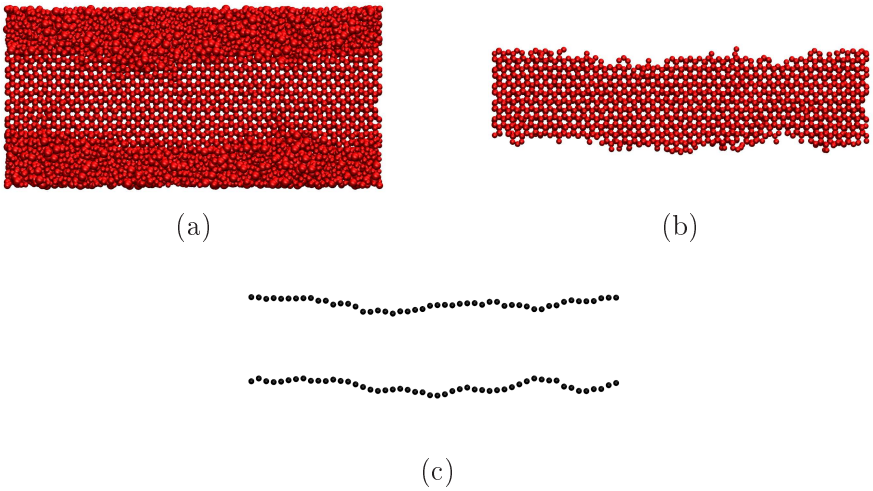

Figura 3.1. Esquema del proceso de localización de la interfase. (a) Sistema con todas las moléculas presentes. (b) Partículas sólidas pertenecientes al agregado de mayor tamaño. (c) Perfil interfacial $h(x_j, y_k)$ calculado con $n_y = 1$.

3.2 Aplicación del modelo del Hamiltoniano Interfacial

El segundo paso consiste en aplicar el modelo del Hamiltoniano Interfacial. Para ello se hace uso de la función $h(x_j, y_k)$ y se le realiza una transformada de Fourier, según:

$$h_q = \frac{1}{n} \sum_j \sum_k h(x_j, y_k) e^{i(q_x x_j + q_y y_k)} \tag{3.1}$$

donde n es el número de puntos donde esta evaluada la función $h(x_j, y_k)$, y $q_x = 2\pi n_{x_j}/L_x$ y $q_y = 2\pi n_{y_k}/L_y$ son las componentes del vector q, a lo largo de los ejes x e y, respectivamente.

Tras haber realizado la transformada de Fourier se calcula $|h_q|^2$ según:

$$|h_q|^2 = h_q \cdot h_q^* \tag{3.2}$$

donde h_q^* es la función compleja conjugada de h_q. Este producto se promedia sobre todas las configuraciones obtenidas durante la simulación, obteniéndose $\langle |h_q|^2 \rangle$, que introducido en la Ec. 2.29 permite obtener la rigidez $\widetilde{\gamma}$ mediante una extrapolación de su valor a $q = 0$.

3.3 Obtención de la energía libre interfacial a partir de la rigidez

Finalmente, una vez que se ha obtenido la rigidez es posible calcular la energía libre interfacial a partir de la Ec. 2.28. Para ello es necesario buscar una forma de evaluar $d^2\gamma/d\theta^2$. Este proceso no es fácil puesto que la dependencia de la energía libre interfacial con la orientación no es sencilla. Sin embargo en esta tesis se han empleado dos métodos que permiten evaluar dicha derivada: el Método de los Armónicos y el Método de la Estimación Numérica de la Curvatura, desarrollado en esta tesis. A continuación se muestran ambos métodos.

3.3.1 Método de los Armónicos

Este método consiste en buscar una expresión para $\gamma(\theta)$ y posteriormente calcular su segunda derivada. Dicha expresión se consigue mediante una expansión en términos armónicos, cuya naturaleza, cúbica o esférica, dependerá de la simetría del sólido.

Sistemas cúbicos

Cuando un sólido presenta simetría cúbica, la dependencia de γ con la orientación se puede obtener mediante una expansión en términos de cúbicos armónicos. Los cúbicos armónicos son una base de funciones ortogonales que permiten la representación de funciones con grupo puntual de simetría cúbico; siendo cada cúbico armónico una función de vectores unitarios sobre la superficie de una esfera.

El uso de estos armónicos está muy extendido en el campo de la mecánica cuántica, puesto que se emplean como base de las combinaciones lineales usadas para representar las funciones de onda de los orbitales atómicos. En el campo de la cristalografía es posible realizar expansiones similares para describir propiedades físicas tales como la energía libre interfacial o la rigidez.

En su artículo de 1976 Fehlner y Vosko proporcionan las expresiones de los cúbicos armónicos en términos de coordenadas cartesianas [65]. Así, según esta aproximación, la energía libre interfacial de una determinada cara cristalográfica, $\gamma(\vec{u})$, se puede expresar como

$$\gamma(\vec{u})/\gamma_0 \approx K_{0,0} + \epsilon_1 K_{4,1} + \epsilon_2 K_{6,1} + \epsilon_3 K_{8,2} + \epsilon_4 K_{10,2} + ... \tag{3.3}$$

donde $\vec{u}$ es el vector que define la cara cristalográfica, γ_0 es la energía libre interfacial promediada sobre todas las orientaciones posibles del cristal, $K_{l,d}$ son cúbicos armónicos (ver Tabla 3.1) y ϵ_k son parámetros que reflejan la anisotropía del sistema. Por tanto, si se quiere evaluar la energía libre interfacial de los planos cristalográficos, es nece-

$K_{0,0} = 1$
$K_{4,1} = \sqrt{21}\frac{1}{4}\,[5Q - 3]$
$K_{6,1} = \sqrt{\frac{13}{2}\frac{1}{8}}\,[462S + 21Q - 17]$
$K_{8,2} = \sqrt{561}\frac{1}{32}\,[65Q^2 - 208S - 94Q + 33]$
$K_{10,2} = \sqrt{\frac{455}{2}\frac{1}{64}}\,[7106QS + 187Q^2 - 3190S - 264Q + 85]$

Tabla 3.1. Cúbicos armónicos normalizados en términos de Q y S, donde $Q = x^4 + y^4 + z^4$ y $S = x^2y^2z^2$.

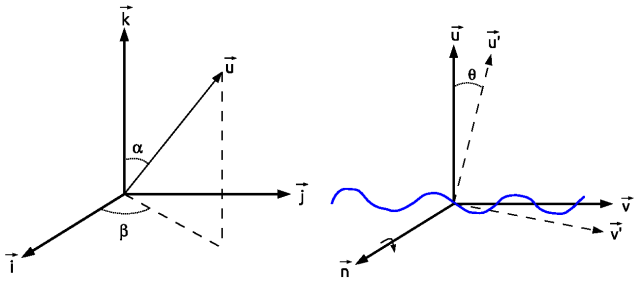

(a) (b)

Figura 3.2. (a) Representación del vector unitario $\vec{u}$, que define la posición de la interfase, en el sistema de referencia $\mathbb{A}$. (b) Representación del vector unitario $\vec{u}$ y del vector unitario, $\vec{u}'$, que define la interfase instantánea, en el sistema de coordenadas auxiliar.

sario conocer los valores correspondientes a los cúbicos armónicos, los parámetros de anisotropía y la energía interfacial promedio.

Para poder obtener los valores de los cúbicos armónicos hay que caracterizar la orientación del plano cristalino expuesto en la interfase. Un plano cristalino arbitrario queda definido mediante un vector unitario $\vec{u}$ perpendicular a dicho plano. A su vez, un vector unitario queda especificado mediante los ángulos α y β, definidos en un sistema de referencia $\mathbb{A}$ (ver Ec. 3.4) , tal y como se muestra en la Figura 3.2a, siendo α el ángulo polar y β el ángulo acimutal.

$$\mathbb{A} = \begin{pmatrix} \vec{i} \\ \vec{j} \\ \vec{k} \end{pmatrix} \tag{3.4}$$

Generalmente, la orientación de dicho plano viene definida en función de sus índices de Miller, mientras que los cúbicos armónicos son funciones de las coordenadas carte-

Plano interfacial	$\gamma(\vec{u})/\gamma_0$
(100)	$1+\frac{1}{2}\sqrt{21}\epsilon_1+\frac{1}{4}\sqrt{26}\epsilon_2+\frac{1}{8}\sqrt{561}\epsilon_3+\frac{1}{16}\sqrt{910}\epsilon_4+\frac{9}{164}\sqrt{451}\epsilon_5$
(110)	$1-\frac{1}{8}\sqrt{21}\epsilon_1-\frac{13}{32}\sqrt{26}\epsilon_2+\frac{9}{128}\sqrt{561}\epsilon_3-\frac{1}{512}\sqrt{910}\epsilon_4+\frac{2517}{20992}\sqrt{451}\epsilon_5$
(111)	$1-\frac{1}{3}\sqrt{21}\epsilon_1+\frac{4}{9}\sqrt{26}\epsilon_2+\frac{1}{27}\sqrt{561}\epsilon_3-\frac{8}{81}\sqrt{910}\epsilon_4+\frac{953}{9963}\sqrt{451}\epsilon_5$
$(11\bar{2})$	$1-\frac{1}{8}\sqrt{21}\epsilon_1+\frac{37}{288}\sqrt{26}\epsilon_2-\frac{173}{3456}\sqrt{561}\epsilon_3+\frac{233}{4608}\sqrt{910}\epsilon_4+\frac{284551}{5101056}\sqrt{451}\epsilon_5$

Tabla 3.2. Expresiones para la energía libre interfacial de distintos planos cristalográficos de un sistema cúbico.

sianas x, y, z, del sistema de referencia correspondiente, $\mathbb{A}$. Por ello es necesario poder expresar la orientación del plano bajo estudio en términos de las coordenadas cartesianas del vector que lo define.

Para un plano cristalino cualquiera, definido por un vector $\vec{u}$ perpendicular a él, con dirección [h k l], podemos expresar su orientación en el sistema de referencia $\mathbb{A}$ como

$$x=\frac{h}{\sqrt{h^2+k^2+l^2}} \quad y=\frac{k}{\sqrt{h^2+k^2+l^2}} \quad z=\frac{l}{\sqrt{h^2+k^2+l^2}} \tag{3.5}$$

ya que los vectores $\vec{i}$, $\vec{j}$, $\vec{k}$ son ortonormales.

Así, una vez que se tienen las coordenadas cartesianas del vector $\vec{u}$ se puede obtener la correspondiente expansión en térmicos de cúbicos armónicos para la energía libre interfacial de los planos cristalográficos de interés a partir de la Ec. 3.3. Los resultados se muestran en la Tabla 3.2.

El siguiente paso es determinar el valor de los parámetros de anisotropía ϵ_k. En nuestro caso la información disponible sobre la interfase viene dada por la rigidez, por lo que tenemos que recurrir a ella para obtener dichos parámetros. La rigidez, al igual que la energía libre interfacial, depende del plano cristalino expuesto en la interfase, pero a su vez depende también de la dirección de propagación de la onda. Por ello, para simplificar la interpretación definimos la matriz $\mathbb{W}$ (ver Ec.3.6) que caracteriza un sistema de referencia auxiliar asociado al plano cristalográfico y a la onda asociada tal y como se muestra en la Figura 3.2b

$$\mathbb{W}=\begin{pmatrix}\vec{n}\\ \vec{v}\\ \vec{u}\end{pmatrix} \tag{3.6}$$

En este sistema $\vec{u}$ define el plano cristalográfico de la interfase, y $\vec{v}$ define la dirección de propagación de la onda, siendo $\vec{v} \perp \vec{u}$. El plano cristalino mostrado instantáneamente en la interfase está definido en este caso por el vector $\vec{u}'$ y que se obtiene mediante una rotación en torno a $\vec{n}$. La magnitud de esta rotación, θ, determina qué plano cristalográfico se esta mostrando en la interfase en cada momento, así como la dirección de propagación de la onda en ese mismo instante, $\vec{v}'$. Puesto que tanto $\vec{u}$ y $\vec{u}'$, como $\vec{v}$ y $\vec{v}'$ forman entre sí un ángulo θ, es posible expresar los nuevo vectores $\vec{u}'$ y $\vec{v}'$ en términos de $\vec{u}$, $\vec{v}$ y θ, manteniéndose $\vec{n}$ inalterado.

$$\begin{aligned} \vec{u}' &= \vec{u}cos(\theta) + \vec{v}sen(\theta) \\ \vec{v}' &= -\vec{u}sen(\theta) + \vec{v}cos(\theta) \end{aligned} \tag{3.7}$$

Esto permite introducir la matriz de rotación $\mathbb{R}$, cuya expresión viene dada por

$$\mathbb{R}' = \begin{pmatrix} 1 & 0 & 0 \\ 0 & -sen(\theta) & cos(\theta) \\ 0 & cos(\theta) & sen(\theta) \end{pmatrix} \tag{3.8}$$

De esta forma el nuevo sistema de referencia auxiliar $\mathbb{W}'$, asociado en este caso a la posición instantánea de la interfase, se puede expresar como

$$\mathbb{W}' = \begin{pmatrix} 1 & 0 & 0 \\ 0 & -sen(\theta) & cos(\theta) \\ 0 & cos(\theta) & sen(\theta) \end{pmatrix} \begin{pmatrix} \vec{n} \\ \vec{v} \\ \vec{u} \end{pmatrix} = \begin{pmatrix} \vec{n}' \\ \vec{v}' \\ \vec{u}' \end{pmatrix} \tag{3.9}$$

Si ahora se tiene en cuenta que $\vec{u} = [hkl]$ y $\vec{v} = [mno]$ podemos reescribir la Ec.3.9 como

$$\mathbb{W}' = \begin{pmatrix} 1 & 0 & 0 \\ 0 & -sen(\theta) & cos(\theta) \\ 0 & cos(\theta) & sen(\theta) \end{pmatrix} \begin{pmatrix} & \vec{n} & \\ m & n & o \\ h & k & l \end{pmatrix} \tag{3.10}$$

lo que permite expresar las coordenadas cartesianas del vector $\vec{u}'$, que define el plano cristalográfico, como

$$x' = h \cdot cos(\theta) + m \cdot sen(\theta) \quad y' = k \cdot cos(\theta) + n \cdot sen(\theta) \quad z' = l \cdot cos(\theta) + o \cdot sen(\theta) \tag{3.11}$$

Estas nuevas expresiones para las coordenadas x', y' y z' en función del ángulo θ son especialmente útiles ya que la rigidez está relacionada con la energía libre interfacial según

$$\widetilde{\gamma}(\vec{u}, \vec{n}) = \left(\gamma(\theta) + \frac{d^2\gamma(\theta)}{d\theta^2} \right)_{\theta=0} \tag{3.12}$$

$\vec{u}$	$\vec{n}$	$\widetilde{\gamma}(\vec{u},\vec{n})/\gamma_0$
100	010	$1-\frac{9}{2}\sqrt{21}\epsilon_1-5\sqrt{26}\epsilon_2-\frac{35}{8}\sqrt{561}\epsilon_3-\frac{27}{8}\sqrt{910}\epsilon_4+\frac{9}{164}\sqrt{451}\epsilon_5$
110	001	$1+\frac{39}{8}\sqrt{21}\epsilon_1+\frac{155}{32}\sqrt{26}\epsilon_2-\frac{455}{128}\sqrt{561}\epsilon_3-\frac{1233}{512}\sqrt{910}\epsilon_4-\frac{109179}{20992}\sqrt{451}\epsilon_5$
110	$\bar{1}10$	$1-\frac{21}{8}\sqrt{21}\epsilon_1+\frac{365}{32}\sqrt{26}\epsilon_2-\frac{175}{128}\sqrt{561}\epsilon_3+\frac{1341}{512}\sqrt{910}\epsilon_4-\frac{278439}{20992}\sqrt{451}\epsilon_5$
111	$1\bar{1}0$	$1+3\sqrt{21}\epsilon_1-\frac{80}{9}\sqrt{26}\epsilon_2-\frac{35}{27}\sqrt{561}\epsilon_3+\frac{16}{3}\sqrt{910}\epsilon_4-\frac{73381}{9963}\sqrt{451}\epsilon_5$
$11\bar{2}$	$1\bar{1}0$	$1+\frac{19}{8}\sqrt{21}\epsilon_1+\frac{1255}{288}\sqrt{26}\epsilon_2+\frac{4795}{3456}\sqrt{561}\epsilon_3-\frac{21041}{4608}\sqrt{910}\epsilon_4-\frac{1318037}{5101056}\sqrt{451}\epsilon_5$
$11\bar{2}$	111	$1-\frac{1}{8}\sqrt{21}\epsilon_1-\frac{2735}{288}\sqrt{26}\epsilon_2+\frac{7315}{3456}\sqrt{561}\epsilon_3-\frac{4123}{4608}\sqrt{910}\epsilon_4-\frac{42502817}{5101056}\sqrt{451}\epsilon_5$

Tabla 3.3. Expresiones para la rigidez de distintos planos y distintas direcciones de propagación de la onda en un sistema cúbico.

Así, introduciendo las nuevas coordenadas cartesianas en los cúbicos armónicos, dados en la Tabla 3.1, y derivando éstos dos veces respecto al ángulo θ se pueden obtener las contribuciones debidas a la curvatura de $\gamma(\theta)$. Esto permite obtener expresiones para la rigidez análogas a las obtenidas para la energía libre interfacial. Estas expresiones han sido halladas para distintos planos cristalinos y distintas direcciones de propagación, y se recogen en la Tabla 3.3.

Por último, una vez que se tienen las expresiones correspondientes basta con resolver el sistema de ecuaciones mostrado en la Tabla 3.3 para obtener los parámetros de anisotropía, ϵ_k, así como γ_0, que permiten obtener la energía libre interfacial de las distintas caras a partir de las ecuaciones recogidas en la Tabla 3.2.

Sistemas hexagonales

Cuando se trabaja con un sistema con simetría hexagonal, cuyo grupo puntual de simetría es D_{6h}, es igualmente posible obtener la energía libre interfacial de los distintos planos cristalográficos, $\gamma(\vec{u})$, de dicho sistema mediante una parametrización. En este caso se lleva a cabo una expansión de la energía libre interfacial en función de los armónicos esféricos según la cual [66]

$$\gamma(\vec{u})/\gamma_0 \approx 1+\epsilon_1 y_{20}(\alpha,\beta)+\epsilon_2 y_{40}(\alpha,\beta)+\epsilon_3 y_{60}(\alpha,\beta)+\epsilon_4 y_{66}(\alpha,\beta) \tag{3.13}$$

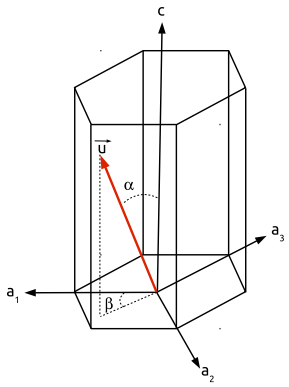

Figura 3.3. Sistema de referencia hexagonal compuesto por cuatro ejes principales. El vector $\vec{u}$ determina el plano cristalográfico mostrado en la interfase, y esta caracterizado por los ángulos α y β.

$y_{20}(\alpha,\beta) = \sqrt{5/16\pi}\,[3cos^2(\alpha) - 1]$
$y_{40}(\alpha,\beta) = \frac{3}{16}\sqrt{1/\pi}\,[35cos^4(\alpha) - 30cos^2(\alpha) + 3]$
$y_{60}(\alpha,\beta) = \frac{1}{32}\sqrt{13/\pi}\,[231cos^6(\alpha) - 315cos^4(\alpha) + 105cos^2(\alpha) - 5]$
$y_{66}(\alpha,\beta) = \frac{1}{64}\sqrt{6006/\pi}\,[1 - cos^2(\alpha)]^3\, cos(6\beta)$

Tabla 3.4. Expresiones para los armónicos esféricos normalizados.

donde $\vec{u}$ es el vector que define el plano cristalográfico, γ_0 es la energía libre interfacial promediada sobre todas las orientaciones, y_{lm} son los armónicos esféricos, recogidos en la Tabla 3.4, ϵ_k son los parámetros de anisotropía del sistema, y α y β son los ángulos polar y acimutal, respectivamente, y que describen el plano cristalográfico expuesto en la interfase.

En este caso, los armónicos esféricos son directamente funciones de los ángulos α y β. Por ello no es necesario hacer ninguna transformación de coordenadas a la hora de realizar la parametrización de la energía libre interfacial, sino que basta con conocer los ángulos que definen el plano cristalográfico mostrado en la interfase. En el caso de un sistema hexagonal los principales planos cristalográficos son el basal o (0001), el prismático primario o $(10\bar{1}0)$ y el prismático secundario o $(11\bar{2}0)$. Los resultados para cada uno de estos planos se recogen en la Tabla 3.5.

Al igual que ocurría con los sistemas cúbicos, para poder utilizar estas expresiones, es necesario conocer los parámetros de anisotropía ϵ_k, para lo cual recurrimos nuevamente

Plano interfacial	$\gamma(\vec{u})/\gamma_0$
(0001)	$1+\frac{1}{2}\sqrt{5/\pi}\epsilon_1+\frac{3}{2}\sqrt{1/\pi}\epsilon_2+\frac{1}{2}\sqrt{13/\pi}\epsilon_3$
$(10\bar{1}0)$	$1-\frac{1}{4}\sqrt{5/\pi}\epsilon_1+\frac{9}{16}\sqrt{1/\pi}\epsilon_2-\frac{5}{32}\sqrt{13/\pi}\epsilon_3-\frac{1}{64}\sqrt{6006/\pi}\epsilon_4$
$(11\bar{2}0)$	$1-\frac{1}{4}\sqrt{5/\pi}\epsilon_1+\frac{9}{16}\sqrt{1/\pi}\epsilon_2-\frac{5}{32}\sqrt{13/\pi}\epsilon_3+\frac{1}{64}\sqrt{6006/\pi}\epsilon_4$

Tabla 3.5. Energía libre interfacial para distintos planos cristalográficos de una estructura cristalina perteneciente a un sistema hexagonal.

a la rigidez. Sin embargo, en este caso, para resolver la Ec. 3.12 no es conveniente cambiar el sistema de referencia, sino que hay que ver cómo varían los ángulos α y β al propagarse la onda.

Teniendo en cuenta que el plano cristalino de la interfase viene definido por el vector $\vec{u}$ y que la onda se propaga en la dirección del vector $\vec{v}$, al producirse una rotación de magnitud θ sobre un eje $\vec{n}$, contenido en el plano interfacial y perpendicular a ambos, se genera un nuevo vector $\vec{u}'$ cuyos ángulos α y β son distintos de los del vector $\vec{u}$. En la Fig. 3.4 se muestran varias posibles rotaciones para los principales planos cristalográficos. Como se puede observar, en todos los casos mostrados, la rotación de magnitud θ en torno a $\vec{n}$ produce una variación de la misma magnitud bien en α o bien en β según sobre qué eje se esté produciendo la rotación, pero en ningún caso se produce variación de ambos ángulos simultáneamente.

Este hecho es de especial interés, puesto que nos permite evaluar $d^2\gamma(\theta)/d\theta^2$ como $d^2\gamma(\alpha,\beta)/d\alpha^2$ o como $d^2\gamma(\alpha,\beta)/d\beta^2$ según corresponda. En la Tabla 3.6 se muestran los valores de α y β que corresponden a cada uno de los planos cristalográficos, así como el ángulo que se ve modificado al producirse una rotación en torno a $\vec{n}$. De esta forma, una vez que se tiene $d^2\gamma(\theta)/d\theta^2$ se pueden obtener las expansiones para la rigidez en función del plano cristalográfico y la dirección de propagación de la onda. Estas expansiones se recogen en la Tabla 3.7.

3.3.2 Estimación Numérica de la Curvatura (ENC)

Una forma alternativa de calcular la energía libre interfacial de un determinado plano cristalográfico, basada igualmente en la Ec.3.12, consiste en hacer una estimación numérica de la segunda derivada de $\gamma(\theta)$. Para ello se lleva a cabo una expansión en series de Taylor de la función en torno a un punto. Según esta expansión:

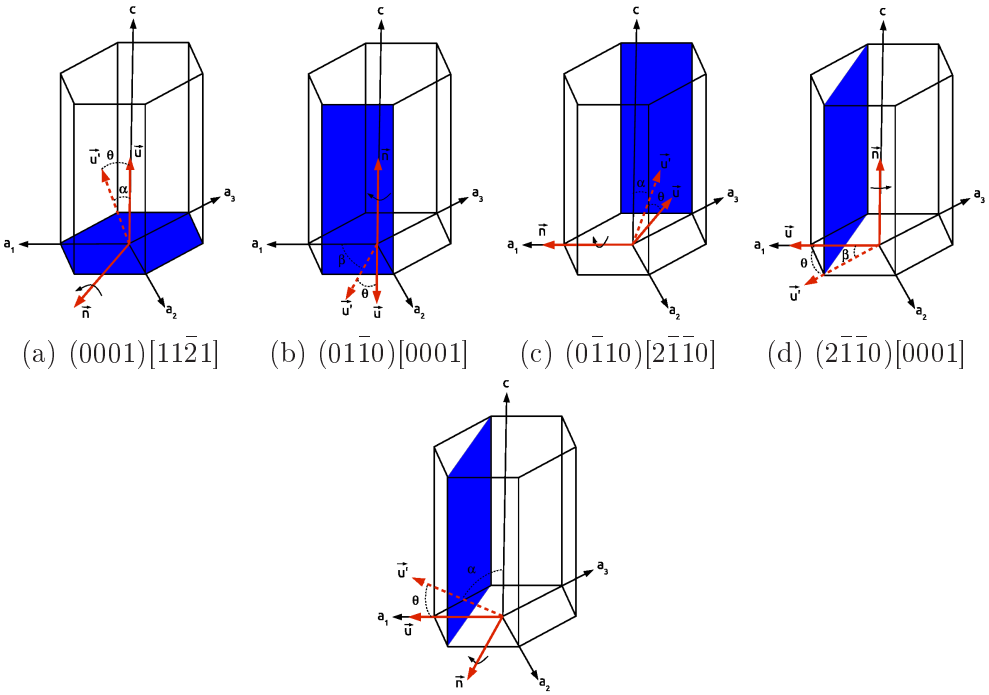

(a) $(0001)[11\bar{2}1]$ (b) $(01\bar{1}0)[0001]$ (c) $(0\bar{1}10)[2\bar{1}\bar{1}0]$ (d) $(2\bar{1}\bar{1}0)[0001]$

(e) $(2\bar{1}\bar{1}0)[01\bar{1}0]$

Figura 3.4. Rotaciones de los principales planos cristalográficos. Entre paréntesis se expresa el plano interfacial, $\vec{u}$. Entre corchetes aparece el eje de rotación, $\vec{n}$. Nótese que los planos $(01\bar{1}0)$ y $(0\bar{1}10)$ mostrados en las figuras 3.4b y 3.4e son equivalentes cristalográficamente al plano $(10\bar{1}0)$, que es el que aparece en las tablas. Igualmente el plano $(2\bar{1}\bar{1}0)$ de las figuras 3.4c, 3.4d y 3.4e es equivalente al plano $(11\bar{2}0)$ de las tablas.

Plano	0001	$10\bar{1}0$		$11\bar{2}0$	
α, β	0, -	$\pi/2$, $\pi/3$		$\pi/2$, $\pi/6$	
Eje de rotación, $\vec{n}$	$11\bar{2}0$	0001	$11\bar{2}0$	0001	$10\bar{1}0$
Ángulo modificado	α	β	α	β	α

Tabla 3.6. Valores de los ángulos que definen el plano interfacial. Para cada uno de los planos planos se muestra el eje de rotación $\vec{n}$ y el ángulo que varía al realizar dicha rotación.

$\vec{u}$	$\vec{n}$	$\widetilde{\gamma}(\vec{u},\vec{n})/\gamma_0$
0001	$11\bar{2}0$	$1-\sqrt{5/\pi}\epsilon_1-\frac{27}{2}\sqrt{1/\pi}\epsilon_2-10\sqrt{13/\pi}\epsilon_3$
$10\bar{1}0$	$11\bar{2}0$	$1+\frac{5}{4}\sqrt{5/\pi}\epsilon_1-\frac{171}{16}\sqrt{1/\pi}\epsilon_2+\frac{205}{32}\sqrt{13/\pi}\epsilon_3+\frac{5}{64}\sqrt{6006/\pi}\epsilon_4$
$10\bar{1}0$	0001	$1-\frac{1}{4}\sqrt{5/\pi}\epsilon_1+\frac{9}{16}\sqrt{1/\pi}\epsilon_2-\frac{5}{32}\sqrt{13/\pi}\epsilon_3+\frac{35}{64}\sqrt{6006/\pi}\epsilon_4$
$11\bar{2}0$	$10\bar{1}0$	$1+\frac{5}{4}\sqrt{5/\pi}\epsilon_1-\frac{171}{16}\sqrt{1/\pi}\epsilon_2+\frac{205}{32}\sqrt{13/\pi}\epsilon_3-\frac{5}{64}\sqrt{6006/\pi}\epsilon_4$
$11\bar{2}0$	0001	$1-\frac{1}{4}\sqrt{5/\pi}\epsilon_1+\frac{9}{16}\sqrt{1/\pi}\epsilon_2-\frac{5}{32}\sqrt{13/\pi}\epsilon_3-\frac{35}{64}\sqrt{6006/\pi}\epsilon_4$

Tabla 3.7. Expresiones para la rigidez en función del plano cristalográfico y del eje de rotación en un sistema hexagonal.

$$\left.\begin{aligned} f(x+\delta x) &= f(x)+f'(x)\delta x+\frac{1}{2}f''(x)\delta x^2 \\ f(x-\delta x) &= f(x)-f'(x)\delta x+\frac{1}{2}f''(x)\delta x^2 \end{aligned}\right\} f''(x)=\frac{f(x-\delta x)-2f(x)+f(x+\delta x)}{\delta x^2} \tag{3.14}$$

Así, considerando el sistema de referencia de la Figura 3.2b, para un determinado plano cristalográfico se obtiene

$$\widetilde{\gamma}\left(\vec{u},\vec{n}\right)=\gamma(\vec{u})+\frac{\gamma(\vec{u}_1')-2\gamma(\vec{u})+\gamma(\vec{u}_2')}{\Delta\theta^2} \tag{3.15}$$

donde $\gamma(\vec{u}_1')$ y $\gamma(\vec{u}_2')$ son las energías interfaciales de dos planos cristalográficos mostrados en la interfase al rotar un ángulo θ en torno a $\vec{n}$ a izquierda y derecha, respectivamente. Así, conociendo la rigidez de tres orientaciones, que se obtienen por rotación en torno al mismo eje, se puede obtener la energía libre interfacial de los tres planos cristalográficos implicados.

En el caso de sistemas con simetría cúbica (en el caso del NaCl, sistemas con simetría C_4) basta con combinar dos orientaciones con un eje de rotación común, ya que la simetría hace que aparezcan direcciones equivalentes. De acuerdo con la Figura 3.5a podemos establecer que:

$$\begin{aligned} &\widetilde{\gamma}_{100}=\widetilde{\gamma}_{010}=\widetilde{\gamma}_{\bar{1}00}=\widetilde{\gamma}_{0\bar{1}0} \text{ y } \gamma_{100}=\gamma_{010}=\gamma_{\bar{1}00}=\gamma_{0\bar{1}0} \\ &\widetilde{\gamma}_{110}=\widetilde{\gamma}_{\bar{1}10}=\widetilde{\gamma}_{\bar{1}\bar{1}0}=\widetilde{\gamma}_{1\bar{1}0} \text{ y } \gamma_{110}=\gamma_{\bar{1}10}=\gamma_{\bar{1}\bar{1}0}=\gamma_{1\bar{1}0} \end{aligned} \tag{3.16}$$

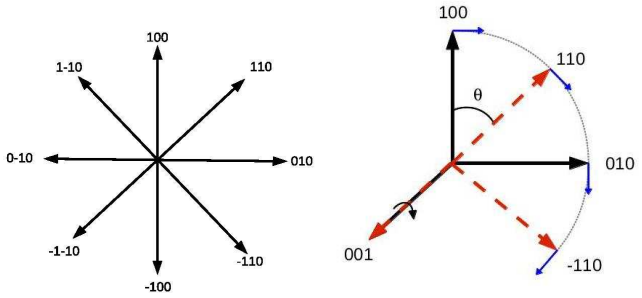

(a) (b)

Figura 3.5. (a) Proyección de un sistema con simetría C_4 a lo largo del eje [001]. Se muestran las direcciones principales. (b) Representación de la propagación de las ondas en los sistemas (100)[001] (negro) y (110)[001] (rojo). Ambos sistemas comparten rotación en torno al eje [001].

De esta forma, aplicando ahora la Ec. 3.15 obtenemos:

$$\begin{aligned} \widetilde{\gamma}_{100} &= \gamma_{100} + \frac{2\gamma_{110} - 2\gamma_{100}}{(\pi/4)^2} \\ \widetilde{\gamma}_{110} &= \gamma_{110} + \frac{2\gamma_{100} - 2\gamma_{110}}{(\pi/4)^2} \end{aligned} \tag{3.17}$$

es decir, un sistema de dos ecuaciones con dos incógnitas que nos permite conocer γ_{100} y γ_{110} a partir de las correspondientes rigidez.

Como se ha comentado anteriormente, es imprescindible que las orientaciones escogidas para realizar los cálculos compartan rotación en torno a un eje común. Esto se ilustra en la Figura 3.5b. En este caso tenemos representados los sistemas (100)[001] y (110)[001]. Si nos fijamos en el primero se puede observar que al propagar la onda hacia el vector [010] aparece el segundo de ellos cuando rotamos un ángulo $\theta = \pi/4$ en torno al vector [001]. Por tanto ambos sistemas son intercambiables mediante rotación en torno al eje [001] y válidos para aplicar el método.

Con el objetivo de validar el método lo hemos aplicado a resultados publicados previamente para el modelo de esferas duras [43]. En dicho trabajo se recogen las rigidez de las orientaciones (100)[001] ($\widetilde{\gamma} = 0{,}44 k_B T \sigma^{-2}$), (110)[001] ($\widetilde{\gamma} = 0{,}70 k_B T \sigma^{-2}$), (110)[$\bar{1}$10] ($\widetilde{\gamma} = 0{,}42 k_B T \sigma^{-2}$) y (111)[$\bar{1}$10] ($\widetilde{\gamma} = 0{,}67 k_B T \sigma^{-2}$), entre otras. Como acabamos de describir, nuestro método se puede aplicar cuando dos orientaciones están relacionadas mediante un eje de rotación común. Por tanto, las combinaciones permitidas en este caso son entre las orientaciones (100)[001] y (110)[001] por un lado (Combinación 1), y (110)[$\bar{1}$10] y (111)[$\bar{1}$10] y por el otro (Combinación 2). Los resultados obtenidos se muestran en la Tabla 3.8 junto con los publicados en [43]. Como se puede observar, los resultados obtenidos por el nuevo método están en perfecto acuerdo con los ya publicados. Este hecho ya de por si interesante cobra más relevancia si se tiene en cuenta la

	Combinación 1	Combinación 2	Ref. [43]
γ_{100}	0.594		0.574
γ_{110}	0.546	0.558	0.557
γ_{111}		0.532	0.546

Tabla 3.8. Comparación de la energía libre interfacial γ, en unidades de $k_BT\sigma^{-2}$ para tres planos cristalográficos.

simplicidad del método propuesto.

Finalmente vamos a mostrar en qué partes de la tesis se han empleado las ecuaciones aquí descritas. En el Capítulo 5 de la parte de resultados se ha hecho uso de las expresiones recogidas en las Tablas 3.5 y 3.7 para calcular la energía libre interfacial de los principales planos cristalográficos del hielo Ih. En el Capítulo 4 se han empleado las expresiones de las Tablas 3.2 y 3.3 para obtener la energía libre interfacial de distintos planos cristalográficos del NaCl, así como su energía libre interfacial promedio. Estas mismas expresiones se han utilizado en el Capítulo 3, pero en este caso aplicadas al sistema Lennard–Jones. En este capítulo, además, se ha hecho uso de la Ec 3.17 para calcular la energía libre interfacial de las planos (100) y (110) de dicho modelo.

Capítulo 4
Teoría de difusión de la interfase y coeficiente cinético

Hasta el momento únicamente se ha hablado de propiedades estáticas de las interfases como son la rigidez, la energía interfacial o la longitud de correlación paralela. Sin embargo, también es posible hacer estudios sobre su dinámica con el fin de obtener más información. En 1993 Karma [67] desarrolló una teoría según la cual la velocidad de avance o retroceso de una interfase sólido–líquido se puede expresar a partir de una ecuación de difusión. A partir de esta teoría es posible calcular el coeficiente cinético μ, es decir, el coeficiente que relaciona la velocidad de avance de la interfase con la temperatura. A conticuación se detalla dicha teoría.

La velocidad de avance de una interfase monodimensional se puede definir como

$$v(x,t) = \mu \Delta T(x,t) \tag{4.1}$$

donde v es la velocidad de avance de la interfase, μ es el coeficiente cinético, y $\Delta T = T_f - T$ es la fuerza motriz que provoca el avance o retroceso de la interfase y que se corresponde con la diferencia de temperatura entre la temperatura de fusión del sistema y la temperatura de trabajo.

Igualmente la velocidad de la interfase se puede expresar como

$$v(x,t) = \frac{dh(x,t)}{dt} \tag{4.2}$$

donde $h(x,t)$ es la función que determina la altura de una interfase monodimensional.

Por tanto, igualando las ecuaciones 4.1 y 4.2 y añadiendo el término η correspondiente al ruido térmico podemos escribir

$$\frac{dh(x,t)}{dt} = \mu \Delta T + \eta(x,t) \tag{4.3}$$

Para una interfase sólido–líquido, que no es plana debido a las ondas capilares, existirá una diferencia de presión entre ambas fases. Si aplicamos la ecuación de Young–Laplace tenemos que la diferencia de presión a través de una interfase viene dada por

$$\Delta p = p_{int} - p_{ext} = -\widetilde{\gamma}\kappa \tag{4.4}$$

donde $\widetilde{\gamma}$ es la rigidez y κ es la curvatura de la interfase. Para expresar la curvatura se recurre a la ecuación de Gibbs–Thomson–Laplace para el equilibrio interfacial local,

$$\kappa = \frac{d^2h(x,t)}{dx^2} = \nabla^2 h(x,t) = \frac{\Delta p(x,t)}{\widetilde{\gamma}} \tag{4.5}$$

Anteriormente hemos visto que la fuerza motriz del desplazamiento de la interfase es el gradiente de temperatura, por lo que tenemos que relacionar éste con el gradiente de presión que acabamos de obtener. Para ello escribimos la sobrepresión de Laplace en términos del subenfriamiento local, $\Delta T(x,t)$, como

$$\Delta p(x,t) = \frac{\Delta H}{v_s T_m}\Delta T(x,t) \tag{4.6}$$

donde, en condiciones de coexistencia, ΔH es la entalpía de fusión molar por unidad de volumen, T_m es la temperatura de fusión y v_s es el volumen molar del sólido.

Por tanto, si ahora hacemos uso de las Ec. 4.5 y 4.6 podemos expresar la curvatura en términos del subenfriamiento

$$\nabla^2 h(x,t) = \frac{\Delta H}{v_s \widetilde{\gamma} T_m}\Delta T(x,t) \tag{4.7}$$

Así, introduciendo esta ecuación en la Ec. 4.3 podemos obtener la dinámica local de h(x,t) como

$$\frac{dh(x,t)}{dt} = \mu\frac{v_s\widetilde{\gamma}T_m}{\Delta H}\nabla^2 h(x,t) + \eta(x,t) \tag{4.8}$$

A partir de esta ecuación ya sería posible extraer el coeficiente cinético si se conociese la evolución de la interfase con el tiempo. Sin embargo, en nuestro caso el estudio se realiza en el espacio de Fourier, por lo que es necesario hacer las transformadas correspondientes tanto a $h(x,t)$ como a $\eta(x,t)$. Así, teniendo en cuenta que

$$\begin{aligned} h(x,t) &= \sum_q h_q(t)e^{iqx} \\ \eta(x,t) &= \sum_q g_q(t)e^{iqx} \end{aligned} \tag{4.9}$$

la solución de la Ec. 4.8 en el espacio de Fourier es

$$\frac{d}{dt}\sum_q h_q(t)e^{iqx} = -\mu\Gamma\sum_q q^2 h_q(t)e^{iqx} + \sum_q g_q(t)e^{iqx} \tag{4.10}$$

donde por comodidad hemos escrito $\Gamma = \frac{v_s\widetilde{\gamma}T_m}{\Delta H}$.

Reagrupando esta ecuación obtenemos

$$\sum_q \left\{ \frac{dh_q(t)}{dt} + \mu\Gamma q^2 h_q(t) - g_q(t) \right\} e^{iqx} = 0 \tag{4.11}$$

Y resolviendo para cada vector q individualmente

$$\frac{dh_q(t)}{dt} = -\mu\Gamma q^2 h_q(t) + g_q(t) \tag{4.12}$$

Llegados a este punto nos interesa resolver la ecuación diferencial que acabamos de obtener, cuya solución viene dada por

$$h_q(t) = h_q(0)e^{-\mu\Gamma q^2 t} + e^{-\mu\Gamma q^2 t}\int_0^t g_q(\tau)e^{\mu\Gamma\tau}d\tau \tag{4.13}$$

La función de correlación temporal de dicha función se puede obtener multiplicando a ambos lados por $h_q(t')^*$ y tomando promedios, obtiéndose

$$\langle h_q(t)h_q(t')^*\rangle = \left\langle |h_q|^2 \right\rangle e^{-\mu\Gamma q^2(t+t')} + e^{-\mu\Gamma q^2(t+t')}\int_0^t\int_0^{t'} \langle g_q(\tau)g_q(\tau')\rangle\, e^{\mu\Gamma q^2(\tau+\tau')}d\tau d\tau' \tag{4.14}$$

Teniendo en cuenta que $\langle g_q(\tau)g_q(\tau')\rangle$ representa la correlación de $g(q)$ a tiempo τ con $g(q)$ a tiempo τ', y que $g(q)$ varía muy rápidamente podemos asumir que $\langle g_q(\tau)g_q(\tau')\rangle$ es sólo función de $|\tau - \tau'|$ y únicamente no vale cero cuando $|\tau - \tau'|$ es muy pequeño. Esto es,

$$\langle g_q(\tau)g_q(\tau')\rangle = \phi_1(|\tau - \tau'|) \tag{4.15}$$

donde ϕ_1 es una función que presenta un máximo muy acentuado en $|\tau - \tau'| = 0$.

Ahora, haciendo el cambio de variables $v = \tau + \tau'$ y $w = \tau - \tau'$ tal y como se hace en [68] se puede resolver la Ec. 4.14 obteniéndose

$$\langle h_q(t)h_q(t')^*\rangle = \left\langle |h_q|^2 \right\rangle e^{-\mu\Gamma q^2(t+t')} + \frac{C}{2\mu\Gamma q^2}\left(1 - e^{-2\mu\Gamma q^2 t'}\right) \tag{4.16}$$

A $t = t'$ y en el límite de tiempos largos se debe cumplir que la parte izquierda de la ecuación debe ser igual a $\langle |h_q|^2\rangle$, lo que nos permite ver cuál es la contribución del ruido. Además, podemos considerar $t' = 0$ obteniendo

$$\langle h_q(t)h_q(0)^*\rangle = \left\langle |h_q|^2 \right\rangle e^{-\mu\Gamma q^2 t} \tag{4.17}$$

Llegados a este punto podemos observar en la Ec. 4.17 que la función de autocorrelación decae con un tiempo característico dependiente del vector de onda, q, que viene dado por $(\mu\Gamma q^2)^{-1}$. Así, obteniendo las funciones de autocorrelación espacio–temporales, se puede obtener el valor del coeficiente cinético μ.

En el Capítulo 2 de la parte de resultados se hace uso de la Ec. 4.17 para calcular los coeficientes cinéticos de distintos planos cristalográficos para tres modelos de potencial: esferas duras, Lennard–Jones y agua TIP4P/2005.

APÉNDICE A: Parámetros de orden

Esta tesis está dirigida al estudio de interfases, profundizando especialmente en las interfases sólido–fluido. Por este motivo es de especial importancia ser capaces de distinguir ambas fases con el fin de poder localizar la posición de la interfase con precisión. Para ello se hace uso de parámetros de orden locales, que son funciones de la posición relativa de una molécula y sus vecinas capaces de clasificar a las partículas en función de su entorno local. Estos parámetros están basados en armónicos esféricos y también se conocen con el nombre de parámetros de Steinhardt [69]. Además de distinguir entre fases fluidas y sólidas son capaces, en ocasiones, de distinguir entre distintas estructuras cristalinas. Por tanto, la elección de un parámetro de orden u otro dependerá tanto de la naturaleza del sistema que estemos analizando, como de la información que queramos obtener.

En este capítulo vamos a explicar los parámetros de orden que se han empleado en esta tesis, así como la forma de optimizarlos para conseguir una separación óptima entre las distintas fases.

Como se acaba de comentar, los parámetros de orden locales están basados en los armónicos esféricos, y la idea es calcular para cada una de las partículas del sistema un vector complejo $q_l(i)$ cuyas componentes dependen de la posición relativa de la partícula i respecto de sus partículas vecinas. Así, cada una de las componentes de dicho vector asociado a la partícula i vendrá dada por

$$q_{lm}(i) = \frac{1}{N_n(i)} \sum_{j=1}^{N_n(i)} Y_{lm}\left(\theta_{ij}, \varphi_{ij}\right) \tag{18}$$

donde $N_n(i)$ es el número de primeros vecinos de la partícula i, l es un número entero cuyo valor se escoge de tal forma que permita distinguir sistemas con distinta simetría y m es un entero cuyos valores van desde $m = -l$ hasta $m = +l$. Las funciones $Y_{lm}\left(\theta_{ij}, \varphi_{ij}\right)$ son los armónicos esféricos y θ_{ij} y φ_{ij} los ángulos polar y azimutal, respectivamente, medidos en un sistema de referencia arbitrario.

Una vez calculadas estas componentes vamos a distinguir los parámetros de orden en dos grandes grupos según el criterio escogido para ver si una partícula es sólida o

no: el grupo basado en el número de conexiones sólidas que tiene cada partícula, al que llamaremos grupo de conexiones sólidas, y el grupo basado en el cálculo de promedios del valor del parámetro de orden, al que le daremos el nombre de grupo de promedios.

Finalmente, una vez etiquetadas todas las partículas de tipo sólido se identifica el agregado más grande de dichas partículas, que se corresponde con el bloque de sólido de la coexistencia sólido–líquido simulada. Nosotros identificamos la interfase con las partículas más externas de dicho bloque. Para construir el agregado de partículas de sólido más grande es necesario establecer una distancia de corte, $r_c(agregado)$, por debajo de la cuál las partículas vecinas pueden pertenecer al mismo.

I Grupo de conexiones sólidas

Este tipo de parámetros de orden, desarrollado por ten Wolde y colaboradores [70] permite distinguir entre fases sólidas y fases fluidas. Para ello se selecciona una partícula i y se calculan las componentes de su vector complejo $q_l(i)$ de acuerdo con la Ec. 18. A continuación se calculan estas mismas componentes para todos los primeros vecinos de dicha partícula (es decir las N_n partículas j situadas a una distancia inferior a la posisición del primer mínimo de la función de distribución radial, r_c), y con ellas se calcula el parámetro de orden de enlace d_l como el producto escalar entre los vectores q_l de las partículas i i j:

$$d_l(i,j) = \frac{4\pi}{2l+1} \sum_{m=-l}^{m=+l} q_{lm}(i) \cdot q^*_{lm}(j) \tag{19}$$

De esta forma $d_l(i,j)$ es una magnitud normalizada que correlaciona los entornos locales de partículas vecinas, tomando valores en el intervalo [-1,1]. Por ejemplo, en una red cúbica fcc perfecta todas las partículas tienen el mismo entorno y, por tanto, el producto escalar entre los vectores asociados a cualquier par de partículas, tomando $l = 6$, es 1. Sin embargo, en condiciones experimentales la agitación térmica hace que este producto escalar disminuya, aunque será siempre mayor para la fase sólida que para la fase fluida. Por tanto podemos considerar que un par de partículas tienen una conexión sólida si el valor de $d_l(i,j)$ supera un cierto valor umbral d_{th}. De acuerdo con [70] este valor umbral se puede determinar representando la distribución de d_l para la fase sólida y determinando el valor a partir del cuál la probabilidad de estar en la fase sólida es no nula. Cabe destacar que este método de caracterización de partículas incluye a los segundos vecinos de la partícula que se esta estudiando ya que, como se observa en la Ec. 19, a la hora de calcular el parámetro de orden d_l aparece el vector $q_l(j)$ que incluye a los primeros vecinos de la partícula j, o lo que es lo mismo, los segundos vecinos de la partícula i.

Modelo	Parámetro	r_c	r_c(agregado)	d_{th}	n_{th}
Esferas duras	d_6	1.4 σ	1.4 σ	0.70	6
NaCl	d_4	4 Å	3.5 Å	0.35	6

Tabla 1. Valores de los parámetros empleados para la selección del agregado sólido más grande presente en el sistema. r_c(agregado) corresponde a la distancia máxima que puede separar a dos partículas para que sean consideradas parte del mismo agregado.

Hasta el momento este criterio no es suficiente ya que en la fase fluida, especialmente a distancias pequeñas, es posible que aparezca cierto orden y que dos partículas del fluido tengan una conexión tipo sólida. Por ello, para que una partícula sea considerada sólida es necesario que presente un número mínimo de conexiones sólidas, n_{th}. Así, para cada partícula, el número de conexiones sólidas, $n_c(i)$, se calcula como

$$n_c(i) = \sum_{j=1}^{N_n(i)} H(d_l(i,j) - d_{th}) \tag{20}$$

donde H es la función escalón de Heaviside, y se considera que una partícula es sólida si $n_c \geq n_{th}$.

Entre los sistemas estudiados en esta tesis se han analizado mediante este parámetro de orden tanto las esferas duras como el cloruro sódico [71, 72]. En ambos casos los valores umbral de los parámetros estaban optimizados en la literatura [73, 74], y son los mostrados en la Tabla 1.

II Grupo de promedios

Una alternativa al grupo de conexiones es el grupo de promedios propuesto por Steinhardt [69], y que ha dado buenos resultados en varios sistemas para distinguir fluido de sólido y distintos sólidos entre sí.

En el estudio original de Steinhardt, se propone una forma de usar los armónicos esféricos con este fin. Sin embargo, nosotros hacemos uso de una modificación propuesta por Lechner y Dellago en 2008 [75] que permite una separación aún mejor de las distintas fases.

Según esta modificación se calcula, para cada partícula i del sistema, el promedio sobre ella y sus vecinas del vector de Steinhardt mostrado en la Ec. 18. Esto es,

$$\bar{q}_{lm}(i) = \frac{1}{\widetilde{N}_n(i)} \sum_{j=0}^{\widetilde{N}_n(i)} q_{lm}(j)\,, \tag{21}$$

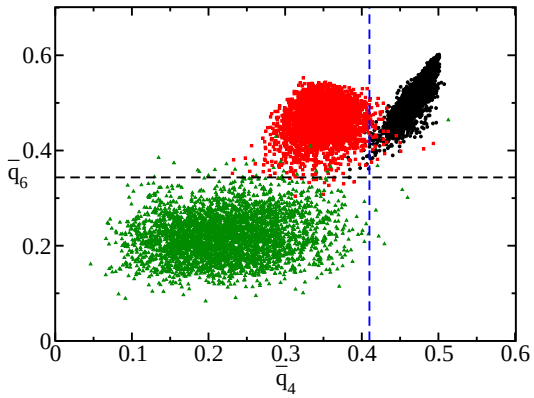

Figura 1. Representación bidimensional de los parámetros de orden locales $\bar{q}_6$ y $\bar{q}_4$ para 3600 moléculas de agua líquida (triángulos verdes), hielo Ih (cuadrados rojos) y hielo Ic (círculos negros) equilibradas a 1bar y 250K. La línea negra horizontal representa el valor umbral empleado para distinguir las fases sólida y líquida ($\bar{q}_{6,th} = 0{,}343$), mientras que la línea azul vertical representa el valor umbral empleado para distinguir entre hielo Ih y hielo Ic ($\bar{q}_{4,th} = 0{,}411$)

donde el sumatorio desde $j = 0$ hasta $\widetilde{N}_n(i)$ actúa sobre todos los vecinos de la partícula i más la propia partícula i. De esta forma se esta incluyendo información de los segundos vecinos de dicha partícula. Una vez que se tienen las componentes del vector $\bar{q}_{lm}(i)$ se puede asignar un valor numérico al nuevo parámetro de orden, $\bar{q}_l(i)$, hallando su módulo

$$\bar{q}_l(i) = \sqrt{\frac{4\pi}{2l+1}\sum_{m=-l}^{l}|\bar{q}_{lm}(i)|^2}, \tag{22}$$

Así una partícula será considerada de una fase o de otra según su valor de $\bar{q}_l$ se encuentre por encima o por debajo de cierto valor umbral $\bar{q}_{l,th}$.

En la Fig. 1 se muestra una distribución bidimensional de los parámetros de orden $\bar{q}_6$ y $\bar{q}_4$ para distintas fases del agua. Como se puede observar, según el parámetro empleado es posible distinguir bien entre agua y hielo (mediante el empleo de $\bar{q}_6$) o bien entre hielo Ih y hielo Ic (empleando $\bar{q}_4$). Con el fin de que la separación de las fases sea lo más precisa posible hay que optimizar el valor umbral para cada uno de los parámetros. Para ello se cuenta el porcentaje de moléculas mal etiquetadas en cada fase para varios valores del valor umbral del parámetro, $\bar{q}_{l,th}$, obteniéndose una curva del porcentaje de moléculas mal etiquetadas en función de dicho valor umbral. Así, por ejemplo, cuando una partícula líquida tenga un valor de $\bar{q}_6$ mayor que cierto valor umbral $\bar{q}_{6,th}$ sera mal etiquetada como una partícula sólida y al revés, si una partícula sólida presenta un valor de $\bar{q}_6$ menor que el valor umbral será mal etiquetada como líquida. En la Fig. 2 se muestra la optmización de los parámetros $\bar{q}_6$ y $\bar{q}_4$ para el modelo TIP4P/2005. El valor

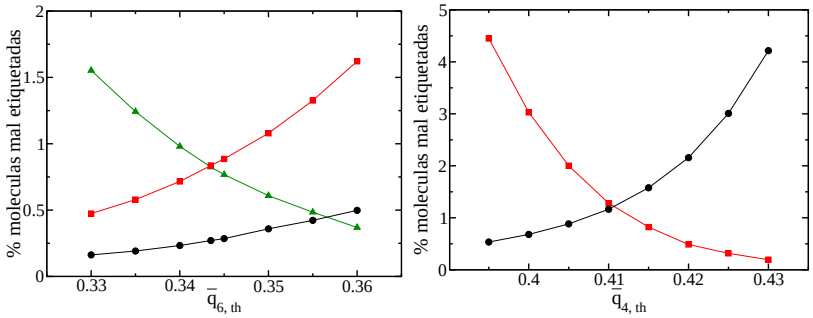

(a) $\bar{q}_6$ (b) $\bar{q}_4$

Figura 2. Porcentaje de moléculas mal etiquetados en función del valor umbral del parámetro de orden $\bar{q}_{l,th}$. La leyenda de colores es la misma que en la Fig. 1.

Modelo	Fases a separar	Parámetro	r_c	r_c(agregado)	$q_{l,th}$
TIP4P/2005	agua - hielo	$\bar{q}_6$	3.5 Å	3.5 Å	0.343
TIP4P/2005	hielo Ih - hielo Ic	$\bar{q}_4$	3.5 Å	3.5 Å	0.411
Lennard-Jones	sólido - líquido	$\bar{q}_6$	1.4 σ	1.4 σ	0.294
Lennard-Jones	fcc - hcp	$\bar{q}_4$	1.4 σ	1.4 σ	0.123

Tabla 2. Valores de los parámetros empleados para la selección del agregado sólido más grande presente en el sistema. r_c(agregado) corresponde a la distancia máxima que puede separar a dos partículas para que sean consideradas parte del mismo agregado.

umbral de cada parámetro se determina como el punto de intersección entre las curvas de moléculas mal etiquetadas de las fases que se quieren separar, ya que en ese punto el error cometido en ambas fases es el mismo.

De los sistemas estudiados en esta tesis, tanto el agua TIP4P/2005 [76] como el modelo de LJ de Broughton y Gilmer [77] se analizan mediante parámetros de orden de esta familia. Los parámetros empleados para el análisis se recogen la Tabla 2

Bibliografía

[1] D. Frenkel and B. Smit, *Understanding Molecular Simulation: From Algorithms to Applications*. Computational science series, Elsevier Science, 2001.

[2] D. McQuarrie, *Statistical Mechanics*. University Science Books, 2000.

[3] N. Metropolis, A. W. Rosenbluth, M. N. Rosenbluth, A. H. Teller, and E. Teller, "Equation of state calculations by fast computing machines," *The Journal of Chemical Physics*, vol. 21, no. 6, 1953.

[4] G. E. Norman and V. S. Filinov, "Investigation of phase transitions by a Monte Carlo method," *High Temp.*, vol. 7, p. 216, 1969.

[5] D. J. Adams, "Chemical potentials of hard sphere fluids by Monte Carlo methods," *Molec. Phys.*, vol. 28, p. 1241, 1974.

[6] D. J. Adams, "Grand canonical ensemble Monte Carlo for a Lennard-Jones fluid," *Molec. Phys.*, vol. 29, p. 307, 1975.

[7] J. I. Siepmann, "A method for the direct calculation of chemical potentials for dense chain systems," *Molec. Phys.*, vol. 70, p. 1145, 1990.

[8] J. I. Siepmann and D. Frenkel, "Configurational-Bias Monte Carlo: A new sampling scheme for flexible chains," *Molec. Phys.*, vol. 75, p. 59, 1992.

[9] J. J. de Pablo, M. Laso, and U. W. Suter, "Simulation of polyethylene above and below the melting point," *J. Chem. Phys.*, vol. 96, p. 2395, 1992.

[10] D. Frenkel, G. C. A. M. Mooij, and B. Smit, "Novel scheme to study structural and thermal properties of continuously deformable molecules," *J. Phys.:Condens. Matter*, vol. 4, p. 3053, 1992.

[11] M. Laso, J. J. de Pablo, and U. W. Suter, "Simulation of phase equilibria for chain molecules," *J. Chem. Phys.*, vol. 97, p. 2817, 1992.

[12] J. L. Siepmann, S. Karaborni, and B. Smit, "Simulating the critical behaviour of complex fluids," *Nature*, vol. 365, p. 330, 1993.

[13] B. Smit, S. Karaborni, and J. I. Siepmann, "Computer simulations of vapor-liquid phase equilibria of n-alkanes," *J. Chem. Phys.*, vol. 102, p. 2126, 1995.

[14] B. Smit, "Grand canonical monte carlo simulations of chain molecules: Adsorption isotherms of alkanes in zeolites," *Molec. Phys.*, vol. 85, pp. 153–172, 1995.

[15] M. N. Rosenbluth and A. W. Rosenbluth, "Monte Carlo simulations of the average extension of molecular chains," *J. Chem. Phys.*, vol. 23, p. 356, 1955.

[16] P. Allen and D. Tildesley, *Computer simulation of liquids*. Oxford science publications, Clarendon Press, 1987.

[17] L. Verlet, "Computer experiments on classical fluids. i. thermodynamical properties of Lennard-Jones molecules," *Phys. Rev.*, vol. 159, p. 98, 1967.

[18] H. C. Andersen, "Molecular dynamics simulations at constant pressure and/or temperature," *J. Chem. Phys.*, vol. 72, p. 2384, 1980.

[19] S. Nosé, "A unified formulation of the constant temperature molecular dynamics methods," *The Journal of Chemical Physics*, vol. 81, p. 511, 1984.

[20] W. G. Hoover, "Canonical dynamics: Equilibrium phase-space distributions," vol. 31, p. 1695, 1985.

[21] G. J. Martyna, M. L. Klein, and M. Tuckerman, "Nosé-hoover chains: The canonical ensemble via continuous dynamics," *The Journal of Chemical Physics*, vol. 97, no. 4, 1992.

[22] D. J. Evans and O. Morriss, "Non-newtonian molecular dynamics," *Computer Physics Reports*, vol. 1, no. 6, pp. 297 – 343, 1984.

[23] H. J. C. Berendsen, J. P. M. Postma, W. F. van Gunsteren, A. DiNola, and J. R. Haak, "Molecular dynamics with coupling to an external bath," *The Journal of Chemical Physics*, vol. 81, no. 8, 1984.

[24] G. Bussi, D. Donadio, and M. Parrinello, "Canonical sampling through velocity rescaling," *J. Chem. Phys.*, vol. 126, no. 1, p. 014101, 2007.

[25] H. J. C. Berendsen, J. P. M. Postma, W. F. van Gunsteren, A. DiNola, and J. R. Haak, "Molecular dynamics with coupling to an external bath," *The Journal of Chemical Physics*, vol. 81, no. 8, 1984.

[26] M. Parrinello and A. Rahman, "Polymorphic transitions in single crystals: A new molecular dynamics method," *J. App. Phys.*, vol. 52, p. 7182, 1981.

[27] J. King and L. Williams, "Utilization of critical fluids in processing semiconductors and their related materials," *Current Opinion in Solid State and Materials Science*, vol. 7, no. 4, pp. 413–424, 2003.

[28] A. Cabañas, D. P. Long, and J. J. Watkins, "Deposition of gold films and nanostructures from supercritical carbon dioxide," *Chemistry of Materials*, vol. 16, no. 10, pp. 2028–2033, 2004.

[29] R. Seemann, M. Brinkmann, E. J. Kramer, F. F. Lange, and R. Lipowsky, "Wetting morphologies at microstructured surfaces," *Proceedings of the National Academy of Sciences of the United States of America*, vol. 102, no. 6, pp. 1848–1852, 2005.

[30] D. Nelson, T. Piran, and S. Weinberg, *Statistical Mechanics of Membranes and Surfaces*. Word Scientific, Singapore, 2004.

[31] L. G. MacDowell, J. Benet, N. A. Katcho, and J. M. Palanco, "Disjoining pressure and the film-height-dependent surface tension of thin liquid films: New insight from capillary wave fluctuations," *Advances in Colloid and Interface Science*, vol. 206, pp. 150 – 171, 2014.

[32] M. V. von Smoluchowski *Annals of Physics*, vol. 25, p. 205, 1908.

[33] L. D. Landau and E. M. Lifshitz, *Mecánica de Fluidos*. Barcelona: Reverté, 1991.

[34] F. P. Buff, R. A. Lovett, and F. H. Stillinger, "Interfacial density profile for fluids in the critical region," *Phys. Rev. Lett.*, vol. 15, pp. 621–623, Oct 1965.

[35] D. S. Fisher and D. A. Huse, "Wetting transitions: A functional renormalization-group approach," *Phys. Rev. B*, vol. 32, pp. 247–256, Jul 1985.

[36] P. de Gennes, F. Brochard-Wyart, and D. Quéré, *Capillarity and wetting phenomena*. Spinger, New York, 2004.

[37] H. Dobbs and J. Indekeu, "Line tension at wetting: interface displacement model beyond the gradient-squared approximation," *Physica A: Statistical Mechanics and its Applications*, vol. 201, no. 4, pp. 457 – 481, 1993.

[38] C. Bauer, S. Dietrich, and A. O. Parry, "Morphological phase transitions of thin fluid films on chemically structured substrates," *Europhys. Lett.*, vol. 47, p. 474, 1999.

[39] A. Vrij, "Possible mechanism for the spontaneous rupture of thin, free liquid films," *Discuss. Faraday Soc.*, vol. 42, pp. 23–33, 1966.

[40] N. Goldenfeld, *Lectures on phase transitions and the renormalization group*. Reading, Masachusets: Perseus Books, 1992.

[41] M. Müller and M. Schick, "Structure and nucleation of pores in polymeric bilayers: A Monte Carlo simulation," *J. Chem. Phys.*, vol. 105, pp. 8282–8292, 1996.

[42] M. Müller and L. G. MacDowell, "Interface and surface properties of short polymers in solution: Monte Carlo simulations and self-consistent field theory," *Macromolecules*, vol. 33, p. 3902, 2000.

[43] R. L. Davidchack, J. R. Morris, and B. B. Laird, "The anisotropic hard-sphere crystal melt interfacial free energy from fluctuations," *J. Chem. Phys.*, vol. 125, p. 094710, 2006.

[44] T. Zykova-Timan, J. Horbach, and K. Binder, "Monte carlo simulations of the solid-liquid transition in hard spheres and colloid-polymer mixtures," *The Journal of Chemical Physics*, vol. 133, no. 1, p. 014705, 2010.

[45] R. E. Rozas and J. Horbach, "Capillary wave analysis of rough solid-liquid interfaces in nickel," *Europhys. Lett.*, vol. 93, no. 2, p. 26006, 2011.

[46] K. R. Mecke and S. Dietrich, "Effective hamiltonian for liquid-vapor interfaces," *Phys. Rev. E*, vol. 59, pp. 6766–6784, Jun 1999.

[47] K. R. Mecke, "Thermal fluctuations of thin liquid films," *Journal of Physics: Condensed Matter*, vol. 13, no. 21, p. 4615, 2001.

[48] J. Q. Broughton and G. H. Gilmer, "Molecular dynamics investigation of the crystal–fluid interface. VI. Excess surface free energies of crystal–liquid systems," *J. Chem. Phys.*, vol. 84, no. 10, pp. 5759–5768, 1986.

[49] J. J. Hoyt, M. Asta, and A. Karma, "Method for computing the anisotropy of the solid-liquid interfacial free energy," *Phys. Rev. Lett.*, vol. 86, pp. 5530–5533, Jun 2001.

[50] S. Angioletti-Uberti, M. Ceriotti, P. D. Lee, and M. W. Finnis, "Solid-liquid interface free energy through metadynamics simulations," *Phys. Rev. B*, vol. 81, p. 125416, Mar 2010.

[51] X.-M. Bai and M. Li, "Calculation of solid-liquid interfacial free energy: A classical nuclea tion theory based approach," *J. Chem. Phys.*, vol. 124, no. 12, p. 124707, 2006.

[52] L. A. Fernández, V. Martín-Mayor, B. Seoane, and P. Verrocchio, "Equilibrium fluid-solid coexistence of hard spheres," *Phys. Rev. Lett.*, vol. 108, p. 165701, Apr 2012.

[53] J. R. Espinosa, C. Vega, and E. Sanz, "The mold integration method for the calculation of the crystal-fluid interfacial free energy from simulations," *The Journal of Chemical Physics*, vol. 141, no. 13, p. 134709, 2014.

[54] R. L. Davidchack, "Hard spheres revisited: Accurate calculation of the solid–liquid interfacial free energy," *J. Chem. Phys.*, vol. 133, no. 23, p. 234701, 2010.

[55] R. L. Davidchack and B. B. Laird, "Direct calculation of the crystal–melt interfacial free energies for continuous potentials: Application to the Lennard-Jones system," *J. Chem. Phys.*, vol. 118, no. 16, pp. 7651–7657, 2003.

[56] J. Wang, P. A. Apte, J. R. Morris, and X. C. Zeng, "Freezing point and solid-liquid interfacial free energy of stockmayer dipolar fluids: A molecular dynamics simulation study," *The Journal of Chemical Physics*, vol. 139, no. 11, p. 114705, 2013.

[57] R. Handel, R. L. Davidchack, J. Anwar, and A. Brukhno, "Direct calculation of solid-liquid interfacial free energy for molecular systems: TIP4P ice-water interface," *Phys. Rev. Lett.*, vol. 100, p. 036104, Jan 2008.

[58] R. L. Davidchack, R. Handel, J. Anwar, and A. V. Brukhno, "Ice ih-water interfacial free energy of simple water models with full electrostatic interactions," *Journal of Chemical Theory and Computation*, vol. 8, no. 7, pp. 2383–2390, 2012.

[59] J. R. Morris and X. Song, "The anisotropic free energy of the Lennard-Jones crystal-melt interface," *J. Chem. Phys.*, vol. 119, no. 7, pp. 3920–3925, 2003.

[60] V. Heinonen, A. Mijailovic, C. V. Achim, T. Ala-Nissila, R. E. Rozas, J. Horbach, and H. Löwen, "Bcc crystal-fluid interfacial free energy in yukawa systems," *The Journal of Chemical Physics*, vol. 138, no. 4, pp.–, 2013.

[61] D. Y. Sun, M. I. Mendelev, C. A. Becker, K. Kudin, T. Haxhimali, M. Asta, J. J. Hoyt, A. Karma, and D. J. Srolovitz, "Crystal-melt interfacial free energies in hcp metals: A molecular dynamics study of Mg," *Phys. Rev. B*, vol. 73, p. 024116, Jan 2006.

[62] J. J. Hoyt and M. Asta, "Atomistic computation of liquid diffusivity, solid-liquid interfacial free energy, and kinetic coefficient in Au and Ag," *Phys. Rev. B*, vol. 65, p. 214106, Jun 2002.

[63] A. Laio and M. Parrinello, "Escaping free-energy minima," *Proc. Natl. Acad. Sci.*, vol. 99, p. 12562, 2002.

[64] E. Sanz, C. Vega, J. R. Espinosa, R. Caballero-Bernal, J. L. F. Abascal, and C. Valeriani, "Homogeneous ice nucleation at moderate supercooling from molecular simulation," *Journal of the American Chemical Society*, vol. 135, no. 40, pp. 15008–15017, 2013.

[65] W. R. Fehlner and S. H. Vosko, "A product representation for cubic harmonics and special directions for the determination of the fermi surface and related properties," *Canadian Journal of Physics*, vol. 54, no. 21, pp. 2159–2169, 1976.

[66] M. Kara and K. Kurki-Suonio, "Symmetrized multipole analysis of orientational distributions," *Acta Crystallographica Section A*, vol. 37, pp. 201–210, Mar 1981.

[67] A. Karma, "Fluctuations in solidification," *Phys. Rev. E*, vol. 48, pp. 3441–3458, Nov 1993.

[68] G. E. Uhlenbeck and L. S. Ornstein, "On the theory of the brownian motion," *Phys. Rev.*, vol. 36, pp. 823–841, Sep 1930.

[69] P. J. Steinhardt, D. R. Nelson, and M. Ronchetti, "Bond-orientational order in liquids and glasses," *Phys. Rev. B*, vol. 28, pp. 784–805, Jul 1983.

[70] P.-R. ten Wolde, M. J. Ruiz-Montero, and D. Frenkel, "Simulation of homogeneous crystal nucleation close to coexistence," *Faraday Discuss.*, vol. 104, pp. 93–110, 1996.

[71] F. Fumi and M. Tosi, "Ionic sizes and born repulsive parameters in the NaCl-type alkali halides I," *Journal of Physics and Chemistry of Solids*, vol. 25, pp. 31–43, 1964.

[72] M. Tosi and F. Fumi, "Ionic sizes and born repulsive parameters in the NaCl-type alkali halides II," *Journal of Physics and Chemistry of Solids*, vol. 25, pp. 45–52, 1964.

[73] P. N. Pusey, E. Zaccarelli, C. Valeriani, E. Sanz, W. C. K. Poon, and M. E. Cates, "Hard spheres: crystallization and glass formation," *Phyl. Trans. Roy. Soc. A*, vol. 367, pp. 4993–5011, 2009.

[74] C. Valeriani, E. Sanz, and D. Frenkel, "Rate of homogeneous crystal nucleation in molten NaCl," *J. Chem. Phys.*, vol. 122, p. 194501, 2005.

[75] W. Lechner and C. Dellago, "Accurate determination of crystal structures based on averaged local bond order parameters," *The Journal of Chemical Physics*, vol. 129, no. 11, p. 114707, 2008.

[76] J. L. F. Abascal and C. Vega, "A general purpose model for the condensed phases of water: Tip4p/2005," *J. Chem. Phys.*, vol. 123, p. 234505, 2005.

[77] J. Broughton and G. Gilmer, "Surface free energy and stress of a lennard-jones crystal," *Acta Metallurgica*, vol. 31, no. 6, pp. 845 – 851, 1983.

Part II

Results

Chapter 1

Disjoining pressure, Healing Distance and Film Height Dependent Surface Tension of Thin Wetting Films

Jorge Benet[1], *Jose G. Palanco*[2], *Eduardo Sanz*[1] *and Luis G. MacDowell*[1]

(1) Departamento de Química Física, Facultad de Ciencias Químicas, Universidad Complutense de Madrid, 28040 Madrid, Spain

(2) Departamento de Química Aplicada, ETSI Aeronáuticos, Universidad Politécnica de Madrid, 28040 Madrid, Spain

Journal of Physical Chemistry C, ***118****, 22079-22089 (2014)*

1.1 Abstract

In this work we simulate the adsorption of wetting liquid Argon films on a model substrate. We calculate the disjoining pressure isotherm and show that it is completely dominated by the long range van der Waals interactions. Thick films exhibit the expected Hamaker power law decay, but a quantitative description of thin films requires to consider the detailed structure of the adsorbed layer. The spectrum of film height fluctuations is calculated, and shown to provide reliable estimates of the disjoining pressure for all films studied. However, it is observed that the full spectrum can only be reproduced provided we account for a film height dependent surface tension proportional to the derivative of the disjoining pressure. A simple theory is worked out which describes well the observed film height dependence. Having at hand both the surface tension and the disjoining pressure, we calculate the healing distance of the liquid films, which differs from the classical expectation by a constant of the same order of magnitude as the bulk

correlation length. We show these findings have important implications on the behavior of adsorbed liquids and determine corrections to the augmented Young-Laplace equation at the subnanometer length scale.

1.2 Introduction

Understanding the properties of wetting films is a matter of great importance in several technological processes, such as painting, printing, the preparation of protective coatings, or the flow of liquids inside microfluidic devices.[1]

The behavior of thick wetting films can be reliably described by standard surface thermodynamics, which amounts to a mere surface free energy balance of the different interfaces that are involved.[2] Not only the equilibrium properties of the films are dictated by these properties. Also the dynamics is controlled to a great extent by the reluctance of the liquid-vapor interface to increase its total surface area.[2]

However, in many applications there is a need for a fine control of the adsorbed layers, which are often prepared with thickness well under the micrometer and into the nanoscale.[3, 4, 5, 6] In such cases, surface thermodynamics is not sufficient to properly describe the wetting layers, and a more detailed description of the molecular interactions is required.[7] In practice, this is usually achieved by introducing the concept of disjoining pressure, which allows to lump the intricate details of the molecular forces into an effective interaction between the substrate and the liquid-vapor interface.[8]

The resulting equation for the balance between surface, bulk and disjoining forces –some times known under the name of augmented Young-Laplace equation–provides the framework for most of our current understanding of adsorption phenomena at the nanometer scale.[2, 9, 10, 11, 12, 13, 14]

Yet, already for some time, there have been claims that the augmented Young-Laplace equation, or alternatively, the interface Hamiltonian model from which it is derived, cannot be deduced exactly from a finer microscopic approach.[15, 16, 17] Of particular interest here is how adsorbed liquid films fluctuate about their average film height. These fluctuations are known as capillary waves, as the restoration is mainly due to capillary forces. The interface Hamiltonian model provides a simple closed expression for the spectrum of such film height fluctuations, which can be compared in principle with both experiments and computer simulations.[18, 19, 20, 21, 22, 23, 24, 25, 26, 27] In the classical model, the capillary wave spectrum (CWS) is given exactly by the liquid-vapor surface tension and the disjoining pressure. More elaborated theoretical studies, however, indicate that at least a film height dependent surface tension must be incorporated to achieve an accurate description of the spectrum.[15, 16, 17, 26, 27]

A correct understanding of these details has several important implications. For

example, the ratio between the surface tension and the disjoining pressure derivative provides the parallel correlation length, or healing distance, of the liquid film.[2, 11, 16, 28] This property dictates the length scale over which perturbations of the liquid film decay. Accordingly, films replicate the roughness of the substrate on length scales larger than the healing distance, but rather heal the substrate's roughness on length scales that are smaller than the healing distance.[29]

Surprisingly, only a few experimental and simulation studies have been devoted up to date to clarify this issue, and, with the exception of Ref. [19], show rather limited or indirect evidence for the conjectured film height dependent surface tension.[18, 20, 21, 25]

Recently, we performed computer simulation studies of the capillary wave spectrum of adsorbed liquid films close to a first order wetting transition. We showed that indeed, the CWS yields effective surface tensions which are strongly film height dependent. Furthermore, we showed that such film height dependence was approximately proportional to the derivative of the disjoining pressure. Unfortunately, our model system was very close to the fluid's triple point. As a result it exhibited very strong layering. This made the theoretical modeling of the disjoining pressure a very difficult issue, and thus precluded a clear unambiguous test of this hypothesis.[26, 27]

In this paper, we perform computer simulations of model wetting liquid films in a regime of complete wetting. The system is chosen such that the disjoining pressure isotherm exhibits a smooth and monotonous behavior, so that it can be easily modeled. Our simulations allow us to confirm the alleged film height dependent surface tension, and the relation of such dependence with the disjoining pressure isotherm. As an important implication, it is found that the augmented Young-Laplace equation develops additional contributions that can be neglected for thick films, but are important at the nanometer scale.

1.3 Theoretical

1.3.1 Review of equilibrium film profiles and capillary wave fluctuations

Consider a liquid film adsorbed onto a flat substrate. The shape of the film profile is specified by the film height $\ell(\mathbf{x})$ above point $\mathbf{x}$ on the plane of the substrate. The free energy of a given realization $\ell(\mathbf{x})$ exhibiting small deviations from planarity is given by the Interface Hamiltonian Model (IH) as:

$$H[\ell] = \int d\mathbf{x} \left[g(\ell) + \frac{1}{2}\,\gamma_{lv}\,(\nabla\ell)^2 - \Delta p\,\ell \right] \tag{1.1}$$

where $g(\ell)$ is the free energy of a flat film of height ℓ at coexistence, or *interface potential*; γ_{lv} is the surface tension and $\Delta p = p_l - p_v$ is the Laplace pressure difference across the liquid-vapor interface, with p_l and p_v the bulk vapor and liquid pressures consistent with the imposed chemical potential.

Thus, the first and third terms provide the free energy of infinitesimal liquid prisms of height $\ell(\mathbf{x})$ and basis $d\mathbf{x}$, while the second term accounts for the liquid-vapor surface area excess over the planar film.

The equilibrium realization of the film profile is obtained by requiring that $H[\ell]$ be a minimum with respect to variations of the film profile $\ell(\mathbf{x})$. This is achieved by searching for the extremal of $H[\ell]$, which provides the more familiar result sometimes known as the augmented Young-Laplace equation:[10, 12]

$$\gamma_{lv}\,\nabla^2\ell + \Pi(\ell) = -\Delta p \tag{1.2}$$

The disjoining pressure, $\Pi(\ell)$ is related to the interface potential as:[30]

$$\frac{dg(\ell)}{d\ell} = -\Pi(\ell) - \Delta p \tag{1.3}$$

In the limit of thick films, $\Pi(\ell)$ vanishes and Eq. (1.2) then becomes the familiar Laplace equation relating the interface curvature to the bulk pressure difference between liquid and vapor phases.

Whereas the result, Eq. (1.2), is the basis for our understanding of many important surface phenomena,[2] a thorough test down to sub-nanometer film heights remains difficult. Experimental, [4, 31] simulation [32, 33, 34] and theoretical studies [30, 35] have been performed in order to assess how well Eq. (1.2) is able to predict film profiles, but often the results are hampered by lack of complete knowledge of $\Pi(\ell)$,[31, 34] or ambiguities related to the definition of the film height.[30, 35]

In this paper we consider an alternative approach, based on a direct test of the Interface Hamiltonian, Eq. (1.1).[19, 25, 26, 27] Wetting films exhibit fluctuations about the average film height. These fluctuations may be decomposed in Fourier modes as:

$$\delta\ell(\mathbf{x}) = \sum_{\mathbf{q}} \delta\ell(\mathbf{q})\, e^{i\mathbf{q}\cdot\mathbf{x}} \tag{1.4}$$

Performing an expansion of $g(\ell)$ up to quadratic order in Eq. (1.1), allows to express the free energy of an instantaneous film profile as:

$$H[\ell] = \frac{1}{2}A\sum_{\mathbf{q}}[g''(\ell) + \gamma_{lv}\,q^2]|\delta\ell(\mathbf{q})|^2 \tag{1.5}$$

where A denotes here the surface area of the flat interface, while a superscript prime denotes differentiation with respect to ℓ. The above result for the free energy is quadratic

in the Fourier modes. Applying equipartition of energy, one can then obtain a closed expression for the mean squared amplitude, which reads:

$$A\langle|\delta\ell(\mathbf{q})|^2\rangle = \frac{k_B T}{g''(\ell) + \gamma_{lv}\, q^2} \tag{1.6}$$

The coefficients of the denominator define a characteristic length scale for the decay of correlations parallel to the substrate:

$$\xi_h^2 = \frac{\gamma_{lv}}{|g''(\ell)|} \tag{1.7}$$

This parallel correlation length, or *healing distance* governs film fluctuations away from planarity. In equilibrium, films deposited on a substrate with roughness of wavelength λ, will replicate the shape of the substrate when $\xi_h/\lambda < 1$, but will remain essentially flat and therefore "heal" the rough surface in the opposite case.[2, 11, 28, 36] Out of equilibrium, unstable films remain stable to fluctuations smaller than ξ_h, but are spontaneously amplified otherwise.[37]

Recently, we performed a computer simulation study of the capillary wave spectrum of adsorbed liquid films in order to test the accuracy of Eq. (1.6).[26, 27] Our results showed that $g''(\ell)$ as obtained from the CWS was fully consistent with independent estimates of the disjoining pressure. However, we found that the coefficient of q^2, which according to Eq. (1.6) is the liquid-vapor surface tension, actually picked up a film height dependence proportional to $g''(\ell)$.

1.3.2 Interface Model

The explanation of these results requires a microscopic theory beyond the coarse-grained phenomenological model of Eq. (1.1).[17, 26, 27] Unfortunately, the results of Ref.[17, 26, 27] are mathematically rather involved and provide limited physical insight as to the origin of the ℓ dependent surface tension.

Here we briefly advance an explanation which is both simple and intuitive. The key point in our treatment is to note that the number density, $\rho(\mathbf{r};\Xi)$ at a point $\mathbf{r} = (\mathbf{x}, z)$ close to an undulated interface, denoted Ξ, is given by the shortest distance $h(\mathbf{r};\ell)$ away from the film profile ℓ as:

$$\rho(\mathbf{r};\Xi) = \rho_\pi(h;\ell) \tag{1.8}$$

where $\rho_\pi(z;\ell)$ is the density profile of a planar interface with average film height ℓ. In general, it is a very complicated mathematical problem to express $h(\mathbf{r};\ell)$ as a function of the film profile $\ell(\mathbf{x})$.[38] In practice, it is enough to consider that $h(\mathbf{r};\ell)$ is given by

the perpendicular distance to $\ell(\mathbf{x})$.[1] For small gradients and for distances away from the profile that are smaller than the wavelength of undulations, the normal is uniquely defined and may be given as:[39]

$$h(\mathbf{r};\ell) = \frac{z-\ell(\mathbf{x})}{\sqrt{1+(\nabla\ell)^2}} \tag{1.9}$$

In the limit where the gradient is very small, $h = z - \ell(\mathbf{x})$ is the vertical distance to the interface, and Eq. (1.8) recovers the classical Buff, Stillinger and Lovett model of capillary waves.[40]

The *ansatz* embodied in Eq.1.8-1.9 has important implications as to the nature of the interface Hamiltonian. To see this, consider, following Ref.[11, 36] that all of the interface potential is dictated by wall-fluid van der Waals interactions, as described by a wall-fluid external field, $V(z)$. The interface Hamiltonian is then written as:

$$H[\ell] = \int \left[\int V(z)\rho_\pi \left(\frac{z-\ell(\mathbf{x})}{\sqrt{1+(\nabla\ell)^2}} \right) dz + \frac{1}{2}\gamma_{lv}\left(\nabla\ell\right)^2 - \Delta p\, \ell \right] d\mathbf{x} \tag{1.10}$$

where it is now clear that the second integral, corresponding to the interface potential, is no longer a simple function of the film height, but also depends on its gradient.

In order to understand the significance of this new feature, we expand $\rho(\mathbf{r};\Xi)$ about a planar interface:

$$\rho(\mathbf{r};\Xi) = \rho_\pi(z;\ell) - \rho'_\pi(z;\ell)\,\delta\ell + \frac{1}{2}\rho''_\pi(z;\ell)\delta\ell^2 - \frac{1}{2}(z-\ell_\pi)\rho'_\pi(z;\ell)(\nabla\ell)^2 \tag{1.11}$$

This profile can now be integrated over $\mathbf{x}$ to yield:

$$\left\langle \rho(\mathbf{r};\Xi)\right\rangle_{\mathbf{x}} = \rho_\pi(z) + \frac{1}{2}\rho''_\pi(z)\left\langle \delta\ell^2\right\rangle_{\mathbf{x}} - \frac{1}{2}(z-\ell)\rho'_\pi(z)\left\langle (\nabla\ell)^2\right\rangle_{\mathbf{x}} \tag{1.12}$$

where $< \ldots >_{\mathbf{x}}$ denotes an unweighted lateral average. Alternatively, performing a thermal average provides the same result as above, with the subscript $_{\mathbf{x}}$ replaced by $_{\Xi}$, denoting a canonical average over all possible interface fluctuations. This shows that the average density profile is different from the mean field profile for a planar interface $\rho_\pi(z;\ell)$, a result that is known as capillary wave broadening. However, contrary to the

[1] Note that generally it is possible to find normals to the film profile that intersect. This means that one can find more than one perpendicular distance to the interface at a point. However, this will occur only for points well away from the interface, where the density is nearly equal to the constant bulk density. Since the properties we aim at are given in terms of density derivatives, which are zero away from the interface, this multiplicity of solutions is therefore not a problem (see Ref.38 and 39 for a detailed discussion).

classical expectations[41, 42] (i.e., first two terms in the right hand side), our approach provides an additional contribution of order squared gradient on the film profile.

The implication of this new term may be immediately assessed by considering the contribution of the wall-fluid potential, $V(z)$ to the interface potential:

$$g_V(\Xi) = \int V(z) \left\langle \rho(\mathbf{r}; \Xi) \right\rangle_{\mathbf{x}} dz \tag{1.13}$$

Substitution of Eq. (1.12) into the above equation, shows that the free energy of a given realization Ξ of the interface roughness may be expanded to quadratic order in the film fluctuations as:

$$g_V(\Xi) = g_V(\ell) + \frac{1}{2} g_V''(\ell) \left\langle \delta\ell^2 \right\rangle_{\mathbf{x}} + \Delta\gamma(\ell) \left\langle (\nabla\ell)^2 \right\rangle_{\mathbf{x}} \tag{1.14}$$

The last term in this expansion is proportional to $(\nabla\ell)^2$ and may be therefore identified with an effective additional film height dependent contribution to the surface tension:

$$\Delta\gamma(\ell) = -\int V(z)(z-\ell)\rho_\pi'(z;\ell)dz \tag{1.15}$$

In order to make explicit the ℓ dependence of the above integral in a more familiar form, we note that, to a good approximation, we can write:

$$-(z-\ell)\rho_\pi'(z;\ell) = \xi_e^2 \rho_\pi''(z;\ell) \tag{1.16}$$

where ξ_e^2 is an empirical parameter of the same order of magnitude as the local interfacial width. The above identity should hold exactly for small distances about $z-\ell$, where the integrand makes most of its contribution. As an example, the familiar $\tanh(z/\xi_b)$ density profile, which has an interfacial width ξ_b, obeys the above result exactly up to order $(z-\ell)^2$, with $\xi_e = 2\xi_b$.

By virtue of this approximation, we can express $\Delta\gamma(\ell)$ explicitly in terms of the familiar disjoining pressure as:[26, 27]

$$\Delta\gamma(\ell) = -\xi_e^2 \frac{d\Pi_V(\ell)}{d\ell} \tag{1.17}$$

where $\Pi_V(\ell)$ denotes the external field contribution to the disjoining pressure (c.f. Eq. (1.30)).

1.3.3 Implications

The implications of the above result may be readily assessed by noticing that $\Delta\gamma(\ell)$ stems from a coupling of the interface fluctuations with the wall–fluid external field. In

the limit where the film is very thick, the external field vanishes at the interface, and we expect to recover the classical result, Eq.1.5-1.6 for the free energy and fluctuations. For the case of thin films, $\Delta\gamma(\ell)$ becomes important and must be added to the free energy. Accordingly, the form of Eq.1.5-1.6 survives, albeit with $\gamma_{\rm lv}$ replaced by a film height dependent surface tension:

$$A\langle|\delta\ell(\mathbf{q})|^2\rangle = \frac{k_B T}{g''(\ell) + \gamma(\ell)\, q^2} \tag{1.18}$$

where the new coefficient of order q^2 is now:[26, 27]

$$\gamma(\ell) = \gamma_{\rm lv} - \xi_e^2 \frac{d\Pi_V(\ell)}{d\ell} \tag{1.19}$$

The above expression is the main result we wish to test in this work.

1.4 Model and Simulations

1.4.1 Model

In our previous work,[26] we studied a model of *Ar* adsorbed onto solid CO_2.[43, 44, 45, 46, 47, 48] Our simulations where performed at the wetting transition, which is very close to the triple point of *Ar* both for the simulation model,[48, 49] and in experiments.[50] For this reason, the adsorbed liquid was strongly layered, and the resulting disjoining pressure isotherm exhibited a rather complex oscillatory behavior.[26, 27] This is interesting *per-se*, but very much complicates the theoretical analysis.

In order to get rid of this complication and test Eq. (1.19) in the more transparent way as possible, we wish to study the adsorption of *Ar* well above the wetting transition, in a state of complete wetting. In principle this could be achieved by simply raising the temperature. Unfortunately, the Ar/CO_2 model exhibits a very high prewetting critical temperature.[44, 48, 51] As a result, it is not possible to avoid the prewetting regime without approaching the critical point of *Ar*, which is even a more serious complication. For that reason, we study Argon well below the critical point, and instead increase the strength of the wall-fluid potential by about a factor of two. This has the effect of pulling down the prewetting critical point,[52] and accordingly, drive the system to a state of complete wetting at moderate temperature. Furthermore, the increase of the wall-fluid interactions increases the range where the disjoining pressure is significant and thus allows for a more clear test of Eq. (1.19).

More specifically, we describe *Ar* by means of a Lennard-Jones model, with pair

interactions $u(r)$ given by:

$$u(r) = \begin{cases} 4\epsilon \left[\left(\frac{\sigma}{r}\right)^{12} - \left(\frac{\sigma}{r}\right)^{6} \right] & r \leq r_c \\ 0 & r > r_c \end{cases} \tag{1.20}$$

where $\epsilon/k_B = 119.8K$ ($995.58\ Jmol^{-1}$) is the depth of the potential well and $\sigma = 3.405$Å is the molecular diameter. Notice that the standard LJ potential is truncated as is usual in this model at $r_c = 2.5\sigma$ for the sake of computational convenience.[44, 45, 46, 47, 48] Relative to the untruncated model, this has the advantage of decreasing the wetting temperature,[46, 53] and avoids complications in the interpretation of the capillary wave spectrum.[38, 54, 55, 56]

As for the CO_2 solid phase, it is described by means of an idealized flat wall with the usual 9-3 potential that results from integrating LJ pair interactions for a semi–infinite solid phase. More specifically, interactions of Ar with CO_2 are modeled by an external field of the form:

$$V(z) = \frac{2\pi}{3}\sigma_{wf}^3 \rho_w \epsilon_{wf} \left\{ \frac{2}{15} \left(\frac{\sigma_{wf}}{z}\right)^9 - \left(\frac{\sigma_{wf}}{z}\right)^3 \right\} \tag{1.21}$$

where z is the perpendicular distance of an Ar atom to the wall, $\sigma_{wf} = 1.096\sigma$ and $\epsilon_{wf} = 2.7908\epsilon$ are the wall–fluid parameters, while $\rho_w \sigma_{wf}^3 = 0.988$ is the substrate's reduced density.

Through out the paper, we simulate at a temperature of T=107.82 K, which in reduced LJ units is $k_B T = 0.90\epsilon$, corresponding to a ratio $T/T_c = 0.71$ relative to the critical temperature of Ar. At this temperature, the coexistence densities are, $\rho_l = 0.7154\sigma^{-3}$ and $\rho_v = 0.02498\sigma^{-3}$. Accordingly, the Hamaker constant, which in terms of the molecular parameters of the model is given by

$$H_w = 4\pi^2 \sigma_{wf}^6 \rho_w \epsilon_{wf} (\rho_l^c - \rho_v^c) \tag{1.22}$$

has the value $H_w = 1.6 \cdot 10^{-19} J$. This falls well in the range $(0.4 - 4) \cdot 10^{-19} J$ of typical Hamaker constants.[7]

1.4.2 Simulation details

All of our results are obtained by means of Monte Carlo simulations (MC) in either the NVT or μVT ensemble. Our systems consist of N molecules placed in a rectangular box with sides $L_x = L_y = 10\sigma$ and $L_z = 50\sigma$. The solid substrate as described by Eq. (1.21) is placed perpendicular to the z direction in one side of the box, while a purely repulsive wall is placed in the opposite side. Periodic boundary conditions are applied in x and y directions.

Our simulations are organized in cycles, where each cycle corresponds to N trial MC moves. Apart from standard Metropolis translation of particles, grand canonical simulations are performed using a biased insertion/deletion scheme.[57, 58] Similarly, the sampling of NVT simulations incorporates a biased random removal and reinsertion of molecules.[59] These movements are attempted randomly in a ratio 1:1. Typically, the systems under study are equilibrated for $2{\cdot}10^5$ cycles and data is collected for $2{\cdot}10^7$ cycles.

Capillary wave spectrum

We study systems of adsorbed films ranging from two to fourteen molecular diameters thick. During the course of the simulations, 20.000 configurations are saved for further analysis. For each configuration a film height profile $\ell(\mathbf{x})$ is determined employing the Intrinsic Sampling Method (ISM) and the Fourier components, $\ell(q)$, evaluated.[60, 61] After performing a thermal average, the spectrum $< |\ell(q)|^2 >$ for each film is fitted to a quadratic polynomial in q^2, in order to obtain estimates for $g''(\ell)$ and $\gamma(\ell)$ (see below).

Disjoining pressure

In previous work,[62, 53, 26] we have usually estimated $\Pi(\ell)$ using a free energy method which directly measures the interface potential $g(\ell)$. The disjoining pressure isotherm can then be obtained from Eq. (1.3). This method provides a wealth of information on wetting properties, but is otherwise computationally expensive.[62, 63, 64, 65]

In this work we adopt an alternative procedure based on the mechanical definition of the disjoining pressure which more directly resembles experimental methods such as the captive bubble technique.[66, 67, 68, 69]

By definition, the disjoining pressure of a liquid film is the pressure such film exerts on the bounding vapor and solid phases, as measured in excess to that of a bulk liquid with the same chemical potential.[8] By reasons of mechanical equilibrium, the normal pressure of the liquid film must equal that of the confining vapor phase, while material equilibrium requires such phases to have also equal chemical potential.[70, 71] Accordingly, the disjoining pressure of a liquid film may be given as:

$$\Pi(\ell) = p_v(\mu) - p_l(\mu) \tag{1.23}$$

where p_v and p_l are the bulk vapor and liquid pressures at chemical potential μ. Cast in this form, one sees that $\Pi(\ell)$ may be estimated from purely bulk properties. Only the precise value of ℓ consistent with the imposed chemical potential is actually a purely surface property.

In the captive bubble technique, the right hand side of this equation is readily estimated from the Laplace pressure difference of a vapor bubble gently confining the

liquid film against a substrate, while the corresponding film height, ℓ, is measured by means of an interferometric technique.[66, 67, 68]

In our simulations, we estimate ℓ using the ISM technique,[60, 61] which, we checked provides similar results as obtained by equating the number of adsorbed molecules $N_{\rm ads} = (\rho_l - \rho_v)A\ell$. The Laplace pressure difference of Eq. (1.23) is estimated in two stages.

Firstly, we estimate the equilibrium chemical potential of the adsorbed film. This is done by means of a restricted grand canonical simulation. i.e., a standard μVT simulation is performed, but the amount of molecules within the system is allowed to fluctuate only by ± 1 molecules about the desired canonical configuration of N_c molecules. This may be achieved in practice by introducing an additional Boltzmann factor $exp(-\beta W_c(N))$, with $W_c(N)$ a weighting function, to the usual grand canonical Monte Carlo acceptance rule. The weighting function is null whenever the system has a number of molecules falling in the interval $[N_c - 1, N_c + 1]$, but is infinity otherwise. Whence, naturally, the grand canonical simulation samples unbiased grand canonical probabilities about $N_c \pm 1$, while attempts to insert or remove particles beyond this interval have always zero probability by virtue of the weighting function.

During the course of the simulation, the probability $P(N)$ of observing N molecules in the system is measured (which, by virtue of the weighting function is restricted to measuring $P(N_c - 1)$, $P(N_c)$ and $P(N_c + 1)$). The chemical potential is then estimated as:[72]

$$\beta(\mu - \mu_0) = -\frac{d \ln P(N)}{dN} \tag{1.24}$$

where μ_0 is the chemical potential imposed during the grand canonical simulation, and $\beta = 1/k_B T$, with k_B the Boltzmann constant. This technique can be viewed as an extension of Widom's test particle method for the calculation of the excess chemical potential. The advantage of our method is that is provides right away the full chemical potential, not just the excess part. Accordingly, it easily allows the calculation of chemical potentials for inhomogeneous systems.

Performing this trick for very thick liquid films, or alternatively, for liquid slabs inside a box with periodic boundary conditions in all three directions also allows to accurately measure the coexistence chemical potential. This procedure is of similar accuracy, but much less time consuming than performing a full multicanonical simulation followed by application of the equal area rule.[73]

In a second stage, we measure the bulk density isotherms $\rho_v(\mu)$ and $\rho_l(\mu)$ over the range of desired chemical potentials. For the vapor phase, this is readily achieved by performing grand canonical simulations at chemical potentials corresponding to the desired film heights. Additional care must be exercised to obtain $\rho_l(\mu)$, since results are needed in a range of chemical potentials where the liquid bulk phase is metastable.[74] The cavitation of the liquid may be avoided by performing simulations in a sufficiently

small system.[75, 62] For our purposes, cubic boxes of $L = 10$ where found to be sufficiently small. Even so, it is advantageous to perform multi-canonical simulations over a restricted range of molecules below the liquid spinodal,[76] and then estimate the density isotherm from Eq. (1.24).

Once the density isotherms have been measured, the right hand side of Eq. (1.23) may be estimated by means of the Gibbs-Duhem equation as:

$$p_l(\mu) - p_v(\mu) = \int_{\mu_c}^{\mu} (\rho_l - \rho_v) d\mu' \tag{1.25}$$

Obviously, this pressure difference could have been estimated directly from the virial.[71, 74] However, measuring the mechanical pressure in a simulation usually provides large error bars, and the precise form of the pressure tensor is dependent of the model. Particularly, for the LJ model studied here, one needs to deal with the impulsive contribution to the pressure that results from the discontinuity of the potential at r_c.

1.5 Results

As mentioned above, all of the results presented in this section correspond to adsorption isotherms of Ar onto a solid model substrate at a temperature T=107.82K. This yields a thermal to molecular energy ratio of $k_BT/\epsilon = 0.9$. In what follows, all energies will be measured in units of the thermal energy k_BT, and all lengths in units of the molecular diameter σ.

1.5.1 Film structure and disjoining pressure

Film structure

The inset of 1.1 displays results for the density profile of an adsorbed liquid phase at coexistence. The profile exhibits strong oscillations with a period of about one molecular diameter, as is known in related systems.[30, 43, 77, 78, 79]

This characteristic structure does not stem from the long range external potential $V(z) \approx z^{-3}$, but rather, is mostly the result of liquid like packing correlations which originate from the steep, short ranged repulsive part of the wall $V(z) \approx z^{-9}$. In such cases, it may be shown that both the period of the oscillations, as well as the decay of the correlations is given by purely bulk liquid properties.[80, 81, 82]

In fact, the density of an adsorbed liquid film may be expressed as:

$$\rho_{wl}(z) = (1 + h_{wl}(z))\rho_l \tag{1.26}$$

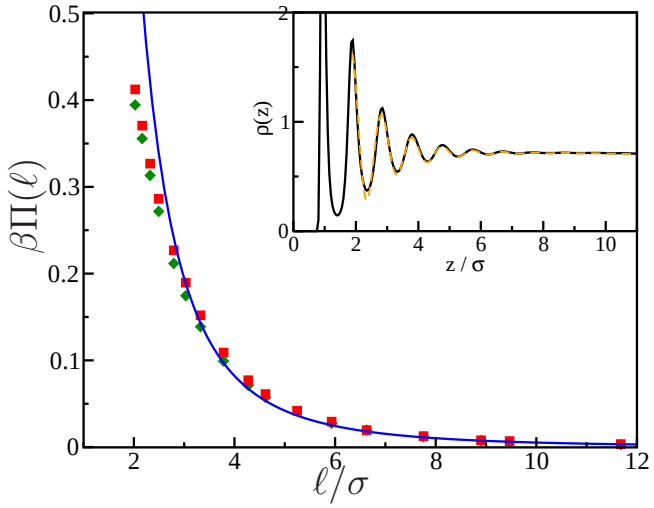

Figure 1.1. Disjoining pressure as a function of film height. Red squares are results for $\Pi(\ell)$ obtained from thermodynamic integration. Green diamonds are results for $\Pi_V(\ell)$ obtained via Eq. 1.13 and the solid blue line corresponds to $\Pi_{HD}(\ell)$, Eq. (1.35). Inset: Density profile of an infinite liquid film adsorbed on the substrate. Simulation results are compared with predictions of Eq. (1.27), using $b_e = 0.8953\sigma^{-1}$, $b_o = 1.9908\sigma^{-1}$ and $k_o = -6.4820\sigma^{-1}$ as obtained from independent fits to the bulk radial distribution function, and B_e, B_o as only adjustable parameters.

where ρ_l is the bulk liquid density, and $h_{wl}(z)$ is the wall-liquid correlation function. An accurate description of the density profile is achieved using density functional theory.[83, 84, 85] At the moderate temperatures studied here, however, $h_{wl}(z)$ may be accurately described beyond one molecular diameter by:[80, 81]

$$h_{wl}(z) = B_e e^{-b_e z} + B_o cos(k_o z + \theta_w) e^{-b_o z} \tag{1.27}$$

where both the inverse correlation lengths $b_e = 0.8953\sigma^{-1}$ and $b_o = 1.9908\sigma^{-1}$, and the wave vector $k_o = -6.4820\sigma^{-1}$ are exactly as those describing the bulk liquid pair correlation function. Only the amplitudes, B_e, B_o and the phase, θ_w are dictated by wall-fluid interactions.

We test Eq.1.26-1.27 by fitting the density profile with only B_e, B_o and θ_w as adjusting parameters, and taking the coefficients b_e, b_o and k_o from independent fits to the bulk liquid pair correlation function obtained in our simulations. 1.1 shows that the description of the adsorbed liquid profile is rather accurate.

Obviously, this description is missing additional correlations related to the wall-fluid long range interactions. However, such correlations are of order $\rho_l \kappa_l V(z)$. Since the bulk liquid compressibility, κ_l is usually small, it hardly affects the much stronger short range packing correlations and may be ignored at the level of qualitative description that is sought here.[27]

Having described the structure of the adsorbed liquid, let us now consider the structure of the liquid films. 1.2 displays results for density profiles of different adsorbed films ranging from 3σ to 14σ. The profiles resemble a liquid-vapor interface $\rho_{\rm lv}(z)$ translated from the wall surface ($z = 0$) by the average film height ℓ, with the wall-liquid oscillations superimposed onto the liquid branch. In fact, the following superposition approximation provides a rather reasonable description:

$$\rho(z) = (1 + h_{wl}(z))\rho_{lv}(z;\ell) \tag{1.28}$$

where $\rho_{lv}(z;\ell)$ is the density profile of a free liquid-vapor interface centered at ℓ.

1.2 shows a fit of the density profiles to the above equation, with h_{wl} borrowed exactly from the previous fit to the wall-liquid density profile, and $\rho_{lv}(z;\ell)$, a fit to a free liquid-vapor interface. In order to account for the different correlation lengths of the liquid and vapor branches of the free interface, we have used a double parabola approximation, whereby the density profile is given as a piece-wise function:[86, 87]

$$\rho_{lv}(z) = \begin{cases} \rho_l - \frac{b_v}{b_v+b_l}(\rho_l - \rho_v)e^{b_l(z-\ell)} & z \le \ell \\ \\ \rho_v + \frac{b_l}{b_v+b_l}(\rho_l - \rho_v)e^{-b_v(z-\ell)} & z > \ell \end{cases} \tag{1.29}$$

Despite its simplicity, the model incorporates naturally the asymmetry of the liquid and vapor phases and is able to provide semi–quantitative results for the density profiles using $b_l = 1.04\sigma^{-1}$ and $b_v = 1.18\sigma{-}1$.

Disjoining pressure

The results for the disjoining pressure isotherm are shown in 1.1. Despite the very strong oscillatory behavior of the liquid films, $\Pi(\ell)$ is a smooth monotonically decaying function for all film heights studied, corresponding clearly to a regime of complete wetting.

Usually, the observation of a stratified density profile is related to measurable oscillations of the disjoining pressure.[77] Indeed, in our previous study of adsorption close to the fluid's triple point, oscillations were clearly visible in $\Pi(\ell)$.[26]

In order to understand how the density oscillations propagate into the disjoining pressure isotherm, we first notice that in our system, $\Pi(\ell)$ is completely dominated by the external field contribution in all the range of film heights studied. This can be shown by calculating the external contribution to $g(\ell)$, Eq. (1.13) exactly, using the measured density profiles from simulation, followed by numerical differentiation with respect to the film height. The result, denoted $\Pi_V(\ell)$ is displayed in 1.1, and shows very good agreement with the full disjoining pressure isotherm obtained from simulation. A similar behavior is often consistent with experimental observations.[66, 67, 68, 69]

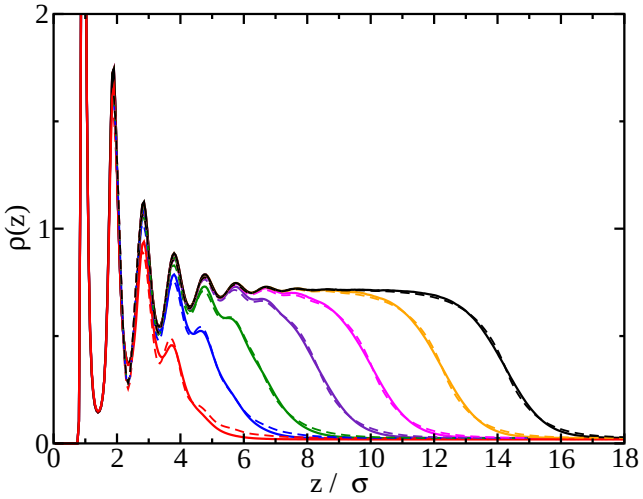

Figure 1.2. Density profiles for several adsorbed films of height ℓ ranging from 3.3, 4.6, 5.9, 7.8, 9.5, 11.7 to 13.7σ (solid lines). The dashed lines are estimations from the superposition model of Eq.1.27-1.29, with ℓ as the only adjustable parameter. For the thickest films the superposition model falls right on top of the simulation results and is hardly visible.

This indicates that essentially $\Pi(\ell) = \Pi_V(\ell)$ in our system, so we can now attempt to give a qualitative understanding of the conjectured oscillatory behavior of $\Pi(\ell)$ in terms of the behavior of $\Pi_V(\ell)$ alone. This can be achieved by noticing, from the definition of disjoining pressure, that:

$$\Pi_V(\ell) = -\int_0^\infty V(z)\frac{d\rho(z;\ell)}{d\ell}dz \tag{1.30}$$

A tractable analytic approximation for this integral may be obtained using the qualitative model for $\rho(z;\ell)$ that is afforded by Eq.1.26-1.29, and noticing that the derivative of $\rho(z;\ell)$ is highly peaked about ℓ. This allows us to expand the leading order attractive contribution of $V(z)$ to zeroth order about ℓ. In order to simplify the resulting expressions, we further assume that the three inverse correlation lengths $b_l = b_v = b_e$ are equal and are denoted simply as b. As a result, we can write:

$$\Pi_V(\ell) = \frac{H_w}{6\pi\ell^3}\left(I_H + I_e + I_o\right) \tag{1.31}$$

where we have split the disjoining pressure into Hamaker, exponential and oscillatory contributions. The Hamaker contribution stems from the structure of the free liquid-vapor interface alone and is given by:

$$I_H = 1 - \frac{1}{2}e^{-b\ell} \tag{1.32}$$

Notice an exponentially decaying correction arising from the tails of the free interface, which is assumed a stepwise function in the Hamaker-Derjaguin model.

An additional contribution stems from the wall-fluid exponentially decaying correlations, and is given by:

$$I_e = \frac{1}{4} B_e (1 + 2b\ell) e^{-b\ell} \tag{1.33}$$

Finally, the last term arises from the damped oscillatory wall-fluid correlations, and reads:

$$I_o = B_o \left[\left(\frac{b}{k_o} \right)^2 \cos(k_o \ell + \theta_w) e^{-b_o \ell} - \frac{1}{2} \frac{b}{k_o} \sin(\theta_w) e^{-b\ell} \right] \tag{1.34}$$

where we have only retained leading order terms in b/k_o for the sake of clarity. This assumption yields an upper bound for the amplitude of the oscillatory contribution.

Clearly, I_H and I_o provide essentially a monotonous decay beyond a few molecular diameters, so that the only source of oscillatory behavior appears in the first contribution to I_o. This term will become large and produce oscillations in $\Pi(\ell)$ only if the amplitude B_o and decay rate of bulk correlations b become large enough, while the decay rate of oscillations, b_o, becomes small enough. This is indeed expected at low temperature.[80, 81, 82] In our system, however, $b \approx \sigma^{-1}$ and $k_o \approx 2\pi/\sigma$, so that the ratio $(b/k_o)^2$ is very small and the disjoining pressure is essentially dominated by the monotonous contribution I_H.

This can be seen right away in 1.1, where we compare the simulation results for $\Pi(\ell)$ with the leading order Hamaker-Derjaguin contribution:

$$\Pi_{HD}(\ell) = \frac{H_w}{6\pi} \ell^{-3} \tag{1.35}$$

Clearly, this simple approximation provides a good description for ℓ larger than about 3σ, and gives further support to the idea that most of $\Pi(\ell)$ is given by van der Waals interactions in our system.

1.5.2 Interface fluctuations and capillary wave spectrum

We now attempt to analyze the capillary wave fluctuations of our thin wetting films in order to assess the adequacy of either the classical result, Eq. (1.6), or the modified expression Eq. (1.18).

To perform this study, we first must take into consideration that our simulations are performed for fairly limited system sizes, so that only small wavelength fluctuations can be studied. Therefore, the application of Eq. (1.6) and Eq. (1.18) to atomic length scales requires to account for contributions of order higher than q^2. In the most general case, the additional contributions are rather complicated.[38, 54, 55] For our model

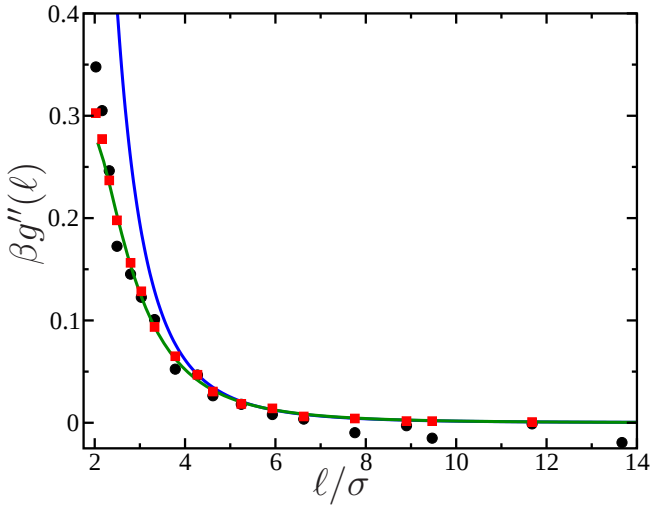

Figure 1.3. Second derivative of the interface potential as a function of ℓ. Black circles are data obtained from CW spectrum, red squares are data obtained from thermodynamic integration, the solid green line was obtained via Eq. (1.13), and the solid blue line corresponds to the Hamaker-Derjaguin model of Eq. (1.35).

system, however, the fluid-fluid interactions are truncated, and therefore, short-ranged. In this case, it is well known that terms odd in q vanish for reasons of symmetry, and the next to leading order contribution is thus of order q^4.[38, 55]

Taking this into account, we can write for the capillary wave spectrum of interfacial fluctuations:

$$\frac{k_B T}{A \langle |\delta \ell^2(q)| \rangle} = g''_{cw}(\ell) + \gamma_{cw}(\ell)\, q^2 + \kappa_{cw}(\ell)\, q^4 \tag{1.36}$$

where the bending rigidity coefficient, κ_{cw}, is incorporated in order to extend the low wave vector result of Eq. (1.6) and Eq. (1.18) to atomic scale fluctuations. In the classical model, Eq. (1.6), $g''_{cw}(\ell) = -\Pi(\ell)$, while $\gamma_{cw}(\ell)$ is a constant equal to γ_{lv}. According to Eq. (1.18), $g''_{cw}(\ell)$ also equals $-\Pi(\ell)$, but now $\gamma_{cw}(\ell) = \gamma(\ell)$ as indicated in Eq. (1.19).

The coefficients $g''_{cw}(\ell)$ and $\gamma_{cw}(\ell)$ obtained from fits of the capillary wave spectrum to Eq. (1.36) are displayed in 1.3-1.4.

1.3 compares the zero order coefficients, g''_{cw} for different film heights, with the ℓ derivative of $\Pi(\ell)$ as obtained independently from thermodynamic integration. Clearly, both properties are in very good agreement in all the range of film heights studied, and suggest that Eq. (1.6) is indeed a correct model for the film height fluctuations, at least to zero order in the wave-vector.

To the best of our knowledge, a similar test of consistency has only been presented previously in our recent work.[26, 27] Also shown in 1.3 is the result for $g''(\ell)$ as expected from the Hamaker model. The good agreement found for this model with the disjoining

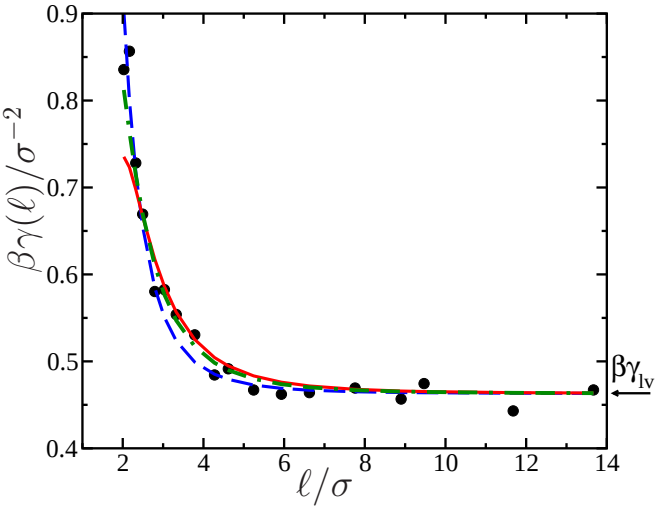

Figure 1.4. Plot of $\gamma(\ell)$ vs ℓ obtained from the capillary wave spectrum (black circles). The arrow indicates the surface tension of the free liquid-vapor interface, $\beta\gamma_{\rm lv} = 0.463\sigma^{-2}$. Different fits to Eq. 1.19, with ξ_e^2 the only adjustable parameter, are shown for different ways of obtaining $\Pi'(\ell)$. Red solid line correspond to $\Pi'(\ell)$ obtained from thermodynamic integration, green dashed-dotted line corresponds to $\Pi'(\ell)$ estimated from Eq. (1.13), and blue dashed line corresponds the Hamaker-Derjaguin model, Eq. (1.35).

pressure isotherm, 1.1, holds in this case only beyond five molecular diameters. However, we can still show that $g''(\ell)$ is dominated by the van der Waals interactions by plotting $g''_V(\ell)$ as obtained from successive numerical differentiation of Eq. (1.13). As found previously for 1.1, the agreement is again very good.

1.5.3 Film height dependent surface tension

Next we plot the coefficients γ_{cw} in the polynomial fit to the capillary wave spectrum, Eq. (1.36). According to the classical theory, Eq. (1.6), such coefficient is constant, independent of ℓ and equal to the liquid-vapor surface tension. Our results, 1.4, show that indeed, γ_{cw} remains nearly constant for thick films beyond $\ell = 8\sigma$, and has a value very close to independent calculations of γ_{lv} as obtained from the virial.

Such results are consistent with previous studies, where it was found that the CWS provides good estimates of the surface tension for free interfaces.[22, 23, 88, 89]

For thin films, however, the coefficients γ_{cw} rise strongly as ℓ becomes smaller. A similar behavior was reported already a while ago by Werner et al. in their study of inmiscible binary polymer melts subject to van der Waals forces.[19] A related, albeit non monotonous dependence was also found in a recent study.[26]

Such behavior cannot be explained in the framework of the classical theory.

In our previous study, we suggested that the anomalous ℓ dependence of the co-

efficient γ_{cw} arises from a coupling of capillary wave fluctuations to the external field. This results in a film height dependent surface tension as indicated by Eq. (1.19).

1.4 displays a test of Eq. (1.19), using the asymptotic γ_{lv} obtained from the simulation of a free interface, our results for $\Pi(\ell)$ as obtained from thermodynamic integration, and the correlation length $\xi_e = 1.0\sigma$ as the only empirical parameter. The fit is clearly in good agreement with the results for γ_{cw}, and lends strong support to Eq. (1.19). The effective correlation length $\xi_e = 1.0\sigma$ is consistent with order of magnitude estimates of the bulk correlation lengths obtained from fits to the density profiles, which recall were $1/b_l = 0.963\sigma$ and $1/b_v = 0.848\sigma$.

A further test of consistency requires to check that the ℓ dependence of γ_{cw} is given by external field contributions, as implied in Eq. (1.19). We test this by estimating γ_{cw} according to Eq. (1.19), but using the numerical derivative of $\Pi_V(\ell)$, instead of the full result $\Pi(\ell)$. The agreement is again very good, and the resulting fit yields almost the same effective correlation length $\xi_e = 1.02\sigma$ as before. Notice, however, the agreement breaks down at about two molecular diameters. This might be signaling a crossover to a regime where short-range contributions become important, but could also be related merely to difficulties in obtaining a meaningful second derivative at the borders of the polynomial fit to $\Pi_V(\ell)$.

As a final remark note that for the simple case where $\Pi(\ell)$ follows exactly the Hamaker-Derjaguin model, Eq. (1.19) then reduces to a result suggested by Bernardino et al. in the framework of a nonlocal theory of interfaces.[17] A fit to this model yields overall a reasonable agreement (1.4), particularly at small ℓ. On the contrary, 1.1 and 1.3 show that the HD model can only be expected to agree at large ℓ. Thus, the overall good performance of this model in the range from $\ell = 2\sigma$ to $\ell = 10\sigma$ is somewhat dictated by the least square fitting procedure, which indeed yields a fit parameter $\xi_e^2 = 0.47\sigma^2$ that is too small compared to our previous more accurate estimate $\xi_e^2 = 1\sigma^2$.

1.5.4 Healing distance

The results of g''_{cw} and γ_{cw} obtained in previous sections allow us to quantify the parallel correlation length of the adsorbed films as $\xi_h^2 = \gamma_{cw}/g''_{cw}$. This quantity dictates the length scale over which correlations decay as a result of a perturbation of the equilibrium film height.[83] An immediate practical result is that adsorbed films are able to *heal* rough substrates with roughness of smaller wavelength than ξ_h, whence, the name of healing distance.[2, 11, 28, 29, 36]

According to the classical theory, $\xi_h^2 \to 0$ as g'' diverges at small ℓ (c.f. Eq. (1.7)). On the contrary, using our theoretical approach, Eq. (1.19), we find:

$$\xi_h^2 = \frac{\gamma_{lv}}{g''(\ell)} + \xi_e^2 \tag{1.37}$$

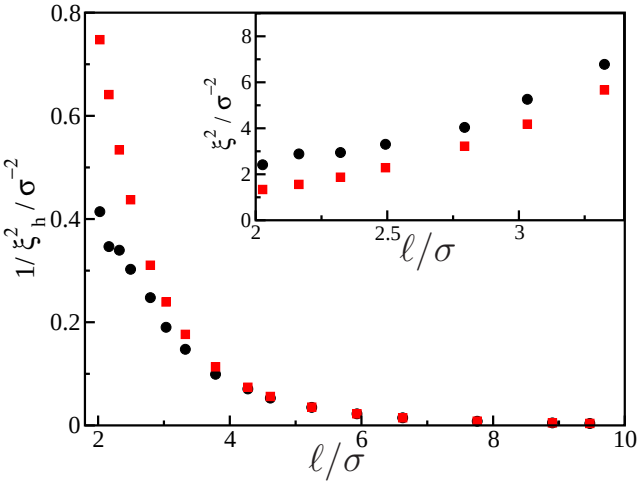

Figure 1.5. Inverse of the healing distance, $1/\xi_h^2$ as a function of ℓ. Black circles correspond to data obtained from the CW spectrum and red squares correspond to the classical result, Eq. (1.7). Inset: amplification of the region of thin films.

This result sets a lower bound to ξ_h, which cannot be smaller than the bulk correlation length of the liquid film.

1.5 displays the results for the healing distance as obtained from our data. Since ξ_h^2 spans several orders of magnitude, we rather plot $1/\xi_h^2$. At large ℓ, the classical estimate matches well the simulation results. As ℓ becomes small, however, the results clearly show a weaker increase of $1/\xi_h^2$ than would be expected from the classical theory. A further check is shown in the inset, where we plot ξ_h^2 in a range of ℓ between 2 and 4 molecular diameters. Results are systematically above the classical expectation. Furthermore, we find the difference to be about constant and very close to $1\sigma^2$, whence, precisely as the value obtained for ξ_e^2 in our fits to γ_{cw}. This is in complete agreement with Eq. (1.37), and lends further support to the *ansatz*, Eq. (1.8), and its consequences, Eq. (1.18) and Eq. (1.19).

1.6 Conclusions and outlook

In this paper we have studied the film height fluctuations of adsorbed liquid films. According to the classical interface Hamiltonian, the spectrum of such fluctuations provides information on the disjoining pressure and the liquid-vapor surface tension of the adsorbed films (Eq. (1.36)). In our study, we have shown that the disjoining pressure estimated from the spectrum of fluctuations is in full agreement with independent results obtained from thermodynamic integration (1.3). However, we show that the corresponding results for the surface tension strongly depend on the film height of the adsorbed

films (1.4). We have shown that the observed film height dependence may be explained by means of a simple theory in which the density at a point is given by the shortest perpendicular distance away from the film profile (Eq. (1.8) and Eq. (1.9)). This provides a mechanism whereby the capillary wave fluctuations couple with the wall-fluid external field, leading to the observed film height dependent contribution to the surface tension (Eq. (1.15) and Eq. (1.17)). An additional consequence is that the healing distance of the fluid is increased with respect to the classical expectation by a constant of the same order of magnitude as the bulk correlation length (Eq. (1.37)).

The results summarized above have important implications in our understanding of adsorbed liquid films. They imply that, close to the substrate, neither the interface potential, nor the related disjoining pressure can possibly be described as a local function of the film profile $\ell(\mathbf{x})$. The nonlocal character of the interface Hamiltonian has been recognized by Andelman et al.[11] and studied in depth by Parry and collaborators both for systems with short range,[16, 17] and long range forces.[17] In our minimal model (Eq. (1.8) and Eq. (1.9)), the nonlocality is described in terms of local functions of the film height *and* its gradient. For the special case where the interface potential is dominated by long range wall-fluid van der Waals forces, this level of description is sufficient to provide accurate expressions for the free energy, Eq. (1.10), and the spectrum of fluctuations Eq. (1.18) and Eq. (1.19).

Whereas more difficult to test in practice, it is more relevant to ask: what is the equilibrium film profile consistent with the nonlocal functional of Eq. (1.10)? The answer to this question is provided by solving for the extremum, and results in the following condition for the film profile:

$$\nabla \cdot \left[\left(\gamma_{lv} - \xi_e^2 \, \frac{d\Pi(\ell)}{d\ell} \right) \nabla \ell \right] + \Pi(\ell) \left[1 - \frac{1}{2} (\nabla \ell)^2 \right] = -\Delta p \tag{1.38}$$

Where, for the sake of simplicity, we have assumed merely a local dependence of $\Pi(\ell)$ on the film height, which must be extended to an additional local dependence in the gradient for the more general case.

Clearly, for equilibrium films that are thick, the disjoining pressure vanishes, and the above result reduces to the Young-Laplace equation. For thin films, however, $\Pi(\ell)$ is significant, and the above result then extends the Young-Laplace equation to the subnanometer length scale, providing corrections which are absent in the augmented Young-Laplace equation. Taking into account the additional contributions could substantially improve our understanding of adsorbed condensates at the nanometer length scale.[2, 4, 31, 33, 34]

Acknowledgements

We thank E. M. Fernández, E. Chacón and P. Tarazona for providing us with a computer code that implements the Intrinsic Sampling Method and A.O. Parry for helpful discussions. This project supported by grant FIS2010-22047-C05-05 from Ministerio de

Economía; EU grant 322326-COSAAC-FP7-PEOPLE-2012-CIG and a Ramón y Cajal research contract (E.S).

Bibliography

[1] R. Seemann, M. Brinkmann, E. J. Kramer, F. F. Lange, and R. Lipowsky, "Wetting morphologies at microstructured surfaces," *Proc. Natl. Acad. Sci.*, vol. 102, pp. 1848–1852, 2005.

[2] P. de Gennes, F. Brochard-Wyart, and D. Quéré, *Capillarity and wetting phenomena*. Spinger, New York, 2004.

[3] G. Reiter, P. Auroy, and L. Auvray, "Instabilities of thin polymer films on layers of chemically identical grafted molecules," *Macromolecules*, vol. 29, pp. 2150–2157, 1996.

[4] H. I. Kim, C. M. Mate, K. A. Hannibal, and S. S. Perry, "How disjoining pressure drives the dewetting of a polymer film on a silicon surface," *Phys. Rev. Lett.*, vol. 82, pp. 3496–3499, Apr 1999.

[5] R. Seemann, S. Herminghaus, and K. Jacobs, "Gaining control of pattern formation of dewetting liquid films," *J. Phys.:Condens. Matter*, vol. 13, pp. 4925–4938, 2001.

[6] A. P. Bowles, Y.-T. Hsia, P. M. Jones, J. W. Schneider, and L. R. White, "Quasi–equilibrium afm measurement of disjoining pressure in lubricant nano–films i: Fomblin z03 on silica," *Langmuir*, vol. 22, pp. 11436–11446, 2006.

[7] E. J. Maginn, A. T. Bell, and D. N. Theodorou, *Sorption Thermodynamics, Siting, and Conformation of long n-Alkanes in Silicalite as Predicted by Configurational-Bias Monte Carlo Integration*, vol. 99. 1995.

[8] B. Derjaguin, "Modern state of the investigation of long-range surface forces," *Langmuir*, vol. 3, no. 5, pp. 601–606, 1987.

[9] A. Vrij, "Possible mechanism for the spontaneous rupture of thin, free liquid films," *Discuss. Faraday Soc.*, vol. 42, pp. 23–33, 1966.

[10] J. R. Philip, "Unitary approach to capillary condensation and adsorption," *J. Chem. Phys.*, vol. 66, no. 11, pp. 5069–5075, 1977.

[11] D. Andelman, J.-F. Joanny, and M. O. Robbins, "Complete wetting on rough surfaces: Statics," *Europhys. Lett.*, vol. 7, no. 8, pp. 731–736, 1988.

[12] A. Sharma, "Equilibrium contact angles and film thicknesses in the apolar and polar systems: Role of intermolecular interactions in coexistence of drops with thin films," *Langmuir*, vol. 9, pp. 3580–3586, 1993.

[13] U. Thiele, M. G. Velarde, and K. Neuffer, "Dewetting: Film rupture by nucleation in the spinodal regime," *Phys. Rev. Lett.*, vol. 87, p. 016104, Jun 2001.

[14] V. M. Starov and M. G. Velarde, "Surface Forces and Wetting Phenomena," *J. Phys.:Condens. Matter*, vol. 21, no. 46, p. 464121, 2009.

[15] M. E. Fisher, A. J. Jin, and A. O. Parry, "On the stiffness of an interface near a wall," *Ber. Bunsenges Phys. Chem.*, vol. 98, pp. 357–361, 1994.

[16] A. O. Parry, C. Rascón, N. R. Bernardino, and J. M. Romero-Enrique, "Derivation of a non–local interfacial hamiltonian for short range wetting: I. double parabola approximation," *J. Phys.:Condens. Matter*, vol. 18, pp. 6433–6451, 2006.

[17] N. R. Bernardino, A. O. Parry, C. Rascón, and J. M. Romero-Enrique, "Derivation of a nonlocal interfacial model for 3d wetting in an external field," *J. Phys.:Condens. Matter*, vol. 21, no. 46, p. 465105, 2009.

[18] J. Wang, M. Tolan, O. H. Seeck, S. K. Sinha, O. Bahr, M. H. Rafailovich, and J. Sokolov, "Surfaces of strongly confined polymer thin films studied by x-ray scattering," *Phys. Rev. Lett.*, vol. 83, pp. 564–567, Jul 1999.

[19] A. Werner, M. Muller, F. Schmid, and K. Binder, "Effect of long-range forces on the interfacial profiles in thin binary polymer films," *J. Chem. Phys.*, vol. 110, no. 2, pp. 1221–1229, 1999.

[20] R. K. Heilmann, M. Fukuto, and P. S. Pershan, "Quenching of capillary waves in composite wetting films from a binary vapor: An x-ray reflectivity study," *Phys. Rev. B*, vol. 63, p. 205405, Apr 2001.

[21] A. Plech, U. Klemradt, M. Aspelmeyer, M. Huber, and J. Peisl, "Solid-liquid interface of a 2-propanol–perfluoromethylcyclohexane mixture: From adsorption to wetting," *Phys. Rev. E*, vol. 65, p. 061604, Jun 2002.

[22] A. Milchev and K. Binder, "Momentum-dependent interfacial tension in polymer solutions," *Europhys. Lett.*, vol. 59, no. 1, pp. 81–86, 2002.

[23] R. L. C. Vink, J. Horbach, and K. Binder, "Capillary waves in a colloid-polymer interface," *J. Chem. Phys.*, vol. 122, no. 13, p. 134905, 2005.

[24] R. E. Rozas and J. Horbach, "Capillary wave analysis of rough solid-liquid interfaces in nickel," *Europhys. Lett.*, vol. 93, no. 2, p. 26006, 2011.

[25] E. M. Fernández, E. Chacón, and P. Tarazona, "Capillary waves spectrum at adsorbed liquid films," vol. 86, p. 085401, 2012.

[26] L. G. MacDowell, J. Benet, and N. A. Katcho, "Capillary fluctuations and film-height-dependent surface tension of an adsorbed liquid film," *Phys. Rev. Lett.*, vol. 111, p. 047802, Jul 2013.

[27] L. G. MacDowell, J. Benet, N. A. Katcho, and J. M. Palanco, "Disjoining pressure and the film-height-dependent surface tension of thin liquid films: New insight from capillary wave fluctuations," vol. 206, no. 0, pp. 150–171, 2014.

[28] D. Quéré, "Rough ideas on wetting," vol. 313, no. 1–2, pp. 32–46, 2002. Fundamental Problems in Statistical Physics.

[29] I. M. Tidswell, T. A. Rabedeau, P. S. Pershan, and S. D. Kosowsky, "Complete wetting of a rough surface: An x-ray study," *Phys. Rev. Lett.*, vol. 66, pp. 2108–2111, Apr 1991.

[30] J. R. Henderson, "Statistical mechanics of the disjoining pressure of a planar film," vol. 72, no. 6, p. 051602, 2005.

[31] A. Checco, P. Guenoun, and J. Daillant, "Nonlinear dependence of the contact angle of nanodroplets on contact line curvature," *Phys. Rev. Lett.*, vol. 91, p. 186101, Oct 2003.

[32] L. G. MacDowell, M. Müller, and K. Binder, "How do droplets on a surface depend on the system size?," vol. 206, pp. 277–291, 2002.

[33] A. R. Herring and J. R. Henderson, "Simulating study of the disjoining pressure profile through a three–phase contact line," *J. Chem. Phys.*, vol. 132, p. 084702, 2010.

[34] N. Tretyakov, M. Muller, D. Todorova, and U. Thiele, "Parameter passing between molecular dynamics and continuum models for d roplets on solid substrates: The static case," *J. Chem. Phys.*, vol. 138, no. 6, p. 064905, 2013.

[35] A. Nold, D. N. Sibley, B. D. Goddard, and S. Kalliadasis, "Fluid structure in the inmediate vicinity of an equilibrium three-phase contact line and assesment of disjoining pressure models using density functional theory," vol. 26, p. 072001, 2014.

[36] M. O. Robbins, D. Andelman, and J.-F. Joanny, "Thin liquid films on rough or heterogeneous solids," *Phys. Rev. A*, vol. 43, pp. 4344–4354, Apr 1991.

[37] A. Vrij and J. T. G. Overbeek, "Rupture of thin liquid films due to spontaneous fluctuations in thickness," *J. Am. Chem. Soc.*, vol. 90, pp. 3074–3078, 1968.

[38] K. R. Mecke and S. Dietrich, "Effective hamiltonian for liquid-vapor interfaces," *Phys. Rev. E*, vol. 59, pp. 6766–6784, Jun 1999.

[39] H. T. Davis, "Capillary waves and the mean field theory of interfaces," *J. Chem. Phys.*, vol. 67, no. 8, pp. 3636–3641, 1977.

[40] F. P. Buff, R. A. Lovett, and F. H. Stillinger, "Interfacial density profile for fluids in the critical region," *Phys. Rev. Lett.*, vol. 15, pp. 621–623, Oct 1965.

[41] J. D. Weeks, "Structure and thermodynamics of the liquid–vapor interface," *J. Chem. Phys.*, vol. 67, no. 7, pp. 3106–3121, 1977.

[42] R. F. Kayser, "Effect of capillary waves on surface tension," *Phys. Rev. A*, vol. 33, pp. 1948–1956, Mar 1986.

[43] C. Ebner and W. F. Saam, "New phase transition in thin argon films," *Phys. Rev. Lett.*, vol. 38, pp. 1486–1489, 1977.

[44] J. E. Finn and P. A. Monson, "Adsorption equilibria in an isobaric ensemble," *Molec. Phys.*, vol. 65, pp. 1345–1361, 1988.

[45] J. E. Finn and P. A. Monson, "Prewetting at a solid–fluid interface via Monte Carlo simulation," vol. 39, pp. 6402–6408, 1989.

[46] S. Sokolowski and J. Fischer, "Wetting transitions at the argon-solid-co_2 interface: Molecular-dynamics studies," vol. 41, pp. 6866–6870, 1990.

[47] Y. Fan and P. W. Monson, "Further studies of prewetting transitions via Monte Carlo simulations," *J. Chem. Phys.*, vol. 99, pp. 6897–6906, 1993.

[48] J. R. Errington, "Prewetting transitions for a model Argon on solid carbon dioxide system," *Langmuir*, vol. 20, pp. 3798–3804, 2004.

[49] S. Toxvaerd, "Molecular dynamics simulation of prewetting," vol. 111, pp. 15621–15624, 2007.

[50] G. Mistura, F. Ancilotto, L. Bruschi, and F. Toigo, "Wetting of argon on CO_2," *Phys. Rev. Lett.*, vol. 82, pp. 795–798, 1999.

[51] W. Shi, X. Zhao, and J. K. Johnson *Molec. Phys.*, vol. 100, pp. 2139–2150, 2002.

[52] J. K. Singh, G. Sarma, and S. K. Kwak, "Thin-thick surface phase coexistence and boundary tension of the square-well fluid on a weak attractive surface," *J. Chem. Phys.*, vol. 128, no. 4, p. 044708, 2008.

[53] R. de Gregorio, J. Benet, N. A. Katcho, F. J. Blas, and L. G. MacDowell, "Semi-infinite boundary conditions for the simulation of interfaces: The Ar/CO_2(s) model revisited," *J. Chem. Phys.*, vol. 136, no. 10, p. 104703, 2012.

[54] M. Napiórkowski and S. Dietrich, "Structure of the effective hamiltonian for liquid-vapor interfaces," vol. 47, pp. 1836–1849, Mar 1993.

[55] E. M. Blokhuis, "On the spectrum of fluctuations of a liquid surface: From the molecular scale to the macroscopic scale," *J. Chem. Phys.*, vol. 130, p. 074701, 2009.

[56] E. Chacón, E. M. Fernández, and P. Tarazona, "Effect of dispersion forces on the capillary-wave fluctuations of liquid surfaces," vol. 89, p. 042406, Apr 2014.

[57] E. J. Maginn, A. T. Bell, and D. N. Theodorou, "Sorption thermodynamics, siting, and conformation of long n-alkanes in silicalite as predicted by configurationa-bias Monte Carlo integration," *J. Phys. Chem.*, vol. 99, pp. 2057–2079, 1995.

[58] B. Smit, "Grand canonical monte carlo simulations of chain molecules: Adsorption isotherms of alkanes in zeolites," *Molec. Phys.*, vol. 85, pp. 153–172, 1995.

[59] L. G. MacDowell, *Termodinámica Estadística de Moléculas Flexibles: Teoría y Simulación*. PhD thesis, Universidad Complutense de Madrid, 2000.

[60] E. Chacon and P. Tarazona, "Characterization of the intrinsic density profiles for liquid surfaces," *J. Phys.:Condens. Matter*, vol. 17, pp. S3493–S3498, 2005.

[61] M. Jorge, P. Jedlovszky, and M. N. D. S. Cordeiro, "A critical assessment of methods for the intrinsic analysis of liquid interfaces. 1. surface site distributions," vol. 114, no. 25, pp. 11169–11179, 2010.

[62] L. G. MacDowell and M. Müller, "Adsorption of polymers on a brush: Tuning the order of the wetting transition," *J. Chem. Phys.*, vol. 124, p. 084907, 2006.

[63] M. Müller and L. G. MacDowell, "Interface and surface properties of polymer solutions: Monte Carlo simulations and self-consistent field theory," *Macromolecules*, vol. 33, pp. 3902–3923, 2000.

[64] E. M. Grzelak and J. R. Errington, "Computation of interfacial properties via grand canonical transition matrix Monte Carlo simulation," *J. Chem. Phys.*, vol. 128, p. 014710, 2008.

[65] K. S. Rane, V. Kumar, and J. R. Errington, "Monte carlo simulation methods for computing the wetting and drying pro perties of model systems," *J. Chem. Phys.*, vol. 135, no. 23, p. 234102, 2011.

[66] T. D. Blake and J. A. Kitchener, "Stability of aqueous films on hydrophobic methylated silica," vol. 68, pp. 1435–1442, 1972.

[67] T. D. Blake, "Investigation of equilibrium wetting films of n–alkanes on α–alumina," vol. 71, pp. 192–208, 1975.

[68] R. Vazquez, R. Nogueira, S. Busquets, J. L. Mata, and B. Saramago, "Wetting films of polar and nonpolar liquids," *J. Colloid Interf. Sci.*, vol. 284, pp. 652–657, 2005.

[69] J. Restolho, J. L. Mata, K. Shimizu, J. N. Canongia Lopes, and B. Saramago, "Wetting films of two ionic liquids: [C8mim][BF4] and [C2OHmim][BF4]," vol. 115, no. 32, pp. 16116–16123, 2011.

[70] D. Henderson, *Fundamentals of Inhomogenous Fluids*. New York: Marcel Dekker, 1992.

[71] D. Bhatt, J. Newman, and C. J. Radke, "Molecular simulation of disjoining-pressure isotherms for free liquid, lennard-jones thin films," vol. 106, no. 25, pp. 6529–6537, 2002.

[72] L. G. MacDowell, "Formal study of nucleation as described by fluctuation theory," *J. Chem. Phys.*, vol. 119, pp. 453–463, 2003.

[73] N. B. Wilding, "Critical–point and coexistence–curve properties of the Lennard–Jones fluid: A finite–size scaling study," vol. 52, pp. 602–611, 1995.

[74] M. Han, "Disjoining properties of ne and ar on graphite surface," vol. 317, no. 1–3, pp. 679–686, 2008.

[75] L. G. MacDowell, P. Virnau, M. Müller, and K. Binder, "The condensation/evaporation transition of liquid droplets," *J. Chem. Phys.*, vol. 120, pp. 5293–5308, 2004.

[76] B. A. Berg and T. Neuhaus, "Multicanonical ensemble: A new approach to simulate first order phase transitions," *Phys. Rev. Lett.*, vol. 68, pp. 9–12, 1992.

[77] R. G. Horn and J. N. Israelachvili, "Direct measurement of structural forces between two surfaces in a nonpolar liquid," *J. Chem. Phys.*, vol. 75, pp. 1400–1411, 1981.

[78] A. A. Chernov and L. V. Mikheev, "Wetting of solid surfaces by a structured simple liquid: Effect of fluctuations," *Phys. Rev. Lett.*, vol. 60, pp. 2488–2491, Jun 1988.

[79] S. H. L. Klapp, S. Grandner, Y. Zeng, and R. von Klitzing, "Asymptotic structure of charged colloids between two and three dimensions: the influence of salt," *J. Phys.:Condens. Matter*, vol. 20, no. 49, p. 494232, 2008.

[80] R. Evans, R. J. F. L. de Carvalho, J. R. Henderson, and D. C. Hoyle, "Asymptotic decay of correlations in liquids and their mixtures," *J. Chem. Phys.*, vol. 100, no. 1, pp. 591–603, 1994.

[81] J. R. Henderson, "Wetting phenomena and the decay of correlations at fluid interfaces," *Phys. Rev. E*, vol. 50, pp. 4836–4846, Dec 1994.

[82] R. Evans and J. R. Henderson, "Pair correlation function decay in models of simple fluids that contain dispersion interactions," *J. Phys.:Condens. Matter*, vol. 21, no. 47, p. 474220, 2009.

[83] R. Evans, "The nature of the liquid-vapor interface and other topics in the statistical mechanics of non-uniform fluids," vol. 28, pp. 143–200, 1979.

[84] Y. Tang and J. Wu, "A density functional theory for bulk and inhomogeneous lennard–jones fluids from the energy route," *J. Chem. Phys.*, vol. 119, pp. 7388–7397, 2003.

[85] P. Bryk, W. Rzysko, A. Malijevsky, and S. Sokołowski, "Capillary condensation in pores with rough walls: A density functional approach," *J. Colloid Interf. Sci.*, vol. 313, no. 1, pp. 41–52, 2007.

[86] T. V. Bykov and X. C. Zeng, "A patching model for surface tension of spherical droplet and tolman length. II," *J. Chem. Phys.*, vol. 111, pp. 10602–10610, 1999.

[87] J. M. G. Palanco, *Termodinámica Estadística de Fluidos Moléculares y sus Interfases*. PhD thesis, Universidad Complutense de Madrid, 2013.

[88] M. Müller and M. Schick, "Structure and nucleation of pores in polymeric bilayers: A Monte Carlo simulation," *J. Chem. Phys.*, vol. 105, pp. 8282–8292, 1996.

[89] A. Aguado, M. Wilson, and P. A. Madden, "Molecular dynamics simulations of the liquid–vapor interface of a molten salt. I. Influence of the interaction potential," *J. Chem. Phys.*, vol. 115, no. 18, pp. 8603–8611, 2001.

Results: Chapter 2

Computer simulation study of surface wave dynamics at the crystal–melt interface.

Jorge Benet, Luis G. MacDowell and Eduardo Sanz

Departamento de Química Física, Facultad de Ciencias Químicas, Universidad Complutense de Madrid, 28040 Madrid, Spain

Journal of Chemical Physics, ***141****, 024307 (2014)*

2.1 Abstract

We study, by means of computer simulations, the crystal-melt interface of three different systems: hard-spheres, Lennard Jones and the TIP4P/2005 water model. In particular, we focus on the dynamics of surface waves. We observe that the processes involved in the relaxation of surface waves are characterized by distinct time scales: a slow one related to the continuous recrystallization and melting, that is governed by capillary forces; and a fast one which we suggest to be due to a combination of processes that quickly cause small perturbations to the shape of the interface (like e. g. Rayleigh waves, subdiffusion, or attachment/detachment of particles to/from the crystal). The relaxation of surface waves becomes dominated by the slow process as the wavelength increases. Moreover, we see that the slow relaxation is not influenced by the details of the microscopic dynamics. In a time scale characteristic for the diffusion of the liquid phase, the relaxation dynamics of the crystal-melt interface of water is around one order of magnitude slower than that of Lennard Jones or hard spheres, which we ascribe to the presence of orientational degrees of freedom in the water molecule. Finally, we estimate the rate of crystal growth from our analysis of the capillary wave dynamics and compare it with previous simulation studies and with experiments for the case of water.

2.2 Introduction

The crystal-melt interface (CMI) has a great relevance in materials science given that its properties have a strong influence in crystal nucleation and growth, as well as on wetting phenomena [1, 2]. Despite its importance, the CMI is far less understood than the fluid-fluid interface because the former is difficult to probe with standard experimental techniques like X-ray diffraction [3]. For example, it is well known that the interfacial tension of liquid water at ambient conditions is 72 mN/m, whereas the reported values for the ice-water interfacial free energy at ambient pressure range from to 25 to 35 mN/m [4]. Also the dynamics of the fluid-fluid interface is far better understood than that of the CMI [5, 6]. Understanding the dynamics of the CMI is of great interest given that it can provide valuable insight to the important process of crystal-growth [7, 8].

The CMI interface is not flat, but rather exhibits relatively large undulations of the local interface position, or surface waves (SW), as a result of thermal excitations (see online movie [9]). For length scales below the capillary length, SW are mainly governed by the interfacial stiffness and are known under the name of capillary waves (CW). The equilibrium and dynamic properties of CW at the fluid–fluid interface have a long history and were already studied by Smoluchowski and Kelvin [10, 11]. For the CMI, the study of the CW spectrum provides static properties, like the interfacial stiffness or the interfacial free energy [12, 13].

At smaller length scales and higher frequencies, the surface of elastic media exhibit thermal excitations known under the name of Rayleigh waves [14]. These are small amplitude, high frequency perturbations that result from the elastic response of the solid.

Rayleigh and CW serve as a benchmark for the study of other surface phenomena in more complex materials. For example, polymer solutions and polymer gels, which are able to support both elastic and viscous response, exhibit a crossover from capillary to elastic SW [15, 16, 17]. The CMI also appears as an interesting system for the observation of SW. The solid phase is elastic and could in principle exhibit Rayleigh waves, while the fluid phase is viscous and could rather favour CW.

Unfortunately, despite the fair amount of theoretical research in the field, there seems to be no appropriate theoretical framework for the study of crystal-melt SW dynamics. Pleiner, Harden and Pincus extended the Rayleigh theory in order to incorporate the viscoelastic response of polymeric materials, but did not consider polymers in contact with a viscous dense phase [18, 19]. The theory was later extended to study a dense fluid on an elastic medium, but capillary forces were neglected [20]. On the contrary, Jeng et al extended the Kelvin theory to study SW at the interface of two dense fluids, but did not incorporate the elastic response of the solid [6]. A suitable theoretical framework is in principle that of Baus and Tejero, who considered SW at the

interface of two fluids baring simultaneously viscous and elastic response. However, the final results were worked out only for the special case of a vapour-liquid interface where one of the phases has negligible viscosity [21, 5].

An alternative rather different approach to study interfacial fluctuations of the crystal-melt interface is employed in the field of crystal growth. The emphasis here is on the hydrodynamic equations of heat and mass transport, and energy dissipation is enforced by introducing gaussian random noise. In the limit of small temperature gradients, this formalism provides a diffusion equation for the interface height fluctuations, and hence a strongly damped interface dynamics [7, 8, 22].

Computer simulations (see e.g. Ref. [23] and references therein) and experiments of colloidal systems [13] have also been used to investigate the CMI. Both approaches allow for the visualization of the CMI at a single-particle scale. Therefore, these techniques are highly suited to improve our understanding of the CMI. Many studies are devoted to obtain relevant static properties of the interface, such as the stiffness or the interfacial free energy, by means of an analysis of the spectrum of interface fluctuations (e.g. [12, 23, 24, 25, 26, 27]). The interfacial free energy can also be obtained by other methods like thermodynamic integration [28, 29, 30, 31, 32], metadynamics [33], or by combining classical nucleation theory with simulations [34, 35, 36]. The study of dynamic properties of the CMI, by contrast, has not received that much attention. The dynamics of the CMI has only been investigated by means of computer simulations for metal models [8] and hard spheres [22], and experimentally for colloidal suspensions [13]. Not only there are just a handful of works dealing with the dynamics of the CMI but the results are in some cases contradictory. For instance, in simulation studies [22] a quadratic dependency of the relaxation frequency with the wave vector is observed whereas the experimental work of Ref. [13] claims that such dependency is instead linear.

Motivated by the importance of gaining a deeper understanding on the dynamics of the CMI we pursue in this paper a computer simulation study of the relaxation of SW for the CMI of three archetypal systems, namely hard spheres (HS), Lennard Jones (LJ) and water. We show that the relaxation of crystal-melt SW is well described by a double exponential given that there are different processes, characterised by different time scales, involved in such relaxation. As the wavelength increases only one process, the relaxation of CW, is observed. We also show that the details of the microscopic dynamics are not important for the relaxation of crystal-melt CW. Moreover, we compare the relaxation dynamics of SW for systems composed of molecules with (water) and without (LJ and HS) orientational degrees of freedom. Finally, following the methodology proposed in Refs. [7, 8], we estimate the kinetic coefficient (the proportionality constant between the speed of crystal growth and the supercooling) from our measurements of the CW relaxation dynamics, and compare our results with independent measurements of such parameter.

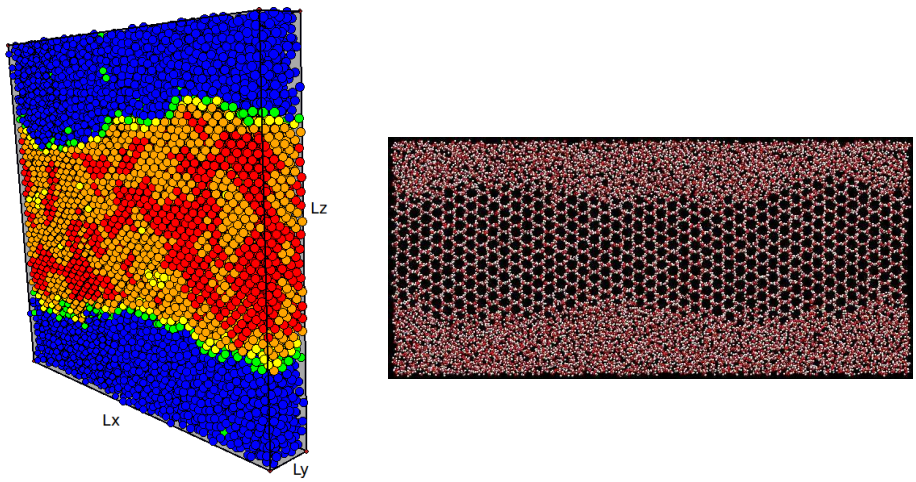

Figure 2.1. Snapshots of the initial configuration for one of the LJ (left) and one of the water systems studied (right). In the LJ system particles are coloured according to the extent to which their local environment resembles that of an fcc lattice (in decreasing order of fcc-like character: red, orange, yellow, green and blue).

2.3 Methods

We simulate a solid in equilibrium with its melt and characterize the dynamics of the SW. To do that we first generate an initial configuration, then simulate the system at coexistence and finally analyze the trajectories generated in our simulations. Below we give some details about this procedure.

2.3.1 Generation of the initial configuration

The first step consists in creating an initial configuration. Snapshots of an initial configuration for LJ and water are given in Fig. 2.1. In the snapshot corresponding to the LJ system we show the way we refer to the edges of the simulation box, L_x, L_y and L_z. By preparing systems as indicated in Fig. 2.1 we study the dynamics of the CMI for the crystal face exposed in the x-y plane and SW propagating along the x direction. This sort of box geometry has already been used in a number of simulation studies of the CMI (see, e. g., Refs. [12, 24, 25, 37]). To specify the crystal orientation we indicate in parenthesis the Miller indexes of the interfacial plane $(x-y)$, and in square brackets the Miller indexes of the crystalline plane parallel to the direction of propagation and perpendicular to the interface $(x-z)$.

In Table 4.2 we summarize the orientation and the size of the systems investigated.

To generate the initial configuration we first start by equilibrating the solid phase

Model	Orientation	L_xxL_yxL_z (σ^3)	Molecules
HS	(100)[001]	47.046x4.705x47.046	10256
	(110)[001]	44.359x4.705x52.058	10726
LJ	(100)[001]	49.101x6.336x49.181	14748
	(111)[11$\bar{2}$]	50.524x6.7313x49.292	16160
TIP4P/2005	(basal)[prismI]	59.418x5.710x29.541	10112
	(prismI)[basal]	57.024x6.962x25.581	10240
	(prismII)[prismI]	58.150x5.710x26.569	8896
	(prismII)[basal]	56.959x6.979x26.552	10670

Table 2.1. Orientation and size of the systems investigated.

with an NpT simulation at the coexistence pressure and temperature. For the equilibration of ice, ordinary Monte Carlo moves were supplemented with full ring reorientation in order to properly sample the hydrogen bond network [38, 39]. The final snapshot of the bulk solid thus equilibrated is rescaled so that the density matches the average equilibrium density. It is important to set L_x and L_y equal to their respective equilibrium values to avoid the solid being stressed in the x-y plane [40]. Then, a configuration of the fluid phase is equilibrated in an Np_zT simulation in a box with the same edges L_x and L_y as the equilibrated solid. In the Np_zT ensemble the pressure is exerted along the z direction. In this way, the box keeps the sides L_x and L_y fixed so it can be subsequently glued to the equilibrated solid along the x-y plane. The fluid is equilibrated at the coexistence temperature and at a pressure higher than the coexistence pressure. After equilibration of the fluid, we bring the solid and the fluid boxes together and remove the fluid particles that are less than a diameter apart from any solid particle. This causes a small drop in the fluid's density, which is partly compensated by the fact that the fluid was equilibrated at a pressure higher than the coexistence pressure. Finally, the system is further equilibrated in the Np_zT ensemble at the coexistence temperature and pressure to ensure that the fluid's density fully relaxes to its coexistence value. The overall density of the initial configuration thus generated must lie in between the densities at coexistence of the liquid and the solid (in Table 2.2 we summarize the coexistence conditions for the three models investigated).

2.3.2 Simulation details

Once we have an initial configuration, production runs are carried out in the NVT ensemble. Given that the overall density of the system lies in between the coexistence

Property	HS	LJ	TIP4P/2005
T	-	1.0 ϵ/k_B	252 K
p	11.54 $k_BT\sigma^{-3}$	4.95 $\epsilon\sigma^{-3}$	1 bar
ρ_c	1.0369 σ^{-3}	1.005 σ^{-3}	0.921 gcm^{-3}
ρ_l	0.9375 σ^{-3}	0.923 σ^{-3}	0.993 gcm^{-3}

Table 2.2. Coexistence values for the temperature, the pressure and the density for the different models. The values for the HS, LJ, and TIP4P/2005 models were taken respectively from Refs. [41], [32] and [42].

densities of the two phases, the interface is stable in an NVT simulation at coexistence temperature.

In principle, NVE simulations provide correct trajectories that preserve local momentum conservation and yield correct hydrodynamics. However, temperature control on long NVE simulations is difficult, particularly for systems exhibiting two phase coexistence. Of course, a sufficiently small time step can always be chosen that will garantee numerical stability in a single, long NVE run, but this would result in prohibitively large CPU time. A possible strategy would be to obtain independent configurations of the crystal-melt interface in a long NVT simulation and use such configurations for short production runs in the NVE ensemble. However, we find we can obtain correct results just from the long NVT simulation (see Appendix C) by using a recently developed version of the velocity-rescaling thermostat due to Bussi, Donadio and Parrinello [43]. Such thermostat, perturbs the dynamics gently by effectively rescaling the velocities over a large period and has met wide acceptance. Theoretical and numerical studies show that this thermostat requires close to minimal perturbation of the correct time evolution for given thermostating performance [44]. In practice, Bussi et al. have shown that this algorithms provides diffusion coefficients that are insensitive to the thermostating relaxation time chosen in a range spaning several orders of magnitude. Similarly, Delgado-Buscalioni et al. note that a thermostat with a sufficiently large thermalising time provides capillary wave dynamics of the liquid–vapor interface that does not differ significantly from results performed in the NVE ensemble [45]. In order to be in the safe side, we employed relatively large relaxation times of $\tau = 1ps$ and $2ps$ for the Lennard-Jones and water systems respectively. The relatively large system sizes that are required to perform our study also help to achieve correct thermostatization with minimal perturation of the dynamics [43, 44]. Moreover, for the Lennard-Jones system we have checked that changing the relaxation time from $\tau = 1ps$ to $\tau = 100ps$ does not change our results.

For the HS model, production runs were carried out using both a conventional

Monte Carlo (MC) algorithm and an event driven molecular dynamics (MD) algorithm based on that provided in Ref. [46]. In order to have enough statistics we simulate ∼1000 trajectories starting from different initial configurations for MD simulations and ∼250 for MC. Every MD trajectory is run for $\sim 4 \times 10^6 (\sigma^2 m/k_B T)^{\frac{1}{2}}$, where σ is the particle diameter, m the mass and k_B the Boltzmann constant. For MC simulations we performed $1.5{\cdot}10^6$ MC cycles where each cycle consists in an attempt of centre of mass displacement per particle. The maximum displacement for the centre of mass was set to $3.8{\cdot}10^{-2}\sigma$. In each trajectory (both MD and MC), 150 configurations were saved in a logarithmic time scale to perform the subsequent analysis.

To simulate water we used the MD GROMACS package [47, 48] and the TIP4P/2005 water model [49]. The time step for the Velocity-Verlet integrator was fixed to 0.003 ps and snapshots were saved every 75 ps. Simulations were run for a total time of $\sim 0.5\mu s$. The temperature was set to 248.5 K. At this temperature, very close to the melting value of 252 K reported in Ref. [49], we found no significant drift of the average height of the ice-water interface.

The LJ system was simulated using the MD GROMACS package. We use the truncated and shifted LJ potential proposed by Broughton and Gilmer [50]. We simulate the GROMACS implementation for Ar: $\sigma = 3.405$ Å, $\epsilon/k_B = 119.87$K, $m = 6.69 \cdot 10^{-26} kg$. The time step for the Velocity-Verlet integrator was fixed to 0.01 ps and snapshots were saved every 2 ps for a total simulation time of 0.1 μs.

For the case of HS we performed several independent short trajectories, whereas for water and LJ we opted for running just one long simulation for each investigated interface.

In order to be able to compare the relaxation dynamics of the different simulated systems in the same time scale we define the following dimensionless time: $t^* = t6D/\sigma^2$, where D is the diffusion coefficient of the fluid at coexistence. The ratio $\sigma^2/(6D)$ is the average time it takes for a fluid particle to diffuse its own diameter and we refer to it as "diffusive time". Therefore, t^* indicates the number of times a fluid particle diffuses its own diameter. For the self diffusion coefficient of the fluid at coexistence we use $D = 0.024(k_B T \sigma^2/m)^{1/2}$ for the HS model with event driven MD [51], $D = 1.456 \cdot 10^{-5}\ \sigma^2$/cycle for the HS model with MC simulations, $D = 3.87 \cdot 10^{-3}\ \sigma^2 ps^{-1}$ for the LJ model (in good agreement with the value reported in Ref. [52]), and $D = 0.3865\ nm^2 ns^{-1}$ for the TIP4P/2005 model.

2.3.3 Dynamics of the surface waves

As shown in Fig. 2.1, the CMI of the systems here investigated is wavy. The purpose of this work is to characterize the dynamics of such waves. To do that we first define the local interface position, or interface profile $h(x_n)$, at discrete positions x_n along the x direction (see below for further details).

The interface profile is then Fourier transformed, and Fourier modes h_q defined as:

$$h_q = \frac{1}{N}\sum_{n=1}^{N} h(x_n) e^{iqx_n} \tag{2.1}$$

where N is the number of discretization points along the L_x side of the simulation box, and each wave mode is associated with a reciprocal space vector, q, that can take values $q = 2\pi k/L_x$, where k is a positive natural number. Small q vectors correspond to wave modes with a large wave length and viceversa.

The time-dependent autocorrelation function of h_q is then given by:

$$f_q(t) = \frac{\langle h_q(0) h_q(t)^* \rangle}{\langle h_q(0) h_q(0)^* \rangle}. \tag{2.2}$$

This function gives information about the way a capillary wave mode relaxes. It depends not only on q, but also on the orientation of the crystal with respect to the fluid: $f_q(t) \equiv f(t, q, (h, k, l), [m, n, o])$. In this paper we analyze the q-dependence of $f_q(t)$ for three different models and for several orientations.

2.3.4 Determination of the interface profile, $h(x_n)$

The definition of a suitable interface profile from a set of atomic positions is a subttle matter [53, 54]. It is now well understood that the evaluation of the function $h(x_n)$ consistent with the capillary wave model requires to properly identify the phase to which atoms may be attributed, and only then, searching for an optimal surface separating each phase [53, 54]. Whereas the optimal process is involving and time consuming [54], it has been observed that dynamic properties are rather insensitive to details of the specific procedure [45]. For this reason, we have chosen a simple method, inspired on that proposed in Ref. [24], that is computationally convenient and is very robust to the arbirary parameters required in practice (c.f. section 2.4.3).

To obtain the discrete function $h(x_n)$ describing the profile of the interface along the x direction we consider the outermost particles of the crystal slab. We first label the molecules in the system as fluid-like or solid-like. To do that we make use of local bond order parameters that are able to distinguish between fluid and solid-like particles in an instantaneous configuration by looking at the relative position of a particle with respect to its neighbours (see Appendix A for details).

Once all molecules are labelled, we remove the fluid-like particles and among all solid-like particles (red, orange, and yellow in Fig. 2.1 (top)) we take those that form the largest cluster. In this way we are left with the crystal phase alone. Note from Fig. 2.1 that due to the geometry of the system we have two independent interfaces. We explain below how we calculate $h(x_n)$ for one of them.

We start by splitting L_y in two, so the interface is divided in two elongated stripes. Each stripe is divided in N equispaced points along L_x. These points define the set of x_n values in which $h(x_n)$ is evaluated. For a point with coordinates (x_n, y_p), with $p = 1, 2$ indicating a given stripe, the local amplitude $h(x_n, y_p)$ is evaluated by averaging the z coordinate of the n_o outermost atoms with y coordinate $\in [y_p - L_y/4 : y_p + L_y/4]$ and x coordinate $\in [x_n - \Delta_x/2 : x_n + \Delta_x/2]$ (Δ_x and n_o are adjustable parameters). In this way, a function $h(x_n, y_p)$ is obtained for each stripe, and the final $h(x_n)$ is obtained as the average between the stripes corresponding to y_1 and y_2.

Thus, the adjustable parameters to obtain a discretized profile of the interface in the way above described are N, Δx, and n_o. The results shown in the remaining of the paper correspond to the following set of analysis parameters: $N = 50$, $\Delta x = 3\sigma$ and $n_o = 4$. In section 2.4.3 we show that our main results are not affected by this particular choice of analysis parameters.

2.3.5 Interfacial stiffness

To test our simulations we make use of the following expression provided by Capillary Wave Theory [55, 56]:

$$\left\langle |h_q|^2 \right\rangle = \frac{k_B T}{A \widetilde{\gamma} q^2} \tag{2.3}$$

that relates the average squared amplitude of the capillary wave mode q, $\langle |h_q|^2 \rangle$, to the interfacial stiffness, $\widetilde{\gamma}$, by means of the equipartition theorem (note from Eq. 2.2 that $\langle |h_q|^2 \rangle$ is equal to the unnormalized $f_q(0)$). In the equation above k_B is the Boltzmann constant and $A = L_x L_y$ is the area of the interface. The interfacial stiffness has been carefully obtained for a number of systems [24, 25, 26, 27], with the HS model among them. Therefore, we can double-check our results by comparing our value for $\widetilde{\gamma}$ with that obtained in Refs. [24, 27].

2.3.6 Kinetic coefficient

An important parameter in crystal growth is the kinetic coefficient, μ. The kinetic coefficient of a CMI is the proportionality constant between the speed at which the interface front advances, v, and the supercooling, ΔT:

$$v = \mu \Delta T \tag{2.4}$$

where $\Delta T = T_m - T$ is the the difference between the melting temperature, T_m, and the temperature of interest, T.

As shown in Refs. [7, 8], by analysing the crystal-melt CW, it is possible to obtain an estimate of μ. The method entails first obtaining $f_q(t)$ via Eq. 2.2 for a number of

q-modes, then fitting each $f_q(t)$ to an exponential function of the type $\exp(-t/\tau_q)$ to get a characteristic decay time τ_q for each mode, and finally obtaining μ from the slope of a representation of $1/\tau_q$ vs q^2:

$$1/\tau_q = \frac{\mu\widetilde{\gamma}T_m}{\Delta h_m \rho} q^2, \tag{2.5}$$

where Δh_m is the molar melting enthalpy, ρ is the crystal density, and $\widetilde{\gamma}$ is the stiffness, that can be obtained via Eq. 5.2 by extrapolating $\widetilde{\gamma}(q)$ to $q = 0$.

Following this method, in this work we compute the kinetic coefficient for all the interfaces investigated. We compare our results for HS with those obtained in Ref. [22] using the same technique, and our results for water with those obtained in a recent publication using a different approach [57].

2.4 Results and discussion

2.4.1 Dynamics of crystal–melt surface waves

For each system described in Table 4.2 we evaluate $f_q(t)$ (Eq. 2.2) for several values of q. Some of these autocorrelation functions are shown in Fig. 3.12 (a), (b) and (c) for a HS, an LJ and a water CMI respectively. As expected, the correlation functions decay from 1 to 0 as the wavemodes relax, and the relaxation for a given interface is the slower the smaller the wave vector q (or the larger the wavelength). It is also apparent that for the wavelengths studied, the surface wave dynamics corresponds to a strongly damped regime, with no signs of oscillatory behaviour in any of our the autocorrelation functions.

This is consistent with previous simulation studies of the CMI, where the decay of the correlation functions were found to be purely exponential, or at least showed a purely monotonous decay [23, 22]. Taking this into account, we first attempt to describe the correlation functions by a single pure exponential $f_q(t) = e^{-t/\tau_{exp}}$, where the characteristic decay time τ_{exp} is the only fitting parameter. However, as seen in Fig. 3.12 (a) (dashed blue curves), an exponential fit does not accurately describe the decay of $f_q(t)$, particularly for curves corresponding to large qs.

Considering that SW could exhibit very different behaviour at high and low frequencies, we then attempted to fit our results using a double exponential:

$$f_q(t) = Ae^{-t/\tau_{ds}} + (1 - A)e^{-t/\tau_{df}}, \tag{2.6}$$

where A, τ_{ds} (characteristic time for a slow relaxation process) and τ_{df} (characteristic time for a fast relaxation process) are the fitting parameters. As it can be seen in Fig.

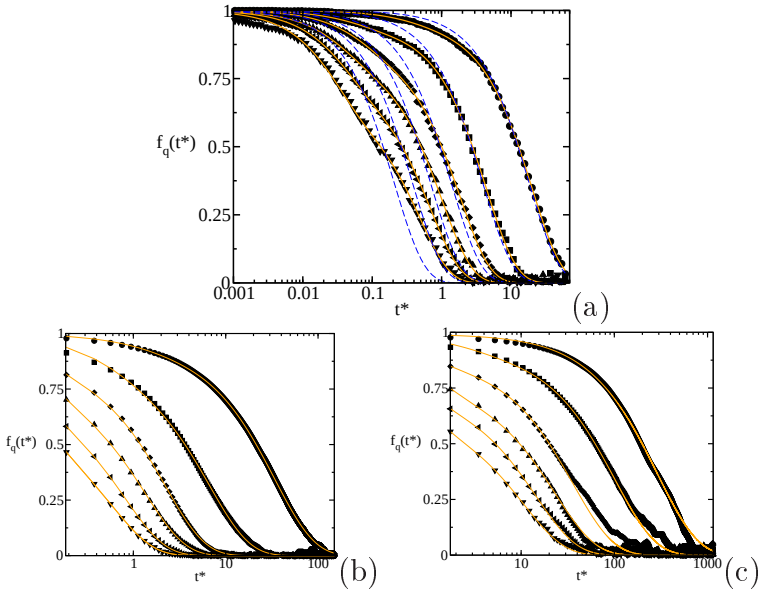

Figure 2.2. (a)-(c), symbols: autocorrelation functions for the HS (100)[001], the LJ (100)[001], and the water (pII)[basal] interfaces respectively (all data correspond to MD simulations). In a given plot, curves from right to left correspond to wavevectors $q = 2\pi k/L_x$, with $k \leq 6$. Lines correspond to different fits: dashed blue to a single exponential, and solid orange to a double exponential.

3.12 (a) (orange solid lines) this fit accurately describes all curves and is significantly better than a single exponential (we also tried fitting our results to a stretched exponential, but the resulting fit was not as good as that of a double exponential and is not shown). The double exponential fit does a good job for all systems investigated. To illustrate this, in Figs. 3.12(b) and (c) we show the correlation functions alongside their corresponding double exponential fits for the LJ (100)[001] and the water (pII)[basal] interfaces respectively. For the case of water the simulations are slower than for the other systems and gathering statistics to obtain quality data for $f_q(t)$ at long times is a very involving task. As a consequence, the values of $f_q(t)$ for the ice-water interface at long times are rather noisy and have not been taken into account to obtain the fits shown in Fig. 3.12(c).

The adequacy of the double exponential fit suggests the existence of two distinct relaxation time scales: a fast one responsible for the initial decay and a slow one responsible for the decay at long times. The presence of two simultaneous relaxation time scales resembles the behaviour observed at the interface of viscoelastic materials [5, 18, 19, 15, 16, 17], where a high frequency relaxation process is related to elastic Rayleigh waves, while that of low frequency is related to CW. Indeed, it has been shown that both elastic Rayleigh waves and capillary Kelvin waves may exhibit an overdamped regime where oscillations are completely suppressed and the relaxation is exponential

[5]. By analogy, we assume in principle that the two different time scales found in our study for the CMI are associated to different relaxation mechanisms.

The parameter $A \in [0:1]$ in Eq. 2.6 quantifies the weight of each mechanism in the relaxation of CMI waves. When A is close to 1 the decay of $f_q(t)$ is dominated by the slow process and when it approaches 0.5 the decay of $f_q(t)$ is affected by both slow and fast processes. In Fig. 2.3 we plot A as a function of q for all systems investigated. In all cases A is close to 1 for the smallest q investigated and decreases as q increases. Therefore, we observe a relaxation essentially dominated by the slow process at low q (large wavelengths) and affected by both slow and fast processes at large q (small wavelengths).

We first attempt to elucidate the nature of the slow relaxation process by analysing the dependence of τ_{ds} on q. By carefully fitting our autocorrelation functions $f_q(t)$ to Eq. 2.6 we obtain $\tau_{ds}(q)$ (Note that obtaining meaningful parameters from a double exponential fit is not trivial. We had to address this issue carefully and give some indications of the fitting procedure in Appendix B). In Fig. 2.4 (a) we represent τ^*_{ds} versus q for all interfaces investigated. In a double logarithmic scale it appears that all curves are parallel to each other within the accuracy of our calculations. This suggest the existence of a power law of the type $\tau_{ds} \propto q^{\alpha}$, with the α exponent common to all systems. A power law is an indication that there is a common mechanism underlying the slow relaxation process of all interfaces investigated. This is remarkable taking into account the different nature of the systems here studied. A visual inspection of the relaxation of large wavelength SW, those more clearly affected by the slow process, suggests that such process can be identified with the continuous recrystallization and melting taking place at the interface (see online movie [9]).

In 1993 Karma published a theory for the relaxation dynamics of crystal-melt CW based on a diffusion equation of the interfacial profile [7]. Karma's theory predicts a power law relation between a characteristic relaxation time and q. The obtained theoretical value for the exponent is $\alpha = -2$. In Fig. 2.4 (a) we include a dashed line with slope -2 in the double logarithmic representation. Within the accuracy of our calculations all curves look parallel to the dashed line. Therefore, the dynamics of the slow process is consistent with Karma's theory [7]. This implies that we can identify the slow process with the relaxation of CW. In other words, the slowly relaxing SW are in fact CW. The description of the relaxation of CW via a diffusion equation in Ref. [7] is consistent both with the view inferred from our movies that the slow process is due to the recrystallization/melting at the interface and with the absence of oscillations in our $f_q(t)$s.

The theory of Karma has been previously tested in simulations of metals [8, 23, 58, 59] and HS [22]. In these works it was suggested that the relaxation of crystal-melt SW can be approximated by a single exponential for all qs. Our results above show that the scenario is more complex due to presence of fast relaxation processes that clearly

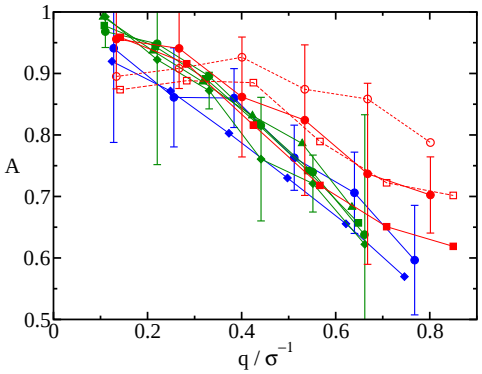

Figure 2.3. Prefactor for the double exponential fit (see main text) as a function of q for all systems investigated. HS, LJ and water data are shown in red, blue and green respectively. HS data are shown for the (100)[001] (circles) and (110)[001] (squares) interfaces; LJ for the (100)[001] (circles) and (111)[11$\bar{2}$] (diamonds) interfaces; and water for the (basal)[prismatic I] (triangles), (prismatic I)[Basal] (circles), (prismatic II)[prismatic I] (squares) and (prismatic II)[basal] (diamonds) interfaces. For the HS system filled (empty) symbols and solid (dashed) lines correspond to MD (MC) simulations. Error bars are shown for one of the orientations of each model potential. Different orientations of the same model have similar error bars but have not been shown for clarity.

affect large q modes.

We can gain further insight into the nature of the slow process by studying the relaxation of the HS CMI with MC simulations. In Fig.2.4 (a) we compare the slow relaxation times, in diffusive units, of HS as obtained by MD and MC simulations. The data coming from both simulation techniques lie on top of each other. The agreement between both simulation techniques is further confirmed in Fig. 2.5, where we compare the whole autocorrelation function for several qs. The superimposition between MC and MD curves in diffusive time units points out the relevance of the diffusive time scale for the relaxation of CMI SW. Moreover, we can tell from the good agreement between MC and MD that the microscopic dynamics is not playing any significant role in the relaxation of CMI CW. This finding strongly contrasts with the case of the fluid-fluid interface [6, 45], although it not so surprising if one takes into account that the crystal has an infinitely large viscosity.

As mentioned in the introduction, we are not aware of a hydrodynamic theory of CW for the CMI. For lack of a better theoretical framework, we discuss here our observations in the context of the CW theory for either a dense or a viscoelastic medium with air [5, 6, 11]. Such systems present first a weakly damped regime at low q, with a damped oscillatory behavior of frequency $\omega \propto q^{3/2} + iq^2$ (Kelvin waves). At larger wavelengths, there is a crossover to a strong damping regime, where the oscillations are completely supressed and the frequency becomes purely imaginary $\omega \propto iq$. In our simulations, we observe only a strongly damped regime, but, at odds with standard

theories for the liquid–vapor interface, the damping is not linear in q, but rather, decays as q^2. Our observation does not rule out the possibility of the aforementioned regimes occurring at smaller wavevectors than are accesible to our simulations. However, it is clear that the damping regime we observe is not the standard overdamped regime linear in q that has been reported elsewhere for the liquid-vapor interface [45]. Also note that a recent experimental study of the CMI of strongly repulsive colloids reported relaxation dynamics in agreement with a linear q dependence [13], but neither our results nor those of Ref.[22] seem to support this conclusion. Interestingly, Jeng et al. noticed in their hydrodynamic theory of surface waves a strongly damped regime with purely imaginary frequency which has both a quadratic and linear contribution in q. However, we do not observe any signature of mixed quadratic and linear dependence in our relaxation times either. Possibly, only a hydrodynamic theory incorporating both the viscous behavior of the liquid and a viscoelastic response of the crystal can predict the behavior observed in our simulations [5].

Fig. 2.4 (b) displays the characteristic times for the fast relaxation process, τ^*_{df}, as a function of the wave vector. For a given q, τ^*_{df} is one or two orders of magnitude lower than τ^*_{ds}. Both τ^*_{df} and τ^*_{ds} decrease as q increases. Altghouh the error bars for τ^*_{df} are quite large, it seems that a power law is not evident from Fig. 2.4 (b). This suggests that the fast relaxation can not be identified with a single process but rather with a combination of different ones. Such processes must be fast as compared to the diffusion of the interfacial front ($\tau^*_{df} << \tau^*_{ds}$) and must cause small perturbations in the interfacial profile (their effect vanishes as q goes to 0, as shown in Fig. 2.3). Having these characteristics in mind, processes such as Rayleigh SW, subdiffusion of the fluid, or the attachment/detachment of single particles to/from the crystal phase are likely to lie behind the fast relaxation of the interface.

In summary, the relaxation of SW is best described by a double exponential in the q-range analyzed in this paper. This is indicative of the existence of two distinct relaxation time scales. The slow one corresponds to the overdamped relaxation of CW by diffusion of the interfacial front (the counterpart of overdamped CW for the fluid-fluid interface, although with a different $\tau(q)$ dependence). The fast one is due to quick, small perturbations of the interface profile possibly caused by Rayleigh waves, subdiffusion, and the attachment/detachment of particles to/from the crystal. In the limit of $q = 0$ the decay of $f_q(t)$ can be entirely described by a single exponential function corresponding to the slow relaxation process.

We conclude this section by comparing the slow relaxation of different systems. Such comparison is enabled by the use of a common time unit: the diffusive time. It is evident from figure 2.4 (a) that the curves corresponding to water lie about an order of magnitude above those corresponding to LJ or HS. This implies that, for a given q, the water interface requires roughly ten times as much diffusive time units as LJ or HS particles in order for the interface to relax. For instance, for the smallest studied q

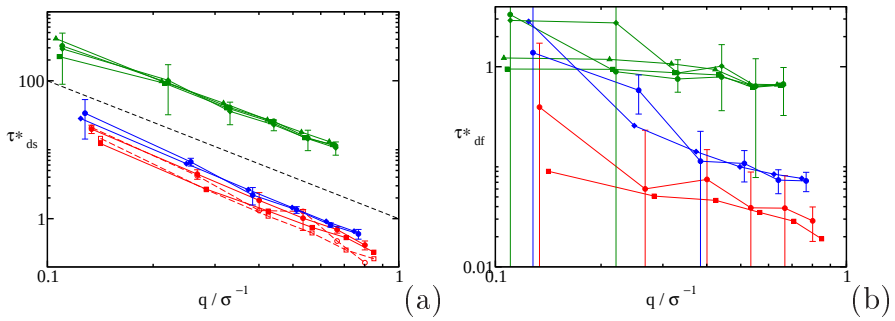

Figure 2.4. (a) Dimensionless characteristic time for the slow relaxation process, τ^*_{ds}, plotted against the wave vector q in a double logarithmic scale for all interfaces investigated. Color code same as in Fig. 2.3. (b) Same as (a) but for the fast relaxation process. The dashed line, included in (a) for visual reference, corresponds to a power law of the type $\tau_{ds} \propto q^{-2}$.

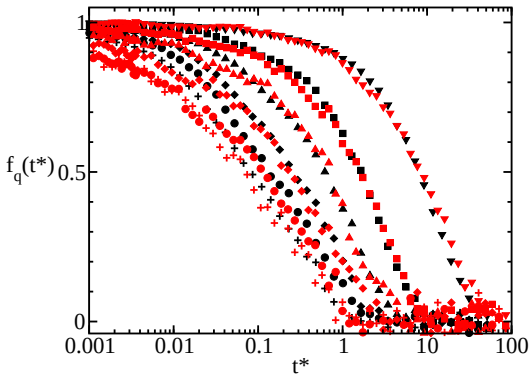

Figure 2.5. Autocorrelation functions for the (110)[001] HS interface obtained by MD (black) and MC (red) simulations. From right to left functions corresponding to wavevectors $q = 2\pi k/L_x$, with $k \leq 6$, are represented.

ice-water CW take to relax the time needed for a molecule to diffuse about 300 times its own diameter, while it only takes about 30 times for the LJ or the HS systems. This difference in time scales is most likely related to the fact that water molecules, contrary to the case of LJ or HS particles, have orientational degrees of freedom and need to be properly oriented to accommodate into the crystal phase.

2.4.2 Kinetic coefficient

As explained in Sec. 2.3.6, the kinetic coefficient, μ, can be estimated by measuring the autocorrelation function $f_q(t)$ for a few CW modes [7, 8]. Using this methodology Amini et al. estimated μ for the HS system [22]. In Fig. 2.6 (a) and (b) we plot the inverse of the relaxation time versus q for an interface of the HS system and compare our results (filled circles) with those of Ref. [22] (filled squares). From the slope of the plot shown

in Fig. 2.6 one can obtain μ via Eq. 2.5. (Alternatively, as shown in Fig. 2.6 (c), a representation of $\tau_{ds}q^2$ vs q gives a horizontal line from which μ can be obtained). As shown in Fig. 2.6, the agreement with Ref. [22] is quite satisfactory, which gives us great confidence in our calculations. The filled circles in Fig. 2.6 were obtained by fitting our $f_q(t)$s to Eq. 2.6 in order to get the characteristic time τ_{ds}. If we get the characteristic relaxation time by fitting $f_q(t)$ to a simple exponential function, disregarding the fact that there are two distinct time scales involved in the relaxation of crystal-melt SW, we get the empty circles in Fig. 2.6, that are not in good agreement with Ref. [22]. Although, to the best of our knowledge, the need of fitting $f_q(t)$ to a double rather than to a single exponential is pointed out for the first time in this work, previous studies that assumed a single exponential behaviour provide results that are consistent with ours [22]. This apparent contradiction is explained by the fact that in Ref. [22] the characteristic time was obtained from the slope of the linear regime in a plot of $\ln f_q(t)$ vs. t [22], which, for long times, gives the characteristic time for the slow relaxation process (note that eq. 2.6 can be approximated by a single exponential for long times given that $\tau_{ds} >> \tau_{df}$). Such decoupling between the fast and the slow process is less and less evident as the relaxation of the q modes becomes faster or, equivalently, as q increases. Therefore, in order to consider large qs for the calculation of μ from a plot like that shown in Fig. 2.6 it is advisable to use Eq. 2.6 to obtain the characteristic time for the slow relaxation process. In fact, with our analysis we are able to extend the linear regime of $1/\tau_{ds}$ vs q^2 to larger qs than in Ref. [22].

In Fig. 2.6 (b) we show a $1/\tau_{ds}$ vs. q^2 representation for the LJ (left) and water (right) systems. All interfaces show, within the accuracy of our measurements, a linear dependency of $1/\tau_{ds}$ vs. q^2. This result had already been anticipated in Fig. 2.4 (all data sets are parallel to the dashed line). From the slopes in Fig. 2.6 we estimate the kinetic coefficients, which we report in Table 2.3. Since we reduce time by the diffusive time (see Sec. 2.3.2) and distance by the particle diameter, the kinetic coefficient in our reduced units tells us how faster the interface advances, in terms of diameters per diffusive time, when the temperature is lowered by 1 K. The data in Table 2.3 reveal that the kinetic coefficient of water is more than an order of magnitude lower than that of LJ. This means that one would need to supercool water ten times more than LJ to get the same speed-up of the interface advance measured in diameters per diffusive time. Our work shows that both the relaxation and the growth of the interface are dramatically slowed down for the case of water, probably due to the role of orientational degrees of freedom in crystallization.

We can also compare our results for water with experimental [60] and simulation [57, 61] measurements of the speed of crystal growth, v. Using Eq. 2.5 and knowing that $v = 0$ for $\Delta T = 0$ we can estimate v *in the vicinity* of the melting temperature from our calculated μ. In Fig. 2.7 we plot v versus the supercooling, ΔT, for the basal plane of water, for which we obtained a kinetic coefficient $\mu = 1.6\ cm/(sK)$.

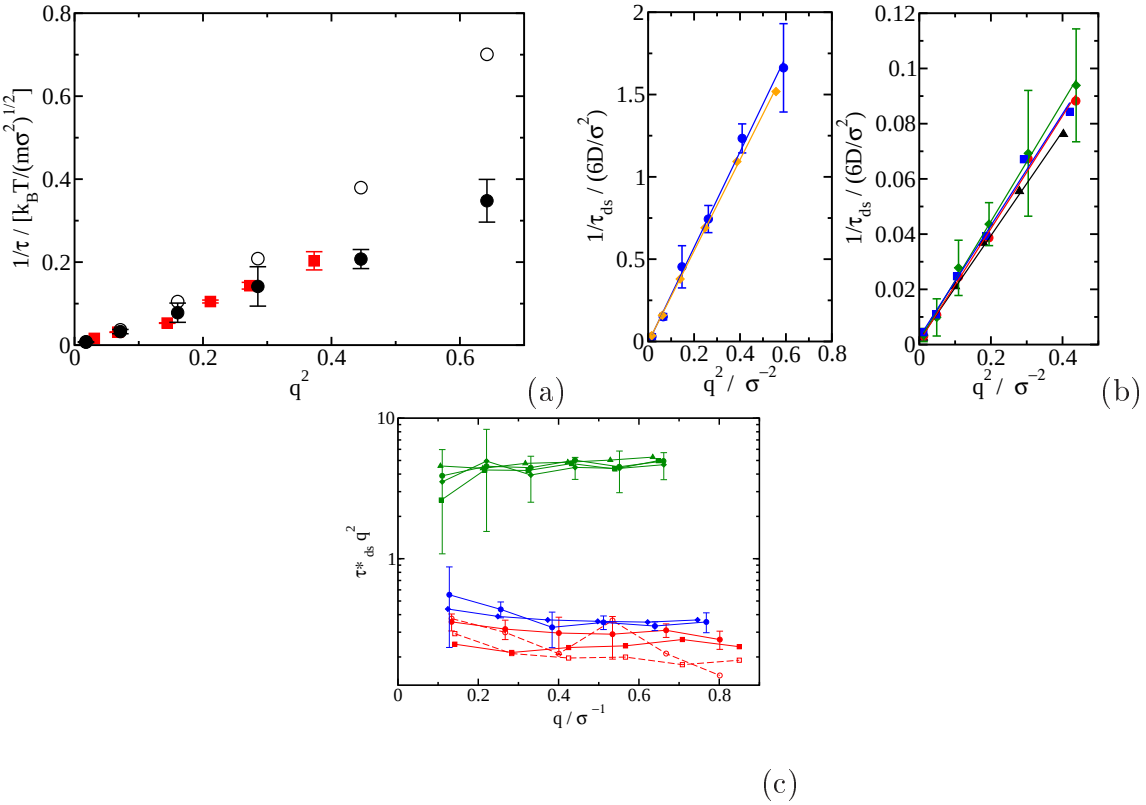

Figure 2.6. Plots of the inverse relaxation time versus q^2. From the slope of these plots the kinetic coefficient can be inferred via Eq. 2.5 [7, 8]. In (a) our results for the (100)[001] HS interface (circles) are compared to those reported in Ref. [22] (squares). Empty (solid) circles correspond to relaxation times estimated by fitting $f_q(t)$ to a single (double) exponential. In (b) we show our results for all interfaces investigated for the LJ (left) and the water (right) systems respectively. (c): $\tau^*_{ds}q^2$ as a function of q in a logarithmic scale for all interfaces investigated. Color code same as in Fig. 2.3.

Model	Orientation	$\mu/[6D/(\sigma K)]$
LJ	100	$(8 \pm 2)\cdot 10^{-2}$
	111	$(5.8 \pm 0.6)\cdot 10^{-2}$
TIP4P/2005	basal	$(2.1 \pm 0.3)\cdot 10^{-3}$
	prismatic I	$(3.0 \pm 0.4)\cdot 10^{-3}$
	prismatic II	$(2.5 \pm 0.5)\cdot 10^{-3}$

Table 2.3. Kinetic coefficient, μ, for the LJ and TIP4P/2005 systems.

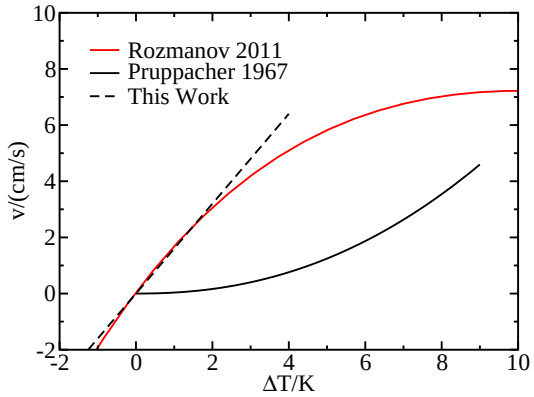

Figure 2.7. Rate of crystal growth versus supercooling. We compare our results (dashed line) with the simulation results of Rozmanov et al. [57] (red solid curve) and with experimental data by Pruppacher [60] (black solid curve).

Our results correspond to the dashed line in Fig. 2.6. A negative v means that the interface recedes because the crystal melts for $\Delta T < 0$. The red solid curve corresponds to the simulation results reported in Ref. [57] (large system), where $v(T)$ for the basal plane was measured by monitoring the height of the interface along time for different temperatures. Remarkably, our estimate of v around the melting temperature is in very good agreement with the results of Ref. [57], obtained by a completely different approach. It should be noted that the proportionality law of Eq. 2.5 only works for a narrow temperature range around melting. Outside that range, the dependence of v with ΔT is not linear any more and even shows a maximum at $\Delta T \approx 12\ K$ [57]. Our kinetic coefficients for the prismatic I, and prismatic II planes are $\mu = 2.2\ cm/(sK)$ and $\mu = 1.8\ cm/(sK)$ respectively. The latter is consistent with a recent simulation study of the speed of crystal growth for the prismatic II plane [61]. The comparison of the model with the experiment [60], solid black curve in Fig. 2.7, is not as satisfactory, though. The experimental v near coexistence is much lower than that predicted by the model. Further work is needed to understand why a model that gives a good agreement with the experiment for the rate of crystal nucleation [36] is not able to accurately predict the rate of crystal growth.

2.4.3 Robustness of our calculations

In order to check if our calculations are robust we asses the dependence of our results on both the choice of the analysis parameters and the system size. Moreover, whenever possible, we compare our results with the existing literature.

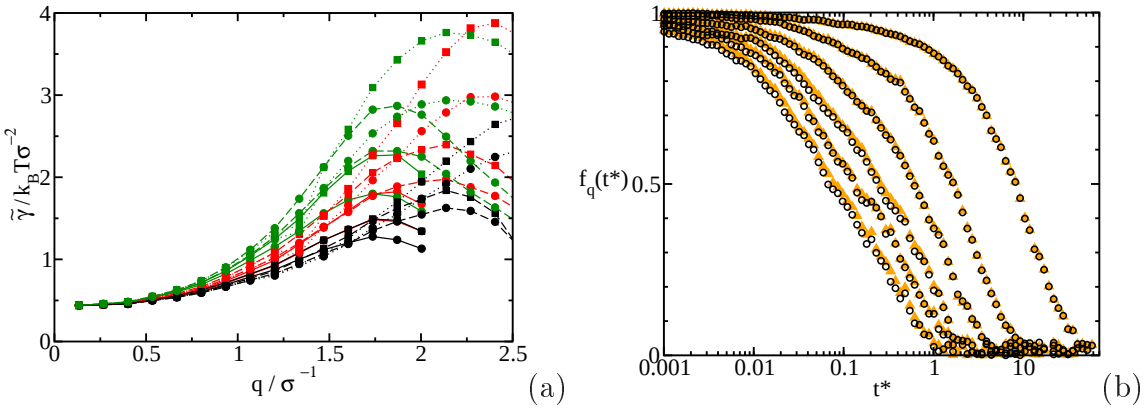

Figure 2.8. (a) Stiffness as a function of q using different parameters to locate the interface for the (100)[001] HS system. $\Delta x/\sigma = 2.0$ (black), 2.5 (red) and 3.0 (green); $n_o = 3$ (circles) and 4 (squares); $N = 30$ (continuous line), 40 (dashed line) and 50 (dotted line). (b) Autocorrelation function (Eq. 2.2) for the (110)[001] HS system using two different sets of parameters to locate the interface: $\Delta x = 3\sigma$, $n_0 = 4$ and $N = 50$ (black circles) and $\Delta x = 2\sigma$, $n_0 = 3$ and $N = 30$ (orange triangles). From right to left wavevectors $q = 2\pi k/L_x$, with $k \leq 6$.

Analysis parameters

The adjustable parameters to obtain a discretized profile of the interface in the way above described are N, Δx, and n_o. To assess the extent to which the choice of these parameters affects our results we calculate the interfacial stiffness via Eq. 5.2 for the HS system using different sets of parameters. As shown in Fig. 2.8 (a) the stiffness is independent on the parameter set for small qs, as we approach the thermodynamic limit. By contrast, for large qs (short wave lengths) $\widetilde{\gamma}$ becomes dependent on the analysis parameters. This dependence is a consequence of the fact that the length scale of the waves becomes comparable to that of the discretization grid for large qs. There are sophisticated ways of dealing with this issue [62], but for our purpose it is enough to stick to the q range where $\widetilde{\gamma}$ is independent of the analysis parameters (i. e., the six smallest wave vectors).

We also analyse the influence of the analysis parameters on the evaluation of the autocorrelation functions. In Fig. 2.8 (b) we compare $f_q(t)$ for the set of analysis parameters used in the main text ($\Delta x = 3\sigma$, $n_0 = 4$ and $N = 50$, black circles) and a completely different one ($\Delta x = 2\sigma$, $n_0 = 3$ and $N = 30$, orange triangles). Both sets of parameters give virtually identical $f_q(t)$s for the range of qs for which the dynamics has been investigated in this work ($q = 2\pi k/L_x$ for $k \leq 6$).

We have also analysed the effect that the order parameter to distinguish between crystal and fluid-like particles has in our results. In the main part of the paper we use for the LJ system the order parameter proposed in Ref. [64] with the specific parameter set given in Appendix A, whereas for the HS system we use the order parameter proposed in

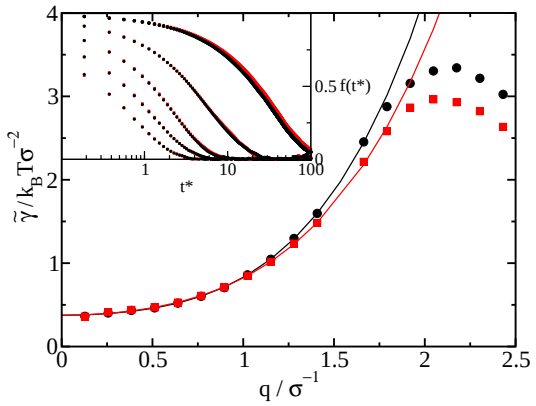

Figure 2.9. Main figure: stiffness of the (100)[001] LJ interface as a function of q for two different order parameters to distinguish between solid and liquid-like particles. Black circles correspond to the order parameter described in Appendix A and red squares correspond to that described in Ref.[63]. Inset: Autocorrelation functions obtained with both order parameters for different wave vectors.

Ref. [65] with the parameter set given in Ref. [63]. Both order parameters are inspired by Ref. [66] and are devised to distinguish an fcc lattice from the fluid, but the order parameter of Ref. [64] gives more importance to second nearest neighbors than that of Ref. [65]. Here, we recalculate the stiffness and the autocorrelation function of the LJ system with the order parameter and set of parameters used for the HS sytem. The comparison of the results obtained with both order parameters is shown in Fig. 2.9. Reassuringly, the results are not sensitive to the specific choice of the order parameter, provided, obviously, that the chosen order parameter is able to distinguish between the solid lattice (fcc in this case) and the fluid.

System size effects

In order to avoid simulating systems with a prohibitively large number of molecules and yet be able to probe small-q CW we use simulation boxes with one side significantly shorter than the others (see Fig. 2.1). This choice results in an elongated interfacial area. As shown in Ref.[25] it is advisable to check if the geometry of the simulation box introduces spurious effects in the surface wave dynamics. This is indeed a potential source of concern, since the very elongated systems employed are quasi 1–dimensional, and the behaviour of CW strongly depends on dimensionality.

In this section we provide some evidence that our choice for the shape of the simulation box does not affect our results.

To check if the typical system size we use in this work yields system-size-dependent results we take the (100)[001] LJ system and compare the results for the size reported in Table 4.2 (black circles in Fig. 2.10) with those obtained by making the short edge of

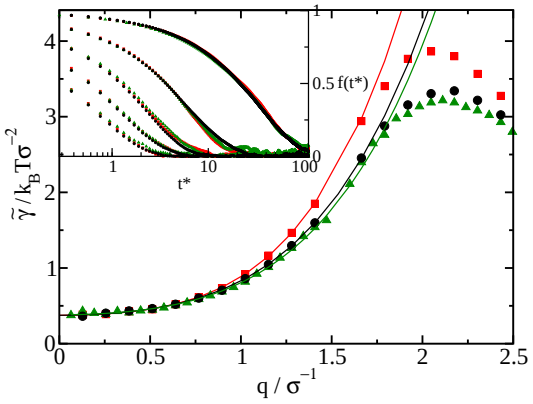

Figure 2.10. Main figure: effect of the interface area in the stiffness. Black circles represent the stiffness for the (100)[001] LJ system with L_x=49.101σ and L_y=6.336σ. Green triangles and red squares represent the stiffness for the same system but with L_x'=2L_x and L_y'=3L_y respectively. Inset: Autocorrelation function for the three systems and different wavevectors.

the interfacial area (y axis) three times longer (red squares in Fig. 2.10). We compare both the stiffness (main Fig. 2.10) and the dynamic autocorrelation function (inset Fig. 2.10) for different wavevectors. Clearly, the typical size for the short axis of the simulation box used in this work causes no significant finite size effects for the q-range we have considered for the analysis of the dynamics ($q = 2\pi k/L_x$ for $k \leq 6$). In Fig. 2.10 we also compare with the results obtained by doubling the long edge (x-axis) of the interfacial area (green curve). Again, no significant finite size effects are seen.

It is important to note, however, that in order to avoid system size artifacts, one must study the dynamics of the laterally averaged interface positions $h(x_n)$. On the contrary, studying the dynamics of the stripes $h(x_n, y_p)$ provides results that are strongly system size dependent.

Consistency with previous results

In the discussion above we have already shown that our results are consistent with previous studies. For instance, in Fig. 2.6(a) we show that we obtain the same kinetic coefficient as in Ref. [22] for HS. Moreover, in Fig. 2.7 we show that our estimate for the rate of crystal growth of ice is in good agreement with Ref. [57], where this quantity is calculated through a completely different approach. To further validate our methodology we show our results for the interfacial stiffness $\widetilde{\gamma}$ by means of Eq. 5.2 for two different orientations of the HS system (See Fig. 4.7) and compare it with previously reported values [24, 27]. The comparison is shown in Table 2.4. Our results are in good agreement with the literature. Moreover we obtain, as expected for an equilibrium property as $\widetilde{\gamma}$, a good agreement between MC and MD. Therefore, the way in which we simulate and

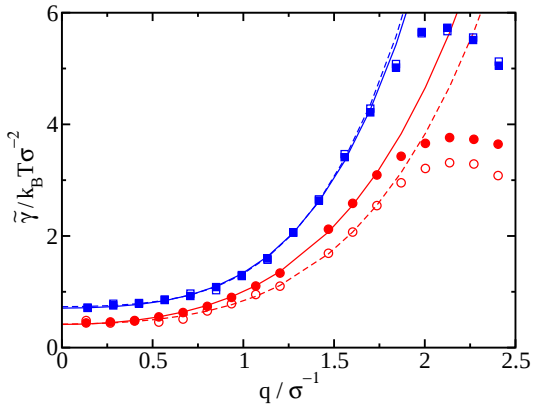

Figure 2.11. Stiffness as a function of q for the HS system and two different orientations: (100)[001] (circles) and (110)[001] (squares). MC and MD results are shown with open and filled symbols respectively. The extrapolation of $\widetilde{\gamma}(q)$ to $q = 0$ in order obtain $\widetilde{\gamma}$ was made by fitting $\widetilde{\gamma}(q)$ to $\widetilde{\gamma} + aq^2 + bq^4$ for small qs, where a and b are fitting parameters. The fits to MC and MD results are shown as dashed and solid lines respectively.

Orientation	MC	MD	Ref.[24]	Ref.[27]
(100)[001]	0.42(2)	0.415(5)	0.44(3)	0.419(5)
(110)[001]	0.73(2)	0.707(4)	0.70(3)	0.769(5)

Table 2.4. Comparison of $\widetilde{\gamma}$ (in k_BT/σ^2) obtained in this work by means of two different simulation methodologies (MC and MD) with that obtained in previous works for the HS system and two different orientations.

analyze the interface gives results for $\widetilde{\gamma}$ that are consistent with previously published values.

2.5 Summary and conclusions

In this paper we present a computer simulation study of the crystal-melt interface for three different systems: hard spheres, Lennard Jones and the TIP4P/2005 model of water. We focus on the dynamics of surface waves. First, we generate an initial configuration in which a crystal slab is surrounded by its melt. The box geometry allows for the study of long wave-length capillary waves without having a prohibitively large number of molecules in the system (see Fig. 2.1 for an example). Then, we do molecular dynamics simulations in the NVT ensemble at the melting temperature. The overall density of the system is comprised in between the coexistence densities of the fluid and the crystal phases, which guarantees that the system stays at coexistence throughout

the NVT simulation. The area of the box side parallel to the interface is chosen in such way that the solid phase is free of any stress.

Once we run the molecular dynamics simulations, we analyse the dynamic autocorrelation function of the surface waves modes (Eq. 2.2). To do that we first obtain a function that describes the profile of the interface, which we do by identifying the outermost crystalline particles of the solid slab.

We carefully checked that our conclusions are not affected by the choice of the parameters needed to locate the interface (Fig. 2.8) or by the geometry of the box or the system size (Fig. 2.10).

We examine in detail the shape of the dynamic autocorrelation function as a function of the wave vector q, and conclude that a double exponential function describes the relaxation dynamics of crystal-melt surface waves much more accurately than a single exponential (Fig. 3.12 (a)). This implies that there are two distinct time scales, fast and slow, involved in the relaxation of crystal-melt surface waves. The slow time scale is due to the recrystallization-melting occurring at the interface, and is governed by capillary forces. The fast relaxation is due to a combination of processes that readily alter the shape of the interface. We speculate these may be related to Rayleigh waves, subdiffusion of the fluid and the attachment/detachment of particles to/from the crystal phase. As the length scale of the capillary wave modes increases (or q decreases) the relaxation becomes increasingly dominated by the slow process and can be just described by a single exponential. Within the uncertainty of our data, we see that the characteristic time for the slow relaxation process is related to q by the power law: $\tau \propto q^{-2}$ for all systems. Note that the conclusions obtained for the surface dynamics of the hard sphere system, which is not affected by posible artifacts from the thermsotat, fully agrees with results for the LJ and water models, where we resorted to thermostated dynamics. This power law was predicted theoretically in Ref. [7] and checked in simulations of metallic systems [8, 58, 23, 59] and hard spheres [22], although the existence of a single relaxation process was assumed in these works. Our results for hard spheres are clearly at odds with claims of a linear overdamped regime observed in the crystal–melt interface of colloids [13].

In addition to molecular dynamics simulations, we also perform Monte Carlo simulations for the hard sphere system. Monte Carlo and molecular dynamics simulations yield virtually identical autocorrelation functions if compared in diffusive time units (Fig. 2.5). This implies that the microscopic dynamics do not play any significant role in the relaxation of CW. Moreover, we compare the relaxation dynamics of different systems in diffusive time units. We see that the crystal-melt interface of water relaxes about ten times slower than that of hard spheres or Lennard Jones. We ascribe this difference to the presence of orientational degrees of freedom in the water molecules.

Following the methodology proposed in Refs. [7, 8] we obtain estimates of the kinetic coefficient (the proportionality constant between the rate of crystal growth and

the supercooling) for all the three systems investigated. We find a good agreement with the results of Ref. [22] for hard spheres (Fig. 2.6 (a)). In our reduced units we can compare the kinetic coefficient for Lennard Jones with that of water. We show that a Lennard Jones crystal grows roughly ten times faster than a water crystal for the same degree of supercooling. From the kinetic coefficient we estimate the rate of crystal growth for ice at moderate supercooling. We compare it with recent calculations of such quantity obtained by a completely different approach [57, 61] and get a quite good agreement (Fig. 2.7). However, the linear dependence of the rate of crystal growth with the supercooling is restricted to fairly small supercooling. We also compare our results for the rate of ice growth with experimental measurements [60] and show that the employed water model predicts significantly faster rates than those seen in the experiments (Fig. 2.7).

Acknowledgements

We would like to thank useful discussions with R. P. Sear, R. E. Rozas, J. Horbach, A. Mijailovic, E. Romero–Enrique, R. Benjamin, and F. Monroy. E. Sanz and J. Benet acknowledge financial support from the EU grant 322326-COSAAC-FP7-PEOPLE-2012-CIG and from a Spanish grant Ramon y Cajal. L.G. MacDowell and J. Benet also acknowledge financial support from project FIS2010-22047-C05-05 (Ministerio de Economia y Competitividad).

Bibliography

[1] W. Boettinger, S. Coriell, A. Greer, A. Karma, W. Kurz, M. Rappaz, and R. Trivedi, "Solidification microstructures: recent developments, future directions," *Acta Materialia*, vol. 48, no. 1, pp. 43 – 70, 2000.

[2] D. P. Woodruff, *The solid-liquid interface*. Cambridge: Cambridge University Press, 1973.

[3] A. W. Adamson and A. P. Gast, *Physical Chemistry of Surfaces*. New York: Wiley-Interscience, 1997.

[4] H. R. Pruppacher, "A new look at homogeneous ice nucleation in supercooled water drops," *J. Atmosph. Sci.*, vol. 52, p. 1924, 1995.

[5] C. F. Tejero and M. Baus, "Viscoelastic surface waves and the surface structure of liquids," *Molec. Phys.*, vol. 54, no. 6, pp. 1307–1324, 1985.

[6] U.-S. Jeng, L. Esibov, L. Crow, and A. Steyerl, "Viscosity effect on capillary waves at liquid interfaces," *J. Phys.:Condens. Matter*, vol. 10, no. 23, p. 4955, 1998.

[7] A. Karma, "Fluctuations in solidification," *Phys. Rev. E*, vol. 48, pp. 3441–3458, Nov 1993.

[8] J. Hoyt, M. Asta, and A. Karma, "Atomistic simulation methods for computing the kinetic coefficient in solid-liquid systems," *Interface Science*, vol. 10, no. 2-3, pp. 181–189, 2002.

[9] See Supplementary Material Document No.XXX for a Molecular Dynamics trajectory for the (prismI)[basal] crystal–melt interface with the TIP4P/2005 model. Capillary waves can be seen propagating along the prismatic I plane of ice Ih and parallel to the basal plane.

[10] M. V. von Smoluchowski *Annals of Physics*, vol. 25, p. 205, 1908.

[11] L. D. Landau and E. M. Lifshitz, *Mecánica de Fluidos*. Barcelona: Reverté, 1991.

[12] J. J. Hoyt, M. Asta, and A. Karma, "Method for computing the anisotropy of the solid-liquid interfacial free energy," *Phys. Rev. Lett.*, vol. 86, pp. 5530–5533, Jun 2001.

[13] J. Hernández-Guzmán and E. R. Weeks, "The equilibrium intrinsic crystal liquid interface of colloids," *Proceedings of the National Academy of Sciences*, vol. 106, no. 36, pp. 15198–15202, 2009.

[14] L. D. Landau and E. M. Lifshitz, *Teoria de la Elasticidad.* Barcelona: Reverté, 1969.

[15] B. H. Cao, M. W. Kim, H. Schaffer, and H. Z. Cummins, "Surface modes on polymer solutions by surface light scattering techniques," *J. Chem. Phys.*, vol. 95, no. 12, pp. 9317–9321, 1991.

[16] R. B. Dorshow and L. A. Turkevich, "First observation of capillary to rayleigh mode crossover on the surface of polymer solutions," *Phys. Rev. Lett.*, vol. 70, pp. 2439–2442, Apr 1993.

[17] F. Monroy and D. Langevin, "Direct experimental oservation of the crossover from capillary to elastic surface waves on soft gels," *Phys. Rev. Lett.*, vol. 81, pp. 3167–3170, 1998.

[18] H. Pleiner, J. L. Harden, and P. Pincus, "Surface modes on a viscoelastic medium," *Europhys. Lett.*, vol. 7, no. 5, p. 383, 1988.

[19] J. L. Harden, H. Pleiner, and P. A. Pincus, "Hydrodynamic surface modes on concentrated polymer solutions and gels," *J. Chem. Phys.*, vol. 94, no. 7, pp. 5208–5221, 1991.

[20] V. Kumaran, "Effect of fluid flow on the fluctuations at th surface of an elastic medium," *J. Chem. Phys.*, vol. 102, pp. 3452–3460, 1995.

[21] M. Baus and C. F. Tejero, "Interfacial hydrodynamics: A microscopic approach," *J. Chem. Phys.*, vol. 78, no. 1, pp. 483–496, 1983.

[22] M. Amini and B. B. Laird, "Kinetic coefficient for hard-sphere crystal growth from the melt," *Phys. Rev. Lett.*, vol. 97, p. 216102, Nov 2006.

[23] J. Hoyt, Z. Trautt, and M. Upmanyu, "Fluctuations in molecular dynamics simulations," *Mathematics and Computers in Simulation*, vol. 80, no. 7, pp. 1382 – 1392, 2010.

[24] R. L. Davidchack, J. R. Morris, and B. B. Laird, "The anisotropic hard-sphere crystal-melt interfacial free energy from fluctuations," *The Journal of Chemical Physics*, vol. 125, no. 9, p. 094710, 2006.

[25] R. E. Rozas and J. Horbach, "Capillary wave analysis of rough solid-liquid interfaces in nickel," *Europhys. Lett.*, vol. 93, no. 2, p. 26006, 2011.

[26] V. Heinonen, A. Mijailovic, C. V. Achim, T. Ala-Nissila, R. E. Rozas, J. Horbach, and H. Löwen, "Bcc crystal-fluid interfacial free energy in yukawa systems," *The Journal of Chemical Physics*, vol. 138, no. 4, pp. –, 2013.

[27] A. Härtel, M. Oettel, R. E. Rozas, S. U. Egelhaaf, J. Horbach, and H. Löwen, "Tension and stiffness of the hard sphere crystal-fluid interface," *Phys. Rev. Lett.*, vol. 108, p. 226101, May 2012.

[28] J. Q. Broughton and G. H. Gilmer, "Molecular dynamics investigation of the crystal–fluid interface. VI. Excess surface free energies of crystal–liquid systems," *J. Chem. Phys.*, vol. 84, no. 10, pp. 5759–5768, 1986.

[29] R. Handel, R. L. Davidchack, J. Anwar, and A. Brukhno, "Direct calculation of solid-liquid interfacial free energy for molecular systems: TIP4P ice-water interface," *Phys. Rev. Lett.*, vol. 100, p. 036104, Jan 2008.

[30] R. L. Davidchack, R. Handel, J. Anwar, and A. V. Brukhno, "Ice ih-water interfacial free energy of simple water models with full electrostatic interactions," *Journal of Chemical Theory and Computation*, vol. 8, no. 7, pp. 2383–2390, 2012.

[31] R. L. Davidchack, "Hard spheres revisited: Accurate calculation of the solid–liquid interfacial free energy," *J. Chem. Phys.*, vol. 133, no. 23, p. 234701, 2010.

[32] R. L. Davidchack and B. B. Laird, "Direct calculation of the crystal–melt interfacial free energies for continuous potentials: Application to the Lennard-Jones system," *J. Chem. Phys.*, vol. 118, no. 16, pp. 7651–7657, 2003.

[33] S. Angioletti-Uberti, M. Ceriotti, P. D. Lee, and M. W. Finnis, "Solid-liquid interface free energy through metadynamics simulations," *Phys. Rev. B*, vol. 81, p. 125416, Mar 2010.

[34] X.-M. Bai and M. Li, "Calculation of solid-liquid interfacial free energy: A classical nuclea tion theory based approach," *J. Chem. Phys.*, vol. 124, no. 12, p. 124707, 2006.

[35] B. C. Knott, V. Molinero, M. F. Doherty, and B. Peters, "Homogeneous nucleation of methane hydrates: Unrealistic under realistic conditions," *J. Am. Chem. Soc.*, vol. 134, pp. 19544–19547, 2012.

[36] E. Sanz, C. Vega, J. R. Espinosa, R. Caballero-Bernal, J. L. F. Abascal, and C. Valeriani, "Homogeneous ice nucleation at moderate supercooling from molecular simulation," *Journal of the American Chemical Society*, vol. 135, no. 40, pp. 15008–15017, 2013.

[37] J. R. Morris and X. Song, "The anisotropic free energy of the Lennard Jones crystal melt interface," *J. Chem. Phys.*, vol. 119, p. 3920, 2003.

[38] S. W. Rick and A. D. J. Haymet, "Dielectric constant and proton order and disorder in ice Ih: Monte Carlo computer simulations," *J. Chem. Phys.*, vol. 118, pp. 9291–9296, 2003.

[39] L. G. MacDowell and C. Vega, "Dielectric constant of ice ih and ice v: A computer simulation study," *J. Phys. Chem. B*, vol. 114, pp. 6089–6098, 2010.

[40] D. Frenkel, "Simulations: the dark side," *arXiv:12111.440*, 2012.

[41] E. G. Noya, C. Vega, and E. de Miguel, "Determination of the melting point of hard spheres from direct coexistence simulation methods," *The Journal of Chemical Physics*, vol. 128, no. 15, p. 154507, 2008.

[42] C. Vega and J. L. F. Abascal, "Simulating water with rigid non-polarizable models: a general perspective," *Phys. Chem. Chem. Phys.*, vol. 13, pp. 19663–19688, 2011.

[43] G. Bussi, D. Donadio, and M. Parrinello, "Canonical sampling through velocity rescaling," *J. Chem. Phys.*, vol. 126, no. 1, p. 014101, 2007.

[44] B. Leimkuhler, E. Noorizadeh, and O. Penrose, "Comparing the efficiencies of stochastic isothermal molecular dynamics methods," vol. 143, no. 5, pp. 921–942, 2011.

[45] R. Delgado-Buscalioni, E. Chacon, and P. Tarazona, "Hydrodynamics of nanoscopic capillary waves," *Phys. Rev. Lett.*, vol. 101, p. 106102, Sep 2008.

[46] D. C. Rapaport, *The Art of Molecular Dynamics Simulation*. Cambridge: University Press, 2004.

[47] H. Berendsen, D. van der Spoel, and R. van Drunen, "Gromacs: A message passing parallel molecular dynamics implementation," *Computer Physics Communications*, vol. 91, no. 1 - 3, pp. 43 – 56, 1995.

[48] B. Hess, C. Kutzner, D. van der Spoel, and E. Lindahl, "Gromacs 4: Algorithms for highly efficient, load-balanced, and scalable molecular simulation," *Journal of Chemical Theory and Computation*, vol. 4, no. 3, pp. 435–447, 2008.

[49] J. L. F. Abascal and C. Vega, "A general purpose model for the condensed phases of water: Tip4p/2005," *The Journal of Chemical Physics*, vol. 123, no. 23, p. 234505, 2005.

[50] J. Broughton and G. Gilmer, "Surface free energy and stress of a lennard-jones crystal," *Acta Metallurgica*, vol. 31, no. 6, pp. 845 – 851, 1983.

[51] R. L. Davidchack and B. B. Laird, "Simulation of the hard-sphere crystal-melt interface," *The Journal of Chemical Physics*, vol. 108, no. 22, 1998.

[52] D. M. Heyes, "Transport coefficients of lennard-jones fluids: A molecular-dynamics and effective-hard-sphere treatment," *Phys. Rev. B*, vol. 37, pp. 5677–5696, Apr 1988.

[53] E. Chacón, E. M. Fernández, D. Duque, R. Delgado-Buscalioni, and P. Tarazona, "Comparative study of the surface layer density of liquid surfaces," *Phys. Rev. B*, vol. 80, p. 195403, 2009.

[54] M. Jorge, P. Jedlovszky, and M. N. D. S. Cordeiro, "A critical assessment of methods for the intrinsic analysis of liquid interfaces. 1. surface site distributions," vol. 114, no. 25, pp. 11169–11179, 2010.

[55] D. Jasnow, "Critical phenomena at interfaces," *Rep. Prog. Phys.*, vol. 47, no. 9, p. 1059, 1984.

[56] D. Nelson, T. Piran, and S. Weinberg, *Statistical Mechanics of Membranes and Surfaces*. Word Scientific, Singapore, 2004.

[57] D. Rozmanov and P. G. Kusalik, "Temperature dependence of crystal growth of hexagonal ice (Ih)," *Phys. Chem. Chem. Phys.*, vol. 13, pp. 15501–15511, 2011.

[58] J. Hoyt, M. Asta, and A. Karma, "Atomistic and continuum modeling of dendritic solidification," *Materials Science and Engineering: R: Reports*, vol. 41, no. 6, pp. 121 – 163, 2003.

[59] J. Monk, Y. Yang, M. I. Mendelev, M. Asta, J. J. Hoyt, and D. Y. Sun, "Determination of the crystal-melt interface kinetic coefficient from molecular dynamics simulations," *Modelling and Simulation in Materials Science and Engineering*, vol. 18, no. 1, p. 015004, 2010.

[60] H. R. Pruppacher, "Interpretation of experimentally determined growth rates of ice crystals in supercooled water," *The Journal of Chemical Physics*, vol. 47, no. 5, pp. 1807–1813, 1967.

[61] R. A. Nistor, T. E. Markland, and B. J. Berne, "Interface-limited growth of heterogeneously nucleated ice in supercooled water," *The Journal of Physical Chemistry B*, vol. 118, no. 3, pp. 752–760, 2014.

[62] E. Chacón and P. Tarazona, "Intrinsic profiles beyond the capillary wave theory: A monte carlo study," *Phys. Rev. Lett.*, vol. 91, p. 166103, Oct 2003.

[63] P. N. Pusey, E. Zaccarelli, C. Valeriani, E. Sanz, W. C. K. Poon, and M. E. Cates, "Hard spheres: crystallization and glass formation," *Phyl. Trans. Roy. Soc. A*, vol. 367, pp. 4993–5011, 2009.

[64] W. Lechner and C. Dellago, "Accurate determination of crystal structures based on averaged local bond order parameters," *The Journal of Chemical Physics*, vol. 129, no. 11, p. 114707, 2008.

[65] P. R. ten Wolde, M. J. Ruiz-Montero, and D. Frenkel, "Numerical calculation of the rate of crystal nucleation in a Lennard-Jones system at moderate undercooling," *J. Chem. Phys.*, vol. 104, p. 9932, 1996.

[66] P. J. Steinhardt, D. R. Nelson, and M. Ronchetti, "Bond-orientational order in liquids and glasses," *Phys. Rev. B*, vol. 28, pp. 784–805, Jul 1983.

Appendices

A Order parameters

To distinguish between solid and liquid-like particles for the LJ and water systems we calculate for each particle a local bond order parameter, $\bar{q}_l(i)$, proposed by Lechner and Dellago [64]. If $\bar{q}_l(i)$ exceeds a certain threshold particle i is considered to be solid-like. The expression for $\bar{q}_l(i)$ reads:

$$\bar{q}_l(i) = \sqrt{\frac{4\pi}{2l+1}\sum_{m=-l}^{l}|\bar{q}_{lm}(i)|^2}, \tag{2.7}$$

where

$$\bar{q}_{lm} = \frac{1}{\widetilde{N}(i)}\sum_{j=1}^{\widetilde{N}(i)} q_{lm}\left(j\right), \tag{2.8}$$

and

$$q_{lm} = \frac{1}{N_n(i)}\sum_{j=1}^{N_n(i)} Y_{lm}\left(r_{ij}\right). \tag{2.9}$$

Here $\widetilde{N}$ includes particle i plus all its N_n neighbours, and Y_{lm} are m^{th} order spherical harmonics. The neighbors are identified over a cut-off distance of 3.5 Å for water and 1.4 σ for LJ.

In order to determine the best choice for the order parameters we calculated the values of two order parameters, namely $\bar{q}_4$ and $\bar{q}_6$, for both the bulk solid and the bulk fluid phases at coexistence. We discuss here the case of water. As it can be seen in Fig. 5.7 $\bar{q}_6$ allows for a better separation between the solids (hexagonal and cubic ice) and the fluid phase in water. Next, to choose the $\bar{q}_6$ threshold ($\bar{q}_{6,t}$) that best separates the liquid from the solids, we count the percentage of mislabelled molecules in each phase for several choices of $\bar{q}_{6,t}$. Whenever a liquid particle has a $\bar{q}_6$ value larger than $\bar{q}_{6,t}$, it will be mislabelled as solid-like. Likewise, if a solid-like particle happens to have a $\bar{q}_6$ smaller than $\bar{q}_{6,t}$, it will be mislabelled as liquid-like. In Fig. 2.13 we plot the percentage of mislabelled molecules as a function of $\bar{q}_{6,t}$. At $\bar{q}_{6,t} = 0.3435$ the liquid and ice-Ih curves cross at a mislabeling percentage of 0.82. We choose that value as the threshold to discriminate between liquid-like and solid-like molecules. The threshold is indicated with a horizontal dashed line in Fig. 5.7. At $\bar{q}_{6,t} = 0.3435$ the percentage of mislabelled ice-Ic molecules is as low as 0.26. This means that ice-Ic molecules would be detected as solid-like, should they appear when the interface recrytallizes. Once molecules are labelled either as solid or as liquid-like, the largest solid cluster is found

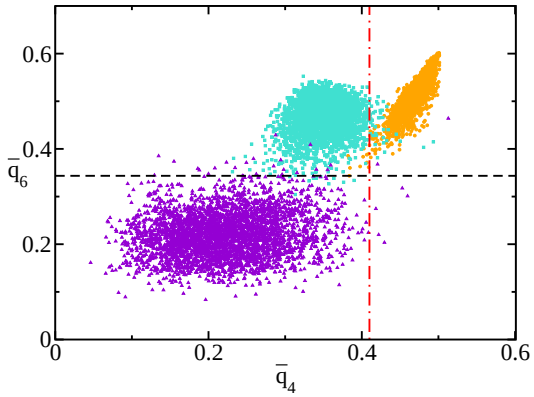

Figure 2.12. Bidimensional representation of the local bond order parameters for different liquid water (green triangles), ice Ih (red squares) and ice Ic (black circles). The corresponding thermodynamic state was T=250K and p=1bar.

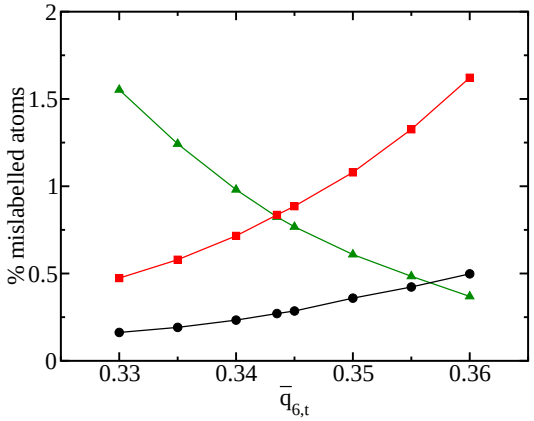

Figure 2.13. Fraction of atoms mislabelled as a function of $\bar{q}_{6,t}$. Liquid water (green triangles), ice Ih (red squares) and ice Ic (black circles).

using a clustering algorithm with a cut-off of 3.5 Å to find neighbors belonging to the same cluster.

For the LJ system we used a $\bar{q}_{6,t}$ value of 0.294 and a cut-off to build the biggest cluster of 1.4σ.

For the HS system we employed an order parameter based on q_6 as described in Ref. [63] to distinguish between solid-like and liquid-like particles.

B Double exponential fits

When fitting the time autocorrelation functions to a double exponential function (Eq. 2.6) it is convenient to have a good initial guess for the fitting parameters to avoid convergence to non-physical results. In order to obtain a good guess for the relaxation time of the slow process, τ_{ds}, we plot $d\ln(t)/dt$ vs t (see Fig. 2.14). Note that for long enough times one can approximate Eq. 2.6 by:

$$f_q(t) \approx Ae^{-t/\tau_{ds}}, \tag{2.10}$$

taking into account that $\tau_{ds} >> \tau_{df}$. If we now take the logarithm of Eq. 2.10 and differenciate with respect to t we obtain:

$$\frac{d\ln(f_q(t))}{dt} \approx \frac{-1}{\tau_{ds}}. \tag{2.11}$$

Therefore, from the intercept of the horizontal region of the plots shown in Fig. 2.14 we can get an estimate of τ_{ds}. Recall that the higher the q the more influenced is the relaxation of the interface by the fast process (see Fig. 2.3). Hence, as expected, the horizontal region in Fig. 2.14 becomes less evident as q increases. Nevertheless, it is enough for our purpose of getting an initial estimate for the fitting parameter τ_{ds}.

Given that for small qs the preexponential factor A is close to 1, we use $A = 1$ as an initial guess to fit the autocorrelation function corresponding to the smallest q. Regarding τ_{df}, we set an initial value two orders of magnitude smaller than τ_{ds}. We use the resulting parameters A and τ_{df} of the fit to the smallest q as an input for the following q. For τ_{ds} we use the value estimated from Fig. 2.14 as explained above. We repeat this process until we obtain a fit for each and every q.

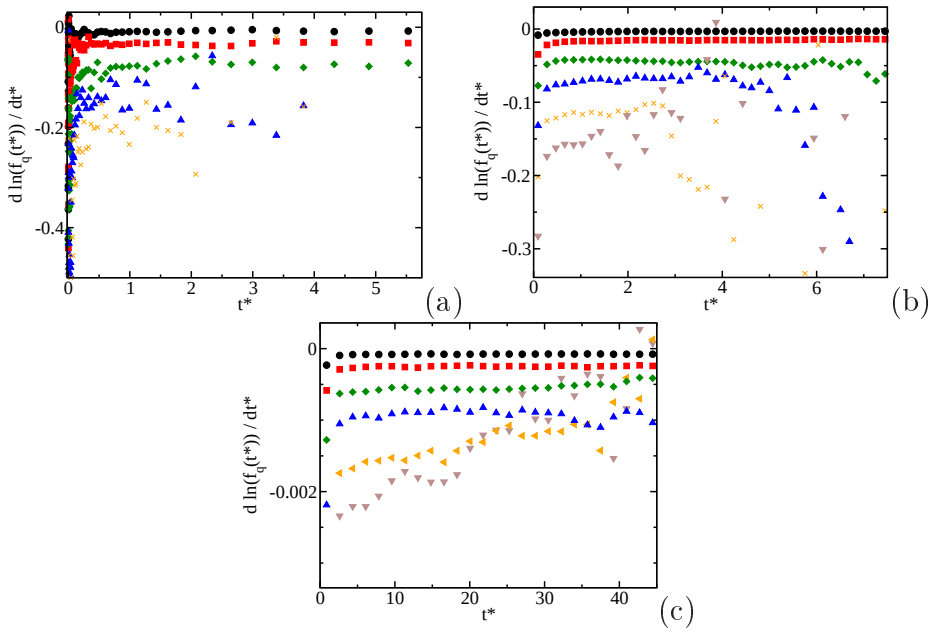

Figure 2.14. Representation of $d\ln(f_q(t)/dt$ vs t for three different systems: (100)[001] HS MD (a), (100)[001] LJ (b) and (pI)[basal] TIP4P/2005 water. From top to bottom in a given plot wavevectors with values of $q = 2\pi k/L_x$ with $k \leq 6$ are shown.

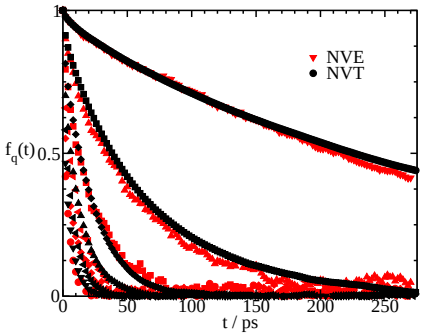

Figure 2.15. Autocorrelation functions for the (100)[001] LJ system as calculated in the NVT and NVE ensembles.

C NVE vs NVT

In Fig.2.15 we compare the autocorrelation functions calculated in many short NVE simulations starting from independent configurations with those obtained in a single, long NVT simulation. NVE simulations are short enough to guarantee energy conservation and, at the same time, long enough to allow for the relaxation of the studied capillary waves modes. Clearly, NVE and NVT give the same results (NVE curves are more noisy because the statistics is not as good).

Results: Chapter 3

Study of the solid–fluid interface for the Lennard–Jones system.

Jorge Benet, Luis G. MacDowell and Eduardo Sanz

Departamento de Química Física, Facultad de Ciencias Químicas, Universidad Complutense de Madrid, 28040 Madrid, Spain

3.1 Abstract

In this work we study the solid–liquid interface of the Lennard–Jones model under coexistence conditions by means of molecular dynamics simulations. We use the Capillary Fluctuation Method [1] to obtain the anisotropic interfacial stiffness of several crystal orientations. We use two different methods to obtain the interfacial free energy from the orientationally dependent stiffness: the Cubic Harmonics Expansion of Fehlner and Vosko [2] and a new one based on a numerical estimate of the curvature of the interfacial free energy as a function of the orientation of the crystal. Moreover, we study the dependence of our results on the geometry of the interface showing that squares (bidimensional interfaces) and stripes (quasi–monodimensional interfaces) give comparable results except when the (111) plane is exposed at the interface. We show that when this plane is exposed at the interface, a phase transition from fcc to hcp structure may occur. We also asses the ability of the employed order parameter to distinguish fcc from hcp–like particles near the interface and show that fcc particles may be mistakenly labelled as hcp.

3.2 Introduction

The study of solid–liquid interfaces is of great interest in many scientific fields ranging from theoretical physics to chemical engineering. Due to its importance much work has been done both in theoretical and experimental studies, to understand the solid–liquid interface [3, 4]. However, in spite of its relevance and of all the work done until the moment, there are still great discrepancies for basic physical magnitudes such as the interfacial free energy, γ_{sl}. This is, in part, due to the lack of a reliable way of estimating γ_{sl} experimentally. Molecular simulation appears then as a promising tool to determine such magnitude, but discrepancies between different works are still very large. For example, for the sodium chloride, which is a very well studied system [5, 6, 7, 8], the calculated values of its interfacial free energy range from 36 $\mathrm{mN{\cdot}m^{-1}}$ [6] to 99 $\mathrm{mN{\cdot}m^{-1}}$ [8]. Taking into account that such magnitude is highly relevant in many fields, e.g, crystal nucleation and growth, wetting, etc. it is desirable to look for a reliable method to determine the interfacial free energy of the solid–liquid interface. Up to date there exist several methods available in the literature to compute γ_{sl} [9, 1, 10, 11, 12, 13, 14, 15, 16] Among them, the Capillary Fluctuation Method (CFM) is one of the most commonly used. This method allows to obtain the anisotropic free energy γ_{sl} by measuring the interfacial height fluctuations, and has been applied to many different systems, e.g. hard spheres [17, 18], Lennard–Jones [19], water [20], charged colloids [21], dipolar fluids [22] and metals [1, 23, 24, 25].

It is a common practice when employing the CFM to simulate systems with quasi–monodimensional interfaces [1, 17, 20, 19, 23, 24, 26] given that it is an easy way to reduce the system size. In spite of being such a common practice, very little work has been done in order to study the effect of employing this geometry [25]. In this sense in Ref. [25] it is shown that the interfacial stiffness of the (100) plane of an embedded–atom potential for Ni does not depend on the interface geometry. Moreover, Ref. [26] shows that the dynamics of capillary waves of the (100)[001] orientation of a LJ model is not affected by the interface geometry neither. Besides these studies, to the best of our knowledge a systematic study of the effect of the interface geometry has not been carried out so far. In this work we calculate the interfacial stiffness and the interfacial free energy of the main crystallographic orientations for a LJ systems in both the quasi–1D and the 2D geometries. We find good agreement between both geometries for all orientations except for the (111) plane. We also study the crystalline structure of the solid phase, showing that an fcc to hcp transition may occur when the (111) plane is exposed. Finally we study the ability of the order parameter to correctly label particles at the interface. We conclude that the Steinhardt–like order parameter [27] widely used to distinguish liquid–like from solid–like particles [28, 29, 30] may give a misleading picture for the interfacial particles. In particular we find that the plane of an fcc lattice

in contact with the liquid is predominantly seen as hcp by such order parameter.

3.3 Methods

3.3.1 Model and System

In this work we have employed the truncated and shifted LJ potential proposed by Broughton and Gilmer [31]

$$U(r) = \begin{cases} 4\epsilon\left[\left(\frac{\sigma}{r}\right)^{12} - \left(\frac{\sigma}{r}\right)^{6}\right] + C_1, & r \leqslant 2.3\sigma \\ C_2\left(\frac{\sigma}{r}\right)^{12} + C_3\left(\frac{\sigma}{r}\right)^{6} + C_4\left(\frac{r}{\sigma}\right)^{2} + C_5, & 2.3 < r < 2.5 \\ 0, & 2.5\sigma \leqslant r \end{cases} \tag{3.1}$$

where ϵ is the depth of the potential well, σ is the particle diameter, and C_k are energy parameters whose values are: C_1=0.016132ϵ, C_2=3136.6ϵ, C_3=-68.069ϵ, C_4=-0.083312ϵ, and C_5=0.74689ϵ.

In order to study the effect of the system geometry we have employed two different setups. The first one consists in an elongated stripe where one of the axis of the interfacial plane is much longer than the other. From now on we will refer to this geometry as quasi–1D geometry. The second one consists in a rectangular interface where both axis of the interfacial plane have roughly the same length. This geometry will be referred to as 2D geometry. The size for all the systems under study are shown in Tables 3.1 and 3.2. In Fig. 3.1 we show the way we refer to the edges of the simulation box for a quasi–1D system. To specify the crystal orientation of our quasi-1D systems we show in parenthesis the Miller indexes of the interfacial plane, which is perpendicular to a vector $\vec{u} \parallel$ z, and in square brackets, the Miller indexes of a plane perpendicular to a vector $\vec{n} \parallel$ y. Thus we study the propagation of the wave in a direction given by $\vec{v}$ which is perpendicular to both $\vec{u}$ and $\vec{n}$.

3.3.2 Simulation details

All our simulations have been done with the molecular dynamics GROMACS 4.5.5 package [32, 33]. In this work we have used the implementation for Ar: $\sigma = 3.405$Å, $\epsilon/k_B = 119.8K$, $m = 6.69 \cdot 10^{-26}kg$. The time step for the velocity–verlet integrator was set to 0.01 ps and a velocity–rescale thermostat [34] with a relaxation time of 1 ps was used to keep the temperature constant. In order to generate the initial configuration we start by equilibrating the solid phase in an NpT simulation at coexistence conditions for the corresponding thermodynamic state (T=1k_B/ϵ, p=4.95ϵ/σ^3 [35]) and the average

Orientation	L_xxL_yxL_z/σ^3	Particles
(100)[001]	49.101 x 6.336 x 49.181	14743
(110)[001]	50.425 x 6.339 x 56.128	17280
(110)[$\bar{1}$10]	50.712 x 6.723 x 53.896	17664
(111)[$\bar{1}$10]	50.425 x 7.764 x 51.608	19440
(111)[11$\bar{2}$]	50.466 x 6.723 x 51.755	16848

Table 3.1. Orientation and size of the quasi–1D systems .

Interfacial plane	L_xxL_yxL_z/σ^3	Particles
(100)	49.101 x 19.007 x 49.181	44244
(110)	39.221 x 39.618 x 51.655	77000
(111)	47.064 x 48.524 x 43.520	94500

Table 3.2. Size of the 2D systems.

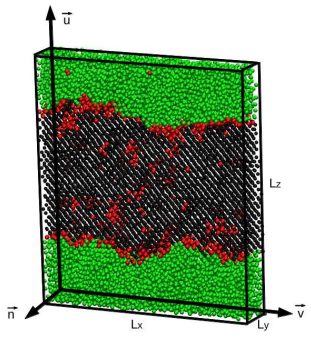

Figure 3.1. Snapshot of an initial configuration in a quasi-1D box geometry.

value of L_x, L_y and L_z is obtained. The values for the crystal and liquid densities for this thermodynamic state were ρ_c=1.005σ^{-3} and ρ_l=0.923σ^{-3}, respectively. The final snapshot is then rescaled to these average values. It is important to set L_x and L_y equal to their equilibrium values in order to avoid any stress in the crystalline structure which may lead to erroneous results [36]. Then a configuration of the liquid is simulated in a box with the same L_x and L_y obtained for the solid phase and is equilibrated in the $\mathrm{Np_zT}$ ensemble at coexistence temperature and a pressure higher than the coexistence pressure to ensure that the final global density will lie in between the solid and liquid coexistence densities. Once we have both snapshots, they are brought together along the z direction and liquid particles which are less than one molecular diameter away from the solid are removed. In this way the liquid density suffers a small drop which is compensated by the fact that it had been equilibrated at pressure higher than coexistence pressure. Then the liquid is allowed to equilibrate in an NVT simulation were the solid particles are kept frozen at their crystalline positions. Finally the whole system is equilibrated in the NVT ensemble for about 5 ns.

Once we have the initial configurations, production runs of about 50 ns are carried out in the NVT ensemble, and snapshots are saved every 10 ps.

3.3.3 Capillary Fluctuation Method

The interfacial free energy of a solid–liquid interface can be obtained by analyzing its equilibrium interface–height fluctuations [1]. According to the capillary wave theory the averaged squared amplitude of a wave mode q, $\langle|h_q|^2\rangle$, is related to the interfacial stiffness, $\widetilde{\gamma}$, by means of the equipartition theorem

$$\left\langle|h_{\vec{q}}|^2\right\rangle = \frac{k_B T}{A\widetilde{\gamma}q^2} \tag{3.2}$$

where k_B is the Boltzmann constant and $A = L_x L_y$ is the interfacial area. The term $\langle|h_{\vec{q}}|^2\rangle$ can be obtained from the interface–height fluctuations by Fourier transform:

$$h_{\vec{q}} = \frac{1}{n_j \cdot n_k}\sum_{j=1}^{n_j}\sum_{k=1}^{n_k} h(x_j, y_k)e^{i\vec{q}(x_j,y_k)} \tag{3.3}$$

where $h(x_j, y_k)$ is a smooth function which describes the interface location in a grid of n_jxn_k points and $\vec{q}$ is a two–dimensional wavevector with components q_x and q_y. In this way we can choose the direction of propagation of the wave we analyse by setting either $q_y = 0$ or $q_x = 0$. In order to obtain $h(x_j, y_k)$ we make use the order parameter $\bar{q}_6$ of Ref. [27] to identify the biggest solid–like cluster of our configurations (a detailed description of how this is done is given afterwards). Then, this discrete function can be obtained by assigning a height to each point (x_j, y_k) of the n_jxn_k grid. To calculate such

$\vec{u}$	$\vec{n}$	$\widetilde{\gamma}(\vec{u},\vec{n})/\gamma_0$	$\gamma(\vec{u})/\gamma_0$
100	010	$1-\frac{9}{2}\sqrt{21}\epsilon_1-5\sqrt{26}\epsilon_2$	$1+\frac{1}{2}\sqrt{21}\epsilon_1+\frac{1}{4}\sqrt{26}\epsilon_2$
110	001	$1+\frac{39}{8}\sqrt{21}\epsilon_1+\frac{155}{32}\sqrt{26}\epsilon_2$	$1-\frac{1}{8}\sqrt{21}\epsilon_1-\frac{13}{32}\sqrt{26}\epsilon_2$
110	$\bar{1}10$	$1-\frac{21}{8}\sqrt{21}\epsilon_1+\frac{365}{32}\sqrt{26}\epsilon_2$	$1-\frac{1}{8}\sqrt{21}\epsilon_1-\frac{13}{32}\sqrt{26}\epsilon_2$
111	$1\bar{1}0$	$1+3\sqrt{21}\epsilon_1-\frac{80}{9}\sqrt{26}\epsilon_2$	$1-\frac{1}{3}\sqrt{21}\epsilon_1+\frac{4}{9}\sqrt{26}\epsilon_2$
111	$11\bar{2}$	$1+3\sqrt{21}\epsilon_1-\frac{80}{9}\sqrt{26}\epsilon_2$	$1-\frac{1}{3}\sqrt{21}\epsilon_1+\frac{4}{9}\sqrt{26}\epsilon_2$

Table 3.3. Expressions for stiffness and the interfacial free energy for the different orientations.

height we average the z coordinate of the n_0 outermost particles whose x,y coordinates are enclosed within a square of side Δ centered at (x_j, y_k). The sets of parameters employed in this work are $n_j = 50$, $n_k = 3$, $\Delta = 3\sigma$ and $n_0 = 4$ for quasi-1D systems and $n_j = 50$, $n_k = 50$, $\Delta = 3\sigma$ and $n_0 = 4$ for 2D systems.

The interfacial stiffness is related to the interfacial free energy by the equation

$$\widetilde{\gamma}(\vec{u},\vec{n}) = \left(\gamma(\theta) + \frac{d^2\gamma(\theta)}{d\theta^2}\right)_{\theta=0} \tag{3.4}$$

where θ is the angle between a vector $\vec{u'}$, perpendicular to the instantaneous interface, and the vector $\vec{u}$, perpendicular to the average orientation of the flat interface.

In order to extract γ from Eq. 3.4 the dependence of the interfacial free energy with the crystal orientation must be established. This is done by applying the cubic harmonics expansion method of Fehlner and Vosko [2].

$$\gamma(\vec{u})/\gamma_0 \approx K_{0,0} + \epsilon_1 K_{4,1} + \epsilon_2 K_{6,1} + ... \tag{3.5}$$

where γ_0 is the averaged interfacial free energy, $K_{l,d}$ are the cubic harmonics and ϵ_k are the anisotropy parameters. In the fourth column of Table 3.3 we give this expression particularized for each interfacial plane studied in this work. Next, we plug Eq. 3.5 into Eq. 3.4 and obtain similar expressions for the stiffness, which are shown in the third column of Table 3.3. Once we have these expressions we can obtain γ_0 and the anisotropy parameters by fitting our simulation data for the stiffness to the equations given in column three of Table 3.3. Then the interfacial free energy of each plane can be obtain by using the equations given in the fourth column of this Table. From now on we will refer to the cubic harmonic expansion method as CHE.

Orientation	$\widetilde{\gamma}_0/\epsilon\sigma^{-2}$	
	quasi-1D	2D
(100)[001]	0.37(2)	0.37(1)
(110)[001]	0.70(4)	0.73(2)
(110)[$\bar{1}$10]	0.37(1)	0.41(2)
(111)[$\bar{1}$10]	0.69(5)	0.75(4)
(111)[11$\bar{2}$]	0.50(4)	0.74(6)

Table 3.4. Comparison of the stiffness values for the quasi–1D and 2D geometries.

3.4 Results

3.4.1 Stiffness and interfacial free energy

We perform production runs of about 50 ns and obtain over 5000 configurations. We analyse these configurations in order to calculate the interfacial profile $h(x_j, y_k)$ of each of the two solid–liquid interfaces present in our simulation box due to the periodic boundary conditions applied. Then we fourier transform these interfacial profiles according to Eq. 3.3 to obtain estimates of $|h_q|^2$ which we average to get $< |h_q|^2 >$. The interfacial stiffness is then obtained via Eq. 4.3. According to capillary wave theory the q-dependence of $\widetilde{\gamma}$ is as follows [37, 38, 39]:

$$\widetilde{\gamma}(q) = \widetilde{\gamma}_0 + aq^2 + bq^4 \tag{3.6}$$

In Fig. 3.2 we plot $\widetilde{\gamma}(q)$ versus q for all the systems studied and fit the data to Eq. 3.6 to obtain $\widetilde{\gamma}_0$. The values thus obtained are shown in Table 3.4. It can be seen that the (100)[001], (110)[001] and (110)[$\bar{1}$10] orientations give comparable results for both quasi-1D and 2D geometries. However, when the (111) plane is exposed at the interface, the agreement between both geometries is broken. Besides, according to the cubic harmonics expansion, both the (111)[$\bar{1}$10] and (111)[11$\bar{2}$] orientations should have the same stiffness value due to geometrical considerations. We observe this behaviour for the 2D system but not for the quasi-1D. Later on we will explore the reason for this unexpected finding.

The stiffness provides a direct measure of the fluctuations of the interface, but it also allows us to obtain γ_{sl} via Eq. 3.4 as seen in the Introduction. In a work published by Morris and Song [40] the CHE is employed to calculate the anisotropic interfacial free energy from the stiffness for a Lennard–Jones system at a different temperature. In their work they compare the results obtained by fitting the data obtained for the stiffness to the equations given in Table 3.3 either by setting $\epsilon_2 = 0$ or by letting it

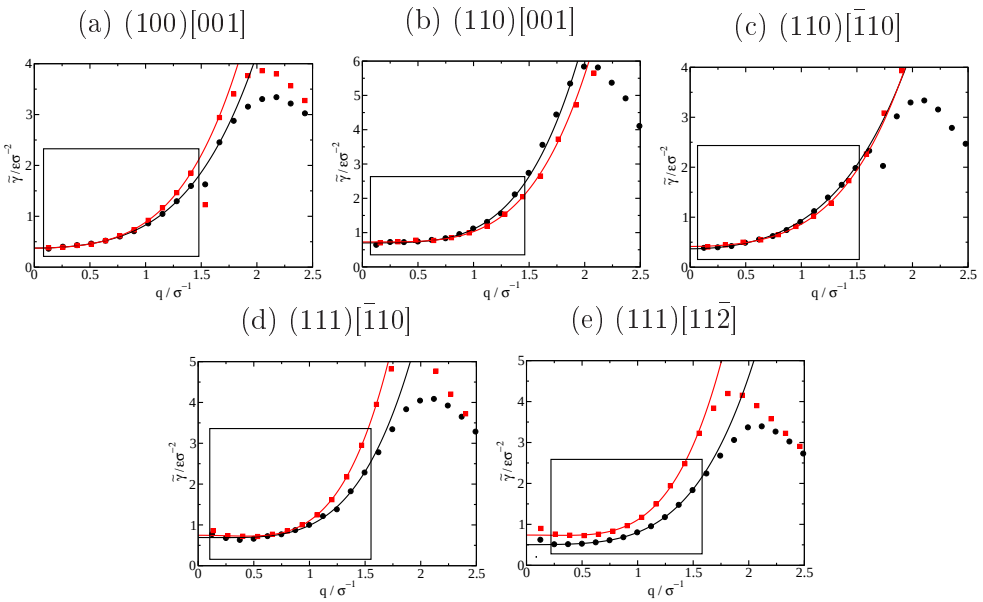

Figure 3.2. Plots of $\widetilde{\gamma}$ vs q for all the systems investigated. Black circles correspond to quasi–1D systems and red squares correspond to 2D systems. Solid lines are fits to the data inside the box.

as a free adjustable parameter. They show that the results obtained in both ways are the same within statistical error. We have followed the same procedure employing the more general approach of letting ϵ_2 to be an adjustable parameter. Since, as seen above, the (111) plane is giving contradictory results we have decided not to include it in our calculations. The results for the interfacial free energy thus obtained are shown in Table 3.5.

We have also applied the Numeric Estimate of the Curvature method (ENC), described in Chapter 3.3.2 of Part I of the Thesis, to calculate the interfacial free energy of the (100) and (110) planes. The results obtained from this method are also shown in Table 3.5 together with those of Ref. [35]. By looking at it we can see that both the quasi-1D and 2D geometries give the same values of γ_0, γ_{100} and γ_{110}, although 2D systems tend to give slightly higher values always between our margin of error. This remark is more noticeable when the ENC method is employed. By comparing our results obtained with those of Ref. [35] it can be seen that our data are in good agreement in all cases. However, the CHE method gives slightly better results. When we compare the interfacial free energy of the interfacial planes obtained by both methods, it is seen that both methods lead to a higher energy for the (100) plane, and again this difference is a bit higher when using the ENC method. In this sense, in spite of being a bit less reliable than the CHE method, the ENC method provides reasonable results for γ.

In a recent paper by Benjamin and Horbach the solid–liquid interfacial free energy

$\gamma/\epsilon\sigma^{-2}$	CHE		ENC		Ref.[35]
	q-1D	2D	q-1D	2D	
γ_0	0.53(3)	0.54(2)	-	-	0.539(4)
γ_{100}	0.55(3)	0.56(1)	0.56(4)	0.58(2)	0.562(6)
γ_{110}	0.52(3)	0.54(2)	0.50(3)	0.54(2)	0.543(6)

Table 3.5. Interfacial free energies as obtained by the CHE and ENC methods without including the (111) plane.

of different crystallographic planes of the Lennard–Jones model are calculated by an improved cleaving method for several temperatures, and a study of the system size dependence of the interfacial free energy for the (100) plane is done [16]. The results of this study are fully consistent with those of Ref. [35]. However, when studying the system size dependence they show that in the thermodynamic limit γ_{100} is increased about a 2% leading to a value of 0.576 ϵ/σ^2. This result may explain the small differences observed in our work for the stiffnesses and interfacial free energies for the quasi-1D and 2D systems.

In order to be able to determine the interfacial free energy of the (111) plane we have included in our calculations the (111) 2D system which we consider more reliable than the quasi-1D system because it gives the same stiffness for both orientations, as expected from the expression of Fehlner and Vosko [2]. Doing this we obtain $\gamma_0 = 0.56\pm0.02\epsilon/\sigma^2$, $\gamma_{100} = 0.58\pm0.02\epsilon/\sigma^2$, $\gamma_{110} = 0.56\pm0.03\epsilon/\sigma^2$ and $\gamma_{111} = 0.54\pm0.02\epsilon/\sigma^2$. We observe that our values of γ tend to increase in all cases. A similar behaviour was found in the work of Rozas and Horbach [25] for solid–fluid interfaces of nickel. In that work they found that the average value of the interfacial free energy suffered a noteworthy increase when the (111) plane was included in their calculations. In this sense it seems that the (111) plane presents an anomalous behaviour which needs to be understood in order to clarify the effect that it has in the calculation of the interfacial free energy values. In spite of that these results are still in fair agreement with our previous ones and with those of Ref. [35] (in that reference the reported value for γ_{111} is $0.508(8)\epsilon\sigma^{-2}$).

3.4.2 Hcp versus fcc

As it is mentioned in the section above, the (111) is the only studied plane that gives a different stiffness for quasi-1D and 2D interfaces. Moreover, when this plane is included in the calculations, the interfacial free energies are overestimated. With the aim of gaining some clues on the anomalous behaviour of the (111) plane we study in some detail the structure of the solid when such plane is exposed to the fluid. We make

System	% HCP
(100)[001] q–1D	0.12
(100) 2D	0.12
(110)[001] q–1D	0.12
(110)[$\bar{1}$10] q–1D	0.12
(110) 2D	0.13
(111)[$\bar{1}$10] q–1D	0.85
(111)[11$\bar{2}$] q–1D	0.15
(111) 2D	0.17

Table 3.6. Percentage of fcc and hcp particles for all the systems investigated. For each orientation 10 independent snapshots have been used.

use of an order parameter [27] which allows us to distinguish liquid–like from solid–like particles and, within the solid particles, those having an fcc environment from those having an hcp one. We set the threshold values for the $\bar{q}_4$ and $\bar{q}_6$ parameters following Ref. [26]. We use the $\bar{q}_6$ order parameter to distinguish between solid–like and liquid–like particles. If a particle has a value of the order parameter higher than the threshold value of $\bar{q}_{6,th} = 0.294$ it is labelled as solid–like. Otherwise it is labelled as liquid–like. Doing so we get rid of all liquid–like particles present in the system. We set the threshold value at $\bar{q}_{4,th} = 0.123$ and consider as hcp–like any particle with a value of the order parameter higher than this threshold and fcc–like otherwise.

In Figs. 3.3 to 3.10 we show a snapshot of all our systems with particles labelled as liquid–like (green), fcc–like (black) or hcp–like (red), according to the value of their order parameters. In all of them, we can see a solid slab placed between liquid–like particles. For all the orientations, except for the quasi–1D (111)[$\bar{1}$10], this solid structure is formed mainly of fcc–like particles with some regions of hcp–like ones. Besides, the majority of these hcp regions are placed at the solid–liquid interface. However, for the quasi–1D (111)[$\bar{1}$10] orientation, the result is completely different, and we can see that a phase transition has occurred in the solid phase. We made sure this result is reproducible by repeating the simulation starting from a different configuration. In this orientation mostly the whole solid has changed from fcc–like to hcp–like, and only two thin stripes of fcc–like particles remain in the bulk of the solid phase. We quantify these results in Table 3.6. There we show the percentage of fcc–like and hcp–like particles, which has been calculated by averaging over several snapshots after equilibration. It can be seen that the percentage of hcp–like particles remains approximately the same for all the systems but for the (111)[$\bar{1}$10] orientation, which has the opposite percentage. It is known that the free energy difference between fcc and hcp structures is very low. On the

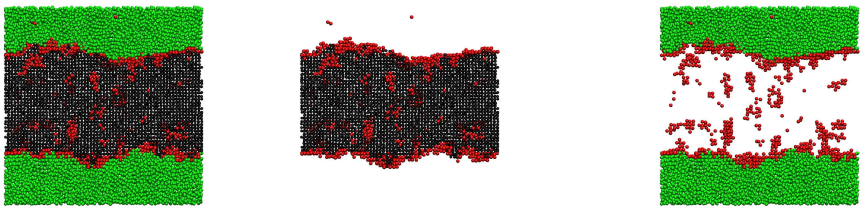

(a) All particles (b) Solid particles (c) Liquid and hcp like particles

Figure 3.3. (100)[001] quasi–1D system. Green: liquid particles, Black: fcc particles, Red: hcp particles

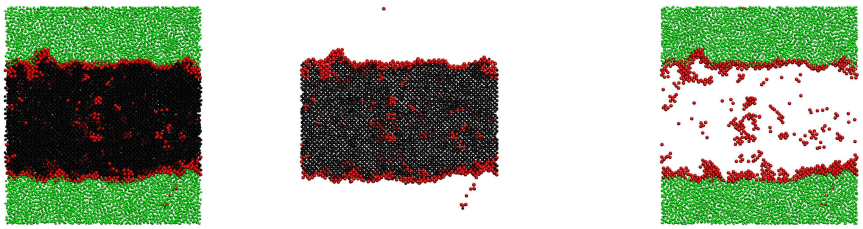

(a) All particles (b) Solid particles (c) Liquid and hcp like particles

Figure 3.4. (110)[001] quasi–1D system. Green: liquid particles, Black: fcc particles, Red: hcp particles

one hand the lattice energy of the hexagonal close packing is lower than that of the cubic close packing [41]. However, when increasing the temperature the fcc structure becomes the more stable one, although the range of stability depends on the modifications of the LJ potential and its range of truncation [42]. Such a small difference between bulk free energies makes possible the appearance of finite size effects. In this sense a slightly higher value in γ_{sl} for the fcc structure than for the hcp structure might change the relative stability of these phases in a finite size system. This result is still quite bothersome, given that it was the quasi–1D (111)[11$\bar{2}$] orientation and not the (111)[$\bar{1}$10] the one with the suspicious stiffness value. In this sense we would have expected that it was the quasi–1D (111)[11$\bar{2}$] orientation the one which suffered from recrystallization, explaining the anomaly in the stiffness.

Taking a closer inspection of the data of Table 3.6 we can see that systems with the (111) plane at the interface have a slightly higher percentage of hcp–like particles than the others. This fact is not unexpected taking into account that the relaxation of the capillary waves at the interface is governed by a melting/recrystallization mechanism [26]. This mechanism allows the appearance of staking faults when the (111) plane of an fcc structure, which is a close packed plane, is exposed at the interface. Thus the appearance of hcp structures is possible in these systems given that fcc and hcp structures only differ on the staking sequence of close packed planes, being A–B–A the

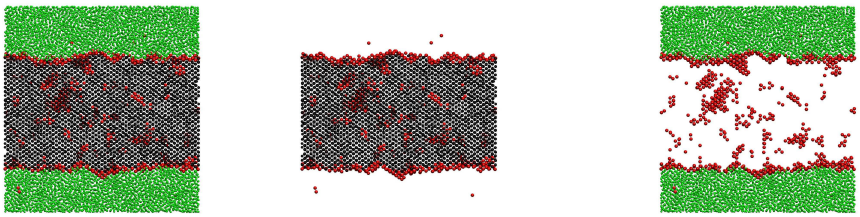

(a) All particles (b) Solid particles (c) Liquid and hcp like particles

Figure 3.5. (110)[$\bar{1}$10] quasi–1D system. Green: liquid particles, Black: fcc particles, Red: hcp particles

(a) All particles (b) Solid particles (c) Liquid and hcp like particles

Figure 3.6. (111)[$\bar{1}$10] quasi–1D system. Green: liquid particles, Black: fcc particles, Red: hcp particles

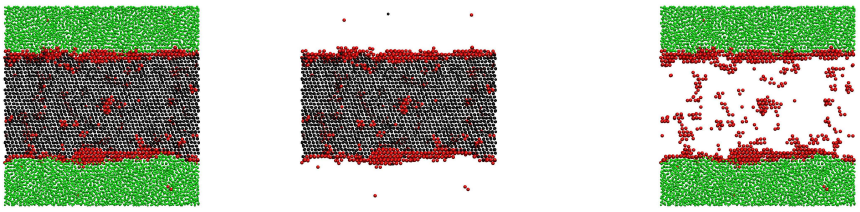

(a) All particles (b) Solid particles (c) Liquid and hcp like particles

Figure 3.7. (111)[11$\bar{2}$] quasi–1D system. Green: liquid particles, Black: fcc particles, Red: hcp particles

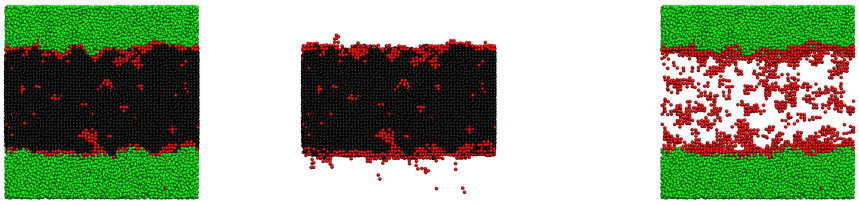

(a) All particles (b) Solid particles (c) Liquid and hcp like particles

Figure 3.8. (100) 2D system. Green: liquid particles, Black: fcc particles, Red: hcp particles

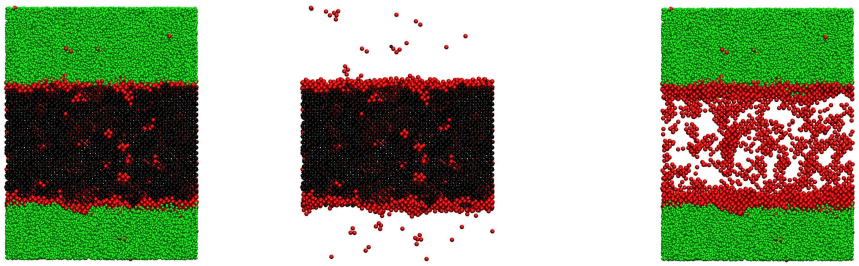

(a) All particles (b) Solid particles (c) Liquid and hcp like particles

Figure 3.9. (110) 2D system. Green: liquid particles, Black: fcc particles, Red: hcp particles

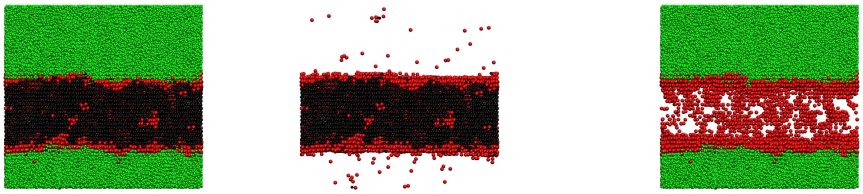

(a) All particles (b) Solid particles (c) Liquid and hcp like particles

Figure 3.10. (111) 2D system. Green: liquid particles, Black: fcc particles, Red: hcp particles

sequence corresponding to the fcc structure, and A–B–C the sequence corresponding to the hcp structure. However, in theory this is only possible when the (111) plane is at the interface and not for any other plane. It is interesting to investigate the origin of hcp-like particles in systems where planes other than the 111 are exposed. We have taken a perfect fcc structure and analyzed it with the $\bar{q}_4$ order parameter. As shown in Fig. 3.11a all the particles are identified as fcc–like. Next we take this solid structure, keep it frozen and place a liquid configuration next to its (100) plane. After letting the liquid diffuse to the solid we have analyzed the resulting configuration. As it is shown in Figs. 3.11b and 3.11c some of the surface particles of the frozen fcc structure, which had been identified previously as fcc–like, are now identified as hcp–like due to the presence of the liquid.

This fact suggests that the hcp–like particles found at the interface for all the systems but for the (111) are not particles in a real hcp environment but fcc–like particles mistakenly labelled as hcp because they are close to the liquid. In fact, bulk hcp particles have $\bar{q}_6$ values that lie in between those typical of liquid and fcc particles. This result is very interesting since it has been argued that the nucleation process of an fcc crystal in a supercooled liquid occurs via an hcp precursor nucleus [28]. In view of the study performed here we think it would be worth checking whether the precursor nucleus is really hcp or rather a small fcc nucleus having most particles in contact with the fluid and therefore being wrongly detected as hcp.

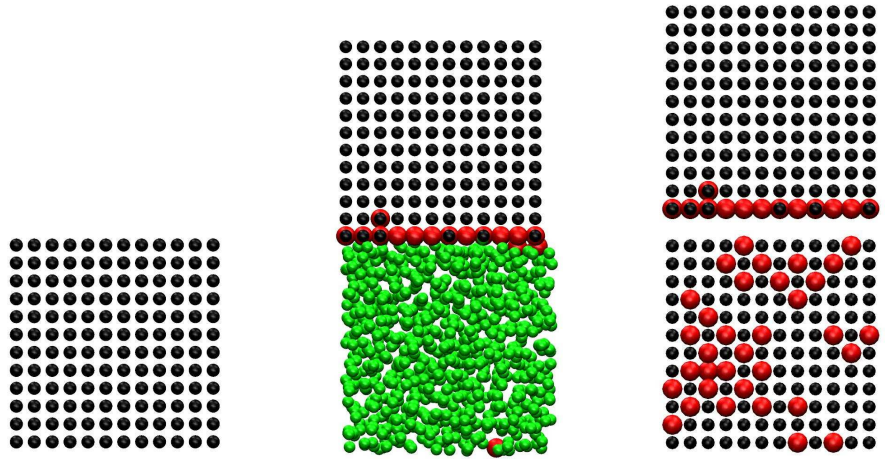

Figure 3.11. Crystalline structure identification according to $\bar{q}_4$ and $\bar{q}_6$ parameters. Green: liquid particles, Black: fcc particles, Red: hcp particles. (a) Ideal fcc structure. (b) Ideal fcc structure placed next to a liquid. (c) Projections of the ideal fcc structure placed next to a liquid phase. Top: lateral projection, Bottom: interfacial plane.

3.5 Conclusions and outlook

In this work we have performed a thorough study of the solid–fluid interface for the Lennard–Jones model in which we have compared two different interface geometries: quasi–1D and 2D. Our results show that the quasi-1D geometry gives slightly lower values for both the interfacial stiffness and the interfacial free energy, but always within the error. In this sense the use of quasi–1D interfaces is a reliable way of reducing the system size when studying interfaces by means of the capillary fluctuation method. However, when using the (111) plane the agreement between both geometries is broken and the values obtained for the interfacial free energy increase. This effect was also observed in a recent work by Rozas and Horbach for Nickel interfaces. Besides, when this plane is exposed at the interface the quasi–1D geometry gives different values for the stiffness depending on the wave propagation direction. This observation disagrees with the cubic harmonics expansion which says that both orientations should have the same stiffness due to symmetry considerations. In order to find the origin of the anomalous behaviour of the (111) plane we have investigated the crystalline structure of the solid phase and we have shown that the quasi–1D (111)$[\bar{1}10]$ orientation suffers a phase transition from fcc to hcp structure, preventing us from calculating the interfacial stiffness of an fcc structure in such orientation. Taking these facts into account more research concerning the (111) plane is needed. Finally we have observed that the identity of a particle may change when a different phase is placed close to it. This result is very

relevant because it reveals the difficulty of correctly labelling interfacial particles. In this sense we state that it is not meaningful to identify a crystal structure at an interface just by looking at the value of the order parameter.

Bibliography

[1] J. J. Hoyt, M. Asta, and A. Karma, "Method for computing the anisotropy of the solid-liquid interfacial free energy," *Phys. Rev. Lett.*, vol. 86, pp. 5530–5533, Jun 2001.

[2] W. R. Fehlner and S. H. Vosko, "A product representation for cubic harmonics and special directions for the determination of the fermi surface and related properties," *Canadian Journal of Physics*, vol. 54, no. 21, pp. 2159–2169, 1976.

[3] D. P. Woodruff, *The solid-liquid interface*. Cambridge: Cambridge University Press, 1973.

[4] A. W. Adamson and A. P. Gast, *Physical Chemistry of Surfaces*. New York: Wiley-Interscience, 1997.

[5] R. J. Speedy, P. G. Debenedetti, R. S. Smith, C. Huang, and B. D. Kay, "The evaporation rate, free energy, and entropy of amorphous water at 150 k," *J. Chem. Phys.*, vol. 105, p. 240, 1996.

[6] T. Zykova-Timan, D. Ceresoli, U. Tartaglino, and E. Tosatti, "Why are alkali halide surfaces not wetted by their own melt?," *Phys. Rev. Lett.*, vol. 94, p. 176105, May 2005.

[7] T. Zykova-Timan, C. Valeriani, E. Sanz, D. Frenkel, and E. Tosatti, "Irreducible finite-size effects in the surface free energy of nacl crystals from crystal-nucleation data," *Phys. Rev. Lett.*, vol. 100, p. 036103, Jan 2008.

[8] C. Valeriani, E. Sanz, and D. Frenkel, "Rate of homogeneous crystal nucleation in molten NaCl," *J. Chem. Phys.*, vol. 122, p. 194501, 2005.

[9] J. Q. Broughton and G. H. Gilmer, "Molecular dynamics investigation of the crystal–fluid interface. VI. Excess surface free energies of crystal–liquid systems," *J. Chem. Phys.*, vol. 84, no. 10, pp. 5759–5768, 1986.

[10] R. L. Davidchack and B. B. Laird, "Direct calculation of the hard-sphere crystal /melt interfacial free energy," *Phys. Rev. Lett.*, vol. 85, pp. 4751–4754, Nov 2000.

[11] S. Auer and D. Frenkel, "Prediction of absolute crystal-nucleation rate in hard-sphere colloids," *Nature*, vol. 409, p. 1020, 2001.

[12] X.-M. Bai and M. Li, "Calculation of solid-liquid interfacial free energy: A classical nuclea tion theory based approach," *J. Chem. Phys.*, vol. 124, no. 12, p. 124707, 2006.

[13] L. A. Fernández, V. Martín-Mayor, B. Seoane, and P. Verrocchio, "Equilibrium fluid-solid coexistence of hard spheres," *Phys. Rev. Lett.*, vol. 108, p. 165701, Apr 2012.

[14] S. Angioletti-Uberti, M. Ceriotti, P. D. Lee, and M. W. Finnis, "Solid-liquid interface free energy through metadynamics simulations," *Phys. Rev. B*, vol. 81, p. 125416, Mar 2010.

[15] J. R. Espinosa, C. Vega, and E. Sanz, "The mold integration method for the calculation of the crystal-fluid interfacial free energy from simulations," *The Journal of Chemical Physics*, vol. 141, no. 13, p. 134709, 2014.

[16] R. Benjamin and J. Horbach, "Crystal-liquid interfacial free energy via thermodynamic integration," *The Journal of Chemical Physics*, vol. 141, no. 4, pp. –, 2014.

[17] R. L. Davidchack, J. R. Morris, and B. B. Laird, "The anisotropic hard-sphere crystal melt interfacial free energy from fluctuations," *J. Chem. Phys.*, vol. 125, p. 094710, 2006.

[18] A. Härtel, M. Oettel, R. E. Rozas, S. U. Egelhaaf, J. Horbach, and H. Löwen, "Tension and stiffness of the hard sphere crystal-fluid interface," *Phys. Rev. Lett.*, vol. 108, p. 226101, May 2012.

[19] J. R. Morris and X. Song, "The anisotropic free energy of the Lennard-Jones crystal-melt interface," *J. Chem. Phys.*, vol. 119, no. 7, pp. 3920–3925, 2003.

[20] J. Benet, L. G. MacDowell, and E. Sanz, "A study of the ice-water interface using the tip4p/2005 water model," *Phys. Chem. Chem. Phys.*, vol. 16, pp. 22159–22166, 2014.

[21] V. Heinonen, A. Mijailovic, C. V. Achim, T. Ala-Nissila, R. E. Rozas, J. Horbach, and H. Löwen, "Bcc crystal-fluid interfacial free energy in yukawa systems," *The Journal of Chemical Physics*, vol. 138, no. 4, pp. –, 2013.

[22] J. Wang, P. A. Apte, J. R. Morris, and X. C. Zeng, "Freezing point and solid-liquid interfacial free energy of stockmayer dipolar fluids: A molecular dynamics simulation study," *The Journal of Chemical Physics*, vol. 139, no. 11, p. 114705, 2013.

[23] J. J. Hoyt and M. Asta, "Atomistic computation of liquid diffusivity, solid-liquid interfacial free energy, and kinetic coefficient in Au and Ag," *Phys. Rev. B*, vol. 65, p. 214106, Jun 2002.

[24] D. Y. Sun, M. I. Mendelev, C. A. Becker, K. Kudin, T. Haxhimali, M. Asta, J. J. Hoyt, A. Karma, and D. J. Srolovitz, "Crystal-melt interfacial free energies in hcp metals: A molecular dynamics study of Mg," *Phys. Rev. B*, vol. 73, p. 024116, Jan 2006.

[25] R. E. Rozas and J. Horbach, "Capillary wave analysis of rough solid-liquid interfaces in nickel," *Europhys. Lett.*, vol. 93, no. 2, p. 26006, 2011.

[26] J. Benet, L. G. MacDowell, and E. Sanz, "Computer simulation study of surface wave dynamics at the crystal–melt interface," *J. Chem. Phys.*, vol. 141, p. 024307, 2014.

[27] W. Lechner and C. Dellago, "Accurate determination of crystal structures based on averaged local bond order parameters," *The Journal of Chemical Physics*, vol. 129, no. 11, p. 114707, 2008.

[28] T. Kawasaki and H. Tanaka, "Formation of a crystal nucleus from liquid," *Proceedings of the National Academy of Sciences*, vol. 107, no. 32, pp. 14036–14041, 2010.

[29] E. Sanz, C. Valeriani, E. Zaccarelli, W. C. K. Poon, P. N. Pusey, and M. E. Cates, "Crystallization mechanism of hard sphere glasses," *Phys. Rev. Lett.*, vol. 106, p. 215701, May 2011.

[30] U. Agarwal and F. A. Escobedo, "Mesophase behaviour of polyhedral particles," *Nature Materials*, vol. 10, pp. 230–235, 2011.

[31] J. Broughton and G. Gilmer, "Surface free energy and stress of a lennard-jones crystal," *Acta Metallurgica*, vol. 31, no. 6, pp. 845 – 851, 1983.

[32] H. Berendsen, D. van der Spoel, and R. van Drunen, "Gromacs: A message passing parallel molecular dynamics implementation," *Computer Physics Communications*, vol. 91, no. 1 - 3, pp. 43 – 56, 1995.

[33] B. Hess, C. Kutzner, D. van der Spoel, and E. Lindahl, "Gromacs 4: Algorithms for highly efficient, load-balanced, and scalable molecular simulation," *Journal of Chemical Theory and Computation*, vol. 4, no. 3, pp. 435–447, 2008.

[34] G. Bussi, D. Donadio, and M. Parrinello, "Canonical sampling through velocity rescaling," *J. Chem. Phys.*, vol. 126, no. 1, p. 014101, 2007.

[35] R. L. Davidchack and B. B. Laird, "Direct calculation of the crystal–melt interfacial free energies for continuous potentials: Application to the Lennard-Jones system," *J. Chem. Phys.*, vol. 118, no. 16, pp. 7651–7657, 2003.

[36] D. Frenkel, "Simulations: the dark side," *arXiv:12111.440*, 2012.

[37] Meunier, J., "Liquid interfaces : role of the fluctuations and analysis of ellipsometry and reflectivity measurements," *J. Phys. France*, vol. 48, no. 10, pp. 1819–1831, 1987.

[38] K. R. Mecke and S. Dietrich, "Effective hamiltonian for liquid-vapor interfaces," *Phys. Rev. E*, vol. 59, pp. 6766–6784, Jun 1999.

[39] E. M. Blokhuis, "On the spectrum of fluctuations of a liquid surface: From the molecular scale to the macroscopic scale," *J. Chem. Phys.*, vol. 130, p. 074701, 2009.

[40] J. R. Morris and X. Song, "The anisotropic free energy of the Lennard Jones crystal melt interface," *J. Chem. Phys.*, vol. 119, p. 3920, 2003.

[41] T. Kihara and S. Koba, "Crystal structures and intermolecular forces of rare gases," *Journal of the Physical Society of Japan*, vol. 7, no. 4, pp. 348–354, 1952.

[42] A. N. Jackson, A. D. Bruce, and G. J. Ackland, "Lattice-switch monte carlo method: Application to soft potentials," *Phys. Rev. E*, vol. 65, p. 036710, Mar 2002.

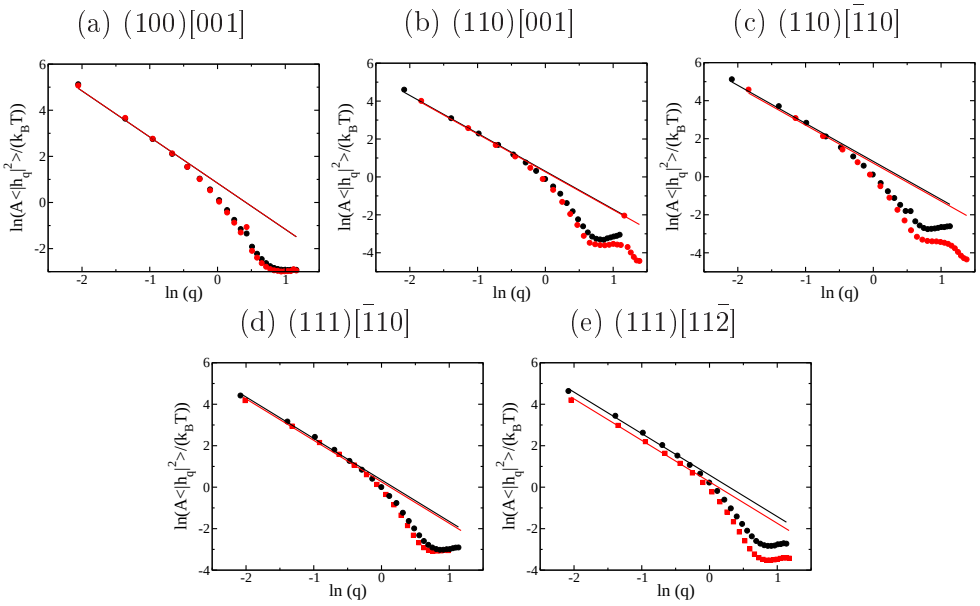

Figure 3.12. Plots of $\ln[< |h_q|^2 > A/k_BT]$ vs $\ln(q)$ for all the systems investigated. $< |h_q|^2 > A/k_BT$ is given in σ^4/ϵ and q is given in σ^{-1}. Black circles correspond to quasi–1D systems and red squares correspond to 2D systems. Solid lines are linear fits of slope -2 in the low q regime. The intercept of these fits is $-\ln(\widetilde{\gamma})$.

Appendix A: Alternative Analysis

In the main text we have obtained the thermodynamic limit of the interfacial stiffness from a fit of the data to Eq. 3.6. This method, which from now on will be referred as method 1, has already been used in previous works [21, 18]. However, apart from this method, there exists an alternative one which has also been used in several works [20, 25, 40]. This alternative method, which will be referred as method 2, obtains the thermodynamic limit of the interfacial stiffness by looking for the region where the stiffness is independent of the wavevector. Such regime can be found from Eq. 4.3 by rearranging it and taking logarithms:

$$\ln \frac{A \left\langle |h_q^2| \right\rangle}{k_B T} = -\ln \widetilde{\gamma} - 2 \ln q \tag{3.7}$$

Thus, by plotting $\ln(A < |h_q|^2 > /(k_BT))$ vs $\ln q$ we should obtain, at least in the low q regime, a region where the data can be fitted to straight line of slope -2. The intercept of such line is $-\ln(\widetilde{\gamma})$. In Fig. 3.12 we show such plots for all the systems here studied, and their corresponding values for the stiffnesses thus obtained are shown in Table 3.7.

As it can be seen, method 2 gives considerably higher values than method 1, some of them even beyond the margin of error. The reason of this behaviour is that method 2

Orientation	$\widetilde{\gamma}_0/\epsilon\sigma^{-2}$			
	Method 1		Method 2	
	quasi-1D	2D	quasi-1D	2D
(100)[001]	0.37(2)	0.37(1)	0.43(2)	0.43(2)
(110)[001]	0.70(4)	0.73(2)	0.74(2)	0.77(2)
(110)[$\bar{1}$10]	0.37(1)	0.41(2)	0.45(3)	0.49(3)
(111)[$\bar{1}$10]	0.69(5)	0.75(4)	0.69(3)	0.76(2)
(111)[11$\bar{2}$]	0.50(4)	0.74(6)	0.56(2)	0.76(3)

Table 3.7. Comparison of the stiffness values for the quasi–1D and 2D geometries obtained by the two different methods of analysis.

$\gamma/\epsilon\sigma^{-2}$	Method 1		Method 2		Ref.[35]
	q-1D	2D	q-1D	2D	
γ_0	0.53(3)	0.54(2)	0.58(2)	0.59(2)	0.539(4)
γ_{100}	0.55(3)	0.56(1)	0.59(2)	0.61(2)	0.562(6)
γ_{110}	0.52(3)	0.54(2)	0.57(2)	0.59(2)	0.543(6)

Table 3.8. Interfacial free energy as obtained by the two different methods of analysis. In both cases the CHE has been used to calculate γ. In this case the (111) plane has not been included in the calculation.

is very sensitive to the number of points included in the fit. By taking a look to Fig. 3.12 it can be clearly seen that as $\ln(q)$ increases data deviate to lower values than that of the linear region. The consequence of this behaviour is that when a point which is in the limit of the linear region is included, the intercept of the fit is lowered. Therefore, as the intercept is related to $\widetilde{\gamma}$ according to

$$\widetilde{\gamma} = e^{-intercept} \tag{3.8}$$

a decrease in the value of the intercept leads to higher values of $\widetilde{\gamma}$.

This increase in the values of the stiffnesses has a non negligible effect in the calculation of γ. As it is shown in Tables 3.8 and 3.9 the values of γ increase in all cases, deviating significantly from our previous results and those obtained in Ref. [35].

Taking into account that the results of [35] have been obtained by a different method which directly measures γ without the need of an extrapolation, it seems that method 1 is giving better results for the stiffness. The drawback of method 2 is that it assumes a region where $\widetilde{\gamma}$ does not depend on q. However, this region only appears

$\gamma/\epsilon\sigma^{-2}$	Method 1	Method 2	Ref.[35]
γ_0	0.56(2)	0.61(3)	0.539(4)
γ_{100}	0.58(1)	0.62(3)	0.562(6)
γ_{110}	0.56(2)	0.60(2)	0.543(6)
γ_{111}	0.54(2)	0.59(3)	0.508(8)

Table 3.9. Interfacial free energy for 2D systems as obtained by the two different methods of analysis. In both cases the CHE has been used to calculate γ.

for very small values of q which are hardly accessible in simulation (see Fig. 3.2 in the main text).

Results: Chapter 4

Interfacial free energy of NaCl solid-liquid interfaces from Capillary Wave Fluctuations

Jorge Benet, Luis G. MacDowell and Eduardo Sanz

Departamento de Química Física, Facultad de Ciencias Químicas, Universidad Complutense de Madrid, 28040 Madrid, Spain

4.1 Abstract

In this work we study, by means of Molecular Dynamics simulations, the solid–liquid interface of NaCl under coexistence conditions. By analysing capillary waves, we obtain the anisotropic stiffness for different orientations of the solid and calculate the interfacial free energy by expanding the dependency of the interfacial free energy with the solid orientation in terms of cubic harmonics. We obtain an average value for the solid–fluid interfacial free energy of 89 ± 6 mN·m^{-1}, that is consistent with previous results based on the measure of nucleation free energy barriers [J. Chem. Phys. **122** 194501 (2005)]. We analyse the influence of the simulation setup on interfacial properties and find that facets prepared as an elongated rectangular stripe give the same results as those prepared as squares for all cases but the 111 face. For some crystal orientations, we observe a surprising decay of the stiffness at low wavevectors and show that this behaviour does not depend on the simulation setup.

4.2 Introduction

The interfacial free energy between a solid and its melt has a great influence in the rate at which crystal nuclei emerge from the undercooled melt, as well as on the speed and shape with which such nuclei grow [1, 2]. The determination of the crystal-melt interfacial free energy, γ, is of great practical importance given the significance of crystallization in industry, material science, geology or biology. Unfortunately, the experimental measures of γ are not as accurate as desirable, as exemplified by the wide range of values –25 to 35 mN/m– reported for the ice/water interface [3].

Computer simulations in combination with good interaction potentials can be used to predict γ. There exist several simulation methods to compute γ [4, 5, 6, 7, 8, 9, 10, 11, 12] that have been applied in the past to a number of systems like e. g. hard-spheres [13, 14, 15, 16, 7, 11, 9], Lennard-Jones [4, 10, 17, 11, 12, 18], sodium chloride [19, 20, 21], dipolar fluids [22], hard dumbbells [23], metals [24, 25, 26], charged colloids [27], or water [28, 29, 30, 31]. For some of the studied systems there seems to be a fair agreement between the results obtained by different groups and different methods. For instance, it appears well established that γ for the (100) crystal plane of the hard spheres system is 0.59 ± 2 $k_B T/\sigma^2$ [13, 32, 11, 33]. Agreements within 5% can also be found for the Lennard-Jones model [18, 10, 34, 11, 12] or the TIP4P/2005 water model [30, 31].

By contrast, a consensus over the crystal-melt interfacial free energy for sodium-chloride has not been reached yet, in spite of the importance of this salt. In 2005 Zykova-Timan and collaborators [20, 21] calculated γ for the Tosi–Fumi NaCl model [35, 36]. They simulated a liquid slab surrounded by its vapor to calculate the liquid–vapor surface tension at the melting point by employing the Kirkwood-Buff formula [37]. Then they obtained the solid–vapor surface free energy by thermodynamic integration. Finally, by measuring the contact angle of a small liquid droplet deposited on top of the solid they calculated γ via Young's equation. The value thus obtained is 36 $mN \cdot m^{-1}$. In the same year, and also for the Tosi-Fumi model, Valeriani and collaborators performed a study of the nucleation of NaCl crystallites from the supercooled melt and calculated the height of the nucleation barrier [19]. Then, Classical Nucleation Theory was employed to estimate γ. The values thus obtained were 100 $mN \cdot m^{-1}$, if the cluster's shape was assumed to be spherical, and 80 $mN \cdot m^{-1}$ for a cubic shape. Either value clashes strongly with the 36 $mN \cdot m^{-1}$ of Refs. [20, 21]. The γ coming from the calculation of nucleation barriers was revisited by both groups in 2008 in an attempt to reconcile the 36 mN/m with the 80-100 mN/m [38]. In Ref. [38], effects like the dependency of γ with temperature, the nucleus compressibility and curvature, the presence of edges and vertex in the nucleus or the arbitrariness with which the surface is detected were taken into account. Unfortunately, none of these factors was able to account for the large

discrepancy.

Motivated by this unresolved discrepancy we pursue an independent measure of γ using the capillary fluctuation method [5], that has been successfully used in the past to evaluate γ for systems like hard spheres [32, 15], Lennard-Jones [17], water [31] or metals [5, 39, 40, 26]. This method uses capillary wave theory to provide values of γ through an analysis of surface waves for several crystal orientations simulated at contact with the melt under coexistence conditions. Using this method we obtain an orientationaly averaged γ of 89 mN/m, in fair agreement with the results derived from nucleation barriers [19, 38]. All studied crystal planes (100, 110, 111 and $11\bar{2}$) give the same γ within the accuracy of our calculations, which is of about 5 percent. Interestingly, we find that the stiffness decays at low wave-vectors for some crystal orientations, suggesting that these may be unstable. We also assess the dependence of the obtained results on the system size and on the shape of the interface (squares versus elongated stripes). For all studied crystal faces except the 111, both interface geometries give identical results. The paper is organised as follows: In Sec. 4.3 we present the simulation model, give simulation details and summarize the capillary fluctuation method. In Sec. 4.4 we present and discuss the results and in Sec. 4.5 we give the main conclusions.

4.3 Methods

4.3.1 Model

There are several models available in the literature to simulate NaCl [41, 42, 43, 35, 36]. We opt for the Tosi-Fumi model [35, 36] to compare with previous studies [19, 20, 21]. The properties of this model are quite close to those of real NaCl [35, 36, 44]. Our study confirms that 1082 K is a good value for the melting temperature of the model because the interface remains stable throughout the simulations. The melting point of the model at normal pressure has been estimated in several simulation works. In Ref. [45] the melting point was calculated by a density of states method and the reported result was 1050 K. However, studies based on free energy calculations have reported values of the melting temperature of 1064K [46] and 1089K [47], while direct simulation of the liquid–solid coexistence has led to values of 1066K [21] and 1063K [48]. In 2012, Aragones and collaborators calculated the melting point of the Tosi-Fumi model by three different routes, namely solid–liquid direct coexistence, free energy calculations and Hamiltonian Gibbs-Duhem integration [44]. The reported melting temperature was 1082K, which is the temperature at which we do our simulations. The melting temperature of the model is close to the experimental one, namely 1074 K.

The Tosi-Fumi (TF) potential is based in the work done by Born [49], Pauling [50, 51], Mayer [52] and Mayer and Huggins [53] and has the following form:

Interaction	$A_{ij}(kJ \cdot mol^{-1})$	ρ_{ij}(Å)	C_{ij}(Å$^6 kJ \cdot mol^{-1}$)	D_{ij}(Å$^8 kJ \cdot mol^{-1}$)
Na^+/Na^+	40870.5	0.317	101.2	48.2
Na^+/Cl^-	121075.5	0.317	674.5	837.0
Cl^-/Cl^-	336258.6	0.317	6985.7	14031.6

Table 4.1. Parameters for the Tosi–Fumi potential for NaCl.

$$U(r_{ij}) = A_{ij} e^{-r_{ij}/\rho_{ij}} - \frac{C_{ij}}{r_{ij}^6} - \frac{D_{ij}}{r_{ij}^8} + \frac{q_i q_j}{4\pi\epsilon_0 r_{ij}} \tag{4.1}$$

The interaction parameters have the values reported in Table 4.1.

4.3.2 Simulation details

We have used the GROMACS 4.5.5 package [54, 55] to perform Molecular Dynamics simulations in the NVT ensemble. The time step for the Velocity-Verlet algorithm was fixed at 0.007 ps and a velocity-rescale thermostat with a relaxation time of 2 ps was used to keep the temperature close to the melting temperature of the model [56]. We have truncated the van der Waals interaction at a distance of 14 Å, while the electrostatics were calculated using the Particle Mesh Ewald method, also truncated at 14 Å in real space. The system was prepared under coexistence conditions (1bar, 1082K) where the densities of the solid and fluid phases are $\rho_s = 1.876 g/cm^3$ and $\rho_l = 1.465 g/cm^3$, respectively [44].

In this work we have studied two different system geometries. In the first one the interface is an elongated stripe which allows us to probe long wave-length capillary waves without dealing with a large number of particles (see Fig. 4.1 for a snapshot of a typical simulation box). From now on we will refer to this geometry as quasi-1D geometry. As shown in in Fig.4.1 the interfacial plane is perpendicular to $\vec{u}$, and the capillary waves propagate along $\vec{v}$, which is perpendicular to both $\vec{u}$ and $\vec{n}$. In the second one the interface is roughly a square with similar simulation box edges L_x and L_y. We will refer to this geometry as 2D geometry. Production runs were performed for a total length of about 20 ns or 50 ns depending on the system geometry; 20 ns for the 2D systems and 50 ns for the quasi-1D systems. Note that the quasi-1D system only allows for the study of one propagation direction (along the long edge of the simulation box).

In order to indicate which combination of crystal plane and wave propagation direction is being studied we refer to our systems as (ijk)[lmn], where (ijk) are the Miller indices of the interfacial plane, that is perpendicular to $\vec{u}$; and (lmn) are the Miller indices of the plane which is perpendicular to $\vec{n}$. A detailed description of each system is given in Tables 4.2 and 4.3.

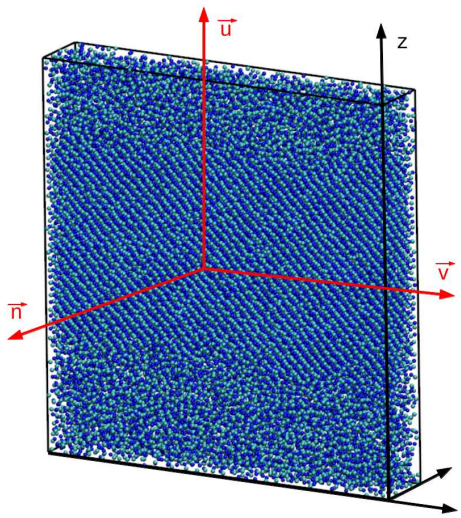

Figure 4.1. Snapshot of the quasi-1D geometry for the (100)[001] orientation.

Orientation	L_xxL_yxL_z (nm^3)	Ions
(100)[001]	17.7612 x 2.9605 x 18.5599	33600
(110)[$\bar{1}$10]	17.7742 x 2.9326 x 9.5694	16800
(111)[1$\bar{1}$0]	17.5818 x 3.6254 x 16.733	35280
(111)[11$\bar{2}$]	18.1294 x 3.7681 x 22.022	48600
(110)[001]	18.0031 x 2.9605 x 9.5028	17200
(11$\bar{2}$)[111]	17.4038 x 4.1020 x 14.4999	36432
(11$\bar{2}$)[1$\bar{1}$0]	17.4320 x 3.6254 x 15.9351	33660

Table 4.2. Size of the quasi-1D systems studied in this work.

Interfacial plane	L_xxL_yxL_z (nm^3)	Ions
(100)	11.8402 x 11.8402 x 16.6172	76800
(110)	11.7210 x 11.8401 x 16.2350	75520
(111)	12.3264 x 12.5586 x 15.3012	79560
(11$\bar{2}$)	12.3261 x 12.3044 x 13.4772	67320

Table 4.3. Size of the 2D systems studied in this work.

4.3.3 Capillary Fluctuation Method

We make use of the Capillary Fluctuation Method (CFM) [5] to obtain the anisotropic stiffness of the system. In this method the interface profile of the solid–liquid interface is analysed under coexistence conditions. The first step consists in labelling the particles as solid–like or liquid–like depending on the value of a local bond order parameter, d_4 [57]. We follow Ref. [19], where two particles are considered to have a solid connection if they have a d_4 value higher than 0.35. A particle is considered as solid–like if it has at least 6 solid connections. Then the biggest cluster of solid–like particles present in the system is identified. A discrete function for the interface profile, $h(x_j, y_k)$, can be then obtained by assigning a height to each point (x_j, y_k) of an n_jxn_k lattice in the xy plane. The height for a given lattice site is calculated by averaging the z-position of the n_0 outermost atoms whose x,y coordinates are enclosed within a square of side Δ centered at the site. The sets of parameters employed in this work for such analysis are n_j=40, n_k=4, Δ = 7.5 Å and n_0=3 for quasi-1D systems and n_j=40, n_k=40, Δ = 7.5 Å and n_0=3 for 2D systems. Once we have $h(x_j, y_k)$ we perform its Fourier transformation:

$$h_{\vec{q}} = \frac{1}{n_j \cdot n_k} \sum_{j=1}^{n_j} \sum_{k=1}^{n_k} h(x_j, y_k) e^{i\vec{q}(x_j, y_k)} \tag{4.2}$$

where $\vec{q}$ is a two–dimensional wave-vector with components q_x and q_y. We can choose which direction of propagation is analysed by setting either $q_x = 0$ or $q_y = 0$.

To obtain the interfacial stiffness, $\widetilde{\gamma}$, we make use of an expression provided by the Capillary Wave Theory, which gives a relationship between $h_{\vec{q}}$ and the interfacial stiffness, $\widetilde{\gamma}$, through the equipartition theorem:

$$\widetilde{\gamma} = \frac{k_B T}{A \left\langle |h_q|^2 \right\rangle q^2} \tag{4.3}$$

where $A = L_x L_y$ is the interfacial area.

The analysis of our simulations via Eq. 4.3 gives us the stiffness but not the interfacial free energy. The interfacial free energy for a given crystal orientation is related to the anisotropic stiffness, $\widetilde{\gamma}(\vec{u}, \vec{n})$, by [58]:

$$\widetilde{\gamma}(\vec{u}, \vec{n}) = \left(\gamma(\theta) + \frac{d^2 \gamma(\theta)}{d\theta^2} \right)_{\theta=0} \tag{4.4}$$

where θ is the angle between the average planar interface defined by $\vec{u}$ and the vector normal to the instantaneous interface $\vec{u'}$.

In order to obtain γ from Eq. 5.3 it is necessary to establish the dependence of the interfacial free energy with the crystal orientation. This is done by applying the cubic harmonic expansion proposed by Fehlner and Vosko in 1976 [59]:

$K_{0,0} = 1$
$K_{4,1} = \sqrt{21}\frac{1}{4}\left[5Q - 3\right]$
$K_{6,1} = \sqrt{\frac{13}{2}}\frac{1}{8}\left[462S + 21Q - 17\right]$
$K_{8,2} = \sqrt{561}\frac{1}{32}\left[65Q^2 - 208S - 94Q + 33\right]$
$K_{10,2} = \sqrt{\frac{455}{2}}\frac{1}{64}\left[7106QS + 187Q^2 - 3190S - 264Q + 85\right]$

Table 4.4. Normalized cubic harmonics in terms of Q y S, where $Q = x^4 + y^4 + z^4$ y $S = x^2y^2z^2$ being x,y,z the Cartesian components of $\vec{u}$.

Interfacial plane	$\gamma(\vec{u})/\gamma_0$
(100)	$1 + \frac{1}{2}\sqrt{21}\epsilon_1 + \frac{1}{4}\sqrt{26}\epsilon_2 + \frac{1}{8}\sqrt{561}\epsilon_3 + \frac{1}{16}\sqrt{910}\epsilon_4 + \frac{9}{164}\sqrt{451}\epsilon_5$
(110)	$1 - \frac{1}{8}\sqrt{21}\epsilon_1 - \frac{13}{32}\sqrt{26}\epsilon_2 + \frac{9}{128}\sqrt{561}\epsilon_3 - \frac{1}{512}\sqrt{910}\epsilon_4 + \frac{2517}{20992}\sqrt{451}\epsilon_5$
(111)	$1 - \frac{1}{3}\sqrt{21}\epsilon_1 + \frac{4}{9}\sqrt{26}\epsilon_2 + \frac{1}{27}\sqrt{561}\epsilon_3 - \frac{8}{81}\sqrt{910}\epsilon_4 + \frac{953}{9963}\sqrt{451}\epsilon_5$
$(11\bar{2})$	$1 - \frac{1}{8}\sqrt{21}\epsilon_1 + \frac{37}{288}\sqrt{26}\epsilon_2 - \frac{173}{3456}\sqrt{561}\epsilon_3 + \frac{233}{4608}\sqrt{910}\epsilon_4 + \frac{284551}{5101056}\sqrt{451}\epsilon_5$

Table 4.5. Expressions for the interfacial free energy for different crystal planes from Eq. 4.5.

$$\gamma(\vec{u})/\gamma_0 \approx K_{0,0} + \epsilon_1 K_{4,1} + \epsilon_2 K_{6,1} + \epsilon_3 K_{8,2} + \epsilon_4 K_{10,2} + ... \tag{4.5}$$

where γ_0 is the interfacial free energy averaged over all orientations, $K_{l,d}$ are the cubic harmonics given in Table 4.4 and ϵ_k are the anisotropy parameters. In Table 4.5 we give the expression above particularized for the different interfacial planes studied in this work. We then plug Eq. 4.5 in Eq. 5.3 by taking the second derivative of Eq. 4.5 with respect to θ (which requires writing the Cartesian coordinates of vectors $\vec{u}$ and $\vec{v}$ as a function of θ). We obtain, as a result, the equations given in Table 4.6. We obtain the anisotropy parameters by combining such equations with our simulation results for the stiffness, and then use them to obtain the interfacial free energy via Eq. 4.5.

4.4 Results

4.4.1 Interfacial Stiffness

In Fig. 4.2 the interfacial stiffness is plotted against the wave-vector modulus, q, for all orientations studied in this work. For each orientation we compare 2D (red squares) with quasi-1D interfaces (black circles). As discussed later, both interfacial geometries give similar results.

$\vec{u}$	$\vec{n}$	$\widetilde{\gamma}(\vec{u},\vec{n})/\gamma_0$
100	010	$1-\frac{9}{2}\sqrt{21}\epsilon_1-5\sqrt{26}\epsilon_2-\frac{35}{8}\sqrt{561}\epsilon_3-\frac{27}{8}\sqrt{910}\epsilon_4+\frac{9}{164}\sqrt{451}\epsilon_5$
110	001	$1+\frac{39}{8}\sqrt{21}\epsilon_1+\frac{155}{32}\sqrt{26}\epsilon_2-\frac{455}{128}\sqrt{561}\epsilon_3-\frac{1233}{512}\sqrt{910}\epsilon_4-\frac{109179}{20992}\sqrt{451}\epsilon_5$
110	$\bar{1}10$	$1-\frac{21}{8}\sqrt{21}\epsilon_1+\frac{365}{32}\sqrt{26}\epsilon_2-\frac{175}{128}\sqrt{561}\epsilon_3+\frac{1341}{512}\sqrt{910}\epsilon_4-\frac{278439}{20992}\sqrt{451}\epsilon_5$
111	$1\bar{1}0$	$1+3\sqrt{21}\epsilon_1-\frac{80}{9}\sqrt{26}\epsilon_2-\frac{35}{27}\sqrt{561}\epsilon_3+\frac{16}{3}\sqrt{910}\epsilon_4-\frac{73381}{9963}\sqrt{451}\epsilon_5$
111	$11\bar{2}$	$1+3\sqrt{21}\epsilon_1-\frac{80}{9}\sqrt{26}\epsilon_2-\frac{35}{27}\sqrt{561}\epsilon_3+\frac{16}{3}\sqrt{910}\epsilon_4-\frac{73381}{9963}\sqrt{451}\epsilon_5$
$11\bar{2}$	$1\bar{1}0$	$1+\frac{19}{8}\sqrt{21}\epsilon_1+\frac{1255}{288}\sqrt{26}\epsilon_2+\frac{4795}{3456}\sqrt{561}\epsilon_3-\frac{21041}{4608}\sqrt{910}\epsilon_4-\frac{1318037}{5101056}\sqrt{451}\epsilon_5$
$11\bar{2}$	111	$1-\frac{1}{8}\sqrt{21}\epsilon_1-\frac{2735}{288}\sqrt{26}\epsilon_2+\frac{7315}{3456}\sqrt{561}\epsilon_3-\frac{4123}{4608}\sqrt{910}\epsilon_4-\frac{42502817}{5101056}\sqrt{451}\epsilon_5$

Table 4.6. Expressions for the stiffness for different crystal orientations from Eqs. 5.3 and 4.5.

The interfacial stiffness is expected to reach a constant value, $\widetilde{\gamma}(0)$, as q goes to 0 and the thermodynamic limit is approached. This behaviour can be clearly seen in Figs. 4.2 (a)-(d). According to capillary wave theory the q-dependence of $\widetilde{\gamma}$ is as follows [60, 61, 62]:

$$\widetilde{\gamma}(q) = \widetilde{\gamma}(0) + aq^2 + bq^4 \tag{4.6}$$

Therefore, by fitting the data to the equation above we can obtain $\widetilde{\gamma}(0)$. Such fits are represented by solid lines in Fig. 4.2, and the q-range where the fit is made is indicated by a rectangle inside each plot (in some of the cases the smallest–q point has been left out of the fit due to a lack of statistics). The stiffnesses drawn from these fits are reported in Table 4.7.

The behaviour shown in plots (e), (f), (g) of Fig. 4.2 is unconventional and, to the best of our knowledge, has not been reported before. In these cases $\widetilde{\gamma}(q)$ drops for low-q values and it is not possible to fit the data to Eq. 6.14 in order to make the extrapolation to q=0. The observed anomalous behaviour of $\widetilde{\gamma}(q)$ is not a system size effect since it can be seen both in 2D and in quasi-1D interfaces. A further assessment of finite size effects is shown in Fig. 4.3, where $\widetilde{\gamma}(q)$ for the (110)[001] orientation is calculated for various box geometries (see caption). Again, the anomaly is robust to system size. As the interfacial stiffness can be understood as the resistance of a certain surface to show crystallographic planes other than that given by $\vec{u}$, a drop of $\widetilde{\gamma}$ for large wave lengths may be interpreted as an instability of the interface. Interestingly, the instability does not occur for particular crystal facets, but rather, for combinations of facets and propagation directions. Whence, capillary waves propagated along the $\vec{v}$ =[001] direction of the (110) plane do not show any sign of instability (see Fig. 4.2 (b)), whereas the [$\bar{1}$10] direction exhibit the large negative slope that we interpret as a signature of instability (see Fig. 4.2 (e)).

One may wonder whether it is possible to get a meaningful value of $\widetilde{\gamma}(0)$ for the 'unstable' orientations. In principle, the anomalous q–dependence of $\widetilde{\gamma}$ makes the extrapolation meaningless. We have nevertheless tried to extrapolate the data by fitting to Eq. 6.14 the q–range that does not include the drop. Such fits are shown by solid lines in Fig. 4.2 (e)-(g). Again, the q–range where the fit is done is indicated by a rectangle inside each plot. In this way we get values for $\widetilde{\gamma}(0)$ of these orientations, that are reported in Table 4.7 with an asterisk to indicate that these should be taken with caution. Although in principle the meaning of $\widetilde{\gamma}(0)$ thus obtained is not clear, we show in the next section that they give reasonable values of γ.

Orientation	$\widetilde{\gamma}(mN \cdot m^{-1})$	
	quasi-1D	2D
(100)[001]	85±2	85±2
(110)[$\bar{1}$10]	77±2	76±3
(111)[1$\bar{1}$0]	126±3	98±4
(111)[11$\bar{2}$]	99±2	102±4
(110)[001]*	78±4	80±8
(11$\bar{2}$)[1$\bar{1}$0]*	80±6	85±5
(11$\bar{2}$)[111]*	77±4	79±5

Table 4.7. Interfacial stiffness for the different orientations studied. The stiffnesses for the orientations marked with an asterisk, *, are obtained by extrapolating data from an intermediate q-range.

Since capillary waves have been shown to be affected by the dimensionality [26] it is worth performing a comparison between 2D and quasi-1D systems. Both the plots of Fig.4.2 and the values obtained for the interfacial stiffness clearly show that both geometries give the same results within error except for one case. This result is somewhat relieving since the capillary fluctuation method has been mainly used with quasi-1D systems so far (see e. g. Refs. [5, 34, 14, 40, 31]).

The only exception to the good accordance between 2D and quasi-1D geometries is the (111)[1$\bar{1}$0] orientation, which gives a considerable higher value for the quasi-1D geometry. In order to clarify which of both values is more reliable we make use of the expressions for the stiffness given in Table 4.6. According to such expressions both the (111)[1$\bar{1}$0] and the (111)[11$\bar{2}$] orientations should have the same stiffness due to symmetry considerations. Our results show that this is true for the 2D but not for the quasi-1D system, which leads us to conclude that the reliable value for the (111)[1$\bar{1}$0] is that given by the 2D geometry.

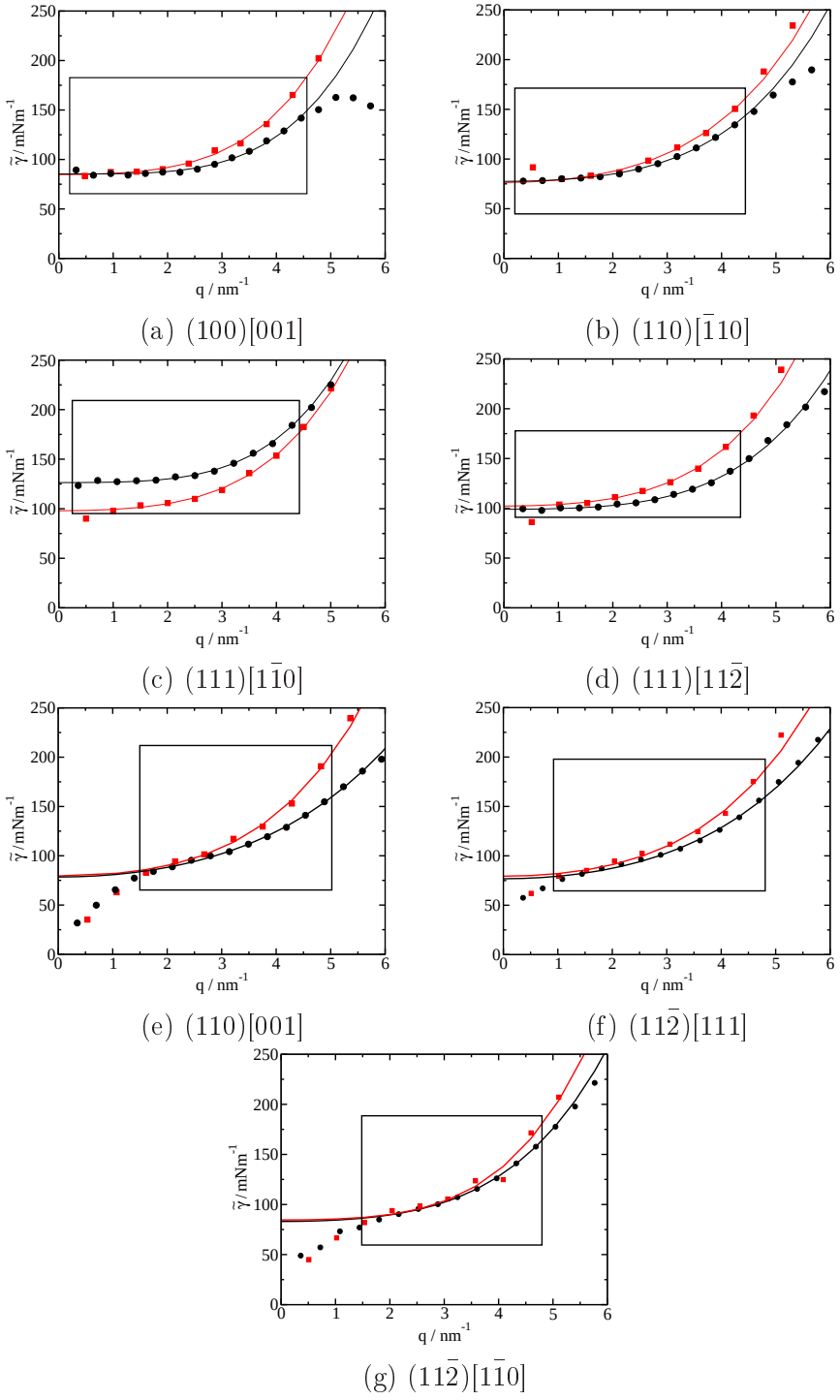

(a) (100)[001] (b) (110)[$\bar{1}$10]

(c) (111)[1$\bar{1}$0] (d) (111)[11$\bar{2}$]

(e) (110)[001] (f) (11$\bar{2}$)[111]

(g) (11$\bar{2}$)[1$\bar{1}$0]

Figure 4.2. Stiffness as a function of wave vector q for all the orientations studied. Black circles correspond to quasi-1D systems, while red squares correspond to 2D systems. Solid lines have been obtained by fitting the data inside the boxes to $\widetilde{\gamma} = \gamma_0 + aq^2 + bq^4$. For (c) the point corresponding to the smallest wavevector for the 2D system has not been included in the fit.

Although we do not know why the quasi-1D (111)[$1\bar{1}0$] system fails to give the right value of $\widetilde{\gamma}$, we suspect it may be related with the ability of the solid to recrystallize with stacking faults when the (111) is exposed to the melt. As we show in Ref. [63], the Lennard–Jones system provides similar conclusions to those drawn here for sodium chloride, i. e., all faces give the same stiffness for the quasi-1D and 2D systems except the (111). In the Lennard–Jones case, however, it is the (111)[$11\bar{2}$] orientation and not the (111)[$1\bar{1}0$] that gives the anomalous value.

NaCl facets with no even indexes are peculiar, because the corresponding bulk crystal carries a net dipole moment perpendicular to the interface, and, accordingly, a net surface charge. Particularly, the (111) facet consists of parallel sheets of oppositely charged ions [64]. At low temperature, such arrangement is electrostatically unstable, and the equilibrium crystal shape is a cube exhibiting only (100) facets [65]. It is thus thought that a crystal when forced to expose the (111) facet undergoes surface reconstruction [66, 67], and adopts an equilibrium structure with saw teeth shape of neutral octopolar cells, rather than a flat face of highly charged sheets [68, 69, 65]. In the case of the crystal–melt interface, the situation might very much change, since the molten salt is a conducting liquid and could therefore screen the charges effectively. In fact, already polar solvents such as urea are able to stabilize the (111) face. This is concluded from the observation of crystal NaCl grown from solutions, which spontaneously forms octahedral (111) rather than cubic (100) crystallites [70]. In our simulations, we find no evidence of unstable (111) facets, but also, from visual inspection (c.f. Fig. 4.4), no sign of the saw teeth structure. Rather, the rough interface seems to consist of a stacking of (111) planes that are cut by the liquid phase. As noticed before, this is not such a concern for the crystal-melt interface, since the stabilization of a highly charged arrangement of charge may be understood in terms of the Gouy–Chapman model of electrostatic screening.

4.4.2 Interfacial Free Energy

Once we know $\widetilde{\gamma}$ for all orientations studied we use the expressions given in Table 4.6 to calculate the anisotropy parameters and the orientationaly averaged interfacial free energy. With these values and using the expressions of Table 4.5 we can obtain γ for all the studied crystal faces.

To calculate γ we follow the same procedure used in Ref. [17] for a Lennard-Jones system. In that work it is shown that the results obtained by fitting the stiffnesses to the equations given in Table 4.6 do not depend on whether the expansion is truncated at ϵ_1 or at ϵ_2. We use the more general option of letting ϵ_2 as a free fitting parameter. To compute γ we exclude the orientations where the stiffness drops for low values of q as well as the quasi-1D (111)[$1\bar{1}0$] system that, as discussed above, gives a "suspicious" value of $\widetilde{\gamma}$. The results thus obtained are shown in the first row of Table 4.8 (analysis

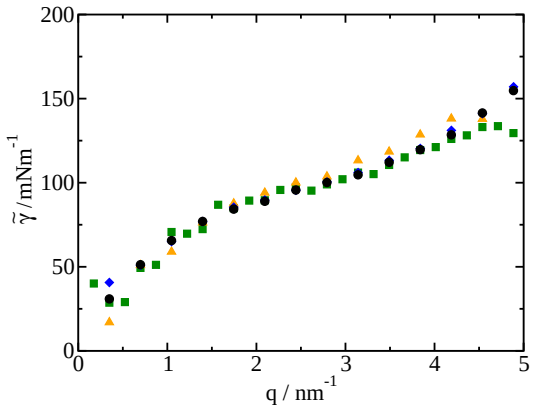

Figure 4.3. Interfacial stiffness as a function of wave vector q for the (110)[001] orientation and different system sizes. Black circles correspond to the original quasi-1D system. Green squares: L_x'=2L_x. Orange triangles: L_y'=2L_y. Blue diamonds: L_z'=2L_z.

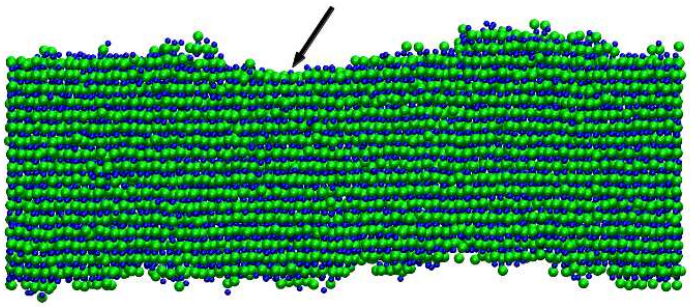

Figure 4.4. Snapshot of solid atoms for a configuration of the quasi-1D (111)[1$\bar{1}$0] orientation. Blue circles represent Na ions, while green ones represent Cl ions. Planar regions of close packed planes can be found while no signs of a saw teeth structure are present.

Analysis	γ_0	γ_{100}	γ_{110}	γ_{111}	$\gamma_{11\bar{2}}$
1	89±6	89±6	89±6	88±6	
2	85±9	85±9	85±9	84±9	85±9

Table 4.8. Interfacial free energy, in $mN{\cdot}m^{-1}$, for several crystal faces obtained from two different analyses. Analysis 1 includes only the stable orientations. Analysis 2 includes all orientations except quasi-1D $(111)[1\bar{1}0]$.

1). The orientationaly averaged interfacial free energy, γ_0, is 89 ± 6 $mN{\cdot}m^{-1}$.

Our value for γ_0 lies between the 80 and 100 $mN{\cdot}m^{-1}$ obtained for cubic and spherical clusters respectively in an earlier study of nucleation free energy barriers [19]. A primitive version of the Tosi-Fumi model (lacking of the r^{-6} and r^{-8} terms) was used in 1998 to estimate γ through a Classical Nucleation Theory analysis of the freezing rate of NaCl clusters in vacuum [71]. The estimated γ for temperatures close to 500 K was around 120 mN/m, not too far from the value obtained in this work and in Ref. [19]. Very little experimental work has been done so far to determine γ for NaCl, partly due to the extreme thermodynamic conditions at which experiments have to be done. In fact, to the best of our knowledge, the only experimental data available are those of Buckle and Ubbelohde [72, 73, 74] who studied homogeneous crystal nucleation in molten NaCl at 905 K. An analysis based on Classical Nucleation Theory of their nucleation data yields a γ of 84 $mN{\cdot}m^{-1}$ for spherical clusters, which is quite close to the prediction we give in this paper for the Tosi-Fumi model. The value of 36 mN/m reported in Refs. [20, 21] is then at odds with our and with previous simulations [19, 71] and with experiments [72, 73, 74]. We think that the problem with the calculations performed in Refs. [20, 21] might be related to the fact that Young's equation can not be safely applied to microscopic droplets due curvature and line tension effects [75, 76].

In Table 4.8 we also report the obtained value of γ for the different crystal planes we have studied. Unfortunately, our calculations are not accurate enough to resolve the anisotropy of γ with the orientation of the crystal.

The results reported in the first row of Table 4.8 exclude unstable orientations from the calculation of γ. When such orientations are included we obtain the results reported in the bottom row of Table 4.8 (analysis 2). The results are in good agreement with our previous analysis. The uncertainty in the data corresponding to this second analysis is even higher, preventing us again from determining if γ depends on the crystal orientation. In any case the good agreement between both analyses suggests that it is possible to obtain meaningful values of $\widetilde{\gamma}$ for the unstable orientations by restricting the analysis to the intermediate q regime where the expected $\widetilde{\gamma}(q)$ dependence given by Eq. 6.14 holds.

4.5 Conclusions and outlook

In this work we study the solid-liquid interface of sodium chloride using the Tosi-Fumi model for alkali halides. We calculate the spectrum of capillary waves under coexistence conditions for different crystal planes and wave propagation directions and use capillary wave theory to obtain an average value for the interfacial free energy of $\gamma = 89 \pm 6$ mN·m^{-1}. This result is in very good agreement with estimates obtained from the calculation of nucleation free energy barriers combined with Classical Nucleation Theory [19, 38]. However, it clashes with the 36 mN·m^{-1} estimated by measuring the contact angle of a liquid drop on top of a crystal surface [20]. We believe the problem of Ref. [20] is that the determination of contact angles for microscopic droplets is affected by the curvature of the droplet and by the effect of line tensions [76].

Interestingly, some of the orientations present a drop in the stiffness for small wavevectors, suggesting that these are unstable. Meaningful stiffnesses can be obtained from unstable orientations by restricting the analysis to an intermediate q regime where the system behaves as predicted by capillary wave theory.

We also compare square and thin rectangular interfaces and obtain the same results for all orientations except for one propagation direction of the 111 plane, where the elongated interface gives a stiffness 25 percent higher.

More work is needed to understand both the discrepancy between elongated and square interfaces for the 111 face and the origin and consequences of the anomalous dependence of the stiffness with the wave-vector observed for some orientations. It would also be worth to work in improving the accuracy of the method so that the anisotropy of γ can be resolved.

Acknowledgements

E. Sanz and J. Benet acknowledge financial support from the EU grant 322326-COSAAC-FP7-PEOPLE-2012-CIG and from a Spanish grant Ramon y Cajal. L.G. MacDowell and J. Benet also acknowledge financial support from project FIS2010-22047-C05-05 (Ministerio de Economia y Competitividad). All authors thank T. Zykova-Timan and D. Frenkel for insightful discussions.

Bibliography

[1] K. F. Kelton, *Crystal Nucleation in Liquids and Glasses*. Boston: Academic, 1991.

[2] D. P. Woodruff, *The solid-liquid interface*. Cambridge: Cambridge University Press, 1973.

[3] H. R. Pruppacher, "A new look at homogeneous ice nucleation in supercooled water drops," *J. Atmosph. Sci.*, vol. 52, p. 1924, 1995.

[4] J. Q. Broughton and G. H. Gilmer, "Molecular dynamics investigation of the crystal–fluid interface. VI. Excess surface free energies of crystal–liquid systems," *J. Chem. Phys.*, vol. 84, no. 10, pp. 5759–5768, 1986.

[5] J. J. Hoyt, M. Asta, and A. Karma, "Method for computing the anisotropy of the solid-liquid interfacial free energy," *Phys. Rev. Lett.*, vol. 86, pp. 5530–5533, Jun 2001.

[6] R. L. Davidchack and B. B. Laird, "Direct calculation of the hard-sphere crystal /melt interfacial free energy," *Phys. Rev. Lett.*, vol. 85, pp. 4751–4754, Nov 2000.

[7] S. Auer and D. Frenkel, "Prediction of absolute crystal-nucleation rate in hard-sphere colloids," *Nature*, vol. 409, p. 1020, 2001.

[8] X.-M. Bai and M. Li, "Calculation of solid-liquid interfacial free energy: A classical nuclea tion theory based approach," *J. Chem. Phys.*, vol. 124, no. 12, p. 124707, 2006.

[9] L. A. Fernández, V. Martín-Mayor, B. Seoane, and P. Verrocchio, "Equilibrium fluid-solid coexistence of hard spheres," *Phys. Rev. Lett.*, vol. 108, p. 165701, Apr 2012.

[10] S. Angioletti-Uberti, M. Ceriotti, P. D. Lee, and M. W. Finnis, "Solid-liquid interface free energy through metadynamics simulations," *Phys. Rev. B*, vol. 81, p. 125416, Mar 2010.

[11] J. R. Espinosa, C. Vega, and E. Sanz, "The mold integration method for the calculation of the crystal-fluid interfacial free energy from simulations," *The Journal of Chemical Physics*, vol. 141, no. 13, p. 134709, 2014.

[12] R. Benjamin and J. Horbach, "Crystal-liquid interfacial free energy via thermodynamic integration," *The Journal of Chemical Physics*, vol. 141, no. 4, pp. –, 2014.

[13] R. L. Davidchack, "Hard spheres revisited: Accurate calculation of the solid–liquid interfacial free energy," *J. Chem. Phys.*, vol. 133, no. 23, p. 234701, 2010.

[14] R. L. Davidchack, J. R. Morris, and B. B. Laird, "The anisotropic hard-sphere crystal melt interfacial free energy from fluctuations," *J. Chem. Phys.*, vol. 125, p. 094710, 2006.

[15] A. Härtel, M. Oettel, R. E. Rozas, S. U. Egelhaaf, J. Horbach, and H. Löwen, "Tension and stiffness of the hard sphere crystal-fluid interface," *Phys. Rev. Lett.*, vol. 108, p. 226101, May 2012.

[16] R. L. Davidchack and B. B. Laird, "Direct calculation of the hard-sphere crystal /melt interfacial free energy," *Phys. Rev. Lett.*, vol. 85, pp. 4751–4754, Nov 2000.

[17] J. R. Morris and X. Song, "The anisotropic free energy of the Lennard Jones crystal melt interface," *J. Chem. Phys.*, vol. 119, p. 3920, 2003.

[18] R. L. Davidchack and B. B. Laird, "Direct calculation of the crystal–melt interfacial free energies for continuous potentials: Application to the Lennard-Jones system," *J. Chem. Phys.*, vol. 118, no. 16, pp. 7651–7657, 2003.

[19] C. Valeriani, E. Sanz, and D. Frenkel, "Rate of homogeneous crystal nucleation in molten NaCl," *J. Chem. Phys.*, vol. 122, p. 194501, 2005.

[20] T. Zykova-Timan, D. Ceresoli, U. Tartaglino, and E. Tosatti, "Why are alkali halide surfaces not wetted by their own melt?," *Phys. Rev. Lett.*, vol. 94, p. 176105, May 2005.

[21] T. Zykova-Timan, D. Ceresoli, U. Tartaglino, and E. Tosatti, "Physics of solid and liquid alkali halide surfaces near the melting point," *The Journal of Chemical Physics*, vol. 123, no. 16, p. 164701, 2005.

[22] J. Wang, P. A. Apte, J. R. Morris, and X. C. Zeng, "Freezing point and solid-liquid interfacial free energy of stockmayer dipolar fluids: A molecular dynamics simulation study," *The Journal of Chemical Physics*, vol. 139, no. 11, p. 114705, 2013.

[23] Y. Mu and X. Song, "Crystal-melt interfacial free energies of hard-dumbbell systems," *Phys. Rev. E*, vol. 74, p. 031611, Sep 2006.

[24] J. R. Morris, "Complete mapping of the anisotropic free energy of the crystal-melt interface in Al," *Phys. Rev. B*, vol. 66, p. 144104, Oct 2002.

[25] D. Y. Sun, M. Asta, and J. J. Hoyt, "Crystal-melt interfacial free energies and mobilities in fcc and bcc Fe," *Phys. Rev. B*, vol. 69, p. 174103, May 2004.

[26] R. E. Rozas and J. Horbach, "Capillary wave analysis of rough solid-liquid interfaces in nickel," *Europhys. Lett.*, vol. 93, no. 2, p. 26006, 2011.

[27] V. Heinonen, A. Mijailovic, C. V. Achim, T. Ala-Nissila, R. E. Rozas, J. Horbach, and H. Löwen, "Bcc crystal-fluid interfacial free energy in yukawa systems," *The Journal of Chemical Physics*, vol. 138, no. 4, pp. –, 2013.

[28] R. L. Davidchack, R. Handel, J. Anwar, and A. V. Brukhno, "Ice ih-water interfacial free energy of simple water models with full electrostatic interactions," *Journal of Chemical Theory and Computation*, vol. 8, no. 7, pp. 2383–2390, 2012.

[29] R. Handel, R. L. Davidchack, J. Anwar, and A. Brukhno, "Direct calculation of solid-liquid interfacial free energy for molecular systems: TIP4P ice-water interface," *Phys. Rev. Lett.*, vol. 100, p. 036104, Jan 2008.

[30] E. Sanz, C. Vega, J. R. Espinosa, R. Caballero-Bernal, J. L. F. Abascal, and C. Valeriani, "Homogeneous ice nucleation at moderate supercooling from molecular simulation," *Journal of the American Chemical Society*, vol. 135, no. 40, pp. 15008–15017, 2013.

[31] J. Benet, L. G. MacDowell, and E. Sanz, "A study of the ice-water interface using the tip4p/2005 water model," *Phys. Chem. Chem. Phys.*, vol. 16, pp. 22159–22166, 2014.

[32] R. L. Davidchack, J. R. Morris, and B. B. Laird, "The anisotropic hard-sphere crystal-melt interfacial free energy from fluctuations," *The Journal of Chemical Physics*, vol. 125, no. 9, p. 094710, 2006.

[33] R. Benjamin and J. Horbach, "Crystal-liquid interfacial free energy of hard spheres via a novel thermodynamic integration scheme," *arXiv:1410.8798*, 2014.

[34] J. R. Morris and X. Song, "The anisotropic free energy of the Lennard-Jones crystal-melt interface," *J. Chem. Phys.*, vol. 119, no. 7, pp. 3920–3925, 2003.

[35] F. Fumi and M. Tosi, "Ionic sizes and born repulsive parameters in the NaCl-type alkali halides I," *Journal of Physics and Chemistry of Solids*, vol. 25, pp. 31–43, 1964.

[36] M. Tosi and F. Fumi, "Ionic sizes and born repulsive parameters in the NaCl-type alkali halides II," *Journal of Physics and Chemistry of Solids*, vol. 25, pp. 45–52, 1964.

[37] J. G. Kirkwood and F. P. Buff, "The statistical mechanical theory of surface tension," *The Journal of Chemical Physics*, vol. 17, no. 3, pp. 338–343, 1949.

[38] T. Zykova-Timan, C. Valeriani, E. Sanz, D. Frenkel, and E. Tosatti, "Irreducible finite-size effects in the surface free energy of nacl crystals from crystal-nucleation data," *Phys. Rev. Lett.*, vol. 100, p. 036103, Jan 2008.

[39] J. J. Hoyt and M. Asta, "Atomistic computation of liquid diffusivity, solid-liquid interfacial free energy, and kinetic coefficient in Au and Ag," *Phys. Rev. B*, vol. 65, p. 214106, Jun 2002.

[40] D. Y. Sun, M. I. Mendelev, C. A. Becker, K. Kudin, T. Haxhimali, M. Asta, J. J. Hoyt, A. Karma, and D. J. Srolovitz, "Crystal-melt interfacial free energies in hcp metals: A molecular dynamics study of Mg," *Phys. Rev. B*, vol. 73, p. 024116, Jan 2006.

[41] L. Dang and D. E. Smith, "Molecular dynamics simulations of aqueous ionic clusters using polarizable water," *J. Chem. Phys.*, vol. 99, p. 6950, 1993.

[42] D. E. Smith and L. X. Dang, "Computer simulations of NaCl association in polarizable water," *J. Chem. Phys.*, vol. 100, p. 3757, 1994.

[43] I. S. Joung and T. E. Cheatham, "Determination of alkali and halide monovalent ion parameters for use in explicitly solvated biomolecular simulations," *The Journal of Physical Chemistry B*, vol. 112, no. 30, pp. 9020–9041, 2008. PMID: 18593145.

[44] J. L. Aragones, E. Sanz, C. Valeriani, and C. Vega, "Calculation of the melting point of alkali halides by means of computer simulations," *The Journal of Chemical Physics*, vol. 137, no. 10, pp. –, 2012.

[45] E. A. Mastny and J. J. de Pablo, "Direct calculation of solid-liquid equilibria from density-of-states Monte Carlo simulations," *J. Chem. Phys.*, vol. 122, p. 124109, 2005.

[46] J. Anwar, D. Frenkel, and M. G. Noro, "Calculation of the melting point of NaCl by molecular simulation," *J. Chem. Phys.*, vol. 118, p. 728, 2003.

[47] D. M. Eike, J. F. Brennecke, and E. J. Maginn, "Toward a robust and general molecular simulation method for computing solid-liquid coexistence.," *J. Chem. Phys.*, vol. 122, p. 014115, 2005.

[48] Q. An, L. Zheng, R. Fu, S. Ni, and S.-N. Luo, "Solid–liquid transitions of sodium chloride at high pressures," *The Journal of Chemical Physics*, vol. 125, no. 15, pp. –, 2006.

[49] M. Born *Verh. d. D. Phys. Ges.*, vol. 21, p. 13, 1919.

[50] L. Pauling, "The influence of relative ionic sizes on the properties of ionic compounds," *J. Am. Chem. Soc.*, vol. 50, pp. 1036–1045, 1928.

[51] L. Pauling, "The sizes of ions and their influence on the properties of salt-like compounds," *Zeitschrift für Kristallographie*, vol. 67, p. 377, 1928.

[52] J. E. Mayer, "Dispersion and polarizability and the van der waals potential in the alkali halides," *J. Chem. Phys.*, vol. 1, pp. 270–279, 1933.

[53] M. L. Huggins and J. E. Mayer, "Interatomic distances in crystals of the alkali halides.," *J. Chem. Phys.*, vol. 1, p. 643, 1933.

[54] H. Berendsen, D. van der Spoel, and R. van Drunen, "Gromacs: A message passing parallel molecular dynamics implementation," *Computer Physics Communications*, vol. 91, no. 1 - 3, pp. 43 – 56, 1995.

[55] B. Hess, C. Kutzner, D. van der Spoel, and E. Lindahl, "Gromacs 4: Algorithms for highly efficient, load-balanced, and scalable molecular simulation," *Journal of Chemical Theory and Computation*, vol. 4, no. 3, pp. 435–447, 2008.

[56] G. Bussi, D. Donadio, and M. Parrinello, "Canonical sampling through velocity rescaling," *J. Chem. Phys.*, vol. 126, no. 1, p. 014101, 2007.

[57] P.-R. ten Wolde, M. J. Ruiz-Montero, and D. Frenkel, "Simulation of homogeneous crystal nucleation close to coexistence," *Faraday Discuss.*, vol. 104, pp. 93–110, 1996.

[58] D. S. Fisher and J. D. Weeks, "Shape of crystals at low temperatures: Absence of quantum roughening," *Phys. Rev. Lett.*, vol. 50, pp. 1077–1080, Apr 1983.

[59] W. R. Fehlner and S. H. Vosko, "A product representation for cubic harmonics and special directions for the determination of the fermi surface and related properties," *Canadian Journal of Physics*, vol. 54, no. 21, pp. 2159–2169, 1976.

[60] Meunier, J., "Liquid interfaces : role of the fluctuations and analysis of ellipsometry and reflectivity measurements," *J. Phys. France*, vol. 48, no. 10, pp. 1819–1831, 1987.

[61] K. R. Mecke and S. Dietrich, "Effective hamiltonian for liquid-vapor interfaces," *Phys. Rev. E*, vol. 59, pp. 6766–6784, Jun 1999.

[62] E. M. Blokhuis, "On the spectrum of fluctuations of a liquid surface: From the molecular scale to the macroscopic scale," *J. Chem. Phys.*, vol. 130, p. 074701, 2009.

[63] J. Benet, L. G. Macdowell, and E. Sanz, "Study of the solid-fluid interface for the lennard-jones system," *To be published.*

[64] W. Hebenstreit, M. Schmid, J. Redinger, R. Podloucky, and P. Varga, "Bulk terminated NaCl(111) on aluminum: A polar surface of an ionic crystal?," *Phys. Rev. Lett.*, vol. 85, pp. 5376–5379, Dec 2000.

[65] A.-C. Shi and M. Wortis, "Relaxation of surface atoms in NaCl: Influence on the equilibrium crystal shape," vol. 47, pp. 9804–9815, Apr 1993.

[66] D. Cappus, M. Haßel, E. Neuhaus, M. Heber, F. Rohr, and H.-J. Freund, "Polar surfaces of oxides: reactivity and reconstruction," *Surface Science*, vol. 337, no. 3, pp. 268–277, 1995. Surface Reconstruction: Structure and Dynamics.

[67] P. A. Mulheran, "Surface free-energy calculations and the equilibrium shape of NaCl crystals," *Modelling Simul. Matter. Sci. Eng.*, vol. 2, pp. 1123–1129, 1994.

[68] A.-C. Shi and M. Wortis, "Equilibrium shape of NaCl crystals: A first-principles calculation," vol. 37, pp. 7793–7805, May 1988.

[69] D. Wolf, "Reconstruction of NaCl surfaces from a dipolar solution to the Madelung problem," *Phys. Rev. Lett.*, vol. 68, pp. 3315–3318, Jun 1992.

[70] N. Radenovic, W. van Enckevort, P. Werwer, and E. Fieg, "Growth and characteristics of the 111 NaCl crystal surface grown from solutions," *Surface Sci.*, vol. 523, pp. 307–315, 2003.

[71] J. Huang, X. Zhu, and L. S. Bartell, "Molecular dynamics studies of the kinetics of freezing of $(NaCl)_{108}$ clusters," *J. Phys. Chem. A*, vol. 102, p. 2708, 1998.

[72] E. R. Buckle and A. R. Ubbelohde, "Studies on the freezing of pure liquids. I. Critical supercooling in molten alkali halides," *Proceedings of the Royal Society of London. Series A. Mathematical and Physical Sciences*, vol. 259, no. 1298, pp. 325–340, 1960.

[73] E. R. Buckle, "Studies on the freezing of pure liquids. II. The kinetics of homogeneous nucleation in supercooled liquids," *Proceedings of the Royal Society of London. Series A. Mathematical and Physical Sciences*, vol. 261, no. 1305, pp. 189–196, 1961.

[74] E. R. Buckle and A. R. Ubbelohde, "Studies on the freezing of pure liquids. III. Homogeneous nucleation in molten alkali halides," *Proceedings of the Royal Society of London. Series A. Mathematical and Physical Sciences*, vol. 261, no. 1305, pp. 197–206, 1961.

[75] P. Tarazona and G. Navascues, "A statistical mechanical theory for line tension," *J. Chem. Phys.*, vol. 75, no. 6, pp. 3114–3120, 1981.

[76] L. G. MacDowell, M. Müller, and K. Binder, "How do droplets on a surface depend on the system size?," vol. 206, pp. 277–291, 2002.

Results: Chapter 5

A study of the ice-water interface using the TIP4P/2005 water model

Jorge Benet, Luis G. MacDowell and Eduardo Sanz

Departamento de Química Física, Facultad de Ciencias Químicas, Universidad Complutense de Madrid, 28040 Madrid, Spain

Physical Chemistry Chemical Physics, ***16****, 22159-22166 (2014)*

5.1 Abstract

In this work we study the ice-water interface under coexistence conditions by means of molecular simulations using the TIP4P/2005 water model. Following the methodology proposed by Hoyt and co-workers [J. J. Hoyt, M. Asta and A. Karma, Phys. Rev. Lett., **86**, 5530, (2001)] we measure the interfacial free energy of ice with liquid water by analysing the spectrum of capillary fluctuations of the interface. We get an orientationally averaged interfacial free energy of 27(2) mN/m, in good agreement with a recent estimate obtained from simulation data of the size of critical clusters [E. Sanz, C. Vega, J. R. Espinosa, R. Caballero-Bernal, J. L. F. Abascal and C. Valeriani, JACS, **135**, 15008, (2013)]. We also estimate the interfacial free energy of different planes and obtain 27(2), 28(2) and 28(2) mN/m for the basal, the primary prismatic and the secondary prismatic planes respectively. Finally, we inspect the structure of the interface and find that its thickness is of approximately 4-5 molecular diameters. Moreover, we find that when the basal plane is exposed to the fluid the interface alternates regions of cubic ice with regions of hexagonal ice.

5.2 Introduction

The interfacial free energy between ice and water, γ_{iw}, is a crucial parameter in ice nucleation and growth [1, 2]. Despite its importance, there is not yet a well established experimental value for γ_{iw}. The spread of experimental data for γ_{iw}, ranging from 25 to 35 mN/m [1], sharply contrasts with the accuracy with which the interfacial free energy of the liquid-vapour interface is known [3]. Unfortunately, there is no accurate experimental technique for the determination of the crystal-melt interfacial free energy.

In order to aid experimentalists in finding a definite value for γ_{iw}, guidance from computer simulation is highly valuable. However, there are not many studies devoted to the estimation of γ_{iw} from simulations. Recently, γ_{iw} has been calculated for a series of water models with [4] and without [5] taking full electrostatic interactions into account. In these works, a variant of the cleaving method [6] was used to compute γ_{iw} and the studied models were TIP4P, TIP4P-Ew and TIP5P-E.

There are numerous water models currently available in the literature with which different predictions of the behaviour of real water can be made. In a recent work, Abascal and Vega have compared the ability of many different rigid, non-polarizable models to predict a comprehensive set of real water properties. The TIP4P/2005 model [7] turned out to be the one that does the best job in the overall description of the behaviour of real water [8]. Therefore, estimating γ_{iw} for such model would be highly relevant.

In a recent publication by some of the authors of this work, γ_{iw} was estimated for the TIP4P/2005 model [9] with a 'seeding' method originally used by Bai and Li to study the crystal-melt interface of the the Lennard-Jones system [10]. This method consists in measuring the critical size of crystalline clusters and then obtaining γ_{iw} from Classical Nucleation Theory [11, 12]. Therefore, this method provides an indirect estimate of γ_{iw}. Moreover, the method by Bai and Li does not provide information about the dependency of γ_{iw} with the orientation of the crystal, since an orientationally averaged γ_{iw} is obtained.

In this paper we evaluate γ_{iw} for the TIP4P/2005 model by means of the Capillary Fluctuation Method [13]. This method has been used, for instance, for the calculation of the interfacial free energy of hard spheres [14], the Lennard-Jones potential [15] and dipolar fluids [16]. Here we evaluate γ_{iw} for the TIP4P/2005 model for the basal, prismatic I and prismatic II planes of ice. We find an average value of γ_{iw} of 27(2) mN/m and a small anisotropy between different orientations. Finally, we inspect the structure of the interface. We estimate the thickness of the interface to be of about 4-5 molecular diameters. Moreover, we find that when the basal plane is exposed to the liquid the interface develops alternating hexagonal and cubic ice regions.

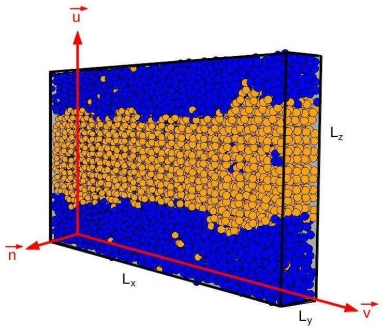

Figure 5.1. Snapshot of a typical configuration. Only oxygen atoms are shown. Particles are coloured in orange if they have a solid-like local environment and in blue otherwise. The edges of the simulation box and the vectors that define the orientation of the crystal and the propagation direction of capillary waves are shown in the figure.

5.3 Methods

We use the Capillary Fluctuation Method [13] to compute the interfacial free energy. The method consists in measuring γ_{iw} by analysing the profile of the interface between ice and water under coexistence conditions. For the TIP4P/2005 model the interface between ice and water is rough, as can be seen in Fig. 5.1, where particles in the ice phase are shown in orange and particles in the liquid phase are shown in blue. Particles are labelled as ice or liquid-like based on local bond order parameters [17, 18]. By knowing which particles belong to each phase, one can establish a discretized interface profile along the x direction, $h(x_n)$ (in Ref. [18] a detailed explanation of the way we establish $h(x_n)$ is given). Then, $h(x_n)$ is Fourier-transformed,

$$h_q = \frac{1}{N}\sum_{n=1}^{N} h(x_n) e^{iqx_n}, \tag{5.1}$$

and an amplitude, h_q, is obtained for each wave vector, q, where q is a multiple of $2\pi/L_x$. Small q vectors correspond to wave modes with a large wave length and vice-versa. In the equation above N is the number of discretization points along the L_x side of the simulation box.

Through the equipartition theorem, Capillary Wave Theory provides the following relation between h_q and the interfacial stiffness, $\widetilde{\gamma}$ [19, 20, 21, 22]:

$$\left\langle |h_q|^2 \right\rangle = \frac{k_B T}{A\widetilde{\gamma} q^2} \tag{5.2}$$

where $A = L_x \cdot L_y$ is the interfacial area, (see Fig. 5.1). The calculated stiffness depends on the crystal plane that is exposed to the fluid and on the direction along which the

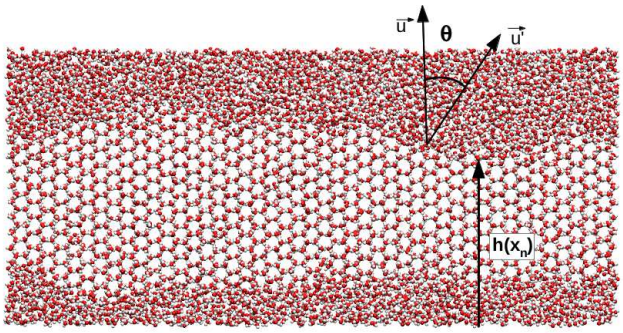

Figure 5.2. Snapshot of a configuration of an ice slab in equilibrium with liquid water. $h(x_n)$ is the interfacial height, $\vec{u}$ is the vector perpendicular to the average interface position, $\vec{u'}$ is the vector perpendicular to the instantaneous interface and θ is the angle between $\vec{u}$ and $\vec{u'}$.

wave propagates. The exposed crystal plane is perpendicular to the vector $\vec{u}$ in Fig. 5.1 and it is identified by its Miller indices. The direction of propagation of the wave is perpendicular to both $\vec{u}$ and $\vec{n}$ and it is specified by the Miller indices of the plane perpendicular to $\vec{n}$. Hence, $\widetilde{\gamma} \equiv \widetilde{\gamma}(\vec{u}, \vec{n})$.

Once the stiffness is known, we use the relation [19]:

$$\widetilde{\gamma}(\vec{u}, \vec{n}) = \left(\gamma(\theta) + \frac{d^2\gamma(\theta)}{d\theta^2} \right)_{\theta=0} \tag{5.3}$$

to obtain the interfacial free energy. In the above expression θ is the angle between the average planar interface defined by $\vec{u}$ and the vector normal to the instantaneous interface $\vec{u'}$. The definition of θ is sketched in Fig. 5.2.

Obtaining γ from Eq. 5.3 requires first defining the dependence of the interfacial free energy with the orientation of the crystal, $\gamma(\vec{u})$. Since the point group of hexagonal ice is $6/mmm$, the orientation dependence of $\gamma(\vec{u})$ can be written as an expansion in terms of Spherical Harmonics [23]:

$$\begin{aligned} \gamma(\vec{u})/\gamma_0 \approx & 1 + \epsilon_1 y_{20}(\alpha, \beta) + \epsilon_2 y_{40}(\alpha, \beta) \\ & + \epsilon_3 y_{60}(\alpha, \beta) + \epsilon_4 y_{66}(\alpha, \beta) + ... \end{aligned} \tag{5.4}$$

where γ_0 is the interfacial free energy averaged over all orientations, α and β are the spherical angles defining a given plane (see Fig. 5.3) and ϵ_k are the anisotropy parameters. The functions $y_{lm}(\alpha, \beta)$ are the normalized spherical harmonics, and they are provided in Table 5.1. In Table 5.2, Eq. 5.4 is expressed for the particular case of the three orientations of ice-Ih we put in contact with liquid water in this work.

By taking the second derivative of Eq. 5.4 with respect to θ and plugging the result into Eq. 5.3 an expansion of $\widetilde{\gamma}$ is obtained. Such expansion is given in Table 5.3 for all the orientations studied in this work. The equations in Table 5.3 combined

$y_{20}(\alpha,\beta) = \sqrt{5/16\pi}\,[3cos^2(\alpha) - 1]$
$y_{40}(\alpha,\beta) = \frac{3}{16}\sqrt{1/\pi}\,[35cos^4(\alpha) - 30cos^2(\alpha) + 3]$
$y_{60}(\alpha,\beta) = \frac{1}{32}\sqrt{13/\pi}\,[231cos^6(\alpha) - 315cos^4(\alpha) + 105cos^2(\alpha) - 5]$
$y_{66}(\alpha,\beta) = \frac{1}{64}\sqrt{6006/\pi}\,[1 - cos^2(\alpha)]^3\,cos(6\beta)$

Table 5.1. Expressions for the normalized spherical harmonics used in Eq.5.4.

Interfacial plane	$\gamma(\vec{u})/\gamma_0$
(0001)	$1 + \frac{1}{2}\sqrt{5/\pi}\epsilon_1 + \frac{3}{2}\sqrt{1/\pi}\epsilon_2 + \frac{1}{2}\sqrt{13/\pi}\epsilon_3$
$(10\bar{1}0)$	$1 - \frac{1}{4}\sqrt{5/\pi}\epsilon_1 + \frac{9}{16}\sqrt{1/\pi}\epsilon_2 - \frac{5}{32}\sqrt{13/\pi}\epsilon_3 - \frac{1}{64}\sqrt{6006/\pi}\epsilon_4$
$(11\bar{2}0)$	$1 - \frac{1}{4}\sqrt{5/\pi}\epsilon_1 + \frac{9}{16}\sqrt{1/\pi}\epsilon_2 - \frac{5}{32}\sqrt{13/\pi}\epsilon_3 + \frac{1}{64}\sqrt{6006/\pi}\epsilon_4$

Table 5.2. Interfacial free energy expansion in terms of spherical harmonics for the different crystallographic planes studied in this work. (0001) corresponds to the basal plane, $(10\bar{1}0)$ to the primary prismatic and $(11\bar{2}0)$ to the secondary prismatic.

with the simulation results for $\widetilde{\gamma}$ allow for the calculation of ϵ_k and γ_0. With these, the interfacial free energy is obtained with the equations provided in Table 5.2.

In summary, we simulate the interface under coexistence conditions and obtain an average amplitude, h_q, for each wave vector, q, via Eq. 5.1 by defining an interfacial profile, $h(x_n)$, for many independent configurations. Then, $\widetilde{\gamma}(q)$ is obtained by means of Eq. 5.2. Once $\widetilde{\gamma}$ has been calculated for different orientations we solve the system of equations given in Table 5.3 to obtain γ_0 and the anisotropy parameters ϵ_k. Finally, we use the calculated γ_0 and ϵ_k to obtain the interfacial free energy of each plane via the expressions given in Table 5.2.

$\vec{u}$	$\vec{n}$	$\widetilde{\gamma}(\vec{u},\vec{n})/\gamma_0$
0001	$11\bar{2}0$	$1 - \sqrt{5/\pi}\epsilon_1 - \frac{27}{2}\sqrt{1/\pi}\epsilon_2 - 10\sqrt{13/\pi}\epsilon_3$
$10\bar{1}0$	$11\bar{2}0$	$1 + \frac{5}{4}\sqrt{5/\pi}\epsilon_1 - \frac{171}{16}\sqrt{1/\pi}\epsilon_2 + \frac{205}{32}\sqrt{13/\pi}\epsilon_3 + \frac{5}{64}\sqrt{6006/\pi}\epsilon_4$
$10\bar{1}0$	0001	$1 - \frac{1}{4}\sqrt{5/\pi}\epsilon_1 + \frac{9}{16}\sqrt{1/\pi}\epsilon_2 - \frac{5}{32}\sqrt{13/\pi}\epsilon_3 + \frac{35}{64}\sqrt{6006/\pi}\epsilon_4$
$11\bar{2}0$	$10\bar{1}0$	$1 + \frac{5}{4}\sqrt{5/\pi}\epsilon_1 - \frac{171}{16}\sqrt{1/\pi}\epsilon_2 + \frac{205}{32}\sqrt{13/\pi}\epsilon_3 - \frac{5}{64}\sqrt{6006/\pi}\epsilon_4$
$11\bar{2}0$	0001	$1 - \frac{1}{4}\sqrt{5/\pi}\epsilon_1 + \frac{9}{16}\sqrt{1/\pi}\epsilon_2 - \frac{5}{32}\sqrt{13/\pi}\epsilon_3 - \frac{35}{64}\sqrt{6006/\pi}\epsilon_4$

Table 5.3. Expansions for the stiffness for the different orientations studied.

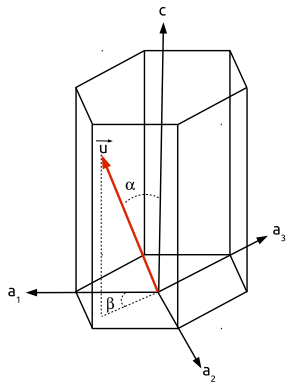

Figure 5.3. Hexagonal reference system for the ice Ih structure. The vector $\vec{u}$ determines the crystallographic plane exposed at the interface and it is characterized by the angles α and β.

5.3.1 Simulation details

To simulate our system we have employed the Molecular Dynamics package GROMACS [24, 25]. Production runs for a total time of $\sim 0.5\mu s$ were carried out in the NVT ensemble with the time step for the Velocity-Verlet integrator fixed to 0.003 ps, and snapshots were saved every 75 ps. The temperature was set to 248.5 K (close to the reported melting temperature of the model [7]) and the density was fixed close to an average value between the coexistence densities at 1 bar of liquid water and ice-Ih. At these thermodynamic conditions the interface fluctuates but the relative ice/water amount stays constant throughout the simulation. To fix the temperature we employed a velocity-rescale thermostat [26] with a relaxation time of 2 ps.

Orientation	L_xxL_yx$L_z(nm^3)$	Molecules
(Basal)[pII]	18.7696x1.8039x9.3319	10112
(pI)[Basal]	18.0134x2.1991x8.0808	10240
(pI)[pII]	17.6430x2.3491x7.8227	10368
(pII)[Basal]	17.9927x2.2047x8.3875	10670
(pII)[pI]	18.3690x1.8037x8.3928	8896

Table 5.4. System size for all ice-water orientations studied in this work.

An initial configuration in which water and ice coexist at 1 bar is prepared as described in Ref. [18]. The L_x and L_y axis of the simulation box are carefully chosen to avoid any stress in the crystal lattice [18, 27]. The size and crystal orientation of the simulated systems are summarized in Table 6.1. The box geometry with a long

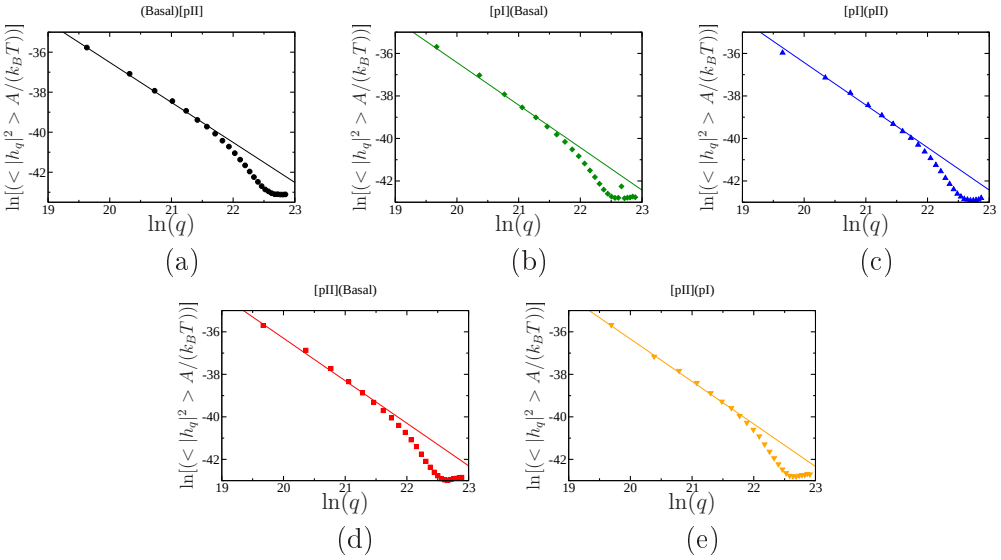

Figure 5.4. Plots of $\ln[< |h_q|^2 > A/(k_BT)]$ vs $\ln(q)$ for all ice-water orientations studied in this work. $< |h_q|^2 > A/(k_BT)$ is given in m^3/N and q is given in m^{-1}. Symbols are our simulation data and straight lines are linear fits of slope minus 2 to the low-q data. The intercept of such fits is $-\ln(\widetilde{\gamma})$.

x axis (see Fig. 5.1) allows for the study of long wave-length capillary waves without having a prohibitively large number of molecules in the system. Moreover, it allows to easily control the direction of wave propagation. It has been shown that the chosen box geometry with a large L_x/L_y ratio gives the same stiffness as boxes with L_x/L_y close to 1 [18, 28].

5.4 Results

5.4.1 Stiffness

By simulating the interface for a long time (~ 0.5 μs) we gather thousands of configurations and obtain interfacial profiles, $h(x_n)$, for each of the two ice-water interfaces present in the simulation box. Then we Fourier-transform each $h(x_n)$ (Eq. 5.1) to obtain estimates of $|h_q|^2$, which we average to get $< |h_q|^2 >$. For a rough interface, by representing $\ln[< |h_q|^2 > A/(k_BT)]$ vs $\ln(q)$ we should obtain, in the q regime where Eq. 5.2 holds, a straight line of slope minus 2 and intercept $-\ln(\widetilde{\gamma})$. Such plots are shown in Fig. 5.4 for all orientations studied in this work. Symbols correspond to our simulation data and straight lines to a linear fit with slope minus 2 to the low-q points. As expected from Eq. 5.2 the fit describes quite well our data, at least for the low-q regime, allowing us to get $\widetilde{\gamma}$ from the intercept. The values of $\widetilde{\gamma}$ thus obtained are reported in Table 5.5.

Crystal Orientation	$\widetilde{\gamma}_{iw}(mN/m)$
(Basal)[pII]	29.8
(pI)[Basal]	28.1
(pI)[pII]	28.1
(pII)[Basal]	24.7
(pII)[pI]	25.1

Table 5.5. Stiffness of all ice-water orientations studied in this work.

Notice that the very good fit of the capillary wave spectrum to Eq. 5.2 indicates that all three crystal faces studied are rough. This observation is further confirmed by visual inspection of snapshots, as can be seen in Figs. 5.1 and 5.2. Experimental studies on the other hand indicate that ice crystals in coexistence with water at about the triple point have a faceted basal plane, and a completely circular perimeter [29]. Such observation is compatible with prismatic planes which are rough, but indicate a basal plane that is below the roughening transition even at the triple point. Even though the experiments of Ref. [29] suggest that the basal plane is not rough, at least for the lengthscales accessible to our simulations the basal plane shows a rough character that enables the calculation of its stiffness and its interfacial free energy by means of the Capillary Fluctuation Method.

5.4.2 Interfacial free energy

Once the stiffness is known for a set of different orientations, we can obtain the interfacial free energy by solving the system of equations given in Table 5.3 and working out the anisotropy parameters, ϵ_k, and the orientationally averaged γ, γ_0. With ϵ_k and γ_0 one can obtain the interfacial free energy for each crystal plane via the expressions given in Table 5.2. Unfortunately, the equations of Table III are not linearly independent, and it is not possible to obtain all 4 anisotropy parameters plus γ_0. In Ref. [30] Sun *et al.* dealt with a similar problem in their study of the crystal/melt interface of Mg, which also exhibits a crystal structure with hexagonal point group symmetry. In this study, it was noticed that some of the ϵ_k hardly contributed to the anisotropy, and could be safely set equal to 0, such that the stiffness data could be accurately fitted with the remaining ϵ_k. Specifically, it was shown that ϵ_1 was necessary to obtain an accurate fit and that the anisotropy parameter ϵ_4 was necessary to resolve the anisotropy. The other two anisotropy parameters, ϵ_2 and ϵ_3, were made equal to zero. Despite the rather different substance studied, our data are completely consistent with this observation, and we have therefore followed the same approach. With this strategy,

Crystal Orientation	TIP4P/2005	TIP4P	TIP4P-Ew
Basal	27(2)	24.5(6)	25.5(7)
Prismatic I	28(2)	27.6(7)	28.9(8)
Prismatic II	28(2)	27.5(7)	28.3(7)

Table 5.6. Interfacial free energy of the ice-water interface, in mN/m, for different crystal orientations and water models. Values for the TIP4P and TIP4P-Ew have been taken from Ref. [4].

we obtain an orientationally averaged interfacial free energy for the TIP4P/2005 model of $\gamma_0 = 27(2)$mN/m. This is in good agreement with the value of $\gamma_0 = 29(3)$mN/m recently estimated from measurements of the critical nucleus size for the same model [9]. It is also similar to the value of γ_0 obtained for other water models in Ref. [4]. In fact, an average of the γ_{iw} calculated for different planes in Ref. [4] gives 26.5 mN/m for the TIP4P model and 27.5 mN/m for the TIP4P-Ew. The comparison with the experiment is not so straightforward as there is not a definite experimental value for γ_0. There are published values ranging from 25 to 35 mN/m [1, 31]. The only thing we can say is that the value we get for the TIP4P/2005 model is at least within the range of the reported experimental values. We have also calculated the interfacial free energy of the different planes and show the results in Table 5.6. We observe a small anisotropy between different planes. It seems that the basal plane has the smallest interfacial free energy. However, the uncertainty of our calculations does not allow us concluding anything definite in this respect. In Table 5.6 we also compare our results with those obtained in Ref. [4] for the TIP4P and TIP4P-Ew models. The similarity between all TIP4P family models is quite strong and, within the error bar, all models give the same interfacial free energy.

5.4.3 Interface structure

Density profile

In order to analyze the structure of the interface we measure the density profile along the z direction, perpendicular to the interface. Such a study must be taken with some caution, however. The width of the interface has an intrinsic contribution, that is characteristic of the substance studied, but also shows an additional capillary wave term, that depends logarithmically on the interface area.[32, 33, 34, 35] For that reason, average profiles extracted from a simulation are not strictly intrinsic properties of the substance, but also depend on the system dimensions. Since the capillary roughening shows a logarithmic dependence on the lateral dimensions, however, the correction to the intrinsic contribution that is typical in a finite simulation box is quite small. Be as

it may, the results that are obtained set an upper bound for the intrinsic contribution. Furthermore, since all faces studied have a rather similar lateral dimension, the comparison between different crystal orientations also remains meaningful despite the capillary wave roughening.

In Fig. 5.5 the density is plotted along the z direction for four different orientations corresponding to the basal plane and to both prismatic planes. As a consequence of the geometry of our simulations (see Fig. 5.1) two interfaces can be observed for each system. To obtain these density profiles we use bins of 0.05 σ and average over a time gap of $\sim$ 35 ns. Using a small bin width allows us to observe the different crystal layers along the system. The horizontal dotted-dashed lines in Fig. 5.5 correspond to the average bulk density of the fluid phase. As it should be, the density given by the profile coincides with the bulk density in the middle of the phase. Profiles given in Figs. 5.5 (c) and (d) correspond to two different wave propagation directions for the same interfacial plane (the primary prismatic plane). As expected, both density profiles are equivalent. Note that the profile corresponding to the basal plane (Fig. 5.5 (a)) shows the twin peaks characteristic of hexagonal planes.

The measure of the thickness of the interface is a somewhat arbitrary task since one has to establish a criterion to locate the interface borders. In order to determine these borders we consider that the interface begins when a density peak does not reach the 90% of the average peak height in the middle of the crystal slab, and that it ends when the density profile becomes flat. We show the interfacial borders thus obtained as dashed vertical lines in Fig. 5.5. We obtain an interfacial width of about 4-5 molecular diameters for all studied planes. These values are similar, but somewhat larger than the ~ 3 molecular diameters reported in Ref. [36] for another TIP4P family model (the TIP4P) and a different system size.

Hexagonal versus cubic ice

As previously mentioned, in order to get an interface profile, $h(x_n)$, we first need to identify the molecules belonging to the ice phase. This is done by means of the $\bar{q}_l$ order parameter proposed by Lechner and Dellago [17]. The order parameter is a scalar number that is assigned to each molecule according to the degree of orientational order in its local environment. In Fig. 5.6 we plot $\bar{q}_6$ versus $\bar{q}_4$ for 3600 bulk molecules of liquid water (magenta), of ice-Ih (cyan) and of ice-Ic (orange). Clearly, $\bar{q}_6$ is a good parameter to distinguish the fluid from either ice polymorph. The $\bar{q}_6$ threshold we use for that purpose is $\bar{q}_{6,t} = 0.34$ (horizontal dashed line in Fig. 5.6). Thus, if a particle has a $\bar{q}_6$ value larger than $\bar{q}_{6,t}$ it is labelled as solid-like, and vice-versa. As it can be seen in Fig. 5.6, molecules belonging to ice-Ih and ice-Ic polymorphs can be distinguished with the $\bar{q}_4$ order parameter with a threshold of $\bar{q}_{4,t} = 0.41$ (vertical dashed-dotted line in Fig. 5.6).

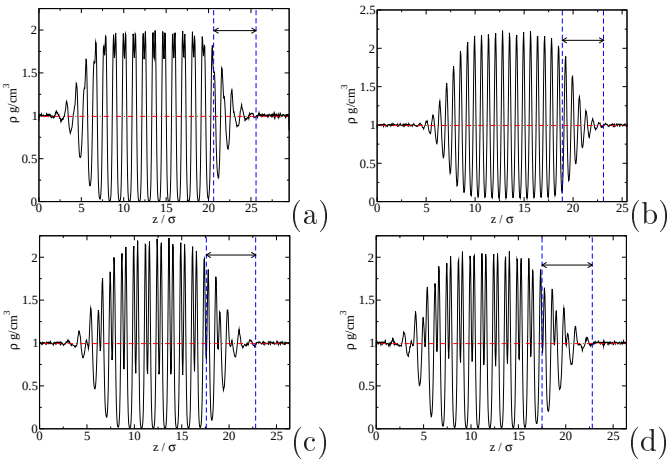

Figure 5.5. Density profile along the z direction (perpendicular to the interface) for four different orientations: (a) (Basal)[pII]; (b) (pII)[basal]; (c) (pI)[basal]; and (d) (pI)[pII]. We calculate density profiles with slabs of thickness 0.05σ. Horizontal dotted-dashed lines correspond to the average bulk density of the fluid phase. Vertical dashed lines correspond to the approximate location of the interface borders.

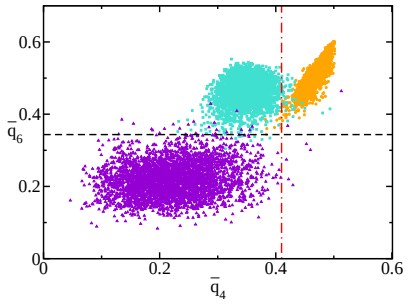

Figure 5.6. Values of the $\bar{q}_6$ versus the $\bar{q}_4$ order parameter [17] for 3600 molecules of the bulk liquid (magenta), ice Ih (cyan), and ice Ic (orange) phases equilibrated under coexistence conditions (1 bar and 250 K). A cut-off distance of 3.5 Åwas used to calculate the order parameter. The dashed black line represents the threshold used to distinguish solid from liquid-like particles $\bar{q}_{6,t} = 0.34$ and the dashed-dotted red line represents the threshold to discriminate between ice Ic and ice Ih $\bar{q}_{4,t} = 0.41$.

Initially, the system is prepared by putting an ice-Ih slab in contact with liquid water. Therefore, by analysing the $\bar{q}_6 - \bar{q}_4$ map of the initial configuration one would obtain points in the region of the pink and the cyan clouds of Fig. 5.6. At the end of the simulations all orientations where a prismatic plane is exposed only show these two clouds of points (see Fig. 5.7 a-d). Therefore, there is only liquid and ice Ih at the end of these simulations. However, the simulation where the basal plane is exposed to the liquid shows an extra cloud of points in the area corresponding to ice-Ic (Fig. 5.7 e). This suggests that some molecules with ice-Ic environment appear along the course of the simulation. To know where these molecules are located we plot in Fig. 5.8 ice molecules with $\bar{q}_{4,t} < 0.41$ in blue (ice Ih) and with $\bar{q}_{4,t} > 0.41$ in red (ice Ic). Clearly, thin ice-Ic layers have developed on some regions of the ice-water interface. In Ref. [18] we show that the relaxation of crystal-fluid capillary waves is due to the continuous recrystallization and melting taking place at the interface. This relaxation mechanism allows for the epitaxial growth of ice Ic on top of the underlying ice Ih. The recrystallization/melting relaxation mechanism also explains our observation that the interfacial regions containing ice Ih and ice Ic dynamically change along the course of the simulation. The reason why this structural transformation is only present when the basal plane is exposed is that hexagonal and cubic ice differ in their stacking sequence along the direction perpendicular to the basal plane (Ice Ic stacking is diamond-like, A,B,C,A,B,C,... whereas ice Ih is wurtzite-like, A,B,A,B,...). Therefore, when the basal plane is exposed an Ic-stacking can grow on top of ice Ih, but the same is not true for the prismatic planes. By analysing a set of over 300 configurations with the basal plane exposed we observe that about 60 % of the ice in contact with water is Ic and the other 40 % is ice Ih. This is not altogether unexpected, since, at least for the TIP4P models, the free energy of ice Ic is very similar to that of ice Ih [37]. Accordingly, growth of regions of ice Ic with a negligible bulk free energy penalty can be realized if the corresponding surface free energy of the newly formed Ih-Ic and Ic-water interfaces is comparable to that of the bare Ih-water interface. The phenomenon above described resembles preferential adsorption of a metastable phase, well known in a variety of systems,[38, 39] as well as in the ice-vapour interface, which is mediated by a thin water layer [40, 41, 42]. However, in the case here studied ice-Ic does not fully cover the interface but dynamically coexists at the interface with ice-Ih.

Therefore, our simulations predict that both ice polymorphs live together in the interface at equilibrium. This is not the only situation in which hexagonal and cubic ice can be found in close contact: there is compelling experimental and simulation evidence that ice grows with a mixed Ic-Ih stacking from supercooled water [43, 44, 45, 46, 47] or from vapour deposition [48].

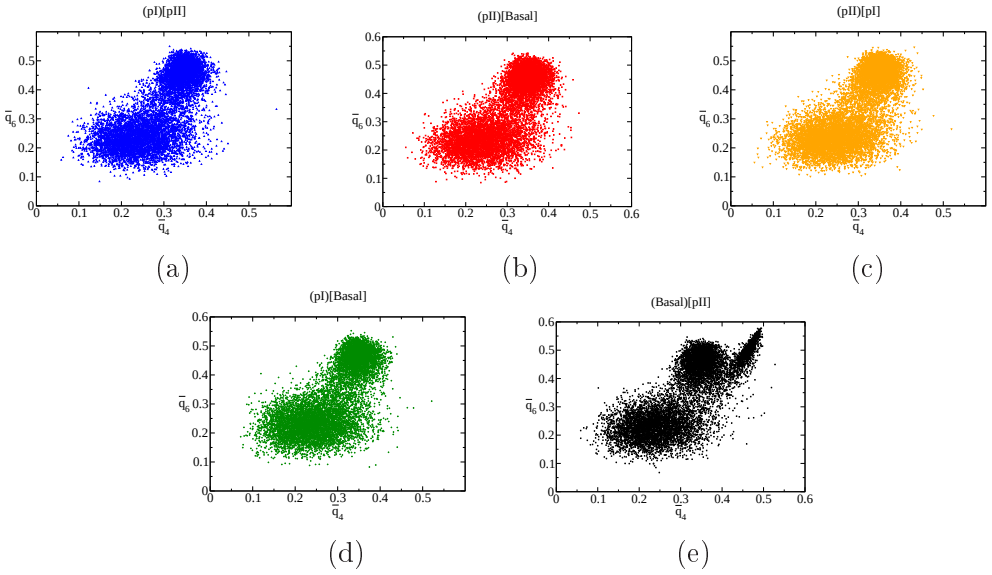

Figure 5.7. $\bar{q}_6 - \bar{q}_4$ maps for the last configuration of each of the systems studied. When the basal plane is exposed, panel (e), a cloud of points at high $\bar{q}_4$ corresponding to ice-Ic emerges.

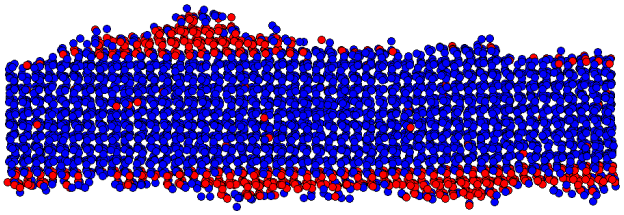

Figure 5.8. Oxygens of the molecules in the ice slab for the system in which the basal plane is exposed to the liquid. Blue: oxygen atoms with ice-Ih environment. Red: oxygen atoms with ice Ic environment.

5.5 Conclusions and outlook

In this work we use the TIP4P/2005 water model to study the ice-water interface by means of computer simulations. We simulate the ice-water interface under coexistence conditions and evaluate the interfacial stiffness and the interfacial free energy by measuring the spectrum of capillary fluctuations. We study different crystal orientations and wave propagation directions. The predictions we get from the TIP4P/2005 model are the following:

- The orientationally averaged interfacial free energy is 27(2) mN/m, in fair agreement with that obtained by analysing, for the same model, the size of critical ice nuclei with Classical Nucleation Theory [9]. Our value is also similar to that obtained for other TIP4P family models by means of a cleaving methodology [4] and is consistent with experimental estimates of the interfacial free energy that range from 25 to 35 mN/m [1].

- We obtain an interfacial free energy of 27(2), 28(2), and 28(2) mN/m for the basal, primary prismatic and secondary prismatic planes respectively. The accuracy of our calculations is not enough to establish definite conclusions about the anisotropy of the interfacial free energy, but our results suggest, in accordance with predictions for other TIP4P family models [4], that the basal plane has the lowest free energy.

- By measuring the density along the direction perpendicular to the interface we estimate an upper bound for the width of the ice-water interface of $\sim$ 4-5 molecular diameters, in fair agreement with the 3 molecular diameters obtained for the TIP4P model [36].

- The ice-water interface for the basal plane shows alternating ice-Ih/ice-Ic regions. These change dynamically due to capillary fluctuations.

In a future, it would be useful to explore how to improve the accuracy of the present methodology in order to capture the small anisotropy of the ice-water interfacial free energy. Moreover, the study of other water models could improve our understanding on the ice-water interface. Of particular interest is perhaps the TIP4P/ICE model [49], whose melting properties are close to those of real water. However, we do not expect large differences with the values reported here for the TIP4P/2005 given the similarity between all TIP4P family models studied so far (TIP4P, TIP4P-Ew and TIP4P/2005). On the other hand, it would be interesting to pursue a more quantitative analysis of the coexistence of cubic and hexagonal ice patches at the ice-water interface, like, e.g., a characterization of the typical size and relaxation times of such regions.

Acknowledgements
E. Sanz and J. Benet acknowledge financial support from the EU grant 322326-COSAAC-FP7-PEOPLE-2012-CIG and from a Spanish grant Ramon y Cajal. L.G. MacDowell and J. Benet also acknowledge financial support from project FIS2010-22047-C05-05 (Ministerio de Economia y Competitividad).

Bibliography

[1] H. R. Pruppacher, "A new look at homogeneous ice nucleation in supercooled water drops," *J. Atmosph. Sci.*, vol. 52, p. 1924, 1995.

[2] H. R. Pruppacher, "Interpretation of experimentally determined growth rates of ice crystals in supercooled water," *The Journal of Chemical Physics*, vol. 47, no. 5, pp. 1807–1813, 1967.

[3] H. J. White, J. V. Sengers, D. B. Neumann, and J. C. Bellows, *Release on the Surface Tension of Ordinary Water Substance*. IAPWS, 1995.

[4] R. L. Davidchack, R. Handel, J. Anwar, and A. V. Brukhno, "Ice ih-water interfacial free energy of simple water models with full electrostatic interactions," *Journal of Chemical Theory and Computation*, vol. 8, no. 7, pp. 2383–2390, 2012.

[5] R. Handel, R. L. Davidchack, J. Anwar, and A. Brukhno, "Direct calculation of solid-liquid interfacial free energy for molecular systems: TIP4P ice-water interface," *Phys. Rev. Lett.*, vol. 100, p. 036104, Jan 2008.

[6] J. Q. Broughton and G. H. Gilmer, "Molecular dynamics investigation of the crystal–fluid interface. VI. Excess surface free energies of crystal–liquid systems," *J. Chem. Phys.*, vol. 84, no. 10, pp. 5759–5768, 1986.

[7] J. L. F. Abascal and C. Vega, "A general purpose model for the condensed phases of water: Tip4p/2005," *J. Chem. Phys.*, vol. 123, p. 234505, 2005.

[8] C. Vega and J. L. F. Abascal, "Simulating water with rigid non-polarizable models: a general perspective," *Phys. Chem. Chem. Phys.*, vol. 13, pp. 19663–19688, 2011.

[9] E. Sanz, C. Vega, J. R. Espinosa, R. Caballero-Bernal, J. L. F. Abascal, and C. Valeriani, "Homogeneous ice nucleation at moderate supercooling from molecular simulation," *Journal of the American Chemical Society*, vol. 135, no. 40, pp. 15008–15017, 2013.

[10] X.-M. Bai and M. Li, "Calculation of solid-liquid interfacial free energy: A classical nuclea tion theory based approach," *J. Chem. Phys.*, vol. 124, no. 12, p. 124707, 2006.

[11] M. Volmer and A. Weber *Z. Phys. Chem.*, vol. 119, p. 277, 1926.

[12] R. Becker and W. Doring *Ann. Phys.*, vol. 24, pp. 719–752, 1935.

[13] J. J. Hoyt, M. Asta, and A. Karma, "Method for computing the anisotropy of the solid-liquid interfacial free energy," *Phys. Rev. Lett.*, vol. 86, pp. 5530–5533, Jun 2001.

[14] R. L. Davidchack, J. R. Morris, and B. B. Laird, "The anisotropic hard-sphere crystal melt interfacial free energy from fluctuations," *J. Chem. Phys.*, vol. 125, p. 094710, 2006.

[15] J. R. Morris and X. Song, "The anisotropic free energy of the Lennard-Jones crystal-melt interface," *J. Chem. Phys.*, vol. 119, no. 7, pp. 3920–3925, 2003.

[16] J. Wang, P. A. Apte, J. R. Morris, and X. C. Zeng, "Freezing point and solid-liquid interfacial free energy of stockmayer dipolar fluids: A molecular dynamics simulation study," *The Journal of Chemical Physics*, vol. 139, no. 11, p. 114705, 2013.

[17] W. Lechner and C. Dellago, "Accurate determination of crystal structures based on averaged local bond order parameters," *The Journal of Chemical Physics*, vol. 129, no. 11, p. 114707, 2008.

[18] J. Benet, L. G. MacDowell, and E. Sanz, "Computer simulation study of surface wave dynamics at the crystal–melt interface," *J. Chem. Phys.*, vol. 141, p. 024307, 2014.

[19] D. S. Fisher and J. D. Weeks, "Shape of crystals at low temperatures: Absence of quantum roughening," *Phys. Rev. Lett.*, vol. 50, pp. 1077–1080, Apr 1983.

[20] V. Privman, "Fluctuating interfaces, surface tension and capillary waves: An introduction," vol. 3, pp. 857–877, 1992.

[21] D. Jasnow, "Critical phenomena at interfaces," *Rep. Prog. Phys.*, vol. 47, no. 9, p. 1059, 1984.

[22] D. Nelson, T. Piran, and S. Weinberg, *Statistical Mechanics of Membranes and Surfaces*. Word Scientific, Singapore, 2004.

[23] M. Kara and K. Kurki-Suonio, "Symmetrized multipole analysis of orientational distributions," *Acta Crystallographica Section A*, vol. 37, pp. 201–210, Mar 1981.

[24] H. Berendsen, D. van der Spoel, and R. van Drunen, "Gromacs: A message passing parallel molecular dynamics implementation," *Computer Physics Communications*, vol. 91, no. 1 - 3, pp. 43 – 56, 1995.

[25] B. Hess, C. Kutzner, D. van der Spoel, and E. Lindahl, "Gromacs 4: Algorithms for highly efficient, load-balanced, and scalable molecular simulation," *Journal of Chemical Theory and Computation*, vol. 4, no. 3, pp. 435–447, 2008.

[26] G. Bussi, D. Donadio, and M. Parrinello, "Canonical sampling through velocity rescaling," *J. Chem. Phys.*, vol. 126, no. 1, p. 014101, 2007.

[27] D. Frenkel, "Simulations: the dark side," *arXiv:12111.440*, 2012.

[28] R. E. Rozas and J. Horbach, "Capillary wave analysis of rough solid-liquid interfaces in nickel," *Europhys. Lett.*, vol. 93, no. 2, p. 26006, 2011.

[29] M. Maruyama, T. Nishida, and T. Sawada, "Crystal shape of high-pressure ice ih in water and roughening transition of the $(10\bar{1}0)$ plane," *The Journal of Physical Chemistry B*, vol. 101, no. 32, pp. 6151–6153, 1997.

[30] D. Y. Sun, M. I. Mendelev, C. A. Becker, K. Kudin, T. Haxhimali, M. Asta, J. J. Hoyt, A. Karma, and D. J. Srolovitz, "Crystal-melt interfacial free energies in hcp metals: A molecular dynamics study of Mg," *Phys. Rev. B*, vol. 73, p. 024116, Jan 2006.

[31] S. C. Hardy, "A grain boundary groove measurement of the surface tension between ice and water," *Philosophical Magazine*, vol. 35, no. 2, pp. 471–484, 1977.

[32] J. D. Weeks, "Structure and thermodynamics of the liquid–vapor interface," *J. Chem. Phys.*, vol. 67, no. 7, pp. 3106–3121, 1977.

[33] B. M. Ocko, X. Z. Wu, E. B. Sirota, S. K. Sinha, and M. Deutsch, "X-ray reflectivity study of thermal capillary waves on liquid surfaces," *Phys. Rev. Lett.*, vol. 72, pp. 242–245, Jan 1994.

[34] A. Werner, F. Schmid, M. Muller, and K. Binder, "Anomalous size-dependence of interfacial profiles between coexisting ph ases of polymer mixtures in thin-film geometry: A monte carlo simulation," *J. Chem. Phys.*, vol. 107, no. 19, pp. 8175–8188, 1997.

[35] L. G. MacDowell, J. Benet, N. A. Katcho, and J. M. Palanco, "Disjoining pressure and the film-height-dependent surface tension of thin liquid films: New insight from capillary wave fluctuations," vol. 206, no. 0, pp. 150–171, 2014.

[36] O. A. Karim and A. D. J. Haymet, "The ice/water interface: A molecular dynamics simulation study," *The Journal of Chemical Physics*, vol. 89, no. 11, pp. 6889–6896, 1988.

[37] E. Sanz, C. Vega, J. L. F. Abascal, and L. G. MacDowell, "Phase diagram of water from computer simulation," *Phys. Rev. Lett.*, vol. 92, p. 255701, 2004.

[38] Y. Cao and E. H. Conrad, "Approach to thermal roughening of ni(110): A study by high-resolution low-energy electron diffraction," *Phys. Rev. Lett.*, vol. 64, pp. 447–450, Jan 1990.

[39] M. Müller, L. G. MacDowell, P. Virnau, and K. Binder, "Interface properties and bubble nucleation in compressible mixtures containing polymers," *J. Chem. Phys.*, vol. 117, pp. 5480–5496, 2002.

[40] M. Elbaum, "Roughening transition observed on the prism facet of ice," *Phys. Rev. Lett.*, vol. 67, pp. 2982–2985, Nov 1991.

[41] L. A. Wilen, J. S. Wettlaufer, M. Elbaum, and M. Schick, "Dispersion-force effects in interfacial premelting of ice," vol. 52, pp. 12426–12433, Oct 1995.

[42] K. G. Libbrecht, "The physics of snow crystals," *Rep. Prog. Phys.*, vol. 68, pp. 855–895, 2005.

[43] T. L. Malkin, B. J. Murray, A. V. Brukhno, J. Anwar, and C. G. Salzmann, "Structure of ice crystallized from supercooled water," *Proceedings of the National Academy of Sciences*, vol. 109, no. 4, pp. 1041–1045, 2012.

[44] E. B. Moore and V. Molinero, "Is it cubic? ice crystallization from deeply supercooled water," *Phys. Chem. Chem. Phys.*, vol. 13, pp. 20008–20016, 2011.

[45] M. Seo, E. Jang, K. Kim, S. Choi, and J. S. Kim, "Understanding anisotropic growth behavior of hexagonal ice on a molecular scale: A molecular dynamics simulation study," *The Journal of Chemical Physics*, vol. 137, no. 15, p. 154503, 2012.

[46] M. A. Carignano, "Formation of stacking faults during ice growth on hexagonal and cubic substrates," *The Journal of Physical Chemistry C*, vol. 111, no. 2, pp. 501–504, 2007.

[47] D. Rozmanov and P. G. Kusalik, "Temperature dependence of crystal growth of hexagonal ice (Ih)," *Phys. Chem. Chem. Phys.*, vol. 13, pp. 15501–15511, 2011.

[48] W. F. Kuhs, C. Sippel, A. Falenty, and T. C. Hansen, "Extent and relevance of stacking disorder in ice Ic," *Proceedings of the National Academy of Sciences*, vol. 109, no. 52, pp. 21259–21264, 2012.

[49] J. L. F. Abascal, E. Sanz, R. G. Fernandez, and C. Vega, "A potential model for the study of ices and amorphous water: TIP4P/Ice," *J. Chem. Phys.*, vol. 122, p. 234511, 2005.

[50] V. Heinonen, A. Mijailovic, C. V. Achim, T. Ala-Nissila, R. E. Rozas, J. Horbach, and H. Löwen, "Bcc crystal-fluid interfacial free energy in yukawa systems," *The Journal of Chemical Physics*, vol. 138, no. 4, pp. –, 2013.

[51] A. Härtel, M. Oettel, R. E. Rozas, S. U. Egelhaaf, J. Horbach, and H. Löwen, "Tension and stiffness of the hard sphere crystal-fluid interface," *Phys. Rev. Lett.*, vol. 108, p. 226101, May 2012.

[52] J. Benet, L. G. MacDowell, and E. Sanz, "A study of the ice-water interface using the tip4p/2005 water model," *Phys. Chem. Chem. Phys.*, vol. 16, pp. 22159–22166, 2014.

[53] J. R. Morris and X. Song, "The anisotropic free energy of the Lennard Jones crystal melt interface," *J. Chem. Phys.*, vol. 119, p. 3920, 2003.

Appendix A: Alternative Analysis

The aim of this appendix, not included in the original publication, is to evaluate the influence of the way of obtaining the thermodynamic limit of the interfacial stiffness.

As seen in Chapter 3 there exist two different methods to achieve this. The first one, which is referred as method 1 consists in fitting the data to the expression given by the capillary wave theory

$$\widetilde{\gamma}(q) = \widetilde{\gamma}_0 + bq^2 + cq^4 \tag{5.5}$$

and has been employed in several works [50, 51]. The second one, which is referred as method 2, provides the thermodynamic limit of the interfacial stiffness by looking for the regime where the stiffness is independent of the wavevector. Such regime can be found from Eq. 5.2 by rearranging it and taking logarithms:

$$\ln \frac{A\left\langle |h_q^2| \right\rangle}{k_B T} = -\ln \widetilde{\gamma} - 2\ln q \tag{5.6}$$

Thus, by plotting $\ln(A < |h_q|^2 > /(k_B T))$ vs $\ln q$ we should obtain, at least in the low q regime, a region where the data can be fitted to straight line of slope -2. The intercept of such line is $-\ln(\widetilde{\gamma})$. This method has also been widely used [52, 28, 53].

In the main text we have employed method 2 to obtain the thermodynamic limit of the interfacial stiffness. In this appendix we employ method 1 to compare the results obtained for both the stiffness and the interfacial free energy by the two different methods.

In Fig. 6.10 we plot $\widetilde{\gamma}(q)$ vs q for all the orientations studied in this work, and fit our data to Eq. 5.5. To make this fit we only use the points which are inside the boxes. The results thus obtained for the interfacial stiffness are shown in Table 5.7, where they are compared with those obtained by method 2. As it can be seen method 1 provides results wich are systematically lower than those obtained by method 2.

Once we have obtained the interfacial stiffnesses we follow the same procedure of the main text to evaluate the interfacial free energies. The results are shown in Table 5.8 where they are compared with those obtained by method 2.

As expected from the stiffnesses values obtained, method 1 gives also lower values for the average value of γ_0 as well as for γ of each of the individual crystallographic planes.

This behaviour was already explained in Chapter 3 where it is noticed that drawback of method 2 is that it looks for a region where $\widetilde{\gamma}$ is independent of the wavevector, which is hardly accessible in simulations.

In spite of this, the results obtained by the two different methods are fully consistent, as they lie in the range of error and provide the same order of energies for the different planes.

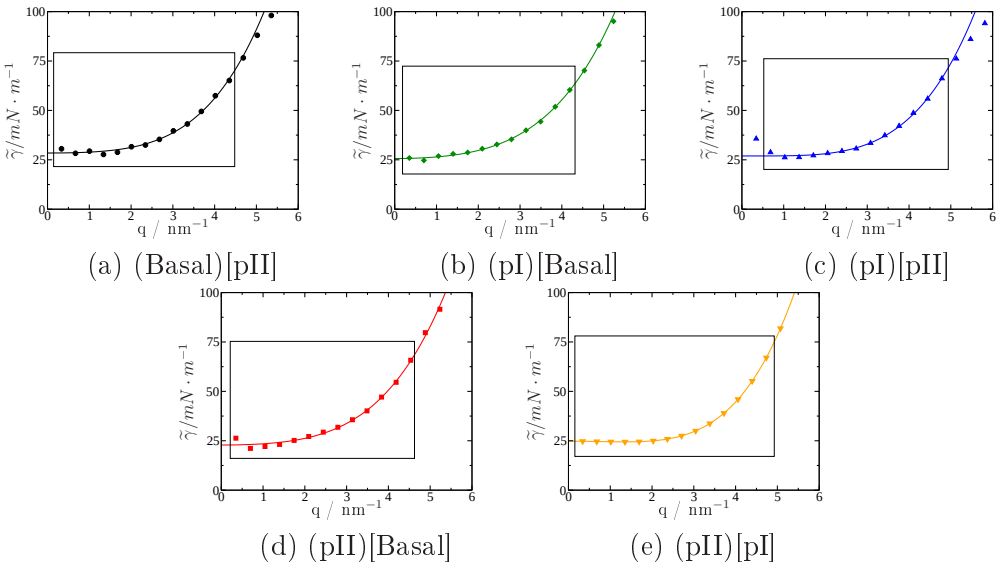

Figure 5.9. Plots of the stiffness vs q for all ice–water orientations studied in this work. Symbols are our simulation data and lines are linear fits of the points inside the box to Eq. 5.5.

Orientation	$\widetilde{\gamma}$/mN·m^{-1}	
	Method 1	Method 2
(Basal)[pII]	28.4	29.8
(pI)[Basal]	25.6	28.1
(pI)[pII]	27.0	28.1
(pII)[Basal]	22.8	24.7
(pII)[pI]	24.8	25.1

Table 5.7. Stiffness of all orientations as obtained by the two different methods.

Crystal plane	γ/mN·m^{-1}	
	Method 1	Method 2
γ_0	26(2)	27(2)
Basal	25(2)	27(2)
Prismatic I	26(2)	28(2)
Prismatic II	26(2)	28(2)

Table 5.8. Interfacial free energies as obtained by the two different methods.

Results: Chapter 6

Structure and fluctuations of the premelted liquid film of ice at the triple point

Jorge Benet, Eduardo Sanz and Luis G. MacDowell

Departamento de Química Física, Facultad de Ciencias Químicas, Universidad Complutense de Madrid, 28040 Madrid, Spain

6.1 Abstract

In this paper we study the structure of the ice/vapor interface in the neighborhood of the triple point. Our results indicate that the bulk solid and vapor phases are separated by a thin premelted film of water. We have studied the fluctuations of the ice/film and film/vapor surfaces that separate the liquid film from the coexisting bulk phases at basal, primary prismatic and secondary prismatic planes. At large lengthscales, the complex ice/vapor interface behaves as a correlated compound system with i) a mean surface exhibiting roughness for all lengthscales studied, with fluctuations that are close but somewhat larger than the sum of the ice/water and water/vapor stiffness. ii) a thin adsorbed film of finite roughness that fluctuates on top of it. For small lengthscales below 4.2 nm, on the contrary, the ice/film and film/vapor surfaces behave very much like independent ice/water and water/vapor interfaces. Our results allow for a quantitative characterization of the extent to which the adsorbed quasi-liquid layer behaves as water, and explains recent experimental observations which have revealed the same activation energies for crystals grown in bulk vapor or bulk water.

6.2 Introduction

Snowflakes offer the opportunity to observe the beautiful structure of ice microcrystals.[1] The striking symmetry that is revealed, is related to the stability of well defined crystal facets, which intersect at the edges making well defined angles.[2] As temperature is increased, some crystal facets altogether disappear, while the edges and sides gradually blur and eventually become rounded.

Whereas ice crystals in snowflakes grow under kinetic control,[1] the process described is an illustration of a thermodynamic surface phase transition.[3, 4, 5, 6, 7, 8] These transitions, which are best characterized for independent well defined facets at equilibrium, determine overall the equilibrium crystal shape of a crystalline solid.[9, 10, 11]

In surface physics there are two main types of phase transitions, roughening and surface melting, that have been characterized on the basis of well understood solvable models.[4, 5, 6, 7, 8]

The roughening transition characterizes the thermal disorder that occurs on facets of a two phase system well away from the triple point. This transition separate smooth facets, with a low number density of defects, and small finite perpendicular fluctuations, from rough surfaces, exhibiting a large number of defects and diverging height fluctuations that do not differ at a coarse scale from those found in fluid-fluid interfaces. It is believed that when the correlation length of parallel height fluctuations becomes larger than the size of the crystal, the facet disappears and becomes round.

Surface melting characterizes a different type of transition that involves three, rather than two phases. It occurs as the crystal is heated close to a triple point. In such cases, it is often found that the metastable phase that is approached from below builds a small surface layer, of finite thickness. This process is known as premelting. Surface melting occurs in those other instances where the thickness of the premelting layer diverges as the triple point is approached, very much as in a wetting transition. Unfortunately, the relation of premelting with the corresponding equilibrium crystal shape remains unclear, and it is a matter of concern whether the premelting transition could round off the edges of a crystal shape as in roughening.[12]

Whereas these two prototypical transitions serve as benchmark to assess surface induced disorder in real systems, they may be well insufficient to describe the variety of complex surface phenomena that are found in real substances. In the case of a roughening transition, for example, one sometimes finds roughening can occur on surfaces which preserve the crystalline structure (the vertical displacements remain congruent with the lattice spacing), as in surfaces of Niquel,[13] while other reports refer to a surface disordering transition with complete loss of the translational order on the surface, as in gold.[14] Already for such simple atomic crystals, it is possible to find surfaces

that neither premelt, nor roughen, that roughen without premelting, or exhibit both roughening and premelting before the triple point is reached.[15]

Given this variety of surface phenomena, it is not unexpected to find how difficult and controversial is the characterization of equilibrium surface properties in such a common and important molecular crystal as ice.[16, 17, 18, 19, 20, 12, 21]

There is currently ample experimental evidence indicating that the ice/vapor crystal surface exhibits premelting at both the basal and prismatic planes close to the triple point.[19, 20, 12, 21] However, several features of this transition layer are still a matter of debate. Firstly, the temperature at which the premelting transition occurs, which varies from -50 °C, to a few Celsius below the triple point depending on the experimental source.[16] Secondly, there is also no consensus on the thickness of the premelting layer, which varies between 10 to several hundred Angstroms close to the triple point.[16] And finally, it is still unresolved whether the premelting layer remains finite,[17, 18, 19] or diverges (surface melting),[20, 12] at the triple point. There is at least a clear evidence that contamination of the water film of the vapor phase largely increases the size of the premelted film,[19, 22, 21], an indication that could reconcile to some extent the conflicting results and favor the hypothesis of incomplete surface melting.[17, 18, 19]

However, this observation is far from solving the puzzling surface physics of ice, since one can actually argue whether experiments have been carried out on true equilibrium crystal structures at all.[23] Indeed, controlled growth of ice crystals at about 10–20 °C below zero, usually produce prisms, with flat basal facets and hexagonal shape, whether as grown from the vapor,[17] or the liquid phase.[24] After the appearance of a thin premelting film, the hexagonal shape of such crystallites is observed to round as the triple point approaches, possibly indicating a roughening transition of the prismatic facets .[17, 24] In such studies, the basal plane is found to remain smooth, indicating no roughening of the basal orientation. Such observations are consistent with an ice surface exhibiting premelting before roughening for the prismatic face, and no roughening at all for the basal face.

On the other hand, there are claims that the equilibrium crystal shape of ice should be completely rounded above -6 °C,[25, 26, 12] an observation which would indicate fully roughened planes. In fact, x-ray reflectivity experiments have reported observation of a fully rough surface of the basal plane before the advent of premelting at about -13 °C.[20, 12] These observations seem reasonable on theoretical grounds, since theoretical estimates of the surface free energy,[23] as well as computer simulations of different ice models, indicate a very small anisotropy of the surface free energy,[27] whence, the expectation of a quasi-spherical equilibrium crystal shape.

Accordingly, it would appear that not only the thickness of the premelting film is unknown. Even the relative order of the premelting and roughening transitions, or the occurrence of the latter altogether, are still a matter of debate.

Simulation studies could be a very useful tool for the study of the ice/vapor in-

terface, since direct observation at atomic scale is possible. Studies up to date have confirmed the presence of a premelting layer, but it is difficult to determine whether these models exhibit surface melting, for problems of limited system sizes and inaccuracy in the location of the melting point.[28, 29, 30, 31] Recently, Limmer and Chandler performed extensive simulations of the ice/vapor interface, and observed clear evidence of a surface melting transition, as well as a rough solid surface of diverging correlation length.[32] This is a very careful study of surface melting, but it is arguable whether the results may be extrapolated to describe a real substance such as water. Clearly, the presence of the surface melting transition is an extremely subtle property which is likely to require a very fine molecular model to describe reliably. Indeed, it has been suggested that the absence of surface melting in water is the result of complicated many-body interactions which require to take into account the time dependent dielectric response of solid and liquid phases, as well as retardation effects. These are fine features that are well beyond the coarse scale of simple non-polarizable point charge models (let alone models that altogether ignore dispersion forces and the electric interactions of water), but can hopefully be incorporated ad-hoc in order to reanalyze the results of simpler models employed to describe at least the short range interactions.[32]

In this work we study the ice/vapor interface of the TIP4P/2005 model of water proposed by Abascal and collaborators.[33] This force field is apparently very close to the best rigid-point charge model of water,[34] and is therefore a good starting point for the study of short range contributions to surface premelting. By introducing a convenient order parameter, we are able to resolve the liquid from the solid, and study the fluctuations of the resulting solid/film and film/vapor surfaces. This offers us a unique opportunity to study for the first time the interplay between premelting and roughening of the solid/film surfaces. Our results show that both basal and prismatic faces exhibit premelting, as well as roughening well before the melting point is reached. Unfortunately, a conclusive statement is still not possible, because some limitations of the model that are unimportant in the study of bulk properties turn out to be major concerns whenever two or more phases are involved, as is the case in our study. Firstly, for reasons of numerical convenience, the dispersive interactions are cut-off at a finite distance. Secondly, the non-polarizable model is known to exhibit a static dielectric constant that is smaller for the solid than for the liquid phase, at odds with real water.[35] Finally, because of the absence of polarizability, no retardation effects are incorporated at all. Fortunately, it is expected that the range where these effects are important is beyond the film thickness observed in our simulations.[18]

6.3 Theory

6.3.1 Roughening transition of an interface

The most significant feature of a roughening transition is a divergence of the parallel and perpendicular correlations of the interface. Whereas this is essentially a general feature in all roughening processes, the detailed physics of the considered interfaces may be quite different. Here we briefly review how such transition comes about in two important cases, namely, and adsorbed premelted film, and a solid surface.

Complete roughening of an adsorbed liquid-vapor interface Consider a system with two bulk phases in coexistence (such as a solid and vapor phases), and a third metastable phase (such as a liquid) that is adsorbed between the solid and vapor. The premelted liquid film exhibits a quasi-liquid-vapor interface, which may be described in terms of its local height above the solid phase, $h(\mathbf{x})$, where $\mathbf{x}$ is a point on the plane of the substrate. In the capillary wave approximation, the free energy $H[h]$ of a given film profile is given as:

$$H_{l/v} = \int d\mathbf{x} \left(g(h) + \gamma_{lv} \sqrt{1 + (\nabla h)^2} \right) \tag{6.1}$$

The first term, $g(h)$ is a binding potential describing the effective interaction of the liquid-vapor interface with the underlying solid substrate. The second term is governed by the liquid-vapor surface tension, γ_{lv}, and penalizes increments of the surface area. Expanding the Hamiltonian to second order in the fluctuations of $h(\mathbf{x})$ away from the equilibrium film height, one finds:

$$\Delta H_{l/v} = \frac{1}{2} \int d\mathbf{x} \left(g'' h^2 + \gamma_{lv} (\nabla h)^2 \right) \tag{6.2}$$

where the primes in g'' denote differentiation with respect to h. The partition function for this Hamiltonian may be worked out by expanding $h(\mathbf{x})$ in Fourier modes. This yields the following result for the spectrum of film height fluctuations:

$$\langle h^2(q) \rangle = \frac{k_B T}{A(g'' + \gamma_{lv} q^2)} \tag{6.3}$$

This spectrum is the signature of a film with finite roughness. For wavevectors of waves that are smaller than a parallel correlation length $\xi = (\gamma_{lv}/g'')^{1/2}$, the fluctuations correspond to a rough interface, which is characterized by fluctuations with a q^{-2} power law. As the wavevector becomes small, however, g'' damps the fluctuations, which become smooth for wavelengths larger than ξ. In the limit where $g'' \to 0$, however, the correlation length becomes infinite, the power law follows down to zero wave-vectors, and the interface becomes rough on all length scales, indicating complete roughness of the interface.

Roughening transition of a solid's surface We now consider a roughening transition that does not correspond to the unbinding of a fluid film from a solid substrate, but rather, to the unbinding of the solid-liquid interface from its own underlying bulk solid substrate. Traditionally, this process has been described using so called Solid on Solid models, which describe the solid as made of prismatic columns, of discrete heights, h_i, that are multiples of the interplane spacing, b.[11, 36] At 0 K, a high symmetry surface is completely smooth, such that all columns are of equal height. Rising a column by one lattice spacing creates a defect of energy J, which, however, increases the surface entropy. The energy of a given realization of column heights may be described qualitatively using the SOS Gaussian model:

$$H_{s/l} = \frac{J}{b^2} \sum_{i,j} (h_i - h_j)^2 \tag{6.4}$$

where the sum runs over all neighboring lattices, and it is understood that the column heights are multiples of the lattice spacing.

Whereas this model offers a rather clear description of the roughening process, it is difficult to solve analytically. For this reason, it is convenient to resort to a somewhat more abstract continuum model, known as the sine-Gordon model, which has the advantage of being solvable. In this way, the energy is now written as:

$$H_{s/l} = \int d\mathbf{x} \left(\frac{1}{2} \tilde{\gamma}_{sl} (\nabla h)^2 - u \cos(\frac{2\pi}{b} h) \right) \tag{6.5}$$

Here, the discrete column heights are now transformed into a continuum surface height, $h(\mathbf{x})$, so that the squared differences of Eq. (6.4) are transformed into a squared gradient. Together with this contribution, a bulk pining field is added in order to favor surface heights that are multiples of the lattice spacing. The parameter $\tilde{\gamma}_{sl}$ is the interface stiffness, [7, 11, 36] which penalizes deviations from the planar configuration, while u is a bulk-surface coupling parameter which dictates the strength of the bulk pining field.

This model exhibits a roughening transition, at a temperature $T_R = 2\tilde{\gamma}_{sl}/b^2$, where the bulk-surface coupling constant effectively vanishes. Above this temperature, the bulk pining field is absent, and the Hamiltonian becomes exactly as the capillary wave Hamiltonian of fluid-fluid interfaces. For highly symmetric crystals with low anisotropy, the stiffness does not show large differences among different facets, and the roughening temperature is mainly governed by the distance between equivalent planes, b. Accordingly, high symmetry faces, with larger interplane spacing, are usually those with highest roughening temperature.

It is instructive to expand the sine-Gordon Hamiltonian to quadratic order in the surface profile. Up to an additive irrelevant constant, we obtain:[36, 37]

$$\Delta H_{s/l} = \frac{1}{2} \int d\mathbf{x} \left(\frac{4\pi^2 u}{b^2} h^2 + \tilde{\gamma}_{sl} (\nabla h)^2 \right) \tag{6.6}$$

Whence, to quadratic order in the surface height, the sine-Gordon Hamiltonian for column fluctuations is essentially equal to the Capillary Wave Hamiltonian for adsorbed films, with an effective pining strength $\upsilon = \frac{4\pi^2 u}{b^2}$ in place of g''. Accordingly, the spectrum of fluctuations is:

$$\langle h^2(q)\rangle = \frac{k_B T}{A(\upsilon + \tilde{\gamma}_{sl}\, q^2)} \tag{6.7}$$

As long as the pinning coefficient u remains finite, the surface height fluctuations are bound, and the surface is said to be smooth. If, however, $u \to 0$, the fluctuations diverge as $q \to 0$ and the surface becomes rough on all length scales. According to the theory of equilibrium crystal shapes, crystal facets of length smaller than the correlation length $(\tilde{\gamma}_{sl}/\upsilon)^{1/2}$ disappear and become round.[16]

6.3.2 Model for coupled interface fluctuations

We now attempt to provide a phenomenological description of interface fluctuations of a premelted solid-vapor interface. Consider, to be specific, a premelted water film (f), that is adsorbed on top of a bulk ice phase (i) separating it from a bulk vapor phase (v). Overall, the ice/vapor interface may be described in terms of two different dividing surfaces, one, separating solid ice from the water film, (*if*), and other, separating the film from the vapor phase (*fv*). In our phenomenological model, we describe the fluctuations of the ice/film surface using the sine-Gordon Hamiltonian, and the film/vapor surface using the Capillary Wave Hamiltonian, as follows:

$$\Delta H_{s/f/v} = \int d\mathbf{x} \left(\frac{1}{2}\tilde{\gamma}_{iw}(\nabla h_{if})^2 - u\cos(\frac{2\pi}{b}h_{if}) + g(h_{fv} - h_{if}) + \gamma_{wv}\sqrt{1 + (\nabla h_{fv})^2} \right) \tag{6.8}$$

where h_{if} and h_{fv} are the local positions of the i/f and f/v surfaces, respectively; $\tilde{\gamma}_{iw}$ is the stiffness of the i/w interface, γ_{wv} is the surface tension of the w/v interface and $g(x)$ is a local interface potential which binds the film of premelted ice to the bulk ice phase.

This Hamiltonian may be simplified by expanding to quadratic order in h_{if} and h_{fv}, as noted previously. This results in a total energy which is essentially the sum of Eq. (6.5) and Eq. (6.1), with h_{if} and h_{fv} coupled via the interface potential. The Hamiltonian may be worked out as before, by writing the film heights in Fourier modes, yielding:

$$\Delta H_{s/f/v} = \frac{1}{2}\sum_{\mathbf{q}} \left\{ [\upsilon + g'' + \tilde{\gamma}_{iw}q^2]|h_{if}^2(\mathbf{q})| + [g'' + \gamma_{wv}q^2]|h_{fv}^2(\mathbf{q})| - 2g''|h_{if}(\mathbf{q})h_{fv}^*(\mathbf{q})| \right\} \tag{6.9}$$

where we have introduced $\upsilon = 4\pi^2 u/b^2$ as the effective bulk crystal field strength, for short.

The statistical weight of this Hamiltonian, $exp(-\Delta H/k_BT)$ yields a Gaussian bivariate distribution for the surface modes analogous to that found for coupled fluid-fluid interfaces under gravity.[38, 39, 40] This can be solved immediately, providing the following result for the spectrum of fluctuations:

$$\begin{aligned}
\langle|h_{if}^2(\mathbf{q})|\rangle &= \frac{k_BT}{A}\frac{g''+\gamma_{wv}q^2}{[\upsilon+g''+\tilde{\gamma}_{iw}q^2][g''+\gamma_{wv}q^2]-g''^2} \\
\langle|h_{fv}^2(\mathbf{q})|\rangle &= \frac{k_BT}{A}\frac{\upsilon+g''+\tilde{\gamma}_{iw}q^2}{[\upsilon+g''+\tilde{\gamma}_{iw}q^2][g''+\gamma_{wv}q^2]-g''^2} \qquad (6.10)\\
\langle h_{if}(\mathbf{q})h_{fv}^*(\mathbf{q})\rangle &= \frac{k_BT}{A}\frac{g''}{[\upsilon+g''+\tilde{\gamma}_{iw}q^2][g''+\gamma_{wv}q^2]-g''^2}
\end{aligned}$$

In order to asses the significance of these equations, it is convenient to introduce parallel correlation lengths characteristic of isolated ice/water and water/vapor interfaces, $\xi_{iw}^2 = \tilde{\gamma}_{iw}/\upsilon$, and $\xi_{wv}^2 = \gamma_{wv}/g''$, respectively. This allows to distinguish a small wavevector regime, where $(\xi_{iw}^2+\xi_{wv}^2)q^2 \ll 1$, and a large wavevector regime, where the contrary holds. The fluctuations in each regime are:

$$\langle|h_{if}^2(\mathbf{q})|\rangle = \begin{cases} \dfrac{k_BT}{A}\dfrac{1}{\upsilon} & (\xi_{iw}^2+\xi_{wv}^2)q^2 \ll 1 \\ \dfrac{k_BT}{A}\dfrac{1}{\tilde{\gamma}_{iw}q^2} & (\xi_{iw}^2+\xi_{wv}^2)q^2 \gg 1 \end{cases} \qquad (6.11)$$

$$\langle|h_{fv}^2(\mathbf{q})|\rangle = \begin{cases} \dfrac{k_BT}{A}\left(\dfrac{1}{\upsilon}+\dfrac{1}{g''}\right) & (\xi_{iw}^2+\xi_{wv}^2)q^2 \ll 1 \\ \dfrac{k_BT}{A}\dfrac{1}{\gamma_{wv}q^2} & (\xi_{iw}^2+\xi_{wv}^2)q^2 \gg 1 \end{cases} \qquad (6.12)$$

$$\langle|h_{if}(\mathbf{q})h_{fv}^*(\mathbf{q})|\rangle = \begin{cases} \dfrac{k_BT}{A}\dfrac{1}{\upsilon} & (\xi_{iw}^2+\xi_{wv}^2)q^2 \ll 1 \\ \dfrac{k_BT}{A}\dfrac{g''}{\tilde{\gamma}_{iw}\gamma_{wv}q^4} & (\xi_{iw}^2+\xi_{wv}^2)q^2 \gg 1 \end{cases} \qquad (6.13)$$

Clearly, in the small wavevector regime, both the ice/fluid and the fluid/vapor fluctuations remain finite and correlated. In lengthscales that are small compared to both

ξ_{iw} and ξ_{wv}, on the contrary, both surfaces become rough and highly uncorrelated, as evidenced from the cross correlations, which decay as q^{-4} instead of q^{-2}.

Most significantly, the results allow for a clear distinction between two different scenarios, namely, 1) the case where a roughening transition has occurred before premelting. In this case, $\upsilon = 0$, and the correlations of both the ice/fluid and fluid/vapor surfaces, as well as the crossed correlations, diverge in the limit of small wavevectors, and 2) the case where the solid surface premelts before the roughening transition. Then υ remains finite, and none of the low wavevector fluctuations diverge, but rather, remain finite.

6.4 Methods

6.4.1 Model and System

Orientation	ice/water interface		ice/vapour interface	
	$L_x x L_y x L_z (nm^3)$	Molecules	$L_x x L_y x L_z (nm^3)$	Molecules
(Basal)[pII]	18.7696x1.8039x9.3319	10112	18.7696x1.8039x9.3319	4632
(pI)[Basal]	18.0134x2.1991x8.0808	10240	18.0577x2.2045x9.5000	5520
(pI)[pII]	17.6430x2.3491x7.8227	10368	17.6430x2.3491x9.0000	5760
(pII)[Basal]	17.9927x2.2047x8.3875	10670	18.0596x2.2063x9.0000	5760
(pII)[pI]	18.3690x1.8037x8.3928	8896	18.3661x1.8035x9.0000	4800

Table 6.1. System sizes of the different systems studied.

We have used the TIP4P/2005 model for real water. Our systems consist of an ice slab placed in the middle of the z direction of a rectangular simulation box of sides L_x, L_y and L_z with the interface placed at the x, y plane. Surrounding this slab there are water molecules if an ice/water system is simulated, or vacuum for an ice/vapor system.

In order to deal with a reasonable number of molecules we set $L_x >> L_y$. In this way our systems present an elongated interfacial area which allow us to study capillary waves propagating along the x direction. The values of the box sides and the number of molecules of each system are shown in Table 6.1.

To be able to analyse our systems we need to find a discrete function $h(\mathbf{x})$ describing the interface. To manage this we make use of the order parameter $\bar{q}_6$ of Lechner and Dellago [41], which allows us to distinguish between solid and liquid molecules.

When analysing water/vapor systems we follow the same procedure as in Ref. [42]. In this procedure we get rid of fluid–like molecules by making use of the order parameter and then find the biggest cluster of solid molecules.

However, for the ice/vapor system the procedure is not always the same, as we can find two different surfaces as mentioned in the introduction: the ice/film surface and the film/vapor surface. For the ice/film surface the procedure is exactly the same as for the ice/water surface, since we are interested only in solid–like molecules. On the contrary, for the film/vapor surface we are interested in the interface between a liquid–like film and a vapor. For this reason we do not make use of any order parameter and we just look for the biggest cluster, regardless it is solid or fluid. By doing this we get rid of any vapor particle.

Finally, once we have isolated the molecules which concern us for each surface we can define a discretized interface profile along the x direction, $h(\mathbf{x})$ (see Ref. [42] for a detailed description of how this is done).

6.4.2 Simulation details

We have employed the Molecular Dynamics package GROMACS [43, 44] to perform our simulations. We prepare our systems by equilibrating an ice Ih configuration at T=250K and 1 bar, close to the triple point of the model [45]. We then rescale the simulation box to the average value of L_x, L_y and L_z to avoid any stress. Next the solid is placed next to a liquid or vacuum, for ice/water and ice/vapor interfaces respectively, and equilibrated in the NVT ensemble until the energy of the systems remains stable.

Then we perform production runs of about 0.5μs in the NVT ensemble with the time step for the Velocity-Verlet integrator fixed to 0.003 ps. Snapshots were saved every 75 ps, resulting in a total of about 6500 snapshots. The temperature of the system was fixed by using the velocity-rescaling thermostat of Bussy, Donadio and Parrinello [46].

6.5 Results

Here we present results for the structure of the ice/water and ice/vapor interface of basal, primary prismatic (pI) and secondary prismatic (pII). The simulations of the ice/water interface are carried out at a temperature of T=248.5K, while those of the ice/vapor interface are simulated at T=248.7K.

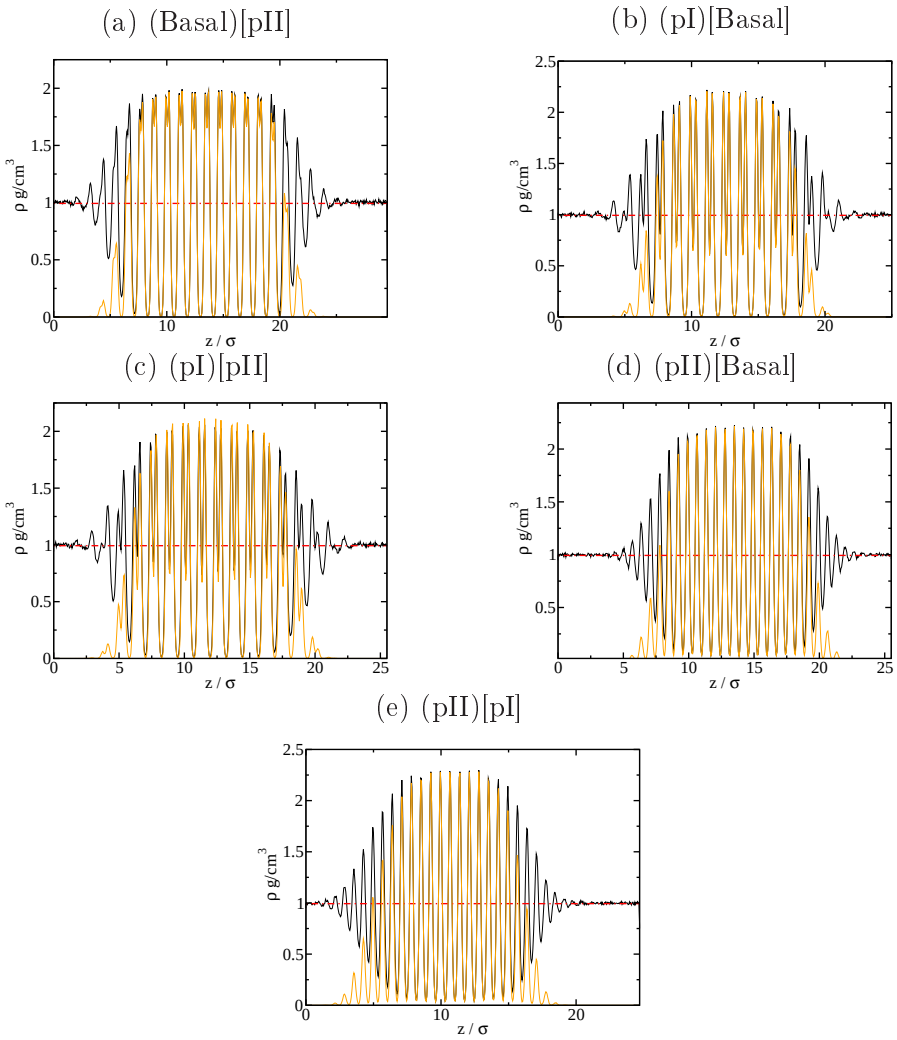

Figure 6.1. Density profiles of ice/water systems along z direction. The density profiles have been calculated with slabs of thickness 0.05σ and averaging over a time gap of $\sim$ 35 ns. Black lines correspond to the whole system and orange lines correspond to ice–like molecules. Horizontal dotted–dashed lines correspond to the average bulk density of the fluid phase.

6.5.1 Density profiles

Ice/water interface

Fig. 6.1 shows results for the density profiles across the ice/water interface for all three planes studied and different surface setups. Obviously, the density profiles are not intrinsic properties of the bulk thermodynamic field, but rather, depend also on the lateral system size. With this caution, however, we can interpret the density profiles in the mean field sense.

For each plane, it is apparent the coexistence of a well equilibrated bulk solid phase, with oscillatory behavior, and a homogeneous liquid phase of uniform density. This can be inferred by comparing the total density profile (black lines), with the density of molecules labeled as solid (orange lines), which are fully coincident within a large slab several layers thick. The bulk solid phase acts on average as a hard wall, whereupon damped oscillations of the liquid phase decay towards the bulk liquid phase due to packing correlations.

Although the thickness of the interface is almost the same in the three planes studied [27] the number of layers involved in it differs. The basal plane exhibits 5 distinct layers of ordered liquid before decaying to the bulk density; the pI plane shows four bimodal oscillations, and the pII is that exhibiting a larger number of layers with about six clear oscillations before decaying to the liquid density. In all cases, there is a clear penetration of the solid density into the region where the liquid is the majority phase. This indicates either a rough interface, or the presence of terraces, such that, along the same layer, a partially filled solid stacking is interrupted by pockets of liquid water.

As expected, the density profiles of equal planes but different geometries, do not differ from each other. Unlike the stiffness coefficients, the density profiles are properties of the plane only, not of a privileged direction for wave propagation within that plane. Hence, the density profiles of the (pI)[basal] and (pI)[pII] setups are essentially identical, and similarly, those of the (pII)[basal] and (pII)[pI] are also equal.

Ice/vapor interface

The density profiles of the ice/vapor interface are shown in Fig. 6.2 for the same planes and geometries studied previously. Again it is possible to identify a bulk solid phase several layers thick, and a vapor phase of very small density (essentially zero density in the scale of the figure). Compared to the ice/water interface, however, the presence of a third liquid phase protruding between the bulk solid and vapor phases is fairly apparent, as indicated by the high density regions with damped oscillations corresponding to water molecules labeled as liquid phase. Whence, it is concluded that the ice/vapor interface is best described as an ice/film/vapor system, with a premelted liquid film between the

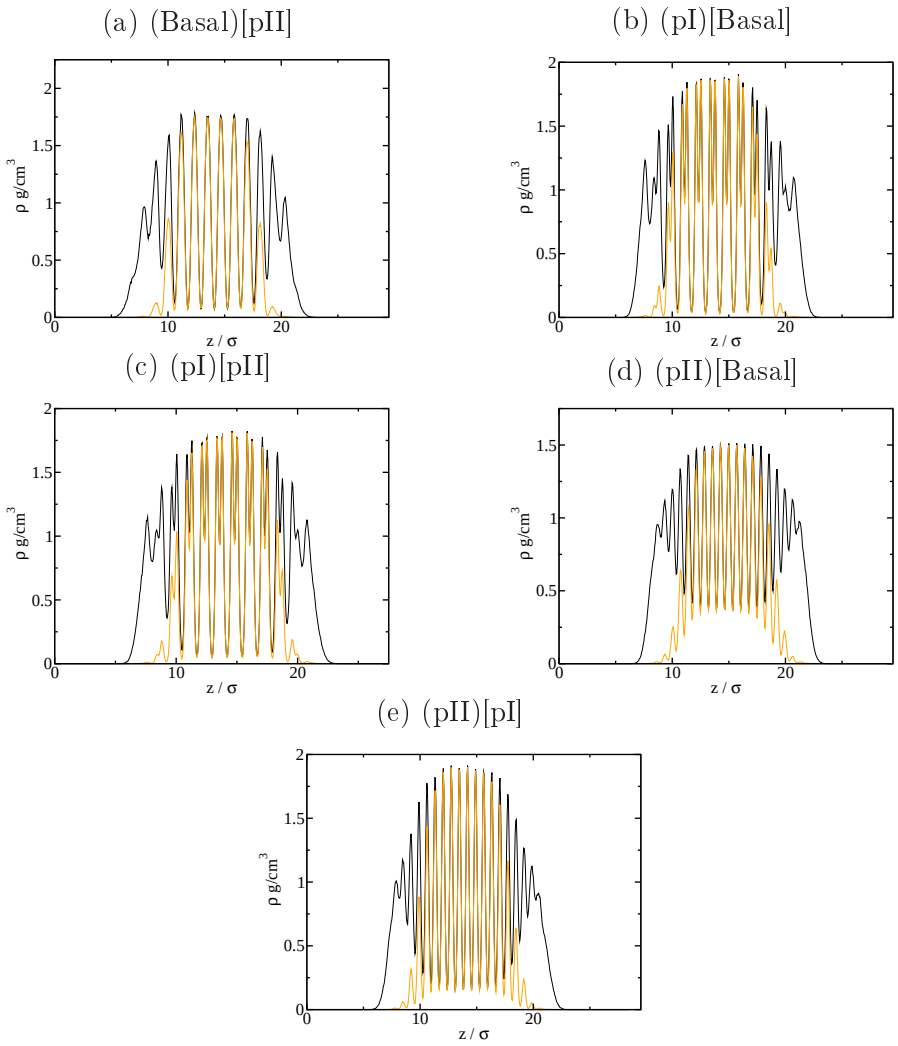

Figure 6.2. Density profiles of the ice/vapour interfaces along z direction. The density profiles have been calculated with slabs of thickness 0.05σ and averaging over a time gap of $\sim$ 35 ns. Black lines correspond to the whole system and orange lines correspond to ice–like molecules.

vapor and the solid. A full characterization of the fluctuating interface then requires to distinguish between the ice/film and the film/vapor surfaces, which could in principle, exhibit different correlations, at least at large wavevectors.

Interestingly, a comparison of the decaying oscillations of the premelted film and the ice/water interface reveals a rather similar structure. This is best seen in Fig. 6.3, where the total density profile of the ice/water and ice/vapor interfaces is compared for all planes studied. The figure clearly shows that the ice/vapor interface is nearly equal to the ice/water interface. Not only it follows the oscillations expected for the bulk solid phase, but also mimics accurately the damped oscillations of the decaying water profile, up to a point where the density suddenly falls to the bulk vapor density.

Similarly, the density profile of solid–like atoms is the same in both the ice/water and ice/vapor interfaces, both within the bulk solid slab, and in the decaying density profile. We test this in Fig. 6.4, where the density profiles of solid–like molecules for the ice/water and ice/vapor interfaces are compared. Clearly, the structure of the density oscillations is nearly equal, with only somewhat smaller solid molecule densities in the ice/vapor system. Such differences are obviously a result of the somewhat smaller chemical potential that is imposed along the sublimation line, as compared to that of the melting line.

Finally, we see from Fig. 6.4 that the structure of the film formed at the ice/vapor interface is the same as that of the liquid phase of the ice/water interface.

These set of figures clearly indicate that the ice/film boundary of the ice/vapor interface is very similar to that of the ice/water boundary, at least at temperatures a few degrees below the triple point. Interestingly, this observation is quite consistent with recent measurement of ice growth, which revealed a similar mechanism for ice crystallites grown in water or vapor bulk phases, and supports the hypothesis that the rate determining step of crystal growth, whether from the liquid or the vapor phase, is the stacking of crystal planes at the liquid/ice boundary [47].

6.5.2 Roughness

As discussed previously, the density profiles of the ice/water and the ice/vapor interface clearly reveal a considerable degree of surface disorder. This is apparent in the ice/vapor interface by the presence of a premelted film, but also, by the interpenetration of the liquid profile into the solid profile across several solid layers (Fig 6.4). This implies that the ice/film surface is either rough or has a large density of steps.

We note at this stage that our previous study of the ice/water interface for the TIP4P/2005 model,[27] revealed that all three basal, pI and pII planes where rough at least up to the largest length scale of our simulation box, i.e., about $\lambda = 17.6nm$.

In Fig. 6.5 we plot the spectrum of capillary wave fluctuations for the ice/film

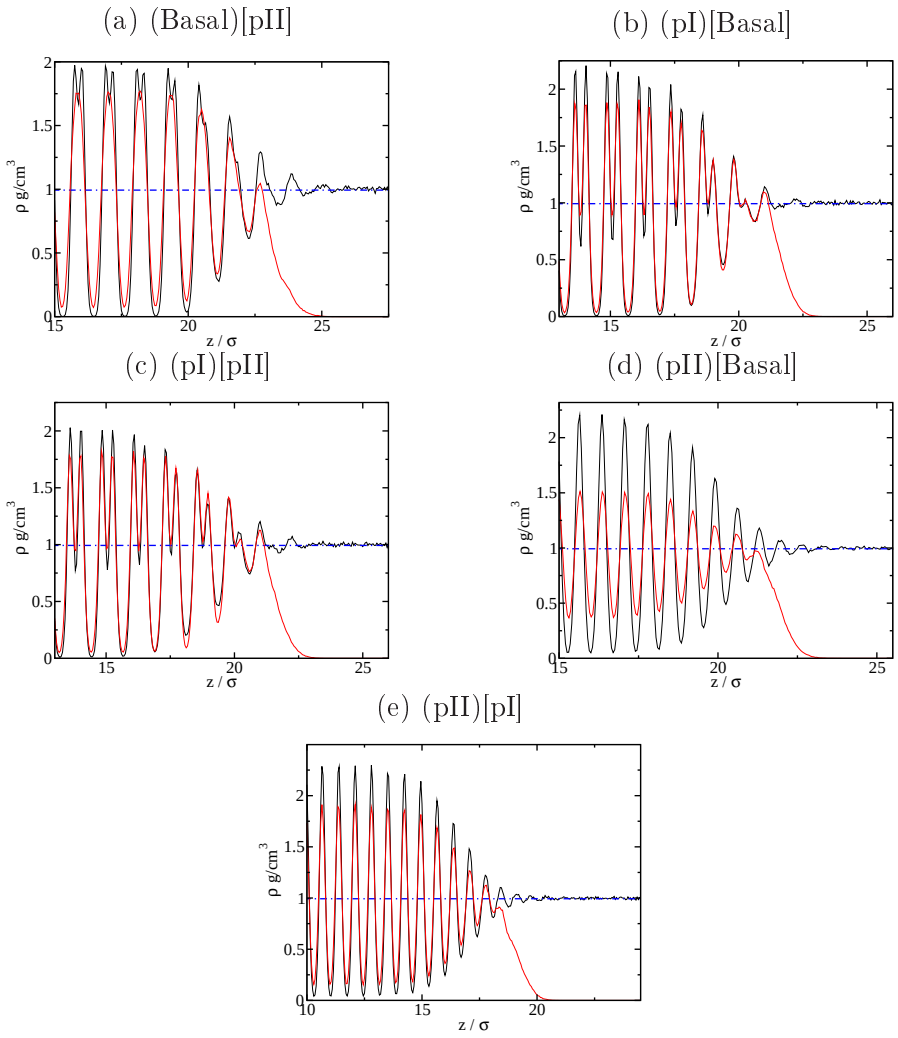

Figure 6.3. Complete density profiles of the ice/water (black) and the ice/vapour (red) systems along z direction. Dashed and dotted blue line correspond to the average density of the fluid phase. The density profiles have been calculated with slabs of thickness 0.05σ and averaging over a time gap of $\sim$ 35 ns.

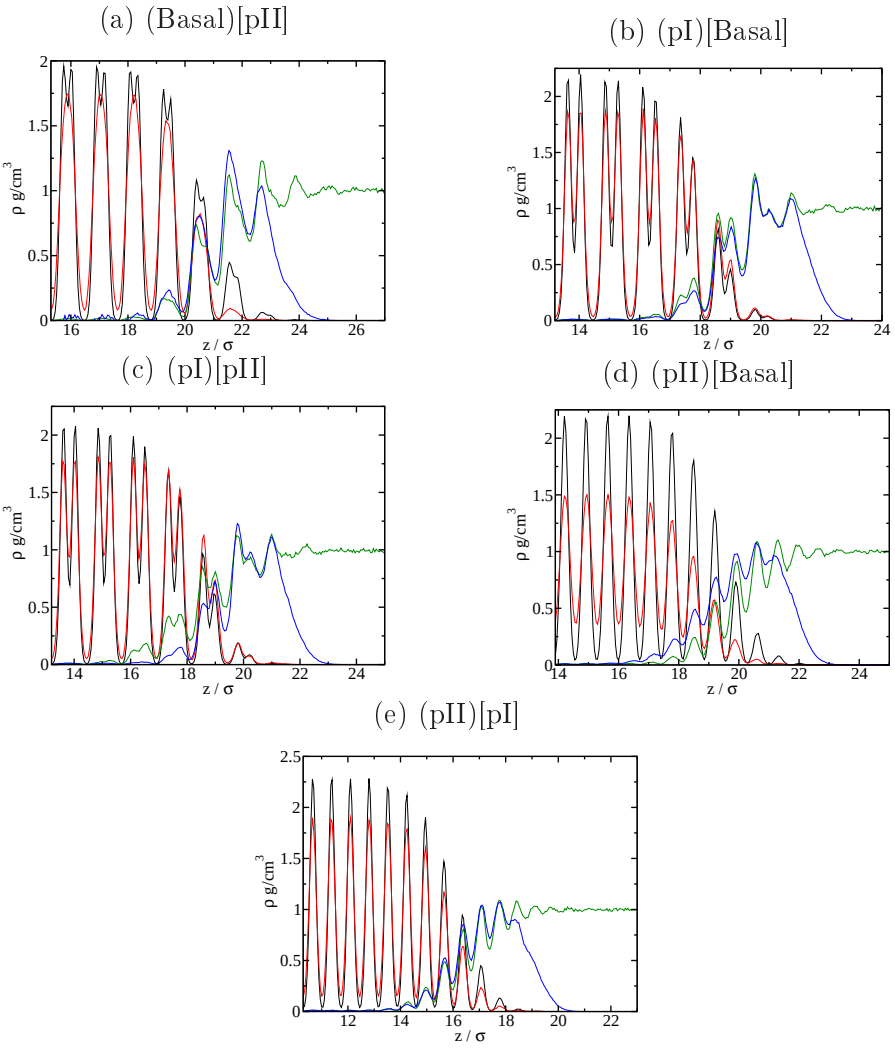

Figure 6.4. Density profiles or the ice/water (black) and the ice/vapour (red) systems along z direction. In each plot we represent solid–like molecules of the ice/water (black) and ice/vapor (red) interfaces and liquid–like molecules of the ice/water (green) and ice/vapor (blue) interfaces. The density profiles have been calculated with slabs of thickness 0.05σ and averaging over a time gap of $\sim$ 35 ns.

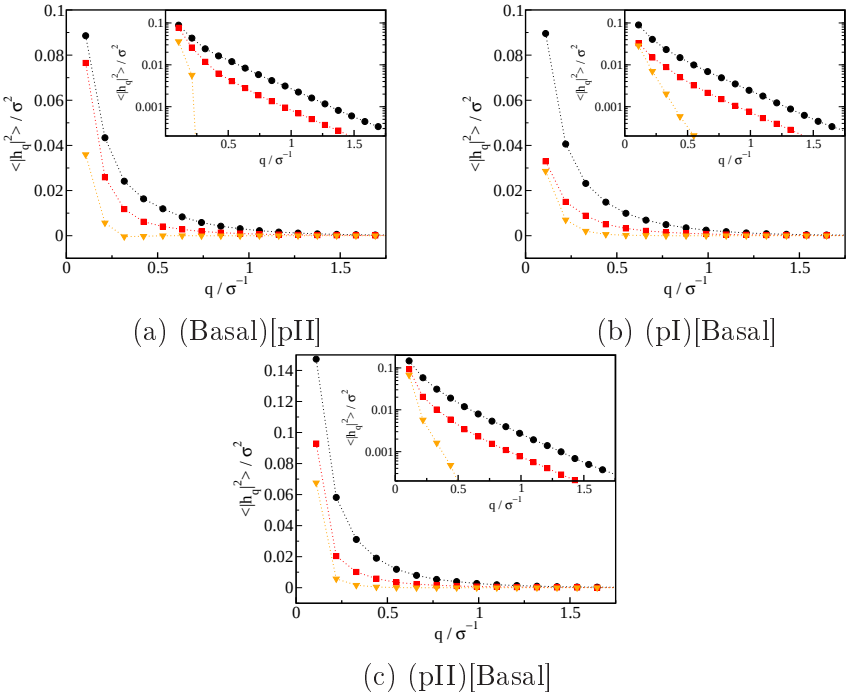

(a) (Basal)[pII]

(b) (pI)[Basal]

(c) (pII)[Basal]

Figure 6.5. Plots of $\langle |h(q)|^2 \rangle$ vs q for all the ice/vapour interfaces studied. Black circles correspond to $h_{if}(q) \cdot h^*_{if}(q)$, red squares correspond to $h_{fv}(q) \cdot h^*_{fv}(q)$, and orange triangles down correspond to $h_{if}(q) \cdot h^*_{fv}(q)$. Inset: same figures but with $\langle |h(q)|^2 \rangle$ in logarithmic scale.

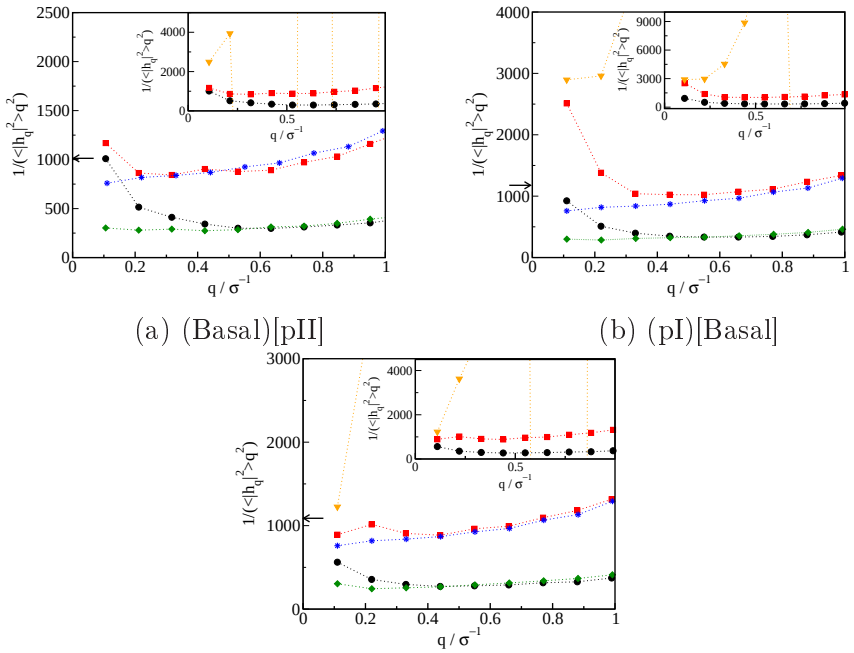

Figure 6.6. Plots of $1/(\langle|h(q)|^2\rangle q^2)$ vs q for all the ice/vapour interfaces studied. Black circles correspond to $h_{if}(q) \cdot h^*_{if}(q)$, red squares correspond to $h_{fv}(q) \cdot h^*_{fv}(q)$, and orange triangles down correspond to $h_{if}(q) \cdot h^*_{fv}(q)$. The results are compared with those of the ice/water interface (green diamonds) and the water/vapor interface (blue stars).

and film/vapor surfaces, as well as their crossed correlations $\langle h_{if}(q)h^*_{fv}(q)\rangle$. According to the model of section 6.3.2, these fluctuations remain finite for a smooth interface (finite ν), but diverge if the interface is rough (vanishing step free energy ν) [48], as indicated in Eq. 6.10. Our results for all three studied planes are clearly indicative of a strong divergence of the surface correlations. Furthermore, as depicted in the inset, which shows the same results in logarithmic scale, the correlations seem to diverge either exponentially or according to a power law.

In order to test this further, Fig. 6.6 now plots $\langle h_X(q)h^*_Y(q)\rangle q^2)^{-1}$ for X and Y equal to either if or fv. Such plots should show a divergence if the interface is smooth, and, on the contrary, should converge to $A(\tilde{\gamma}_{iw} + \gamma_{wv})/k_BT$ as $q \to 0$, for all three correlation functions studied, with the pure correlations converging from below, and the crossed correlations converging from above.

Whereas the plot shows that we are still somewhat away from the zero wavevector limit, it does seem that all three correlations could be converging to the same value. Unfortunately, the crossed correlations decay to zero so fast (orange line), that they change sign erratically due to statistical uncertainty, so that their inverse crosses from plus to minus infinity regularly, and only the first few data points are meaningful in this plot.

To further check for converged values of the inverse fluctuations, we have indicated with an arrow in the figures the $q = 0$ limit expected from the model for a rough interface (i.e., $\frac{k_BT}{A(\tilde{\gamma}_{iw}+\gamma_{wv})}$). A smooth extrapolation of the simulated data (as performed by visual inspection), would seem to indicate that the model provides an order of magnitude estimates of the $q = 0$ limit, and this would seem to favor the hypothesis of a completely rough ice/film interface for all three facets. Unfortunately, the model would seem to be providing somewhat too small values for the $q = 0$ limit. This could indicate the need to consider additional contributions to the phenomenological Hamiltonian of Eq. 6.8, that could be important in the limit of $q = 0$.

Despite these strong indications, it must be noted that one cannot completely rule out the absence of roughness at length scales larger than the size of our simulation box. Indeed, Libbrecht has suggested that the ice interface, remains rough up to fairly large length scales of about 20 unit cells, but that could eventually become smooth at larger length scales [47].

Moreover, a visual inspection of the ice/water and ice/vapor interfaces might suggest that the basal and pI planes are not completely rough at the temperature here studied. This is clearly seen in Fig. 6.7, where it is shown that these two planes show a stepped interface.

In the absence of any apparent divergence, we are at least in a position to give a lower bound for the parallel correlation length of the ice/film interface, which must be larger than the largest length scale accessible in our simulations, $2\pi/q_{min} = L_x$.

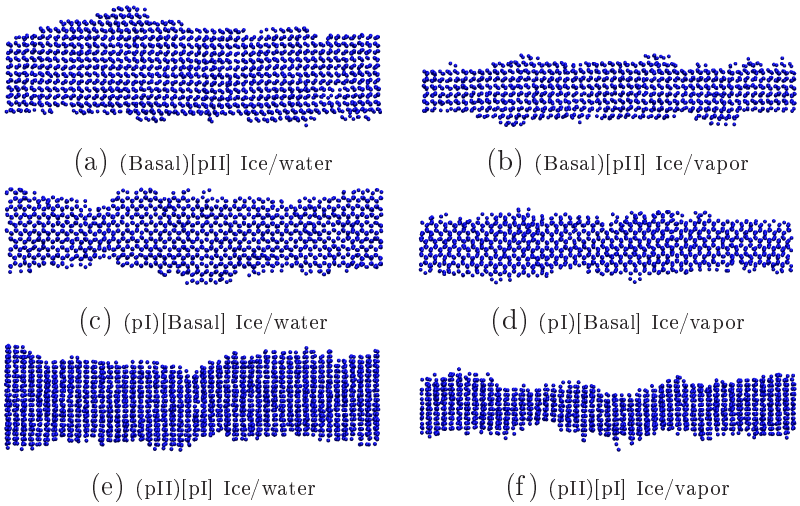

(a) (Basal)[pII] Ice/water (b) (Basal)[pII] Ice/vapor

(c) (pI)[Basal] Ice/water (d) (pI)[Basal] Ice/vapor

(e) (pII)[pI] Ice/water (f) (pII)[pI] Ice/vapor

Figure 6.7. Ice structures for different interfaces.

Accordingly, it follows that $\xi_{if} > 18nm$. This sets an upper bound for the step free energy per unit length, $J/b = \tilde{\gamma}_{iw} b^3/4\pi^2\xi_{if}^2$ of less than $2{\cdot}10^{-16}$ J/m. Unfortunately, this small energy scale seems to be at odds with expectations from recent crystal growth measurements, which suggest a step energy of about $J/b \approx 10^{-13}$ J/m.[49]

6.5.3 Test of model

In the previous section we have interpreted the spectrum of fluctuations on the basis of the capillary wave model of section 6.3.2, and concluded that the ice/film surface is rough. Furthermore, the results have provided us with an upper bound for the step free energy of the ice surface.

We now test whether the model serves as a quantitative description of the ice/vapor interface. We note that, according to that model, the spectrum of fluctuations for the ice/film and film/vapor surfaces should become equal to that of the ice/water and water/vapor surfaces, respectively, for large enough wave vectors (c.f. Eqs. 6.11 and 6.12).

We test this hypothesis by comparing the fluctuations of such surfaces in Fig. 6.6. The results show that the fluctuations are indeed very similar for wavevectors beyond about $q = 0.47\sigma^{-1}$ (1.5 nm^{-1}).

Thus, for wavelengths smaller than $\lambda = 4.2$ nm, the ice surface cannot tell the difference between the bulk liquid phase or the thin premelted film. Similarly, the liquid/vapor surface cannot tell whether it limits a bulk liquid phase or a thin premelted film in contact with bulk ice.

Essentially, what this means is that for such wavelengths, the ice/film and film/water

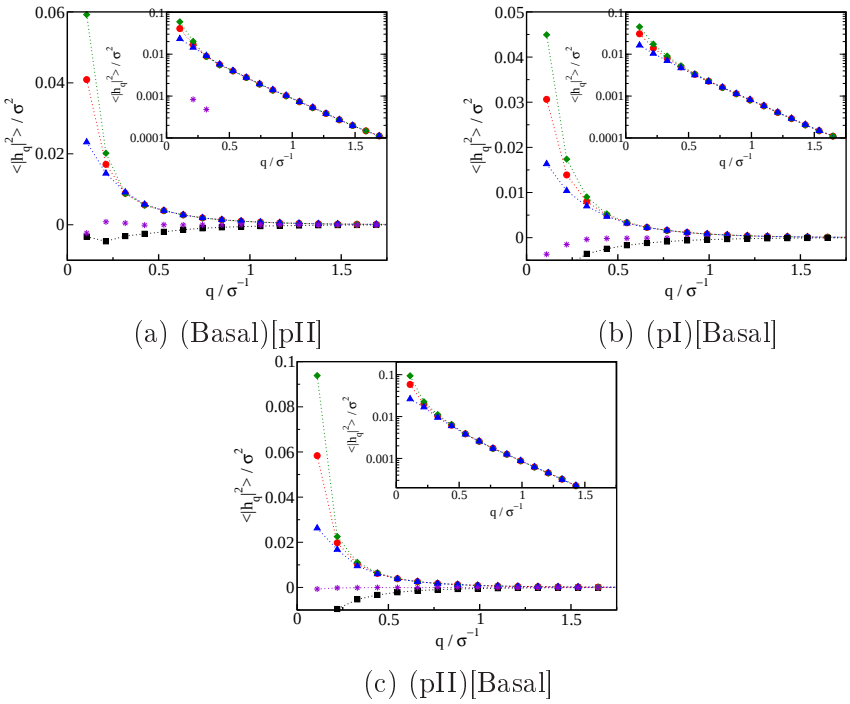

(a) (Basal)[pII]

(b) (pI)[Basal]

(c) (pII)[Basal]

Figure 6.8. Plots of $\langle |h(q)|^2 \rangle$ vs q for all the ice/vapour interfaces studied. Green diamonds correspond to $h_+(q) \cdot h_+^*(q)$, blue triangles up correspond to $h_-(q) \cdot h_-^*(q)$, violet stars correspond to $h_+(q) \cdot h_-(q)$, red circles correspond to $1/4\,(h_{wv}(q) + h_{iw}(q))$ and black squares correspond to $1/4\,(h_{wv}(q) - h_{iw}^*(q))$. Inset: same figures but with $\langle |h(q)|^2 \rangle$ in logarithmic scale.

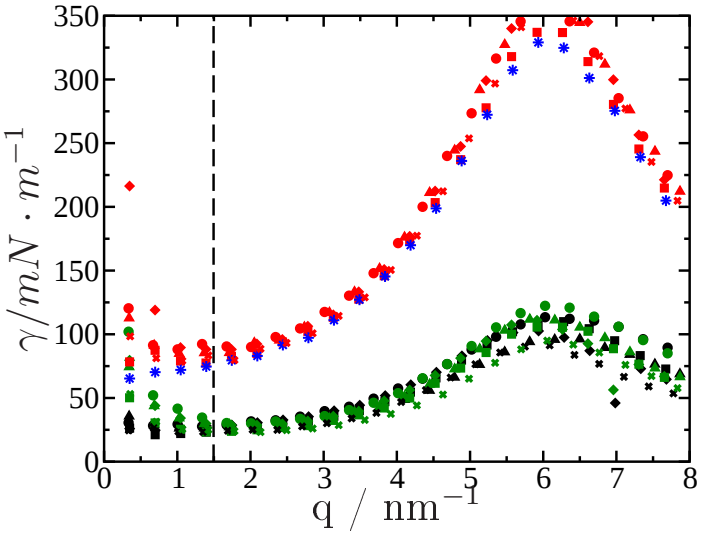

Figure 6.9. Stiffness of the ice/film (green), ice/water (black), film/vapor (red) and ice/water (blue) interfaces as a function of the wavevector for all the interfaces studied. (Basal)[pII]: circles, (pI)[Basal]: diamonds, (pI)[pII]: triangles, (pII)[Basal]: squares and (pII)[pI]: crosses. The vertical dashed line defines the region where the surfaces are uncorrelated.

surfaces behave independently from each other, and are therefore uncorrelated. For that reason, the cross correlations $\langle |h_{if}(q)h^*_{fv}| \rangle$ shown in Fig. 6.6 are seen to decay much faster than the $\langle |h^2_{if}(q)| \rangle$ and $\langle |h^2_{fv}(q)| \rangle$ correlations, as predicted by Eq. 6.13.

Orientation	$\tilde{\gamma}_{iw}(mN/m)$	$\tilde{\gamma}_{if}(mN/m)$	$\gamma_{fv}(mN/m)$
(Basal)[pII]	28.4	30.8	88.7
(pI)[Basal]	25.6	30.3	87.1
(pI)[pII]	27.0	29.2	84.6
(pII)[Basal]	22.8	24.2	79.3
(pII)[pI]	24.8	25.3	79.2

Table 6.2. Stiffness and interfacial tension of the ice/water and ice/vapor interfaces. The value of the interface tension of the ice/water interface is $\gamma = 72.7mN/m$.

An interesting corollary of this fact is that, in that regime of wavevectors where the surfaces are uncorrelated, the fluctuations should be similar to those expected for the ice/water and water/vapor interfaces, so that it should be possible to extract from such data an estimate of $\tilde{\gamma}_{iw}$ and γ_{wv}. We test this hypothesis in Fig. 6.9, where the stiffnesses of the ice/film and film/vapor surfaces are compared with those of the ice/water and water/vapor interfaces. As it is is clear from the figure, in the regime where the surfaces

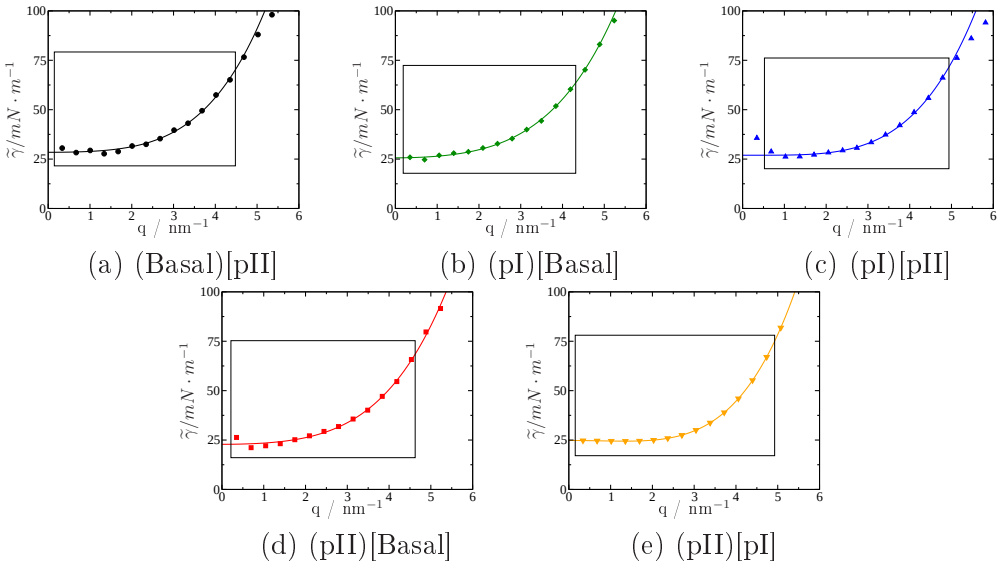

Figure 6.10. Plots of the stiffness vs q for the ice/water interface. Symbols are our simulation data and lines are linear fits of the points inside the box to $\widetilde{\gamma}(q) = \widetilde{\gamma}_0 + \kappa q^2 + cq^4$.

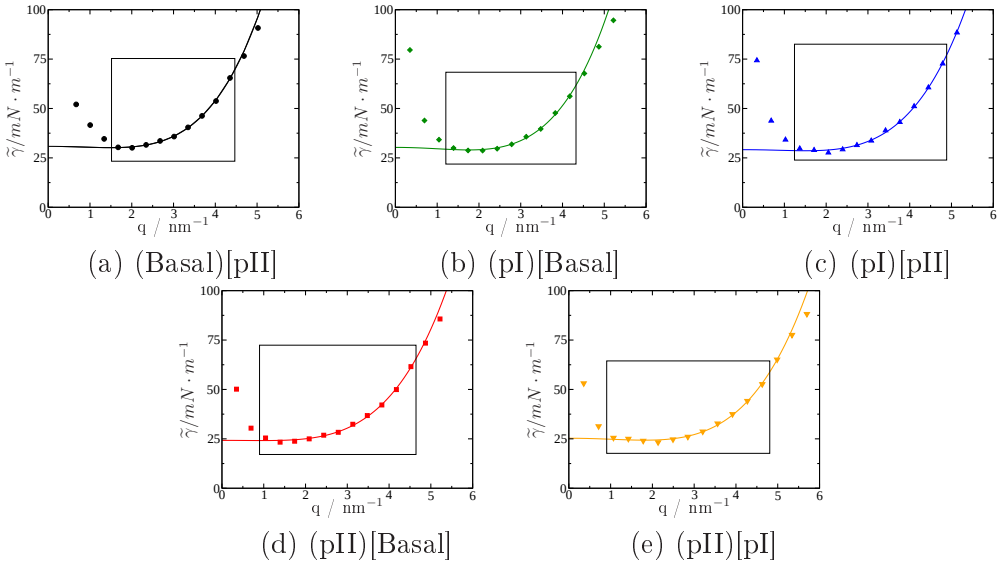

Figure 6.11. Plots of the stiffness vs q for the ice/film surface. Symbols are our simulation data and lines are linear fits of the points inside the box to $\widetilde{\gamma}(q) = \widetilde{\gamma}_0 + \kappa q^2 + cq^4$.

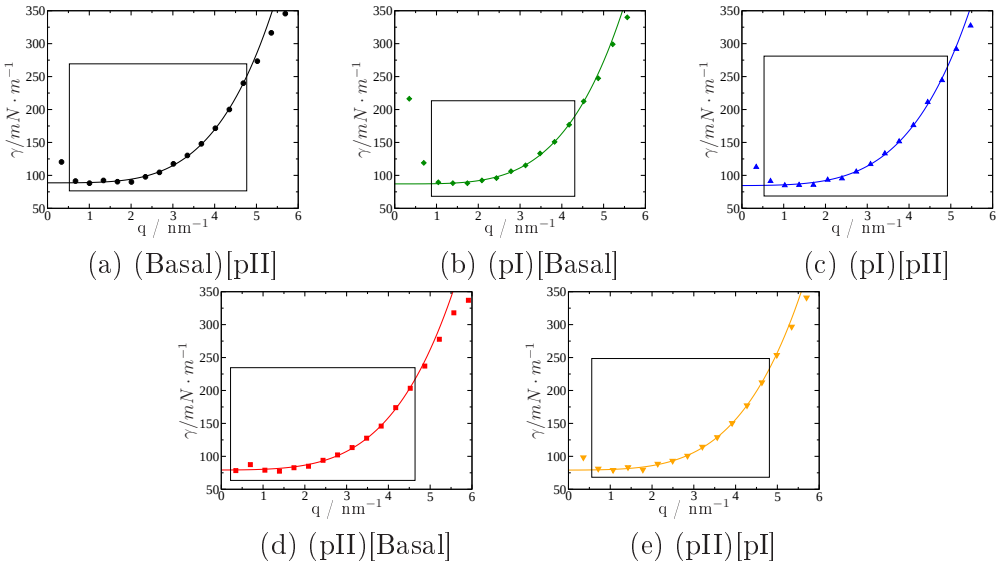

Figure 6.12. Plots of the surface tension vs q for the film/vapor surface. Symbols are our simulation data and lines are linear fits of the points inside the box to $\gamma(q) = \gamma_0 + \kappa q^2 + cq^4$.

are uncorrelated (right part of the plot) the ice/film and film/water surfaces mimic the ice/water and water/vapor interfaces, respectively.

In order to compare the interfacial stiffness of each surface we plot them separately in Figs. 6.10, 6.11, and 6.12. Then we fit our data to the expression given by the capillary wave theory [50, 51, 52]:

$$\widetilde{\gamma}(q) = \widetilde{\gamma}_0 + aq^2 + bq^4 \tag{6.14}$$

Table 6.2 collects the data obtained this way, together with the corresponding results obtained for the water/vapor stiffness.

The estimates obtained from the fluctuations of the premelting film are in reasonable agreement with the data for the independent interfaces, albeit systematically too large. A closer inspection shows that in fact this could have been expected from our model. Indeed, since the stiffness coefficients are actually not constants, but rather, are q dependent, it follows that the bending rigidity coefficients feed into the apparent stiffness obtained from Figs. 6.11 and 6.12, so that, in fact, the fits yield the stiffness coefficients up to a constant small factor of:

$$1 + \frac{g''}{\gamma_{iw}\gamma_{wv}}(\kappa_{iw} + \kappa_{wv}) \tag{6.15}$$

Since the bending rigidities are positive, and we expect g'' also to be small but positive, this factor is larger than unity, and explains the somewhat larger coefficients obtained in Table 6.2.

Obviously, as the lengthscale becomes larger, eventually the surfaces must feel each other and behave overall as expected for the full ice/vapor interface. In order to test this, we now analyse our results as is often done in the study of membrane fluctuations.[53] For this purpose, we define a mean surface, $h_+ = \frac{1}{2}(h_{if} + h_{fv})$, as well as a measure of the local film thickness, $h_- = \frac{1}{2}(h_{if} - h_{fv})$. According to our model, Eq. (6.10), the expected spectrum of fluctuations is given by:

$$\langle h_+(\mathbf{q}) \cdot h_+^*(\mathbf{q}) \rangle = \frac{k_B T}{A} \frac{g'' + \frac{1}{4}\gamma_+ q^2}{g''\gamma_+ q^2 + \gamma^2 q^4} \tag{6.16}$$

$$\langle h_-(\mathbf{q}) \cdot h_-^*(\mathbf{q}) \rangle = \frac{k_B T}{A} \frac{\frac{1}{4}\gamma_+ q^2}{g''\gamma_+ q^2 + \gamma^2 q^4} \tag{6.17}$$

$$\langle h_+(\mathbf{q}) \cdot h_-^*(\mathbf{q}) \rangle = \frac{k_B T}{A} \frac{\frac{1}{4}\gamma_- q^2}{g''\gamma_+ q^2 + \gamma^2 q^4} \tag{6.18}$$

where $\gamma_+ = (\gamma_{fv} + \tilde{\gamma}_{if})$, $\gamma_- = (\tilde{\gamma}_{if} - \gamma_{fv})$ and $\gamma^2 = \tilde{\gamma}_{if}\gamma_{fv}$. The model clearly shows that, for small wavevectors, the mean surface fluctuates as a single rough surface, with a surface tension which is the sum of the ice/water and water/vapor tensions. On the other hand, as the lengthscale becomes large enough, the fluctuations of the film thickness become bound, with amplitudes that are dictated by the interface potential binding the prewetting film to the solid phase.

We test this expectations by plotting $\langle |h_\pm(\mathbf{q}) h_\pm^*(\mathbf{q})| \rangle$ as a function of q (Fig. 6.8). As expected from the model above, the fluctuations of $\langle |h_+(\mathbf{q}) h_+^*(\mathbf{q})| \rangle$ and $\langle |h_-(\mathbf{q}) h_-^*(\mathbf{q})| \rangle$ behave identically at large wavevectors. That behavior corresponds essentially to a superposition of the ice/film and film/vapor fluctuations, which as noted previously, behave as independent ice/water and water/vapor surfaces.

For large wavelengths, however, a distinct behavior between the mean surface and the mean thickness becomes apparent. The mean surface shows a strong divergence, while the mean thickness grows with a much smaller slope. As noted previously, we expect the mean thickness would eventually converge to a finite value inversely proportional to g''. However, for the wavelengths studied it would seem that the crossover to damped fluctuations has not yet set in clearly. This precludes us from obtaining a precise estimate of the binding strength g''. However, we can still obtain a lower bound. Indeed, the fact that there is no convergence, implies that still $g''\gamma_+ q^2 \approx \gamma^2 q^4$ for the smallest wavelength studied, $q_{min} = 2\pi/18\ nm^{-1}$, whence, it follows that $g'' < \gamma^2/\gamma_+ q_{min}^2$, which gives $g'' < 2.8 \cdot 10^{15} Jm^{-4}$ Assuming g'' stems mainly from dispersion forces, and considering film thickness of about $\Delta h \approx 1\ nm$, this gives us for the ice/film Hamacker constant a rough estimate of $A_{if} \approx g''h^4 \approx 10^{-21}\ J$, which is within the lower side of accepted Hamacker constants.[54]

J/b / (J· m^{-1})	ξ_{if} nm	g" / (J·m^{-4})	ξ_{fv} / nm
$2 \cdot 10^{-16}$	18	$2.8 \cdot 10^{15}$	3

Table 6.3. Values of the structural properties of the ice/vapor interface.

Alternatively, we may exploit the fact that, according to Eq. 6.17, $\langle |h_-(\mathbf{q}) h_-^*(\mathbf{q})| \rangle$ becomes a linear function of q^2, with an intercept at $q = 0$ equal to $\frac{k_B T}{4Ag''}$. By extrapolating the first few points to zero, we now obtain a value for g'' which is an order of magnitude higher. This value determines the upper limit of g''. With our estimates for g'', we can now define a correlation length for the fluctuations of the premelting film as $\xi_{fv}^2 = \gamma^2/(\gamma_+ g'')$. This gives as a rather small correlation length of about $\xi_{fv} = 3{\cdot}10^{-9}$ m. This is a much smaller scale than the lower bound for the correlations of the ice/film interface, which we showed must be larger than 18 nm. The implication is that the premelted films can hardly heal the roughness of the underlying ice surface at this temperature.

As a final remark, we note that the low wavevector limit of the crossed correlations seems to converge smoothly to negative values. The reason for this behavior is apparent in Eq. 6.18, which shows that the $q = 0$ limit here is a finite value proportional to $\gamma_- = \tilde{\gamma}_{iw} - \gamma_{wv}$. Since $\tilde{\gamma}_{iw}$ is about half of γ_{wv} for all three planes studied, γ_- is negative and the intercept at $q = 0$ occurs for negative correlations.

Table 6.3 collects the data we have gathered for the structural properties of the ice/vapor interface, including upper and lower bounds for J/b and ξ_{if}, respectively, and semi-quantitative predictions for g'' and ξ_{fv}.

6.6 Conclusions

In this paper we have studied the structure of the solid/vapor interfaces of water in the neighborhood of the triple point for the TIP4P/2005 model. Our results show that the three most important planes of ice, basal, primary prismatic and secondary prismatic exhibit a thin premelted liquid layer of about 0.85 nm. This implies that the ice/vapor interface may be described in terms of two additional surfaces, separating the premelting layer from the bulk solid and bulk vapor phases. We have studied the fluctuations of these two surfaces, and analysed them in terms of a simple phenomenological model of coupled surface fluctuations.

According to our phenomenological model, the fluctuations of the premelting film may be described by two independent ice/water and water/vapor interfaces, coupled by a binding potential which limits the growth of the premelting layer.

Our results suggest that the ice/film surface is rough for all length scales beyond

the smallest wavevector accessible in our simulations, $q_{min} \approx 0.35$ nm, with a very small step free energy of about 10^{-16} J/m. On the contrary, the film/vapor surface exhibits only incomplete roughness, as it is bound by a finite binding potential which damps its parallel fluctuations beyond a few nanometers.

We test the phenomenological model by comparing the ice/film and film/vapor fluctuations with those obtained from independent simulations of the ice/water and water/vapor interfaces. The results clearly demonstrate a crossover from a microscopic regime of length scales smaller than about 0.45 nm, where the premelted surfaces fluctuate independently, and nearly as those of the ice/water and water/vapor interfaces. For larger wavelengths, on the contrary, the two surfaces become correlated and behave as a single interface with fluctuations governed by a stiffness which is close to, but somewhat larger than the sum of the ice/water stiffness and the water/vapor surface tension, whence, about 100 mJ/m^2.

Our results lend support to a recent study, which indicate that the crystal growth of ice crystallites in either bulk water or bulk vapor follows a similar mechanism [47]. This implies, for the crystal growth in the vapor phase, a process that is limited by the crystallization of water molecules within the premelted liquid film.

Bibliography

[1] K. G. Libbrecht, "The physics of snow crystals," *Rep. Prog. Phys.*, vol. 68, pp. 855–895, 2005.

[2] W. C. Pfalzgraff, R. M. Hulscher, and S. P. Neshyba, "Scanning electron microscopy and molecular dynamics of surfaces of growing and ablating hexagonal ice crystals," vol. 10, pp. 2927–2935, 1010.

[3] W. K. Burton, N. Cabrera, and F. C. Frank, "The growth of crystals and the equilibrium structure of their surfaces," vol. 243, pp. 299–358, 1951.

[4] H. van Beijeren, "Exactly solvable model for the roughening transition of a crystal surface," *Phys. Rev. Lett.*, vol. 38, pp. 993–996, May 1977.

[5] D. B. Abraham, "Solvable model with a roughening transition for a planar ising ferromagnet," *Phys. Rev. Lett.*, vol. 44, pp. 1165–1168, May 1980.

[6] "Critical surface phenomena at first-order bulk transitions," *Phys. Rev. Lett.*, vol. 49, pp. 1575–1578, 1982.

[7] D. S. Fisher and J. D. Weeks, "Shape of crystals at low temperatures: Absence of quantum roughening," *Phys. Rev. Lett.*, vol. 50, pp. 1077–1080, Apr 1983.

[8] R. Lipowsky, "Surface-induced disorder and surface melting," in *Magnetic Properties of Low-Dimensional Systems II* (L. M. Falicov, F. Mejia-Lira, and J. L. Moran-Lopez, eds.), vol. 50 of *Springer Proceedings in Physics*, (Heidelberg), pp. 158–166, Springer-Verlag, 1990.

[9] C. Herring, "Some theorems on the free energies of crystal surfaces," *Phys. Rev.*, vol. 82, pp. 87–93, Apr 1951.

[10] C. Rottman and M. Wortis, "Equilibrium crystal shapes for lattice models with nearest-and next-nearest-neighbor interactions," vol. 29, pp. 328–339, Jan 1984.

[11] P. M. Chaikin and T. C. Lubensky, *Principles of Condensed Matter Physics*. Cambridge: Cambridge University Press, 1995.

[12] H. Dosch, A. Lied, and J. H. Bilgram, "Glancing angle x-ray scattering studies of the premelting of ice surfaces," *Surface Sci.*, vol. 327, pp. 145–164, 1995.

[13] Y. Cao and E. H. Conrad, "Approach to thermal roughening of ni(110): A study by high-resolution low-energy electron diffraction," *Phys. Rev. Lett.*, vol. 64, pp. 447–450, Jan 1990.

[14] D. Gibbs, B. Ocko, D. Zehner, and S. Mochrie, "Absolute x-ray reflectivity study of the au(100) surface," vol. 38, pp. 7303–7310, Oct 1988.

[15] Q. S. Mei and K. Lu, "Melting and superheating of crystalline solids: From bulk to nanocrystals," vol. 52, pp. 1175–1262, 2007.

[16] J. G. Dash, A. W. Rempel, and J. S. Wettlaufer, "The physics of premelted ice and its geophysical consequences," vol. 78, pp. 695–741, 2006.

[17] M. Elbaum, "Roughening transition observed on the prism facet of ice," *Phys. Rev. Lett.*, vol. 67, pp. 2982–2985, Nov 1991.

[18] M. Elbaum and M. Schick, "Application of the theory of dispersion forces to the surface melting of ice," *Phys. Rev. Lett.*, vol. 66, pp. 1713–1716, 1991.

[19] M. Elbaum, S. G. Lipson, and J. G. Dash, "Optical study of surface melting on ice," vol. 129, pp. 491–505, 1993.

[20] A. Lied, H. Dosch, and J. H. Bilgram, "Surface melting of ice I_h single crystals revealed by glancing angle x-ray scattering," *Phys. Rev. Lett.*, vol. 72, pp. 3554–3557, 1994.

[21] H. Bluhm, D. F. Ogletree, C. S. Fadley, Z. Hussain, and M. Salmeron, "The premelting of ice studied with photoelectron spectroscopy," *J. Phys.:Condens. Matter*, vol. 14, pp. L227–L233, 2002.

[22] J. Wettlaufer, "Impurity effects in the premelting of ice," *Phys. Rev. Lett.*, vol. 82, pp. 2516–2519, Mar 1999.

[23] K. G. Libbrecht, "On the equilibrium shape of an ice crystal," *arXiv:1205.1452 [cond-mat.mtrl-sci]*, 2013.

[24] M. Maruyama, T. Nishida, and T. Sawada, "Crystal shape of high-pressure ice ih in water and roughening transition of the $(10\bar{1}0)$ plane," *The Journal of Physical Chemistry B*, vol. 101, no. 32, pp. 6151–6153, 1997.

[25] T. Gonda and T. Yamakazi, "Morphology of ice droxtals grown from supercooled water droplets," vol. 45, no. 10, pp. 66–69, 1978.

[26] S. C. Colbeck, "Ice crystal morphology and growth rates at low supersaturations and high temperatures," *J. App. Phys.*, vol. 54, no. 5, pp. 2677–2682, 1983.

[27] J. Benet, L. G. MacDowell, and E. Sanz, "A study of the ice-water interface using the tip4p/2005 water model," *Phys. Chem. Chem. Phys.*, vol. 16, pp. 22159–22166, 2014.

[28] Y. Furukawa and H. Nada, "Anisotropic surface melting of an ice crystal and its relationship to growth forms," vol. 101, no. 32, pp. 6167–6170, 1997.

[29] M. M. Conde, C. Vega, and A. Patrykiejew, "The thickness of a liquid layer on the free surface of ice as obtained from computer simulation," *J. Chem. Phys.*, vol. 129, no. 1, pp. –, 2008.

[30] R. G. Pereyra and M. A. Carignano, "Ice nanocolumns: A molecular dynamics study," vol. 113, no. 29, pp. 12699–12705, 2009.

[31] D. Pand, L.-M. Liu, B. Slater, A. Michaelides, and E. Wang, "Melting the ice: On the relation between temerature and size for nanoscale ice crystals," vol. 5, pp. 4562–4569, 2011.

[32] D. T. Limmer and D. Chandler, "Premelting, fluctuations, and coarse-graining of water-ice interfaces," *The Journal of Chemical Physics*, vol. 141, no. 18, 2014.

[33] J. L. F. Abascal and C. Vega, "A general purpose model for the condensed phases of water: Tip4p/2005," *The Journal of Chemical Physics*, vol. 123, no. 23, p. 234505, 2005.

[34] C. Vega and J. L. F. Abascal, "Simulating water with rigid non-polarizable models: a general perspective," *Phys. Chem. Chem. Phys.*, vol. 13, pp. 19663–19688, 2011.

[35] L. G. MacDowell and C. Vega, "Dielectric constant of ice ih and ice v: A computer simulation study," *J. Phys. Chem. B*, vol. 114, pp. 6089–6098, 2010.

[36] D. Nelson, T. Piran, and S. Weinberg, *Statistical Mechanics of Membranes and Surfaces*. Word Scientific, Singapore, 2004.

[37] S. A. Safran, *Statistical Thermodynamics of Surfaces, Interfaces and Membranes*. Reading: Addison-Wesley, 1994.

[38] M. Li, A. M. Tikhonov, D. J. Chaiko, and M. L. Schlossman, "Coupled capillary wave fluctuations in thin aqueous films on an aqueous subphase," *Phys. Rev. Lett.*, vol. 86, pp. 5934–5937, Jun 2001.

[39] M. Fukuto, O. Gang, K. J. Alvine, and P. S. Pershan, "Capillary wave fluctuations and intrinsic widths of coupled fluid-fluid interfaces: An X-ray scattering study of a wetting film on bulk liquid," *Phys. Rev. E*, vol. 74, p. 031607, Sep 2006.

[40] P. S. Pershan and M. Schlossman, *Liquid Surfaces and Interfaces: Synchrotron X-ray Methods*. Cambridge: Cambridge University Press, 2012.

[41] W. Lechner and C. Dellago, "Accurate determination of crystal structures based on averaged local bond order parameters," *The Journal of Chemical Physics*, vol. 129, no. 11, p. 114707, 2008.

[42] J. Benet, L. G. MacDowell, and E. Sanz, "Computer simulation study of surface wave dynamics at the crystal–melt interface," *J. Chem. Phys.*, vol. 141, p. 024307, 2014.

[43] H. Berendsen, D. van der Spoel, and R. van Drunen, "Gromacs: A message passing parallel molecular dynamics implementation," *Computer Physics Communications*, vol. 91, no. 1 - 3, pp. 43 – 56, 1995.

[44] B. Hess, C. Kutzner, D. van der Spoel, and E. Lindahl, "Gromacs 4: Algorithms for highly efficient, load-balanced, and scalable molecular simulation," *Journal of Chemical Theory and Computation*, vol. 4, no. 3, pp. 435–447, 2008.

[45] C. Vega and J. L. F. Abascal, "Simulating water with rigid non-polarizable models: a general perspective," *Phys. Chem. Chem. Phys.*, vol. 13, pp. 19663–19688, 2011.

[46] G. Bussi, D. Donadio, and M. Parrinello, "Canonical sampling through velocity rescaling," *J. Chem. Phys.*, vol. 126, no. 1, p. 014101, 2007.

[47] K. G. Libbrecht, "Towards a comprehensive model of snow crystal growth: 3. The correspondence between ice growth from water vapor and ice growth from liquid water," *arXiv:1407.0740 [cond-mat.mtrl-sci]*, 2014.

[48] J. D. Weeks and G. H. Gilmer, "Dynamics of crystal growth," *Adv. Chem. Phys.*, vol. 40, pp. 157–228, 1979.

[49] K. G. Libbrecht and M. E. Rickerby, "Meassurements of surface attachment kinetics for faceted ice crystal growth," vol. 377, pp. 1–8, 2013.

[50] Meunier, J., "Liquid interfaces : role of the fluctuations and analysis of ellipsometry and reflectivity measurements," *J. Phys. France*, vol. 48, no. 10, pp. 1819–1831, 1987.

[51] K. R. Mecke and S. Dietrich, "Effective hamiltonian for liquid-vapor interfaces," *Phys. Rev. E*, vol. 59, pp. 6766–6784, Jun 1999.

[52] E. M. Blokhuis, "On the spectrum of fluctuations of a liquid surface: From the molecular scale to the macroscopic scale," *J. Chem. Phys.*, vol. 130, p. 074701, 2009.

[53] P. Tarazona, E. Chacón, and F. Bresme, "Thermal fluctuations and bending rigidity of bilayer membranes," *J. Chem. Phys.*, vol. 139, no. 9, p. 094902, 2013.

[54] E. J. Maginn, A. T. Bell, and D. N. Theodorou, *Sorption Thermodynamics, Siting, and Conformation of long n-Alkanes in Silicalite as Predicted by Configurational-Bias Monte Carlo Integration*, vol. 99. 1995.

Results: Chapter 7

The area distribution of the intrinsic surface

Jorge Benet, Eduardo Sanz and Luis G. MacDowell

Departamento de Química Física, Facultad de Ciencias Químicas, Universidad Complutense de Madrid, 28040 Madrid, Spain

7.1 Abstract

In this paper we examine the probability distribution of the intrinsic surface area of an interface for the first time. In particular, we use the Lennard–Jones model to measure the instantaneous surface area of a liquid–vapor interface and calculate its probability of appearance.

By developing a model which takes into account both enthalpic and entropic contributions, we show that the surface area probability follows a Gamma distribution from which a coefficient related to the macroscopic surface tension can be obtained. Our results show that the values of this coefficient depend strongly on the resolution employed to locate the interface.

Finally, we show that the surface tension obtained from surface area distributions is closely related to the bending rigidity of the interface, which also depends on the resolution employed. This relationship reveals that for an interface where the bending rigidity is zero, the surface tension obtained with our model equals the macroscopic surface tension.

7.2 Introduction

According to classical surface thermodynamics, the interface between two coexisting phases is described in terms of a flat dividing surface, whose area dictates the extensive properties of the surface. Additionally, a number of intensive thermodynamic fields such as temperature and pressure are required to fully describe the state of the system.[1] At a microscopic level, this description is embodied in mean field theories of the interface, where it is possible to define a unique *intrinsic* density profile, $\rho(z)$, that depends only on the perpendicular distance to the interface, z.[1, 2, 3] The implicit picture in this description is that of a flat interface, that exhibits no inhomogeneities along its parallel direction.

Obviously, such a description is an idealization, and one can well understand that instantaneously, an interface is never completely flat, but rather, exhibits local fluctuations of the interface position due to thermal agitation. As a result, a snapshot of the interface is better described as a sum of undulated surface waves, which convey a rough texture to the ideally flat dividing surface. Since such fluctuations increase the instantaneous surface area, they are penalized by the surface tension, and are therefore known as surface capillary waves.[4, 5, 6, 1, 7]

This coarse grained description of a rough interface can be hardly contested on intuitive grounds. Surprisingly, the implications are, on the contrary, far less intuitive, and have been the matter of controversy for many years.[6, 8, 9, 10, 11, 12] Most noticeably, in the absence of a pining external field (such as gravity) this scenario leads to an interface with diverging perpendicular correlations, whence, of infinite roughness in the thermodynamic limit.[6] Whereas this prediction has been the matter of much debate, it has been later confirmed by field theoretical renormalization of the Cahn-Hillard Hamiltonian.[13, 14, 15] This result has been sometimes interpreted rather counterintuitively as meaning that an interface cannot exist in the thermodynamic limit, but such a viewpoint is arguable and can be contested.[5]

A far less studied issue refers to the intrinsic surface area distribution of the rough interface. In the original formulation of capillary wave theory [4] large area increments are exponentially suppressed as $exp(-\beta\gamma_b\Delta A)$, with γ_b dictating the cost of area increments. This suggests a monotonous decay of the probability distribution. However, larger surface areas bear a larger entropy, and this, on the other hand, enhances the likelihood of surface area fluctuations. This is analogous to the usual competition between entropic and enthalpic contributions in statistical thermodynamics, which usually results in a highly peaked gaussian distribution.[16] Surprisingly, this issue, which hinges on the entropic nature of capillary waves seems to have been seldom explored.

A related issue refers to the coefficient dictating the free energy penalty of the surface area increments, γ_b, which is, somehow, a measure of the surface tension. Using

the techniques of thermodynamic density functional theory, it is possible to assess the cost of increasing the surface area from the intrinsic density profile of a mean field theory.[6] However, one expects that such a mean field measure of the surface tension cannot incorporate free energy contributions steaming from fluctuations beyond the bulk correlation length. For that reason, in capillary wave theory a distinction is usually made between the mean field surface tension, otherwise known as the *bare* surface tension, γ_b, and the macroscopic surface tension, $\gamma_{\rm lv}$, which incorporates somehow the effect of neglected capillary wave fluctuations. Since a rough interface with nominal surface area, A_0 bears a number of, say, n capillary wave modes, with an average energy of $\frac{1}{2}k_BT$, it is expected that $\gamma_{\rm lv}$ should be related to γ_b by additive terms of order nk_BT, but the exact nature of this relation is somewhat a matter of debate.[4, 6, 17, 12, 18] This situation if further complicated if one explicitly considers that the area increments are a result of bending the interface, and have therefore an extra free energy penalty related to the resulting finite curvature of the rough interface.[17] An averaged surface tension then incorporates a new contribution related to the bending rigidity coefficient, and this further obscures our understanding of how the bare surface tension is related to the measured surface tension in experiments.

In fact, the need for a bare surface tension in the capillary wave Hamiltonian has been contested on theoretical grounds,[8], and is actually at odds with several known results. 1) According to the classical theory, the amplitude of low wavevector fluctuations of the interface height is related to the bare surface tension, γ_b, rather than to the macroscopic surface tension, $\gamma_{\rm lv}$. Yet, there is an ample simulation evidence showing that the low wave vector fluctuations are suppressed essentially by $\gamma_{\rm lv}$, rather than by a related bare surface tension. 2) Also according to the classical theory, the interfacial roughness is dictated by the bare surface tension. However, for the Ising model in two dimensions, the exact result of the density profile rather shows that the roughness is dictated by the macroscopic surface tension.[19] This view is confirmed also in computer simulations of three dimensional systems.[20] A possible way to reconcile this problem was suggested by Meunier already some time ago. According to this author, the flaw of classical capillary wave theory is related to the approximation of the surface area as a quadratic expansion in Fourier modes. Meunier showed that it is possible to include terms of quartic order using renormalization techniques. This allows to describe the quadratic fluctuations with renormalized coefficients which transform the bare surface tension into the macroscopic surface tension, and furthermore, remove the unpleasant ultraviolet divergence of the perpendicular correlation length that results in the quadratic approximation.[17]

In this chapter, we perform computer simulations of a free liquid–vapor interface in order to study the probability distribution of intrinsic surface area increments that result from capillary waves. As expected (but seldom stressed), we confirm a highly peaked distribution, which is, however, generally not gaussian, but rather, follows a Gamma

distribution, whence, approaches a true gaussian distribution only in the thermodynamic limit. The problem is one closely related to the distribution of the speed of molecules in an ideal gas, but for many dimensions. We find that the coefficient governing the suppression of area increments is certainly not the liquid-vapor surface tension, but rather, a related bare surface tension, which incorporates, at least, the cost of bending the interface at small wavelengths. Smoothly changing the resolution chosen to describe the interface location allows to find a surface with zero bending rigidity, which has a bare surface tension that equals the zero wave vector surface tension.

7.3 Theory

The presence of capillary waves on an interface leads to an interfacial profile $h(x, y)$ which accounts for deviations from the flat interface. Capillary waves of different wavelengths have an associated wavevector or fourier mode q. Each fourier mode has an amplitude h_q which is related to the interfacial profile by fourier transformation of the latter:

$$h_q = \frac{1}{N} \sum h(x, y) e^{iq(x,y)} \tag{7.1}$$

where N is the number of points where the interfacial profile is evaluated.

The increments of the surface area due to capillary waves can be obtained in terms of the amplitudes of the fourier modes according to:

$$\frac{\Delta A}{A_0} = \frac{1}{2} \sum q^2 h_q^2 \tag{7.2}$$

where A_0 is the area of the flat interface and ΔA is the area increment. In this expression h_q is a random variable which follows a gaussian distribution of the form:

$$f(h_q) = \left(\frac{\beta A_0 \gamma_q q^2}{2\pi} \right)^{1/2} e^{-\frac{1}{2}\beta A_0 \gamma_q q^2 h_q^2} \tag{7.3}$$

Alternatively $\Delta A/A_0$ can be related to a different random variable $t = q^2 h_q^2$

$$\frac{\Delta A}{A_0} = \frac{1}{2} \sum t_q \tag{7.4}$$

which follows a distribution $f(t_q)$. According to the transformation theorem for random variables, both variables are related by

$$f(h_q) dh_q = f(t_q) dt_q \tag{7.5}$$

from where the distribution of t_q can be expressed as

$$f(t_q) = f(h_q)\left|\frac{dh_q}{dt_q}\right| \tag{7.6}$$

and by calculating the derivative dh_q/dt_q one obtains

$$f(t_q) = \frac{1}{2}\left(\frac{\beta A_0 \gamma_q}{2\pi}\right)^{1/2} t_q^{-1/2} e^{-\frac{1}{2}\beta A_0 \gamma_q t_q} \tag{7.7}$$

If we now define

$$\beta_q = \frac{2}{\beta A_0 \gamma_q} \tag{7.8}$$

and plug it into Eq. 7.7 we obtain

$$f(t_q) = \frac{1}{2}(\pi\beta_q)^{-1/2} t_q^{-1/2} e^{-\frac{t_q}{\beta_q}} \tag{7.9}$$

an expression which can be rearranged to

$$f(t_q) = \frac{1}{2\sqrt{\pi}} \frac{t_q^{-1/2}}{\beta_q^{1/2}} e^{-\frac{t_q}{\beta_q}} \tag{7.10}$$

The above equation follows a Gamma distribution $f(t_q; 1/2; \beta_q)$.

This allows us to show the random variable $\Delta A/A_0$ in Eq. 7.4 is a sum of Gamma distributed random variables. As a result we can follow the Moschopoulos method [21] to obtain the distribution of the area increments (see Appendix):

$$f(\Delta A) = \frac{\prod(\beta\gamma_q)^{1/2}}{\Gamma(n/2)}\left[\Delta A^{n/2-1} - \frac{1}{n}\sum_q \beta\Delta\gamma_q \Delta A^{n/2} + ...\right] e^{-\beta\gamma_{lv}\Delta A} \tag{7.11}$$

where n is the number of fourier modes, Γ is the gamma function, $\Delta\gamma_q = \gamma_q - \gamma_{lv}$ and γ_{lv} is the macroscopic liquid–vapour surface tension.

Finally we can rewrite Eq. 7.11 in an approximate form as

$$f(\Delta A) \simeq \frac{\prod(\beta\gamma_q)^{1/2}}{\Gamma(n/2)} \Delta A^{n/2-1} e^{-\beta\langle\gamma\rangle\Delta A} \tag{7.12}$$

where $\langle\gamma\rangle = \gamma_{lv} + \langle\Delta\gamma_q\rangle$ and $\langle\Delta\gamma_q\rangle = \frac{1}{n}\sum\Delta\gamma_q$.

Eq. 7.12 provides the probability of having an increment of the surface area of a magnitude ΔA. As it can be seen, this probability consists of a polinomic and an exponential term. The exponential term lessens the probability of large increments of

the surface area exponentially, in a factor related to the interfacial free energy. On the other hand, the polinomic term increases the probability of such increments. As mentioned in the Introduction, this increase is related to the entropy of the surface since larger surface areas have higher entropy and, therefore, are more likely to occur.

According to the statistical thermodynamics the free energy of a given configuration is related to the probability of the latter as:

$$\Delta G = -k_B T \ln f(\Delta A) \tag{7.13}$$

where ΔG is the Gibbs free energy, k_B is the Boltzmann constant and T is the temperature. This equation can be exploited to obtain thermodynamic properties of our system. By taking logarithms in Eq. 7.12 we obtain to an additive constant

$$\ln f(\Delta A) = \ln \prod (\beta\gamma_q)^{1/2} + (n/2-1)\ln \Delta A - \beta \langle\gamma\rangle \Delta A \tag{7.14}$$

and, by comparing Eqs. 7.13 and 7.14 we obtain

$$\Delta G/k_B T = -\ln \prod (\beta\gamma_q)^{1/2} + \beta \langle\gamma\rangle \Delta A - (n/2-1)\ln \Delta A \tag{7.15}$$

This equation will be employed afterwards to obtain $\langle\gamma\rangle$ from a plot of $\Delta G/k_B T$ vs ΔA.

7.3.1 Estimation of $\langle\gamma\rangle$

We start defining $\langle\gamma\rangle$ as

$$\langle\gamma\rangle = \frac{1}{n}\sum_{q=1}^{n} \gamma_q \tag{7.16}$$

where n is the number of fourier modes. Taking this into account we rewrite the equation above as

$$\langle\gamma\rangle = \frac{\sum \gamma_q}{\sum 1} \simeq \frac{\int \gamma_q d\vec{q}}{\int d\vec{q}} \tag{7.17}$$

If we assume that $\gamma_q = \gamma_{lv} + \kappa q^2$, we find

$$\langle\gamma\rangle = \frac{\int (\gamma_{lv} + \kappa q^2)\, q dq}{\int q dq} = \gamma_{lv} + \frac{\frac{1}{2}\kappa\,(q_{max}^4 - q_{min}^4)}{(q_{max}^2 - q_{min}^2)} \tag{7.18}$$

For large enough systems $q_{min} \to 0$, so we can rewrite Eq. 7.18 as

$$\langle\gamma\rangle = \gamma_{lv} + \frac{1}{2}\kappa q_{max}^2 \tag{7.19}$$

Since it is not possible to attribute q_{max} a physical meaning, we cannot elucidate the meaning of $\langle\gamma\rangle$ from Eq. 7.19.

Given that $\langle\gamma\rangle$ is an average surface tension it should be related to the average intrinsic surface area, $\langle\Delta A\rangle$. Taking into account that Eq. 7.12 follows a Gamma distribution $f(\Delta A; n/2; 1/\beta\langle\gamma\rangle)$, the average value of $\langle\Delta A\rangle$ can be written as:

$$\langle\Delta A\rangle = \frac{n}{2}\frac{1}{\beta\langle\gamma\rangle} \tag{7.20}$$

The relationship between $\langle\Delta\gamma\rangle$ and $\langle\Delta A\rangle$ is given by an average interfacial energy, $\langle\Delta H\rangle$. This energy can be obtained from the equipartition theorem as

$$\langle\Delta H\rangle = \frac{n}{2}k_B T \tag{7.21}$$

and can be interpreted as the averaged surface energy associated to capillary waves.

Finally by dividing Eq. 7.21 by Eq. 7.20 we get that

$$\langle\gamma\rangle = \frac{\langle\Delta H\rangle}{\langle\Delta A\rangle} \tag{7.22}$$

7.4 Methods

7.4.1 Model and System

In this work we employ the truncated and shifted Lennard–Jones potential proposed by Broughton and Gilmer [22]

$$U(r) = \begin{cases} 4\epsilon\left[\left(\frac{\sigma}{r}\right)^{12} - \left(\frac{\sigma}{r}\right)^{6}\right] + C_1, & r \leqslant 2.3\sigma \\ C_2\left(\frac{\sigma}{r}\right)^{12} + C_3\left(\frac{\sigma}{r}\right)^{6} + C_4\left(\frac{r}{\sigma}\right)^{2} + C_5, & 2.3 < r < 2.5 \\ 0, & 2.5\sigma \leqslant r \end{cases} \tag{7.23}$$

where ϵ is the depth of the potential well, σ is the molecular diameter, and C_k are energy parameters whose values are: C_1=0.016132ϵ, C_2=3136.6ϵ, C_3=-68.069ϵ, C_4=-0.083312ϵ, and C_5=0.74689ϵ.

Our simulations are performed by placing a liquid slab in a rectangular box with interfacial area L_xxL_y (with lateral areas $L = L_x = L_y$ = 12, 14, 16, 18 and 20 σ) and length L_z = 50 σ. The width of this liquid slab is $\sim 30\sigma$.

7.4.2 Simulation Details

We use the Molecular Dynamics GROMACS package[23, 24] and its implementation for Argon: $\sigma = 3.405$Å, $\epsilon/k_B = 119.8K$, and $m = 6.69 \cdot 10^{-26}kg$. We prepare our systems at

the triple point of the model [25], that is $T = 0.617\epsilon/k_B$ and $p = -0.02\epsilon\sigma^{-3}$. Under these conditions the liquid's coexistence density is $\rho_l = 0.828\sigma^{-3}$. Our systems are prepared by placing an equilibrated liquid slab in the middle of the simulation box. Then NVT simulations of 10 ns are carried out to equilibrate the system. Finally, production runs of 1000 ns are performed in the NVT ensemble. The time step for the Velocity–Verlet integrator was fixed to 0.01 ps ($0.0046\sqrt{\sigma^2 m/\epsilon}$ in LJ units) and snapshots were saved every 100 ps. In order to keep the temperature constant we use a velocity–rescaling thermostat [26].

7.4.3 Intrinsic Surface Location

In order to locate the intrinsic surface we divide our systems in a square lattice of $n = n_j \cdot n_k$ equispaced points with coordinates (x_j, y_k). For each of these points, we need to know the value of the function which describes the intrinsic surface, $h(x_j, y_k)$. To do this, we define squares of side Δ centered at each point and look for particles whose x, y coordinates are enclosed within these squares. Then, the value of $h(x_j, y_k)$ for a given square centered at (x_j, y_k) is calculated as the average z coordinate of the n_0 outermost particles belonging to that square. In this way we can locate the intrinsic surface making use of four parameters, namely, n_j, n_k, Δ and n_0. From these parameters, n_j and n_k dictate the number of points where the intrinsic surface is located, while Δ is the one which allows us to change the resolution of our definition of the surface. Large values of Δ will give smooth interfaces and thus low resolution, while small values of the parameter will lead to sharp interfaces of high resolution. The optimal value of Δ should give rough interfaces but without the sharp peaks obtained for very high resolutions, which are physically meaningless. Finally, the parameter n_0 must be chosen in a way that only interfacial particles, and not those corresponding to the bulk, are taken into account. Thus, the value of n_0 is related to Δ through the surface density. We find that a value of about 0.45 particles/σ^2 for this density leads to reasonable surfaces.

7.4.4 Calculation of the Interfacial Area

The intrinsic surface area of a given configuration can be obtained by dividing it in triangles, calculating the area of these triangles and then expressing the intrinsic surface area as the sum of the areas of each single triangle. A sketch of this procedure is shown in Fig. 7.1 and it is detailed below.

First of all we take $h(x_j, y_k)$, whose coordinates give us the points needed to divide the intrinsic surface into triangles. For a given point of this function, say n in Fig. 7.1,

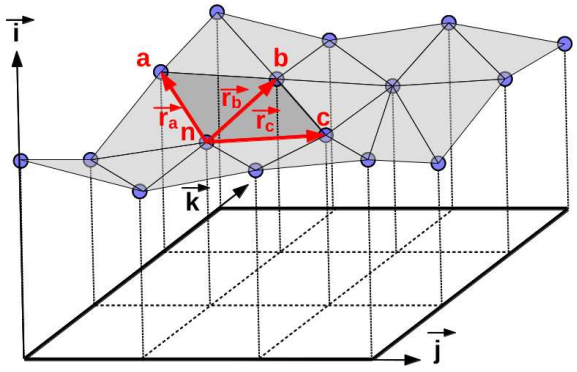

Figure 7.1. Sketch for the calculation of the interfacial area. $\vec{j}$, $\vec{k}$ and $\vec{i}$ are vectors parallel to L_x, L_y and L_z respectively. $\vec{r}_a$ is a vector going from point n to point a, $\vec{r}_b$ is a vector going from point n to point b and $\vec{r}_c$ is a vector going from point n to point c.

with coordinates (x_j, y_k), we look for its neighbours a, b, and c, being:

$$\begin{aligned} a &\equiv (x_{j-1}, y_{k+1}) \\ b &\equiv (x_j, y_{k+1}) \\ c &\equiv (x_{j+1}, y_k) \end{aligned} \tag{7.24}$$

Then we define vectors $\vec{r}_a$, $\vec{r}_b$, and $\vec{r}_c$ as follows:

$$\begin{aligned} \vec{r}_a &= [x(a) - x(n)]\vec{j} + [y(a) - y(n)]\vec{k} + [z(a) - z(n)]\vec{i} \\ \vec{r}_b &= [x(b) - x(n)]\vec{j} + [y(b) - y(n)]\vec{k} + [z(b) - z(n)]\vec{i} \\ \vec{r}_c &= [x(c) - x(n)]\vec{j} + [y(c) - y(n)]\vec{k} + [z(c) - z(n)]\vec{i} \end{aligned} \tag{7.25}$$

Once we have these vectors, we can calculate the area of the individual triangles Δnab and Δnbc as:

$$\begin{aligned} A(\Delta nab) &= \tfrac{1}{2}\sqrt{\vec{r}_a \times \vec{r}_b} \\ A(\Delta nbc) &= \tfrac{1}{2}\sqrt{\vec{r}_b \times \vec{r}_c} \end{aligned} \tag{7.26}$$

which allows us to calculate the area corresponding to point n_{jk} as:

$$A(n_{jk}) = A(\Delta n_{jk}ab) + A(\Delta n_{jk}bc) \tag{7.27}$$

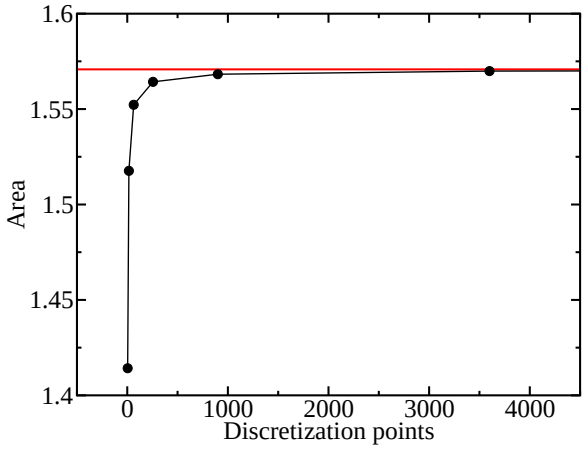

Figure 7.2. Area calculated for a semicylinder of radius 0.5 and length 1 as a function of discretization points. Red solid line corresponds to the analytic area, $\pi/2$.

By doing this for all the points of the lattice we can calculate the total area corresponding to the intrinsic surface as:

$$A = \sum_j \sum_k A(n_{jk}) \tag{7.28}$$

It comes from Eq. 7.28 that the value of the total area calculated by this procedure depends on the number of points employed in the discretization. The larger the number of discretization points, the larger the area calculated. However, it is expected that the value of the area converges to a finite value for a given number of discretization points. We have made this test for a simple geometry, a semicylinder of radius 0.5 and length 1. For this geometry its corresponding analytic area is $\pi/2$ so the areas calculated with our procedure should converge to this value. In Fig. 7.2 we plot the area calculated for this geometry as a function of the number of discretization points. As it can be seen our procedure converges to the correct value of the interfacial area for a large enough number of discretization points.

7.5 Results

Our results have been obtained by using different resolutions to locate the interface. The specific values of the analysis parameters employed for each resolution are shown in Table 7.1.

First of all we check if our method for locating the interface gives consistent results regardless of the resolution. With this aim we make use of the capillary wave theory to obtain γ_{lv} and compare our results with that of Ref. [27]. According to the capillary

Set of parameters	Δ/σ	n_0	ρ/particles$\cdot\sigma^{-2}$
1	10.000	44	0.440
2	6.667	20	0.450
3	5.000	11	0.440
4	4.000	7	0.437
5	3.333	5	0.450
6	2.857	4	0.490
7	2.500	3	0.480
8	2.222	2	0.405
9	2.000	1	0.250

Table 7.1. Analysis parameters for different resolutions.

wave theory, the q dependent surface tension of a liquid–vapour interface is given by [28]

$$\gamma_q = \frac{k_B T}{A \langle |h_q|^2 \rangle q^2} \tag{7.29}$$

and it is known that it follows a dependence with q which is given by [17, 29, 30]

$$\gamma_q = \gamma_{lv} + \kappa q^2 + c q^4 \tag{7.30}$$

In Fig. 7.3 we show our results for the capillary wave spectrum of the system of $L = 20\sigma$ for the different resolutions here studied. It can be seen that although the shape of γ_q is different for each resolution, most of them seem to converge to the same value at $q = 0$. To determine this value we fit our data to Eq. 7.30. We show such fits in Fig. 7.3 as solid lines, and the fitting parameters γ_{lv} and κ thus obtained in Table 7.2. By analysing our results we see that all resolutions but the three lower ones report a value for γ_{lv} of $0.73\epsilon\sigma^{-2}$. We compare this value with Ref. [27]. In that work γ_{lv} of a very similar LJ potential is calculated at different temperatures. By extrapolating their results to our temperature (T^*=0.617) a value of $0.78\epsilon\sigma^{-2}$ is obtained. Taking into account that both models are not equal, and that the surface tension is very sensitive to small variations of the potential as shown also in [27], we can conclude that our results are in reasonable good agreement.

As we have seen, besides giving reasonable results, our method for locating the interface is robust for most resolutions, so it appears as a reliable method when calculating γ_{lv}. With respect to the discrepancies observed only for low resolutions (resolutions 1, 2 and 3 in Table 7.1), they appear because of a slow convergence of γ_q, which hampers the extrapolation to $q = 0$ for such a small system.

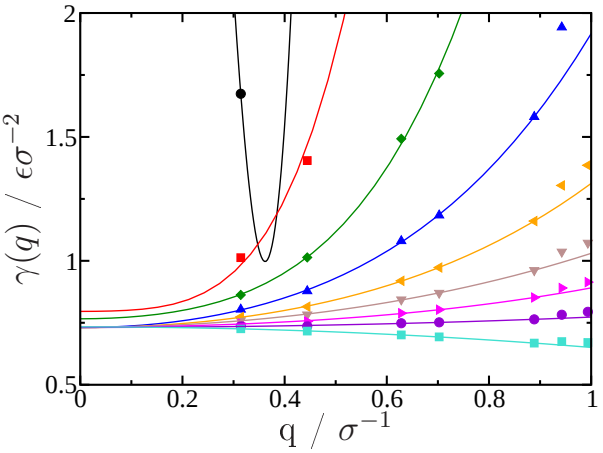

Figure 7.3. Spectrum of capillary waves for the 20x20 system obtained for different resolutions shown in Table 7.1. 1 (black circles), 2 (red squares), 3 (green diamonds), 4 (blue triangles up), 5 (orange triangles left), 6 (brown triangles down), 7 (magenta triangles right), 8 (purple circles) and 9 (cyan squares).

Another interesting issue is the determination of the bending rigidity coefficient, κ. In this case, our results depend on a great extend on the resolution, so a definite value cannot be obtained. However it is worth to notice that the value of this coefficient decreases as we increase the resolution, going from positive to negative values. In Fig. 7.3 we can see that for resolution 8 γ_q is nearly flat in the range of q studied, which is associated with a value of $\kappa = 0$. This result, which is confirmed in Table 7.2, is very interesting since it suggest that we can define an interface with no bending rigidity, and will be discussed later.

Once we are capable of calculating the intrinsic surface area in a reliable way we test Eq. 7.15 to prove the validity of our model. To do this we calculate $f(\Delta A)$ for our L=20σ system. In order to determine it we make use of the parameters of resolution 6 to calculate the intrinsic surface area of our configurations. Then the probability of a given value of ΔA is obtained by making an histogram of ΔA with bin width of 0.1σ. Finally we calculate $\Delta G/k_BT$ via Eq. 7.13. We show our results as green diamonds in Fig. 7.4. We fit our data to Eq. 7.15 (red solid line) and compare it with a fit to a gaussian distribution (black dashed line). As it can be seen the fit to Eq. 7.15 is clearly better showing the goodness of our model to describe the functionality of $f(\Delta A)$. This result reveals that although we obtain the increments of the surface area from the random variable h_q, which follows a gaussian distribution, our random variable ΔA follows a Gamma distribution as shown in the theory.

Given that our model is capable of describing $f(\Delta A)$ we should be able to obtain $\langle\gamma\rangle$ via Eq. 7.15 from the linear coefficient of our fit. The value thus obtained is $0.99\epsilon\sigma^{-2}$. It is noteworthy that this value is higher than that shown in Table 7.2 for

Resolution	$\gamma_{lv}/\epsilon\sigma^{-2}$	κ/ϵ	$\langle\gamma\rangle/\epsilon\sigma^{-2}$
1	12.17	-170.61	2.41
2	0.79	0.38	1.62
3	0.76	0.73	1.26
4	0.73	0.67	1.14
5	0.73	0.41	1.21
6	0.73	0.26	0.99
7	0.73	0.13	0.88
8	0.73	0.04	0.75
9	0.73	-0.08	0.59

Table 7.2. Columns 2 and 3: fitting parameters of the capillary wave spectrum to $\gamma_q = \gamma_{lv} + \kappa q^2 + cq^4$ for different resolutions. Column 4: $\langle\gamma\rangle$ obtained from fitting the data in Fig. 7.6 to Eq. 7.15.

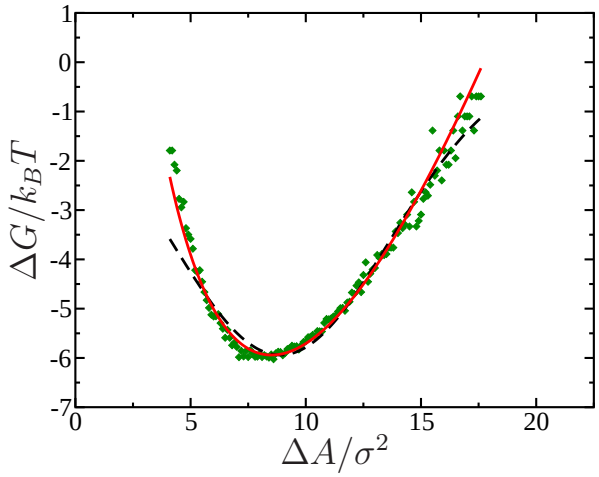

Figure 7.4. Symbols: free energy of the 20x20 system obtained for resolution 6. Solid red line correspond to a fit to Eq. 7.15. Black dashed line correspond to a fit to a gaussian distribution of $f(\Delta A)$.

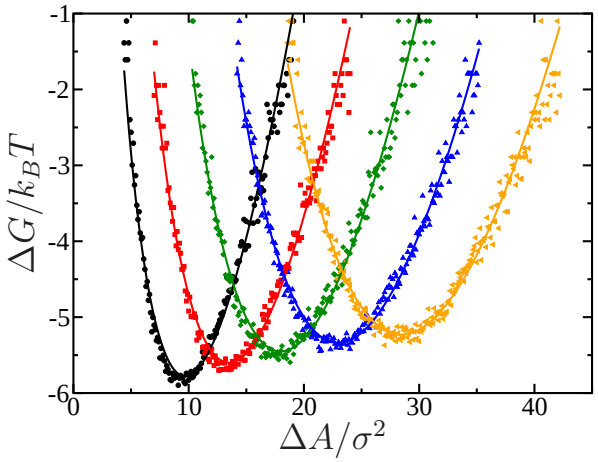

Figure 7.5. Free energy for different nominal areas obtained with the set of parameters 6 from Table 7.1. From left to right: 12x12 (black circles), 14x14 (red squares), 16x16 (green diamonds), 18x18 (blue triangles up) and 20x20 (orange triangles left).

the same resolution. However, this is expected since $\langle\gamma\rangle$ does not correspond to γ_{lv} necessarily but to an average of γ_q as seen in Eq. 7.16 instead.

We now check if our results for $\langle\gamma\rangle$ depend on the nominal area of the interface. With this aim we calculate $\Delta G/k_BT$ for the different system sizes here studied and plot it versus ΔA in Fig. 7.5. By fitting our data to Eq. 7.15 we obtain values for $\langle\gamma\rangle$ of 1.00, 1.00, 0.98, 0.99 and 0.99 $\epsilon\sigma^{-2}$ for systems with lateral areas of 12, 14, 16, 18 and 20 σ, respectively. These results show that our model provides robust values for $\langle\gamma\rangle$ irrespective of the nominal interfacial area.

Finally we want to analyse the dependence of $\langle\gamma\rangle$ with the resolution. For this task we use our system of L=20σ. In Fig. 7.6 we plot $\Delta G/k_BT$ vs ΔA for all the resolutions given in Table 7.1, together with their corresponding fits to Eq. 7.15. The values of $\langle\gamma\rangle$ thus calculated are shown in the fourth column of Table 7.2. It is clear from that table that $\langle\gamma\rangle$ depends on the resolution to a high extent. The results show an evident decrease of the value of $\langle\gamma\rangle$ as the resolution is increased, moving to values even lower than that of $0.73\epsilon\sigma^{-2}$ corresponding to the thermodynamic limit.

7.6 Discussion

For a given surface, which is defined at the molecular scale, we can identify different intrinsic surfaces depending on the resolution to locate it.

By taking a look to Fig. 7.3 we can see that the values of γ_q usually increase with the wavevector, being this increase more pronounced for low resolutions. Taking this fact into account and given that $\langle\gamma\rangle$ is an average of γ_q as shown in Eq. 7.16, it is

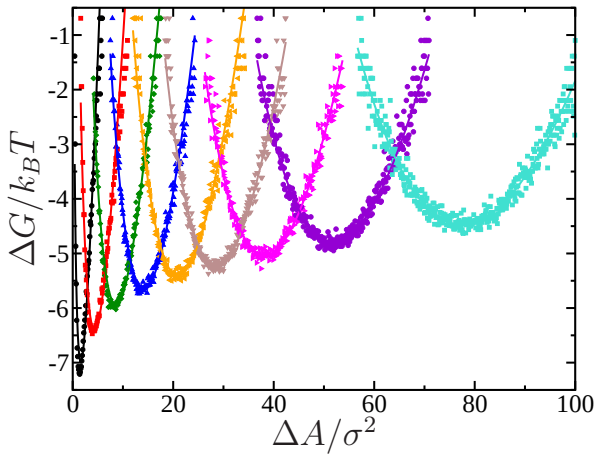

Figure 7.6. Free energy of the 20x20 system obtained for different resolutions shown in Table 7.1. From left to right: 1 (black circles), 2 (red squares), 3 (green diamonds), 4 (blue triangles up), 5 (orange triangles left), 6 (brown triangles down), 7 (magenta triangles right), 8 (purple circles) and 9 (cyan squares).

expected to obtain a value of $\langle\gamma\rangle$ which decreases with increasing resolution. We confirm this behaviour by obtaining $\langle\gamma\rangle$ for different resolutions from the intrinsic surface area distributions.

In spite of the simplicity of our method for locating the interface, we can be confident in our results since more precise methods, such as the Intrinsic Surface Method, have shown the same dependence of γ_q with resolution [31].

However, this result is at odds with expectations from Eq. 7.19. In principle, as the resolution employed for locating the interface is increased, one should be able to obtain meaningful information of wavevectors of higher value. In this sense, one would expect to obtain higher values of $\langle\gamma\rangle$ for high resolutions since the value of q_{max} is increased.

In order to clarify this misleading behaviour we take a look to Fig. 7.6. There it can be clearly seen that the shape of the -ln of the Gamma distribution depends strongly on the arbitrary choice of the intrinsic surface. The region to the left of the minimum is mainly dictated by the number of surface modes chosen to describe the intrinsic surface. The region to the right of the minimum, on the other hand, depends on an average surface tension, which is also dependent on the choice of the intrinsic surface. The theoretical expectation is that the average surface tension should increase with the resolution as κq_{max}^2, where κ is the bending rigidity and q_{max} is the maximum wavevector that can be meaningfully described by the degree of resolution with which the intrinsic surface is determined. However, since κ also depends on the choice of interface in a non-trivial manner, we find that in fact the average surface tension actually decreases as the resolution is increased. At sufficiently large resolution, κ vanishes and then the average surface tension coincides with the expected macroscopic surface tension. Although this

can explain the behaviour of γ_q it cannot provide us the correct value of γ_{lv} since the value of q_{max} remains unknown.

Alternatively, we could use Eq. 7.22 to obtain $\langle\gamma\rangle$. In this expression both $\langle\gamma\rangle$ and $\langle\Delta A\rangle$ depend on the resolution. The dependence of both magnitudes follows opposite trends with $\langle\gamma\rangle$ decreasing for high resolutions and $\langle\Delta A\rangle$ increasing. In this sense, the product $\langle\gamma\rangle \cdot \langle\Delta A\rangle$ would be expected to be constant leading to a density of interfacial energy $\langle\Delta H\rangle / A_0$, which is an intensive property of the system.

Finally, we focus our attention on the definition of the intrinsic surface area. This definition is a matter of debate as it determines the value of many thermodynamic properties. Our results for the surface tension of Fig. 7.3 show that γ_q is nearly flat for resolution number 8 (purple curve). This means that for this resolution the bending coefficient is nearly zero, so the surface thus calculated has no bending rigidity. It is very interesting to see that this is the only resolution that provides the correct value of the surface tension when the area probability is analysed. In this sense it would be desirable to find an effective way of locating an interface with no bending rigidity since it would provide a way of obtaining the surface tension directly.

7.7 Conclusions

In this chapter we have studied the intrinsic area probability distribution of an undulating fluid interface subject to thermal capillary waves.

The distribution is a result between competing free energy contributions. An enthalpic like contribution penalizes the increase of the surface area. An entropic contribution, on the other hand, favors a rough interface with large surface area. Our simulation results confirm that as a result of this competition, the intrinsic surface area follows a Gamma distribution, as expected from our theoretical model.

Our study hinges on some of the puzzling and long standing problems of capillary wave theory, which are essentially unavoidable inconsistencies that appear at short lengthscales in statistical mechanical coarse graining approaches.

According to statistical mechanics, the probability of a given microscopic configuration depends precisely on the microscopic Hamiltonian via the Boltzmann weight $exp(-\beta H)$. In capillary wave theory, one attempts to weight the probability of specific surface configurations by measuring solely the surface area of that configuration, as $\approx exp(-\beta\gamma\Delta A)$. Unfortunately, the surface area is not unambiguously defined, but rather, depends on an arbitrary choice of the intrinsic surface. Accordingly, we find that choices that result in a larger surface area, ΔA, will need to assume a smaller surface tension γ in order to produce the correct invariant Boltzmann factor for that configuration.

Despite this inconsistency, we find that the small lengthscale details related to the

choice of intrinsic surface do not upset the consistency of capillary wave theory at small wavevectors, so that for reasonable choices of the intrinsic surface the $q = 0$ limit of the spectrum of fluctuations consistently provides the expected surface tension.

Bibliography

[1] J. Rowlinson and B. Widom, *Molecular Theory of Capillarity*. Oxford: Clarendon, 1982.

[2] S. A. Safran, *Statistical Thermodynamics of Surfaces, Interfaces and Membranes*. Reading: Addison-Wesley, 1994.

[3] N. Goldenfeld, *Lectures on Phase Transitions and the Renormalization Group*. Reading, Massachusetts: Perseus Books, 1992.

[4] F. P. Buff, R. A. Lovett, and F. H. Stillinger, "Interfacial density profile for fluids in the critical region," *Phys. Rev. Lett.*, vol. 15, pp. 621–623, Oct 1965.

[5] J. D. Weeks, "Structure and thermodynamics of the liquid–vapor interface," *J. Chem. Phys.*, vol. 67, no. 7, pp. 3106–3121, 1977.

[6] R. Evans, "The nature of the liquid-vapor interface and other topics in the statistical mechanics of non-uniform fluids," vol. 28, pp. 143–200, 1979.

[7] D. Nelson, T. Piran, and S. Weinberg, *Statistical Mechanics of Membranes and Surfaces*. Word Scientific, Singapore, 2004.

[8] J. D. Weeks, W. van Saarloos, D. Bedeaux, and E. Blokhuis, "Consistency of capillary wave theory in three dimensions: Divergence of the interface width and agreement with density functional theory," *J. Chem. Phys.*, vol. 91, no. 10, pp. 6494–6504, 1989.

[9] M. Requardt and H. Wagner, "Does the three-dimensional capillary wave model lead to a universally valid and pathology-free description of the liquid-vapor interface nearg=0? a controversial point of view," vol. 64, no. 3-4, pp. 807–821, 1991.

[10] M. R. Moldover and R. W. Gammon, "Capillary rise, wetting layers, and critical phenomena in confined geometry," *The Journal of Chemical Physics*, vol. 80, no. 1, pp. 528–535, 1984.

[11] R. F. Kayser, "Effect of capillary waves on surface tension," *Phys. Rev. A*, vol. 33, pp. 1948–1956, Mar 1986.

[12] M. P. Gelfand and M. E. Fisher, "Finite-size effects in fluid interfaces," vol. 166, no. 1, pp. 1–74, 1990.

[13] D. Jasnow and J. Rudnick, "Interfacial profile in three dimensions," *Phys. Rev. Lett.*, vol. 41, pp. 698–701, Sep 1978.

[14] D. Jasnow, "Critical phenomena at interfaces," *Rep. Prog. Phys.*, vol. 47, no. 9, p. 1059, 1984.

[15] M. Köpf and G. Münster, "Interfacial roughening in field theory," *Journal of Statistical Physics*, vol. 132, no. 3, pp. 417–430, 2008.

[16] D. A. McQuarrie, *Statistical Mechanics*. New York: Harper & Row, 1976.

[17] Meunier, J., "Liquid interfaces : role of the fluctuations and analysis of ellipsometry and reflectivity measurements," *J. Phys. France*, vol. 48, no. 10, pp. 1819–1831, 1987.

[18] D. Bonn and G. Wegdam, "Capillary waves and ellipsometry experiments," *JP-I*, vol. 2, pp. 1755–1764, 1992.

[19] D. B. Abraham, "Capillary waves and surface tension: An exactly solvable model," *Phys. Rev. Lett.*, vol. 47, pp. 545–548, Aug 1981.

[20] M.-D. Lacasse, G. S. Grest, and A. J. Levine, "Capillary-wave and chain-length effects at polymer/polymer interfaces," *Phys. Rev. Lett.*, vol. 80, pp. 309–312, Jan 1998.

[21] P. Moschopoulos, "The distribution of the sum of independent gamma random variables," *Annals of the Institute of Statistical Mathematics*, vol. 37, no. 1, pp. 541–544, 1985.

[22] J. Broughton and G. Gilmer, "Surface free energy and stress of a lennard-jones crystal," *Acta Metallurgica*, vol. 31, no. 6, pp. 845 – 851, 1983.

[23] H. Berendsen, D. van der Spoel, and R. van Drunen, "Gromacs: A message passing parallel molecular dynamics implementation," *Computer Physics Communications*, vol. 91, no. 1 - 3, pp. 43 – 56, 1995.

[24] B. Hess, C. Kutzner, D. van der Spoel, and E. Lindahl, "Gromacs 4: Algorithms for highly efficient, load-balanced, and scalable molecular simulation," *Journal of Chemical Theory and Computation*, vol. 4, no. 3, pp. 435–447, 2008.

[25] J. Q. Broughton and G. H. Gilmer, "Molecular dynamics of the crystal-fluid interface. V. Structure and dynamics of crystal-melt systems," *The Journal of Chemical Physics*, vol. 84, no. 10, pp. 5749–5758, 1986.

[26] G. Bussi, D. Donadio, and M. Parrinello, "Canonical sampling through velocity rescaling," *J. Chem. Phys.*, vol. 126, no. 1, p. 014101, 2007.

[27] A. Trokhymchuk and J. Alejandre, "Computer simulations of liquid/vapor interface in Lennard-Jones fluids: Some questions and answers," *The Journal of Chemical Physics*, vol. 111, no. 18, 1999.

[28] V. Privman, "Fluctuating interfaces, surface tension and capillary waves: An introduction," vol. 3, pp. 857–877, 1992.

[29] K. R. Mecke and S. Dietrich, "Effective hamiltonian for liquid-vapor interfaces," *Phys. Rev. E*, vol. 59, pp. 6766–6784, Jun 1999.

[30] E. M. Blokhuis, "On the spectrum of fluctuations of a liquid surface: From the molecular scale to the macroscopic scale," *J. Chem. Phys.*, vol. 130, p. 074701, 2009.

[31] P. Tarazona and E. Chacón, "Monte carlo intrinsic surfaces and density profiles for liquid surfaces," *Phys. Rev. B*, vol. 70, p. 235407, Dec 2004.

Appendix A: Obtaining the distribution of area increments

In this appendix we show how to get to Eq. 7.11 by using the Moschopoulos method [21].

Let x_i to be a random variable which follows a Gamma distribution

$$f(x_i) = \frac{x_i^{\alpha_i - 1} e^{-x_i/\beta_i}}{\beta_i \Gamma(\alpha_i)} \equiv G(x_i; \alpha_i; \beta_i) \tag{7.31}$$

and let y to be sum of this variable

$$y = x_1 + x_2 + ... + x_n \tag{7.32}$$

Then

$$f(y) = C \sum_k \delta_k y^{\rho+k-1} \frac{e^{-y/\beta_1}}{\Gamma(\rho+k)\beta_1^{\rho+k}} \tag{7.33}$$

with

$$C = \prod_i (\beta_1/\beta_i)^{\alpha_i} = \prod_i (\beta_1/\beta_i)^{1/2} \tag{7.34}$$

$$\rho = \sum_i \alpha_i = n/2 \tag{7.35}$$

$$\delta_{k+1} = \frac{1}{k+1} \sum_{i=1}^{k+1} i\gamma_i \delta_{k+1-i} \quad ; \quad \delta_0 = 1 \tag{7.36}$$

$$\gamma_k = \sum_{i=1}^{n} \alpha_i \left(1 - \beta_1/\beta_i\right)^k / k \tag{7.37}$$

In our particular case we have:

$$x_i = q^2 h_q^2 \quad ; \quad \beta_i = \tfrac{2}{\beta A_0 \gamma_i} \quad ; \quad \alpha_i = 1/2 \tag{7.38}$$

so we can now define

$$\begin{gathered} \gamma_1 = \tfrac{1}{2} \textstyle\sum_i (1 - \beta_1/\beta_i) = \tfrac{1}{2} \sum_i \tfrac{\Delta\beta}{\beta_i} \\ \delta_1 = \gamma_1 \delta_0 = \gamma_1 \end{gathered} \tag{7.39}$$

By plugging these equations in Eq. 7.33 we get:

$$f(y) = \prod_i \left(\frac{\beta_1}{\beta_i}\right)^{1/2} \left\{ \frac{y^{n/2-1}}{\Gamma(n/2)\beta_1^{n/2}} + \frac{1}{2} \sum_i \frac{\Delta\beta}{\beta_i} \frac{y^{n/2}}{\Gamma(n/2+1)\beta_1^{n/2+1}} + ... \right\} e^{-y/\beta_1} \tag{7.40}$$

Considering Eq. 7.38 we can note that

$$\frac{\Delta\beta}{\beta_i} = 1 - \frac{\beta_1}{\beta_i} = 1 - \frac{\gamma_i}{\gamma_1} = \frac{\gamma_1 - \gamma_i}{\gamma_1} = -\frac{\Delta\gamma_i}{\gamma_1} \tag{7.41}$$

so by plugging Eq. 7.41 into Eq. 7.40 we obtain:

$$f(y) = \prod_i \left(\frac{\gamma_i}{\gamma_1}\right)^{(1/2)} \left\{ \frac{y^{n/2-1}}{\Gamma(n/2)\beta_1^{n/2}} - \frac{1}{2}\sum_i \frac{\Delta\gamma_i}{\gamma_i} \frac{y^{n/2}}{\Gamma(n/2+1)\beta_1^{n/2+1}} + ... \right\} e^{-y/\beta_1} \tag{7.42}$$

If we now make use of Eq. 7.38 we can rewrite Eq. 7.42 to get:

$$f(y) = \frac{\prod_i \left(\frac{\beta A_0 \gamma_i}{2}\right)^{(1/2)}}{\Gamma(n/2)} \left\{ y^{n/2-1} - \frac{1}{4}\frac{\Gamma(n/2)}{\Gamma(n/2+1)} \beta A_0 \sum_i \Delta\gamma_i y^{n/2} + ... \right\} e^{\frac{1}{2}\beta A_0 \gamma_1 y} \tag{7.43}$$

We now take into account that

$$y = \sum_q q^2 h_q^2 = \frac{2\Delta A}{A_0} \tag{7.44}$$

so we can finally rewrite Eq. 7.43 as

$$f(\Delta A) = \frac{\prod_i (\beta\gamma_i)^{1/2}}{\Gamma(n/2)} \left[\Delta A^{n/2-1} - \frac{1}{n}\sum_i \beta\Delta\gamma_i \Delta A^{n/2} + ... \right] e^{-\beta\gamma_1 \Delta A} \tag{7.45}$$

Here it can be clearly seen that the equation above is the same as Eq. 7.11 with $i = q$ and $\gamma_1 = \gamma_{lv}$.

Part III

Conclusiones y Perspectivas

Conclusiones y Perspectivas

En esta tesis hemos hecho un estudio de las ondas capilares mediante técnicas de simulación, abordando una serie de interfases de distinta complejidad: interfases adsorbidas, interfases sólido–fluido e interfases sólido–vapor.

De nuestro estudio se desprenden conclusiones tanto de comportamiento físico general, como de comportamiento específico de los modelos estudiados; además de conclusiones sobre la metodología empleada. A continuación se enuncian las conclusiones más relevantes de esta tesis, ordenadas en estos tres bloques:

En cuanto a comportamiento físico general llegamos a las siguientes conclusiones:

- La tensión superficial de una película líquida adsorbida sobre un sustrato sólido depende del espesor de la película. Para el caso de sistemas dominados por fuerzas de largo alcance, esta dependencia se puede explicar recurriendo únicamente al potencial que el sustrado sólido ejerce sobre la película adsorbida.

  Como consecuencia de esta dependencia, la longitud de correlación paralela se ve modificada en un término dado por la longitud de correlación de la fase volumétrica.

- Las ondas superficiales de la interfase sólido–líquido relajan en dos regímenes temporales distintos. El régimen lento sigue una relajación exponencial cuyo tiempo característico escala con q^{-2}, corresponidente a un proceso de difusión del frente interfacial. Este proceso de difusión se debe al continuo fundir y recristalizar de la interfase. El proceso de relajación rápido está posíblemente relacionado con modos de vibración del cristal y con vibraciones atómicas.

- Las distribución de probabilidad del area intrínseca de una interfase rugosa depende de un balance entre entropía, que tiende a aumentar el area, y la energía interfacial, que tiende a disminuirla. Los valores obtenidos de la energía libre interfacial a partir de dichas distribuciones dependen del grado de resolución con que se mide el área. Existe un grado de resolución microscópico para el que se obtiene una energía interfacial coincidente con la tensión superficial macroscópica.

  En cuanto al comportamiento de sistemas específicos tenemos:

Para el cloruro sódico:

- La energía libre interfacial sólido–líquido del modelo de Tosi-Fumi para el cloruro sódico, obtenida mediante el método de fluctuaciones capilares, es de 89 ± 6 mN·m^{-1}. Este resultado concuerda con el obtenido mediante el cálculo de barreras de nucleación mientras que discrepa con el calculado mediante la medida del ángulo de contacto. Dentro de la precisión de nuestros cálculos todas las caras tienen la misma energía interfacial.

- La rigidez de algunas orientaciones del cloruro sódico presenta un decaimiento anómalo al acercarnos al límite termodinámico. Este decaimiento puede ser interpretado como una inestabilidad de las caras implicadas para algunas direcciones de propagación de la onda.

Para las interfases del agua:

- Las interfases hielo/agua y hielo/vapor del modelo de agua TIP4P/2005 son rugosas.

- La energía libre interfacial promedio sólido–líquido para el modelo de agua TIP4P/2005 es de 27 ± 2 mN·m^{-1}. Aunque no se ha podido resolver la anistropía de la energía libre interfacial de cada una de las caras, nuestros resultados sugieren que el plano basal es el menos energético.

- El modelo TIP4P/2005 predice que al exponer la cara basal del hielo hexagonal al agua la interfase presenta regiones alternantes de hielo cúbico y hexagonal que cambian dinámicamente.

- En las interfases hielo/vapor aparece una película de agua adsorbida sobre el hielo que da lugar a dos superficies: la hielo/película y la película/vapor. Hemos encontrado que a escala microscópica ambas superficies fluctuan como las correspondientes superficies independientes hielo/agua y hielo/vapor. Sin embargo a escala mesoscópica dichas fluctuaciones están subordinadas a la rugosidad del sólido subyacente y vienen dadas por una rigidez que es la suma de la rigidez hielo/agua y la tensión superficial agua/vapor.

Y como aspectos metodológicos:

- El método de ondas capilares es capaz de proporcionar valores de la energía interfacial de superficies rugosas, tanto sólido–vapor como sólido–líquido, para sistemas de distinta naturaleza y complejidad tales como esferas duras, Lennard–Jones, agua o cloruro sódico.

- La dependencia de la energía interfacial con la orientación del cristal se puede expandir en cúbicos o esféricos armónicos para obtener la energía libre interfacial a partir de la rigidez de sistemas cúbicos o hexagonales, respectivamente.

- La precisión del método de ondas capilares no ha permitido, en la mayor parte de los sistemas estudiados, resolver la anisotropía de la energía interfacial con respecto a la orientación del sólido.

- Las geometrías interfaciales quasi-monodimensionales y bidimensionales proporcionan el mismo valor de la rigidez interfacial para todos los sistemas y orientaciones cristalográficas estudiadas en esta tesis, con la excepción de aquellas que muestran el plano (111).

Además de las conclusiones que se detallan anteriormente esta tesis deja abiertos interesantes aspectos sobre el comportamiento de las interfases. En este sentido, a continuación se discuten dichos aspectos que podrían ser objeto de futuras investigaciones inspiradas en el trabajo aquí realizado:

- Como mostramos en el capítulo 4, el comportamiento de la rigidez para algunas caras y direcciones de propagación de onda del NaCl es anómalo debido a que ésta disminuye en lugar de converger a medida que nos acercamos al límite termodinámico. Este comportamiento no había sido anteriormente observado en ningún sistema y sugiere que hay ciertas caras del NaCl que son inestables. Esta interesante observación deja varias preguntas abiertas: ¿Será cero o incluso alcanzará la rigidez valores negativos en el límite termodinámico para las orientaciones "inestables"? ¿Por qué las anomalías surgen solo en un sólido iónico como el NaCl y no en los demás sistemas estudiados? ¿Por qué algunas orientaciones presentan la anomalía y otras no?

- Desde un punto de vista metodológico es importante saber si el empleo de sistemas con interfases quasi-monodimensionales es una forma fiable de reducir el tamaño del sistema, dado que el comportamiento de las ondas capilares se puede ver afectado por la dimensionalidad de la interfase. En los capítulos 3 y 4 hemos comparado interfases quasi-monodimensionales y bidimensionales, y en todos los casos, salvo para el plano 111, los resultados son equivalentes. Esta observación da lugar a las siguientes preguntas: ¿Por qué únicamente este plano muestra discrepancias entre ambas geometrías? ¿Se debe a efectos de apilamiento en la dirección perpendicular al plano?

- En el capítulo 6 hemos estudiado la rugosidad de la interfase hielo/vapor para el modelo TIP4P/2005. El modelo teórico que desarrollamos, basado en la amplitud

de las ondas capilares parece indicar que estas interfases son rugosas. Sin embargo, debido al tamaño finito de nuestro sistema, no estamos en disposición de afirmar si este comportamiento se mantiene hasta el límite termodinámico. Esto, unido al hecho de que la inspección visual de las interfases sugiere la presencia de interfases claramente escalonadas, nos hace plantearnos la pregunta: ¿Son realmente rugosas las interfases hielo/vapor?

- En el capítulo 7 mostramos que es posible obtener una tensión superficial promedio, $\langle\gamma\rangle$, a partir de la distribución de probabilidad de área de la superficie intrínseca. Hemos comprobado que $\langle\gamma\rangle$ está relacionada con la tensión superficial macroscópica γ_{lv}, y que además depende del grado de resolución con que se localiza la interfase. En este sentido sería muy interesante resolver las siguientes preguntas: ¿Es posible establecer a priori con que grado de resolución hay que medir el area intrínseca para que $\langle\gamma\rangle$ coincida con γ_{lv}? Y en caso negativo ¿sería posible obtener γ_{lv} a partir de $\langle\gamma\rangle$ para cualquier grado de resolución?